Synaptic dysfunction in lysosomal storage disorders: pathogenic mechanism and potential therapeutic applications

Camila de Britto Pará de Aragão

Faculty of Medicine

Department of Anatomy and Cell Biology

McGill University, Montreal

Quebec, Canada

August 2020

A thesis submitted to McGill University in partial fulfillment of the requirements of the degree of Doctor of Philosophy

TABLE OF CONTENTS

LIST OF FIGURES

LIST OF TABLES

LIST OF ABBREVIATIONS

3OST	Glucosaminyl 3-O-sulfotransferase
6OST	6-O-sulfotransferase
ACSF	Artificial cerebrospinal fluid
AD	Alzheimer's disease
ARF	ADP-ribosylation factor
ALS	Amyotrophic lateral sclerosis
AP	Adaptor protein
ApoE	Apolipoprotein E
AP-2	Adaptor protein 2
ARSA	Arylsulfatase A
AZ	Active zone
BBB	Blood-brain barrier
BLA	Basolateral amygdala
BMDM	Bone marrow-derived macrophages
BM	Bone marrow
BMT	Bone marrow transplantation
Camk2a	Calcium-calmodulin dependent protein kinase 2 alpha

CLEAR	Coordinated lysosomal expression and regulation
Cltc	Clathrin heavy chain
CNS	Central nervous system
CS	Chondroitin sulfate
CTSD	Cathepsin D
DI	Discrimination index
DIV	Day *in vitro*
Dnm1	Dynamin 1
DS	Dermatan sulfate
ECM	Extracellular matrix
EM	Electron microscopy
EPSC	Excitatory postsynaptic currents
FA	Formic acid
fEPSP	Field excitatory postsynaptic potential
FTD	Frontotemporal dementia
FTLD	Frontotemporal lobar degeneration
GABA	γ-aminobutyric acid
GAG	Glycosaminoglycan
GAP	GTPase-activating protein

Gcase	β-glucocerebrosidase
GD	Gaucher disease
GGA	Golgi-localizing, γ-adaptin ear domain homology
GlcA	Glucuronic acid
GlcNAc	N-acetylglucosamine
GM-CSF	Granulocyte-macrophage colony stimulating factor
HA	Hyaluronic acid
HGSNAT	Heparan sulphate acetyl-CoA: α-glucosaminide N-acetyltransferase
HS	Heparan sulfate
HSC	Hematopoietic stem cell
HSCT	Hematopoietic stem cell transplantation
HSPC	Hematopoietic stem and progenitor cells
HSPG	Heparan sulfate proteoglycan
IPSC	Inhibitory postsynaptic currents
KS	Keratan sulfate
LGNd	Lateral geniculate nuclei
LV	Lentivirus
LVST	Lentiviral stem cell transplantation
LSD	Lysosomal storage disease

LTD	Long-term depression
LTP	Long-term potentiation
M6P	Mannose-6-phoshphate
MCSF	Macrophage colony stimulating factor
mEPSC	Miniature excitatory postsynaptic currents
mIPSC	Miniature inhibitory postsynaptic currents
ML IV	Mucolipidosis IV
MLD	Metachromatic leukodystrophy
MMP-9	Matrix metalloproteinase 9
MOI	Multiplicity of infection
MPS	Mucopolysaccharidosis
NAGLU	α-N-acetylglucosaminidase
Napb	NSF attachment protein beta
NCL	Neuronal ceroid lipofuscinosis
NDST	N-deacetylase/N-sulfotransferase
NF-M	Neurofilament medium chain
NPC1	Niemann-Pick type C 1
NEU1	Neuraminidase 1
NF-M	Neurofilament medium chain

Nlgn2	Neuroligin 2
PD	Parkinson’s disease
PPCA	Protective protein cathepsin A
PSD	Postsynaptic density
PSD-95	Postsynaptic density protein 95
Pttg1	Pituitary tumor transforming gene 1
RBC	Red blood cells
ROCK 2	Rho-associated coiled-coil containing protein kinase 2
RRP	Readily releasable pool
SGSH	N-sulfoglucosamine sulfohydrolase
Stxbp1	Syntaxin-binding protein 1
SC	Schaffer collaterals
sIPSC	Spontaneous inhibitory postsynaptic currents
SV	Synaptic vesicles
Syn1	Synapsin 1
Syn2	Synapsin 2
TDP-43	TAR-DNA binding protein 43
TEM	Transmission electron microscopy
TFEB	Transcription factor EB

TGN	Trans-Golgi network
TLR	Toll-like receptors
TTX	Tetrodotoxin
UBR-4	Ubiquitin protein ligase E3 component n-recognin 4
VDAC1	Voltage-dependent anion channel 1
vGAT	Vesicular GABA transporter
vGLUT1	Vesicular glutamate transporter
VPM	Ventral posterior medial
ZFN	Zinc finger nuclease

ABSTRACT

Sanfilippo type C syndrome (mucopolysaccharidosis type IIIC; MPS IIIC) is a rare untreatable genetic disorder caused by mutations in the *HGSNAT* gene and lysosomal storage of heparan sulfate. In humans, MPS IIIC causes rapid neurological decline, however the mechanisms underlying the neuropathophysiology are still not well understood, preventing the development of a therapy. HGSNAT KO (knockout) mice show hyperactivity and progressive cognitive decline matching the phenotype of patients.

The first aim of this thesis was to analyze the synapses in cultured hippocampal neurons and in the CA1 neurons in the HGSNAT KO and WT (wild-type) mice. Our study revealed that MPS IIIC neurons show a decrease or abnormal distribution of multiple synaptic markers including synapsin-1 and the glutamatergic synaptic protein PSD-95. Importantly, deficiency of PSD-95 in MPS IIIC neurons was rescued by treatment with lentivirus encoding human HGSNAT enzyme. The formation and maturation of dendritic spines, in the MPS IIIC pyramidal neurons, were significantly reduced as early as postnatal day 10. In cultured neurons the spines were immature, reflecting a shift from an axospinous to an axodendritic pattern. MPS IIIC neurons present a disorganised microtubule network, sparse synaptic vesicles and reduced postsynaptic densities. Proteomic analysis of synaptosomes showed a reduction of vesicle trafficking-associated proteins (Clathrin, Dynamin, AP-2 subunits, Rab7a) suggestive of defects in axonal transport, recycling of synaptic vesicle proteins and reduced microtubule stability. This data was confirmed by live imaging of cultured neurons, that showed that synaptic vesicles in the MPS IIIC neurons moved slower than in the WT cells. Electrophysiological studies revealed that MPS IIIC neurons presented altered frequency and amplitude of miniature excitatory postsynaptic currents (mEPSCs) while inhibitory currents

(mIPSCs) were not affected, indicating an imbalance between excitatory and inhibitory signaling.

After the characterization of synaptic abnormalities, in the second aim of this thesis, I tested a new therapeutic approach based on correcting the HGSNAT enzyme deficiency in the brain microglia cells by lentiviral (LV) gene transfer of hematopoietic stem and progenitor cells (HSPC) followed by their transplantation in mice. Microglia derived from monocytes expressing supraphysiological levels of HGSNAT are able to cross the blood brain barrier and digest the excess of heparan sulfate accumulated in the brain of MPS IIIC mice, thus reducing neuroinflammation and neurodegeneration. In addition, most recent evidence from our laboratory suggests that HGSNAT can be secreted from the cells overexpressing this enzyme as part of exosomes and transferred to the neighbouring cells including neurons. HSPC transduced with LV-HGSNAT-GFP with 11.4-fold increase of HGSNAT activity were transplanted in HGSNAT KO mice myeloablated with busulfan. Thirteen weeks post-transplantation, mice showed increased levels of HGSNAT in the bone marrow and the spleen which correlated with the engraftment rate. Moreover, despite the lack of significant HGSNAT increase in the brain, we observed partial rescue of hyperactivity and reduced anxiety in treated mice.

Altogether, our results provide strong evidence that hippocampal neurons in MPS IIIC mice show abnormal neurotransmission, especially in the excitatory synapses. This correlates with reduced synaptic plasticity and long-term potentiation and most probably contributes to memory impairment, cognitive defects and seizures in Sanfilippo patients. Based on our results, *ex vivo* gene therapy may become an effective approach to treat this disorder, the design of the clinical LV vector should be improved to achieve higher levels of HGSNAT activity in the brain.

RÉSUMÉ

Le syndrome de Sanfilippo de type IIIC (mucopolysaccharidose de type IIIC; MPS IIIC) est une maladie génétique rare non traitable causée par des mutations du gène *HGSNAT* et le stockage lysosomal de l'héparane sulfate. Chez l'homme, la MPS IIIC provoque un déclin neurologique rapide, mais les mécanismes sous-jacents à la neuropathophysiologie ne sont toujours pas bien compris, limitant le développement d'une thérapie efficace. Les souris HGSNAT KO (knockout) présentent une hyperactivité et un déclin cognitif progressif correspondant au phénotype des patients humains.

Le premier objectif de cette thèse était d'analyser les synapses dans les neurones hippocampiques en culture et dans les neurones CA1 chez les souris HGSNAT KO et WT (wild-type). Notre étude a révélé que les neurones MPS IIIC montrent une diminution ou une distribution anormale de plusieurs marqueurs synaptiques, notamment la synapsine-1 et la protéine synaptique glutamatergique PSD-95. Surtout, la carence en PSD-95 dans les neurones MPS IIIC a été secourue par un traitement avec un lentivirus codant pour l'enzyme HGSNAT humaine. La formation et la maturation des épines dendritiques dans les neurones pyramidaux MPS IIIC ont été considérablement réduites dès le 10e jour postnatal. Dans les neurones en culture, les épines étaient immatures, reflétant un passage d'un schéma axospineux à un schéma axodendritique. Les neurones MPS IIIC présentent un réseau de microtubules désorganisé, des vésicules synaptiques clairsemées et des densités postsynaptiques réduites. L'analyse protéomique des synaptosomes a montré une réduction des protéines associées au trafic des vésicules (Clathrine, Dynamine, sous-unités AP-2, Rab7a) suggérant des défauts dans le transport axonal, le recyclage des protéines des vésicules synaptiques et une stabilité réduite des microtubules. Ces données ont été confirmées par l'imagerie en direct de neurones en culture, qui a montré que les vésicules synaptiques dans les neurones MPS IIIC se déplaçaient plus lentement que dans les cellules WT. Des études électrophysiologiques ont révélé que les

neurones MPS IIIC présentaient une fréquence et une amplitude de courants post-synaptiques excitateurs miniatures (mEPSC) altérées alors que les courants inhibiteurs (mIPSC) n'étaient pas affectés, indiquant un déséquilibre entre la signalisation excitatrice et inhibitrice.

Après la caractérisation des anomalies synaptiques, dans le deuxième objectif de cette thèse, j'ai testé une nouvelle approche thérapeutique basée sur la correction du déficit enzymatique HGSNAT dans les cellules microgliales du cerveau par transfert de gène par lentivirus dans des cellules souches et progénitrices hématopoïétiques (HSPC), suivi par leur transplantation chez la souris. Les microglies dérivées de monocytes exprimant des niveaux supraphysiologiques de HGSNAT sont capables de traverser la barrière hémato-encéphalique et de digérer l'excès d'héparane sulfate accumulé dans le cerveau des souris MPS IIIC, réduisant ainsi la neuroinflammation et la neurodégénérescence. En outre, les résultats les plus récents de notre laboratoire suggèrent que l'enzyme HGSNAT peut être sécrétée par les cellules surexprimant cette enzyme par le biais des exosomes et transférée aux cellules voisines, y compris les neurones. Les HSPC transduites avec le LV-HGSNAT-GFP avaient une augmentation de l'activité de HGSNAT de 11,4 fois et ont été transplantées à des souris HGSNAT KO myéloablées avec du busulfan. Treize semaines après la transplantation, les souris ont montré des niveaux accrus de HGSNAT dans la moelle osseuse et la rate, qui corrélaient avec le taux de greffe. De plus, malgré l'absence d'augmentation significative du HGSNAT dans le cerveau, nous avons observé un sauvetage partiel de l'hyperactivité et une diminution de l'anxiété chez les souris traitées.

Dans l'ensemble, nos résultats fournissent des preuves solides que les neurones hippocampiques chez les souris MPS IIIC présentent une neurotransmission anormale, en particulier dans les synapses excitatrices. Cela est en corrélation avec une plasticité synaptique et une potentialisation à long terme réduites et contribue très probablement à des troubles de la mémoire, des défauts cognitifs et des convulsions chez les patients de Sanfilippo. Sur la base

de nos résultats, la thérapie génique combinée à la thérapie par cellules souches peut devenir une approche efficace pour traiter ce trouble, et la conception du vecteur clinique lentiviral devrait être améliorée pour atteindre des niveaux plus élevés d'activité HGSNAT dans le cerveau.

ACKNOWLEDGEMENTS

First, I would like to express my sincere gratitude to my PhD supervisor, Dr. Alexey V. Pshezhetsky, for the continuous support and for believing in my ability to manage this research project. During my whole stay in his lab, he was always present and was always confident about my good work and perseverance. Additionally, he was always willing to give me precious opportunities to share my research in several international conferences and he also allowed me to do several trainings in the field of microscopy. I can say that during my stay in his laboratory, I grew as a person, as professional and as a researcher.

I would like to extend my thanks to my advisory committee members for their insightful feedbacks and encouragements, Dr. Carlos Morales, for his co-supervision and for his precious advice on electron microscopy, Dr. Christian Rocheleau, Dr. Nathalie Lamarche-Vane and a special thanks to Dr. Graziella Di Cristo who gave me valuable insights to develop this research project and for letting me use her confocal microscope in which I collected most of the images for this thesis.

I thank all the funding agencies that supported me with doctoral scholarships, the Applied Network of Genetic Medicine (RMGA), the Merit Scholarship Program for Foreign Students (PBEEE, Quebec-Brazil) and the Quebec Research Fund – Nature and Technologies (FRQNT). I also owe a big thanks to the patients' organizations JLK Sanfilippo Research Foundation, Jonah's Just Begun and The Sanfilippo Children's Research Foundation for supporting our lab.

I would like to thank my former and current lab fellows who were always willing to offer me help and to teach me something new, Anne Fougerat, Victoria Smutova, Carla Martins, Afitz da Silva, Ekaterina Demina, Poulome Bose, Mahsa Taherzadeh, Kalley Kho, Rachel Héon-Roberts and Tianmeng Xu. I give a special thanks to Xuefang Pan, who taught

me many lab techniques and helped me handling mice. She always supported me during the difficult times and believed in me even when I did not believe myself and for that I will always be thankful.

This work would not be possible without the collaborations we made. So, I would like to thank Dr. Jean-Claude Lacaille and Erika Freemantle from the University of Montreal, to kindly perform the miniature postsynaptic currents in my neuronal cultures. Dr. Pierre Thibault and Éric Bonneil from the Proteomics Platform of University of Montreal for performing the proteomic analysis of my samples. Jeannie Mui from the Facility for Electron Microscopy Research (FEMR) from McGill University for preparing my samples for electron microscopy and for giving me training to use the electron microscope. Dr. Christian Beauséjour and Gaël Moquin-Beaudry for producing the lentiviral plasmid used in this thesis. Dr. Monty McKillop and Dr. Jeffrey Medin for producing the lentivirus. Ines Boufaied for the help on the flow cytometry analysis.

I also would like to thank the personnel from the CHU Sainte-Justine animal facility, in special Véronique and Sonja for taking so good care of the animals used in this thesis, for their help in defining the pregnancy stage of the animals used for neuronal cultures and also for their valuable help in injecting cells through the tail vein of mice.

My path in research would not be possible without the guidance of Dr. Luiz Santana, so I would like to show my appreciation for all the support that he gave to me during my BSc and MSc in Brazil, for giving me the opportunity to develop the passion for the rare diseases and for helping me to get in touch with my current supervisor. I have a lot of admiration for his work and I am forever grateful to have him now as a friend.

I would like to thank my family, my parents Jayme and Lília, for a whole life support of my education and my emotional health, my sister Luciana and my brother Rodrigo, that I

know, even not so close to me, they were cheering for my success and also my big sister, Tatiana, who has been my biggest friend and, together with my parents, helped me a lot during my worst moments of depression. I also want to express my gratitude to my ex-husband Marcio, even though our paths went in different ways, I could not start this PhD without his support, especially in in the beginning, when we decided to leave Brazil to start a life in Canada. Last, but not least, I give a special thanks to my boyfriend, Leandro, for putting up with my frustrations and depressive moments in a daily basis, always showing me that he was there for me and helping me to go through my final years of this PhD.

PREFACE

This thesis is written in the traditional format in accordance with the Graduate and Postdoctoral Studies of McGill University thesis guidelines for thesis preparation. Literature review and the data presented here is the original work of the candidate.

CONTRIBUTION TO ORIGINAL KNOWLEDGE

In my doctoral research project, I demonstrated that synaptic defects occur in the neurons of MPS IIIC mice. I specifically demonstrated that synaptic spines in neurons of MPS IIIC mice are immature and show reduced density. I have also shown that levels of synaptic markers synapsin 1 and PSD-95 are reduced in the neurons of MPS IIIC mice as well as in post-mortem brain tissues of patients with different types of MPS and that these proteins can be rescued by correcting the primary genetic defect with a lentiviral vector. Using electron microscopy, I established that neurons of MPS IIIC mice present scarce density of synaptic vesicles and reduced size of postsynaptic densities. MPS IIIC mouse neurons present alterations in frequency and amplitude of miniature excitatory and inhibitory postsynaptic currents, disorganised microtubule network and partially impaired axonal transport of synaptic proteins. Together, our experiments demonstrate that lysosomal storage causes alterations in synaptic structure and abnormalities in neurotransmission originating from disrupted vesicular transport and preceding the first cognitive symptoms. In this thesis, I also demonstrate for the first time the use of lentiviral-mediated gene stem cell therapy to treat MPS IIIC. I designed a pilot study with 4 MPS IIIC mice and I found that this therapeutic approach is able to increase the HGSNAT enzyme in the spleen and partially corrects the anxiety and hyperactivity of MPS IIIC mice. Even though I did not achieve overall correction of HGSNAT expression in all the organs, this pilot study gives enough insights to ameliorate the transduction and transplantation protocol for future studies.

During the development of my doctoral project, I participated in the following publications:

1. Xuefang Pan, Camila De Britto Para De Aragão, Juan P. Velasco-Martin, David A. Priestman, Harry Y. Wu, Kohta Takahashi, Kazunori Yamaguchi,

Luisella Sturiale, Domenico Garozzo, Frances M. Platt, Nathalie Lamarche-Vane, Carlos R. Morales, Taeko Miyagi and Alexey V. Pshezhetsky. (2017). Neuraminidases 3 and 4 regulate neuronal function by catabolizing brain gangliosides. The FASEB Journal. : 1-17.

2. Camila Pará, Poulomee Bose and Alexey V. Pshezhetsky. Neuropathophysiology of lysosomal storage diseases: synaptic dysfunction as a starting point for disease progression. Journal of Clinical Medicine. 2020 Feb 25;9(3). pii: E616. doi: 10.3390/jcm9030616.

3. Camila de Britto Pará de Aragão, Luigi Bruno, Poulomee Bose, Xuefang Pan, Chanshuai Han, Peter S. McPherson, Erika Freemantle, Jean-Claude Lacaille, Éric Bonneil, Pierre Thibault, Claire O'Leary, Brian Bigger, Graziella DiCristo, Carlos R. Morales**,** Alexey V. Pshezhetsky. Early defects in lysosomal storage disease disrupt excitatory synaptic transmission. (In communication, bioRxiv 2020.07.06.186809; doi: https://doi.org/10.1101/2020.07.06.186809).

CONTRIBUTION OF AUTHORS

Camila de Britto Pará de Aragão: Prepared neuronal, HEK293, HSPC and macrophage cell cultures, performed immunofluorescence analyses of samples with confocal, spinning disk and electron microscopes, performed western blots, collected and processed mouse tissues, measured enzyme activity in cells and mouse tissues, cloned pDY plasmid into pENTR1A plasmid, performed transduction experiments, processed samples for flow cytometry, isolated synaptosomes, collected and transplanted hematopoietic stem and progenitor cells, performed the behavior tests, performed all statistical analyses and microscope image processing.

Erika Freemantle: Performed the whole-cell patch clamp to record miniature events in cultured neurons.

Éric Bonneil: Performed the LC/MS proteomic analysis of synaptosomes.

Jeannie Mui: Processed samples and prepared grids for electron microscopy.

Gaël Moquin-Beaudry: Produced the lentiviral plasmid.

Monty McKillop: Produced the lentivirus.

Ines Boufaied: Performed cell sorting and assisted with flow cytometry analysis.

Chapter 1

INTRODUCTION AND LITERATURE REVIEW

A. Lysosomes and lysosomal storage diseases

1. Lysosomes

Lysosomes are membrane-enclosed cellular compartments, containing more than 60 soluble hydrolytic enzymes (1) including proteases, nucleases, glycosidases, lipases, phospholipases, phosphatases and sulfatases. The lysosomal lumen has acidic pH that varies between 4.6 and 5.0 (2, 3). Newly synthetized soluble proteins that are targeted to the lysosomes are modified in the trans-Golgi network (TGN) with a mannose-6-phosphate (M6P) group that binds to M6P receptors in the TGN helping their packaging in clathrin-coated vesicles that are directed to the lysosomes (2, 4). In contrast, the delivery of newly synthesized lysosomal membrane proteins from the TGN does not require their binding to M6P receptors, and occurs either by an indirect route via the plasma membrane or by a direct intracellular route (4) involving clathrin-adaptor proteins that recognize short amino acid motifs (i.e., tyrosine- or dileucine-based motifs) located in a cytosolic region of the lysosomal transmembrane protein, usually in its N- or C-terminal end (5). The consensus sequences for the tyrosine-based motifs, are (Fx)NPXY and (G)YXXØ, where Phi is a bulky hydrophobic amino acid. For the dileucine-based signals, the sequences are [DE]XXXL[LI] or DXXLL (5, 6). YXXØ and [DE]XXXL[LI] signals are recognized with high specificity by the adaptor protein (AP) complexes AP-1, AP-2, AP-3, and AP-4, whereas DXXLL signals are recognized by another family of adaptors known as GGAs (Golgi-localizing, γ-adaptin ear domain homology, ADP-ribosylation factor (ARF)-binding proteins) (6). Other non-conventional transport mechanisms of lysosomal transmembrane proteins have also been described with different motifs, for

example, lysosomal-associated transmembrane proteins (LAPTM5, LAPTM4A and LAPTM4B) require PY motifs (5).

The lysosomal biogenesis is regulated by the transcription factor EB (TFEB) that triggers the expression of lysosomal genes. When TFEB is translocated from the cytoplasm to the nucleus, it activates the Coordinated Lysosomal Expression And Regulation (CLEAR) network (7). TFEB is phosphorylated at the lysosomal surface by the mTORC1 kinase (8) that causes its activation and translocation to the nuclei leading to an increase in a number of lysosomes and enhanced catabolic activity of the cell (9, 10). TFEB is inactivated by the phosphatase calcineurin, which activity in turn is induced by calcium release from lysosomes (11).

Lysosomes degrade materials arriving from four different pathways, macroautophagy, endo(phago)cytosis, microautophagy and chaperone-mediated autophagy (12) (Fig. 1). During macroautophagy, formation of autophagosomes starts with the encapsulation of cytosolic components such as denatured proteins, lipids, carbohydrates and old or damaged organelles. Further autophagosomes fuse with lysosomes and late endosomes forming autolysosomes, for degradation of their content by lysosomal hydrolases (13). The degradation of material taken up by endocytosis occurs within late endosomes and multivesicular bodies. The late endosome membrane fuses with the lysosomal membrane either in a complete manner or transiently (kiss-and-run). The microautophagy involves the pinocytosis of cytosolic regions surrounding lysosomes and during the chaperone-mediated autophagy proteins expressing KFERQ motif are delivered to the lysosome by the chaperone Hsc-70 that interacts with the lysosomal membrane protein 2A (LAMP-2A) (12).

Besides being the terminal degradative compartment of the endocytic pathway and participating in digestion of intracellular material segregated during the process of autophagy,

(4) lysosomes are also involved in the various other physiological processes such as cholesterol homeostasis, plasma membrane repair, bone and tissue remodeling, pathogen defense cell death and cell signaling (14).

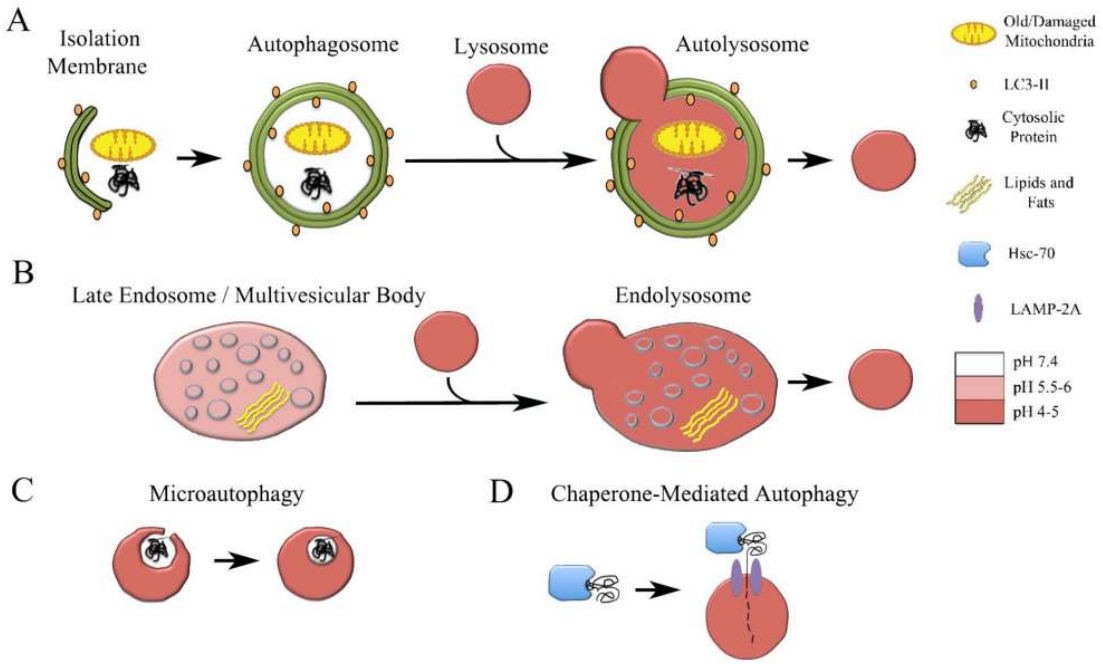

Figure 1: Lysosomes as catabolic centers of the cell.

Lysosomes are involved in degradation of cellular material arriving from 4 different pathways: macroautophagy (A), endocytosis (B), microautophagy (C) and chaperone-mediated autophagy (D). Reproduced with permission from Platt *et al.* 2012, copyright© Platt *et al.* 2012 under a Creative Commons License (Attribution–Noncommercial–Share Alike 3.0 Unported license, as described at http://creativecommons.org/licenses/by-nc-sa/3.0/).

2. Lysosomal storage diseases (LSD)

Lysosomal storage diseases (LSD) are inherited errors of metabolism characterized by a primary accumulation of specific macromolecules or monomeric compounds inside organelles of the endosomal-autophagic-lysosomal system. The concept of a biochemical mechanism of LSD has been first provided by H. G. Hers (15) who discovered that deficiency of acid α-glucosidase causes accumulation of glycogen in several tissues of patients affected with Pompe disease (glycogen storage disease type II), a severe hereditary disease manifesting with cardiomyopathy and muscle weakness.

The clinical phenotype, the age of onset and the spectrum of symptoms presented by the LSD patients vary depending on the degree of protein function affected by specific mutations, the nature of the stored material and the cell/tissue types where the storage occurs (12). Of more than 50 LSD described in humans, the majority are caused by mutations in one of the lysosomal hydrolases. However, defective catabolite export and membrane trafficking may also lead do traffic jams and to secondary storage in the lysosome (1). Besides, LSD can also be caused by defects in non-enzymatic lysosomal proteins, involved in protection/activation of lysosomal enzymes, their post-translational processing, or trafficking to the lysosome as well as lysosomal membrane channels and transporters necessary to maintain the function of the lysosome (16). For instance, one of the causative genes for neuronal ceroid lipofuscinosis (NCL, Batten disease), *CLN8*, encodes for a protein regulating the lysosomal biogenesis, therefore its deficiency leads to depletion of multiple lysosomal enzymes (17).

Historically LSD are classified according to the nature of the accumulating substrate such as mucopolysaccharidoses (MPS), sphingolipidoses, olygosaccharidoses (glycoproteinoses), glycogenoses and lipidoses (16). Although individually rare, combined, LSD have a frequency as high as 1 per 2200 live births (18). While majority of them are

autosomal recessive, Fabry, Danon and Hunter (MPS II) syndromes are X-linked (19). In all known recessive LSD, ~50% reduction of the catabolic activity does not cause lysosomal storage phenotype in the cells, however recent studies provided evidence that haploid insufficiency of several lysosomal enzymes is the major genetic cause of adult neurological diseases, primarily Parkinson's but the pathological mechanisms are yet to be discovered (20).

3. Neurological forms of LSD (20)

About two-thirds of patients with LSD exhibit at least some neurological impairment (21) but the symptoms are heterogeneous and emerge at different ages. In children, these manifestations can include seizures, hearing loss, intellectual disability, neuromotor regression, developmental delay and extra-pyramidal signs. In late-onset neurological LSD, adults can experience depression, dementia, psychosis and other neurological deficits (19, 22, 23). Neurological manifestations are typically present in MPS I, II, III and VII, sphingolipidoses (G_{M1} and G_{M2} gangliosidosis, Gaucher disease, Niemann-Pick disease, metachromatic leukodystrophy, Krabbe disease and Farber disease), mucolipidoses, oligosaccharidoses (alpha- and beta-mannosidosis, fucosidosis, Schindler disease, aspartylglucosaminuria, sialidosis and galactosialidosis), multiple sulfatase deficiency, and NCL (23). A list of the neurological forms of LSD is summarized in Table 1.

Table 1: List of LSD with neurological involvement (23, 24).

General class	Class of Storage	Diseases	Affected peptide
Sphingolipidosis	Gangliosides	Tay-Sachs	Alfa subunit of hexosaminidase
		Sandhoff disease	Beta subunit of hexosaminidase
		Deficiency of the GM2 activator protein	GM2 activator
		GM1 gangliosidoses	β-galactosidase
	Glucocerebroside	Gaucher disease (types 2 and 3)	Glucocerebrosidase
	Sphingomyelin	Niemann-Pick disease (type A and B)	Sphingomyelinase
		Niemann-Pick disease type C	NPC1 and NPC2
	Sulfatide	Metachromatic leukodystrophy	Arylsulfatase A; Protein activator saposin B
	Galactocerebroside	Krabbe disease	Galactocerebrosidase
	Ceramide	Farber disease	Acid ceramidase
Neuronal ceroid lipofuscinosis	Auto-fluorescent lipopigment	CLN1	Palmitoyl-protein thioesterase-1
		CLN2	Tripeptidyl peptidase 1
		CLN3	CLN3 protein
		CLN4	cysteine string protein
		CLN5	CLN5 protein
		CLN6	CLN6 protein
		CLN7	CLN7 protein
		CLN8	transmembrane protein of the endoplasmic reticulum
		CLN10	aspartic protease cathepsin D gene
Mucopolysaccharidosis	Dermatan and heparan sulphate	MPS I	α-L-iduronidase
		MPS II	Iduronate-2-sulfatase
	Heparan sulphate	MPS III A	heparin-N-sulfatase
		MPS III B	α-N-acetylglucosaminidase
		MPS III C	CoA:a-glucosaminide-N-acetyltransferase
		MPS III D	N-acetylglucosamine6-sulfatase
	Dermatan Sulfate, heparan sulfate and chondroitin sulfate	MPS VII	β-glucuronidase
Mucolipidosis		ML II	N-acetylglucosamine-1-phosphotransferase
		ML III Alpha/beta	N-acetylglucosamine-1-phosphotransferase
		ML III gamma	N-acetylglucosamine-1-phosphotransferase gamma subunit
		ML IV	transient receptor potential cation channel MCOLN1
Multiple Enzyme deficiencies	Sulfatides, GAGs	Multiple sulfatase deficiency	sulfatase-modifying factor-1
		Galactosialidosis	cathepsin A (secondary ß-galactosidase and neuraminidase deficiency)

Oligosaccharidosis	mannose-containing residues	Alpha-Mannosidosis	α-mannosidase
		Beta-Mannosidosis	β-mannosidase
	fucose containing poly-and oligosaccharides and glycolipids	Fucosidosis	Fucosidase
	sialylated and asialoglycopeptides	Schindler disease type I and III	α-N-acetylgalactosaminidase
	Sialoligosaccharides glycopeptides	Sialidosis	neuraminidase 1
	aspartylglucosamine	Aspartylglycosaminuria	N-aspartyl-betaglucosaminidase

Importantly, neurological LSD show genetic association and share multiple pathophysiological mechanisms with other neurodegenerative diseases such as Parkinson's disease (PD), Alzheimer disease (AD), Dementia with Lewy Bodies and others. For instance, mutations in the gene *GBA*, encoding for β-glucocerebrosidase (Gcase), deficient in Gaucher disease (GD), are the highest genetic risk factor associated with PD (25-27). Besides, pathogenic variants in *SCARB2*, encoding the receptor required for lysosomal targeting of GCase, and *PSAP*, encoding the precursor of saposin C, a requisite co-factor for enzymatic GCase activity on its natural substrate glucosylceramide, also enhance PD susceptibility(28). The molecular basis of this association is still unclear but the increased levels of glucosylceramide, have been linked to α-synuclein accumulation, the main cause of neuronal death in PD (29). Other genes encoding for lysosomal enzymes and associated with PD susceptibility include *SMPD1* (acid sphingomyelinase) *CTSD (*cathepsin D*)*, *ASAH1* (acid ceramidase) and GALC (lysosomal galactosylceramidase) (28, 30).

On the other side, proteins that have been implemented into pathology of adult neurodegenerative diseases, such as tau protein and amyloid-β peptides are also involved in CNS pathology in multiple LSD including MPS (reviewed in (31)). Other examples include TAR-DNA binding protein 43 (TDP-43) and TMEM106B. TDP-43 that forms cytoplasmic aggregates in neurons of amyotrophic lateral sclerosis (ALS), AD and frontotemporal lobar

degeneration (FTLD) patients (32) also shows altered expression and mislocalization in the Niemann-Pick type C mouse and in a human neuronal model of the disease in which the mutated gene is the *NPC1* (33). TMEM106B associated with frontotemporal dementia (FTD) and PD (34) is involved in lysosomal trafficking and function(35-37). Finally, dominant mutations in *NAGLU* (α-N-acetylglucosaminidase) which is responsible for the degradation of heparan sulfate (HS) in the lysosomes lead to a late dominant painful axonal sensory neuropathy and sensory ataxia, while recessive variants cause the lysosomal storage disease MPS IIIB (38).

4. Sialidosis

Sialidosis, also known as mucolipidosis I or "cherry-red spot myoclonus syndrome"(39), is a rare autosomal recessive LSD that results in storage of sialic acid-rich macromolecules and urinary excretion of sialyl-oligosaccharides due to mutations in the lysosomal sialidase (neuraminidase 1; NEU1) gene (40, 41). In a clinically related disease, galactosialidosis, the mutations in protective protein/cathepsin A (PPCA) lead to secondary combined deficiency of β-galactosidase and neuraminidase, since these enzymes are active only when they form a lysosomal multienzyme complex with PPCA (reviewed in Pshezhetsky and Ashmarina, 2001) (42). Sialidosis can be divided in two distinct forms according to the phenotype. Patients with sialidosis type I develop myoclonus and mild ataxia and have a juvenile or adult onset while patients with sialidosis type II have an early infantile, neonatal or even prenatal onset, with several dysmorphisms, such as coarse facial features and skeletal dysplasia, psychomotor delay, ataxia and generalized seizures (43). Because even in type I patients myoclonus usually worsens with age and is often associated with seizures and ataxia, sialidosis is included in the group of progressive myoclonus epilepsies (39, 44).

5. Mucopolysaccharidoses (MPS)

MPS are LSD resulting from a deficiency of any of 11 lysosomal enzymes involved in the degradation of specific glycosaminoglycans (GAG) (16). Seven subtypes of MPS are currently known (Table 2). Typical symptoms of MPS can include coarse face, developmental delay, dysostosis multiplex, hearing loss and hepatosplenomegaly. Patients affected with MPS I, II, III and VII also present involvement of the central nervous system (CNS), such as neurodegeneration and progressive mental retardation, presumably resulting from impaired or incomplete degradation of HS (45).

Table 2: Classification of MPS.

DS, dermatan sulfate; HS, heparan sulfate; KS, keratan sulfate; CS, chondroitin sulfate; HA, hyaluronic acid.

Type	Gene/Locus	Deficient Enzyme	GAG accumulated
MPS I (Hurler/Scheie/Hurler-Scheie)	IDUA (4p16)	α-L-iduronidase	DS and HS
MPS II (Hunter)	IDS (Xq28)	Iduronate-2-sulphatase	DS and HS
MPS III (Sanfilippo)			HS
Type A	SGSH (17q25)	Heparan-N-sulfatase	
Type B	NAGLU (17q21)	α-N-acetylglucosaminidase	
Type C	HGSNAT (8p11)	Acetyl CoA: α-Glucosaminide N-acetyltransferase	
Type D	GNS (12q14)	N-acetylglucosamine-6-sulfatase	
MPS IV (Morquio)			KS and CS
Type A	GALNS (16q24)	N-acetylgalactosamine-6-sulfatase	
Type B	GLB1 (3p21	β-Galactosidase	
MPS VI (Maroteaux-Lamy)	ARSB (5q14)	Arylsulfatase B	DS and CS

MPS VII (Sly)	GUSB (7q11)	β-glucuronidase	DS, HS and CS
MPS IX	HYAL1 (3p21)	Hyaluronidase	HA

a) Heparan sulfate (HS)

HS is a GAG composed by a chain of repeated disaccharides (up to 200 units) of N-acetylglucosamine (GlcNAc) and glucuronic acid (GlcA) that are negatively charged due to the presence of both carboxyl and sulfate groups (2). The biosynthesis of HS begins from attachment of the GlcNAc residue to the non-reducing end of the acceptor linkage glucuronosyl-galactosyl-galactosyl-xylosyl (GlcAβ1,3Galβ1,3Galβ1,4Xyl) tetrasaccharide region, covalently bound to a core-protein serine residue (46), by the members of EXTL family of glycosyltransferases (47, 48). The HS chain is further extended by the functional HS-polymerase complex (EXT1 and EXT2 enzymes) that transfers GlcNAc and GlcA residues to the growing polymer (47) (Fig. 2). Several glycosyltransferases, sulfotransferases and an epimerase in the lumen of Golgi apparatus will act together producing the necessary modifications in the structure of HS (49). This includes for example N-deacetylation/N-sulfation of GlcNAc residues by NDST (N-deacetylase/N-sulfotransferase) enzymes and O-sulfation by the glucosaminyl 6-O-sulfotransferases (6OST), and the glucosaminyl 3-O-sulfotransferases (3OST) (46, 47, 49).

HS chains become further attached to core proteins forming heparan sulfate proteoglycans (HSPG) and can be presented at the cell surface (e.g. attached to syndecans and glypicans), and/or in the extracellular matrix (ECM e.g. attached to agrin, perlecan and collagen XVIII in the basement membranes) (47, 50). Some HSPG such as serglycin are also found in secretory vesicles that play a role in packaging granular contents, maintaining proteases in active state and participating in several biological processes such as coagulation, host defense and wound repair (50). HSPG can bind to cytokines, chemokines, growth factors as well as

proteases acting as inhibitors or receptors of these enzymes. Membrane HSPG cooperate with integrins and other cell adhesion receptors to facilitate cell-ECM attachment, cell-cell interactions and cell motility (50).

HSPG metabolic degradation is initiated in the extracellular space. Two endosulfatases (SULF1 and SULF2) remove 6-*O*-sulfate groups from HS (51) and the secreted enzyme heparanase cleaves the extracellular HS chains from core proteins (52). The final degradation of HS chains occurs in the lysosomes through the stepwise action of several hydrolases and one transferase (53). A scheme summarizing HS biosynthesis and degradation is shown on Fig. 2.

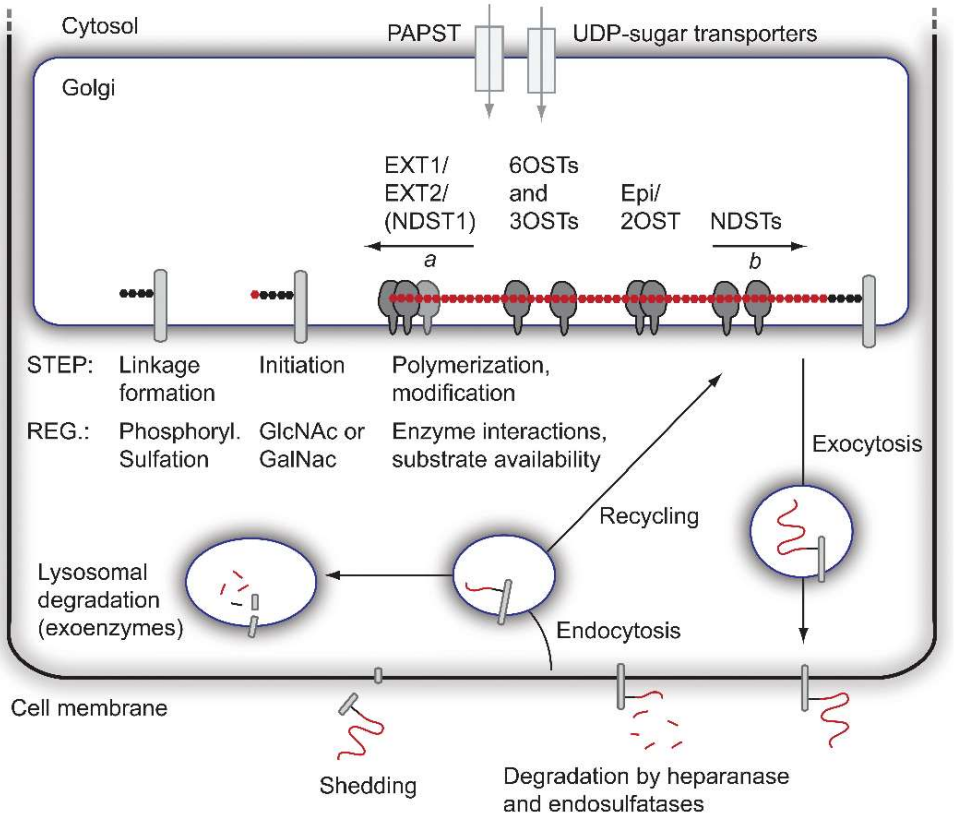

Figure 2: Heparan sulfate metabolism (47).

Reproduced with permission from Kreuger and Kjellén, 2012, copyright© 2012 by SAGE Publications.

b) Mucopolysaccharidosis type III (MPS III, Sanfilippo syndrome)

MPS type III is the most prevalent MPS disorder occurring with a frequency of 0.28–4.1 in 100,000 live births (54, 55). MPS III has four subtypes, A to D, associated with deficiencies of specific enzymes essential for the breakdown of HS (Fig. 3) (56, 57).

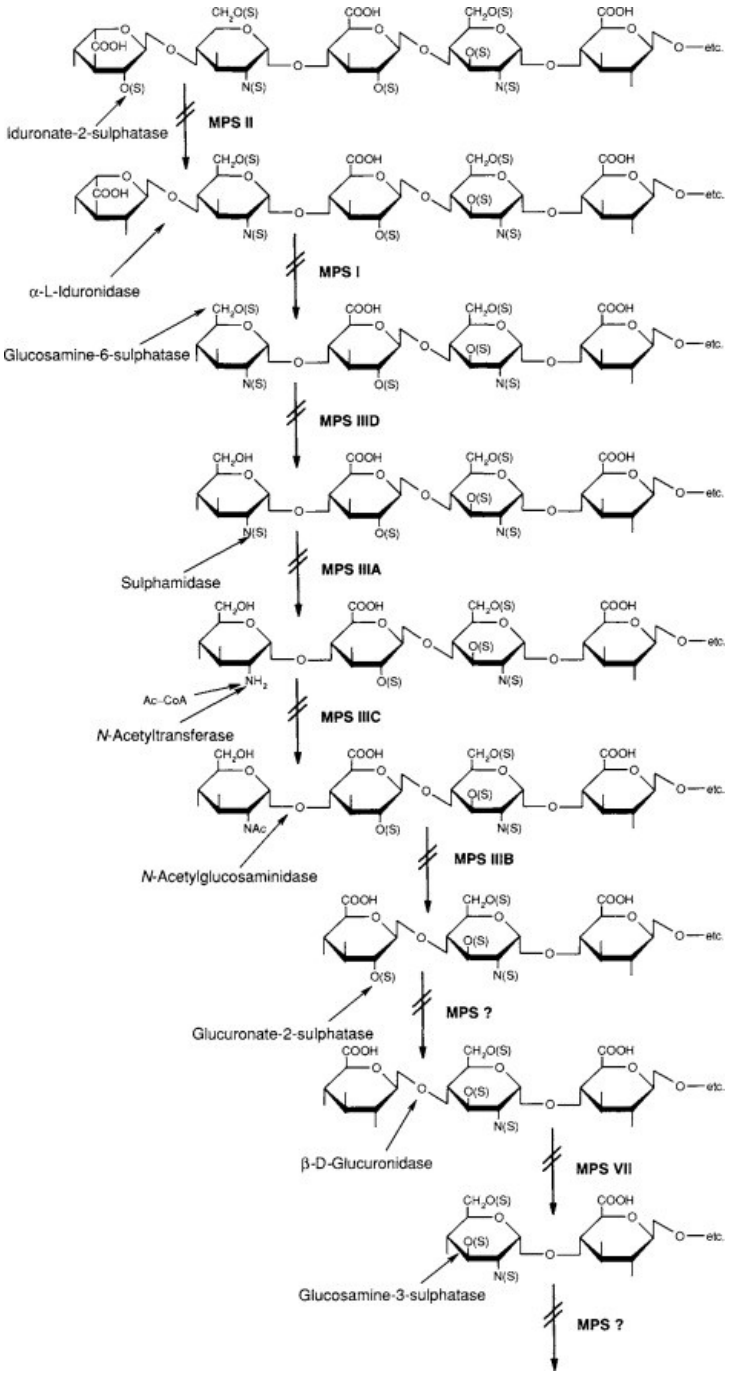

Figure 3: Heparan sulfate catabolic pathway .

Blockage of any of the 8 enzymatic steps of HS degradation leads to its accumulation in the lysosome, causing one of the subtypes of MPS depicted in the diagram. Reproduced with permission from Meikle et al.,2005 (58), copyright© by Elsevier.

As other types of MPS, MPS III is a progressive disorder with a wide spectrum of severity. In the most severe cases, the onset of symptoms can occur at the age from 1 to 3 years. Delay of the cognitive and speech development is often noticed before other symptoms (59). The symptoms manifesting during different phases of the disease progression are summarized in Fig. 4. Facial dysmorphism in MPS III varies in accordance with the disease severity and mildly affected patients often have only slightly coarse facial features (Fig. 5)

Phase*	Signs/Symptoms†
Presymptomatic	Apparently normal development
Phase 1	Neurocognitive
	Developmental delay
	Speech delay
	Somatic
	Mild facial dysmorphism (can be very subtle)
	Frequent ear infections
	Frequent upper respiratory infections
	Cardiac valve disease
	Hernia (umbilical, inguinal)
	Hepatomegaly
	Diarrhoea
Phase 2	Neurocognitive
	Progressive cognitive decline/mental retardation
	Decline in speech/lack of speech
	Behavioural disturbances
	Hyperactivity
	Impulsivity
	Aggression
	Restlessness
	Anxious behaviour
	Compulsive behaviour
	Autistic-like behaviour
	Decline in motor skills
	Seizures
	Somatic (those in phase 1, plus the following)
	Hearing loss
	Orthopaedic manifestations
	Scoliosis
	Kyphosis
	Lumbar lordosis
	Hip dysplasia and pain
	Carpal tunnel syndrome
	Trigger digits
	Joint contractures
Phase 3	Neurocognitive
	Profound mental retardation progressing to vegetative state
	Lack of speech or communication
	Behavioural disturbances cease
	Difficulty swallowing progressing to inability to swallow
	Spasticity
	Seizures
	Somatic
	Those in phases 1 and 2

*The timing of the disease course in attenuated patients is more variable than that seen in severe patients, but progression through these phases is common to all MPS III patients.

†Not all signs and symptoms may be present in any individual patient.

Figure 4: The three phases of MPS III and associated signs and symptoms.

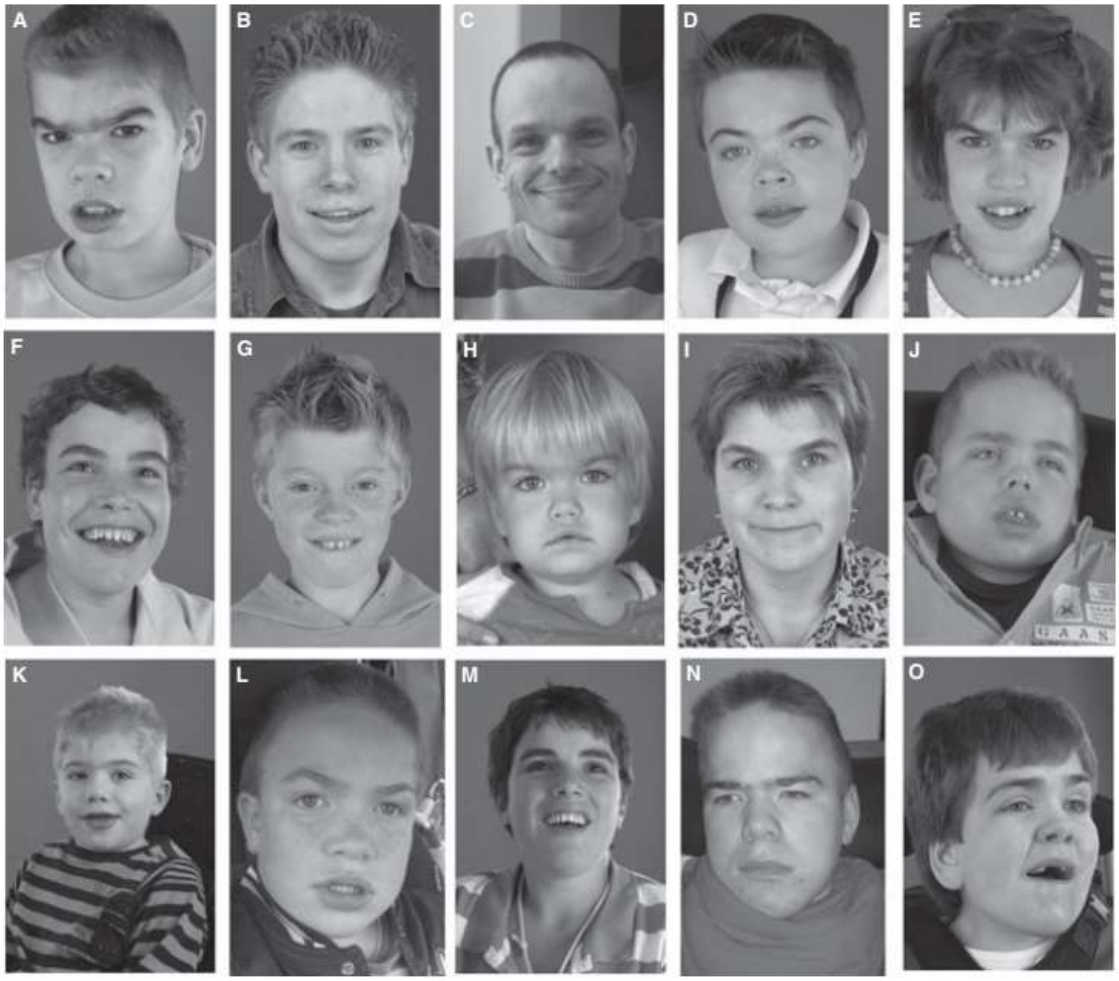

Figure 5: Gallery of facial images of MPS III patients.

(A) male, MPS IIIC, 10 years; (B) male, MPS IIIB, 21 years; (C) male, MPS IIIA, 43 years; (D) male, MPS IIIC, 10 years; (E) female, MPS IIIC, 13 years; (F) female, MPS IIIB, 18 years; (G) male, MPS IIIB, 11 years; (H) female, MPS IIIC, 4 years; (I) female, MPS IIIA, 20 years; (J) male, MPS IIIA, 10 years; (K) male, MPS IIIA, 6 years; (L) male, MPS IIIA, 11 years; (M)

female, MPS IIIB, 20 years; (N) male, MPS IIIA, 12 years; (O) female, MPS IIIA, 14 years. Reproduced with permission from Wijburg *et al*., 2013 (59). Copyright© by Foundation Acta Pædiatrica under the terms of Creative Commons Deed, Attribution 2.5 (CC BY 2.5, https://creativecommons.org/licenses/by/2.5/).

c) MPS IIIC (Sanfilippo syndrome Type C)

MPS III type C is caused by the deficiency of the lysosomal transmembrane enzyme, heparan sulphate acetyl-CoA: α-glucosaminide N-acetyltransferase (HGSNAT). Over 50 mutations affecting all 18 exons and many introns of the gene have been described including nonsense, splice-site, deletions, insertions and missense alterations (60). A list of described mutations is attached in Appendix A, described by Martins *et al.* (2019) (60) Missense mutations result in a single amino acid change that can affect either one of the 11 transmembrane segments of the enzyme as well as the luminal and the cytosolic domains (61), (Fig. 6).

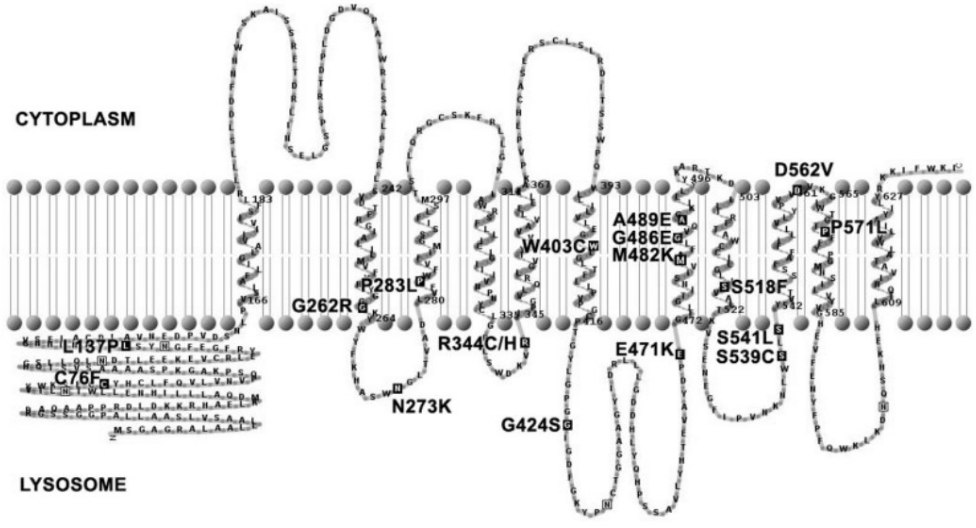

Figure 6: Distribution of some missense mutations in HGSNAT protein.

Mutated residues are shown in white letters in black background and predicted N-glycosylation sites are boxed. Reproduced with permission from Feldhammer *et al*., 2009 (61), copyright© by Human Mutation.

Usually the first symptoms in MPS IIIC patients appear when they are around 3.5-year-old (60). They further suffer from progressive and severe neurological manifestations, such as hyperactivity, aggressiveness, lack of attention, neurocognitive deficiency, macrocephaly, speech and motor problems, coarse facial features, sleep disturbances, neuropsychiatric problems, mental retardation and hearing loss (60, 62). Other frequent symptoms are ear and sinus infections, hypertrichosis, hepatomegaly and dysostosis multiplex.

Studies of animal models for MPS IIIC revealed primary accumulation of HS in the CNS and secondary accumulation of gangliosides and misfolded proteins(63). The undegraded HS acts directly on the Toll-like receptor 4 (TLR4) on brain microglia and activates it, resulting in production of pro-inflammatory cytokines and reactive oxygen species to perpetuate the inflammatory process (64-67). Consequently, MPS IIIC mice develop progressive neuroinflammation, abnormalities in neuronal mitochondrial energy metabolism, impaired autophagy and neurodegeneration (63).

6. Main aspects of CNS pathology in neurological LSD (20).

Neurodegeneration and neuroinflammation manifesting with microgliosis and astrocytosis are described as the most common hallmarks of the brain pathology in neurological LSD with a propensity for an early onset (63, 64, 68-72). In the mouse model of MPS IIIC, for example, astrocytosis and microgliosis are observed as early as at 4 months in the somatosensory cortex, when mice do not yet present behavioral abnormalities (63). HS-derived oligosaccharides, the storage product common to all neurological forms of MPS, and presumably linked to CNS manifestations (45) is directly capable of triggering an inflammatory

response in the CNS by acting on toll-like receptors (TLR) of microglial cells (66). This results in release of pro-inflammatory cytokines such as TNF-α and MIP-1-α (63, 73). In the *Npc1*^{nmf164} mice, the mouse model of Niemann Pick type C 1 (NPC1) with a late onset of the disease, the transmembrane NPC1 that is involved in endosomal lipid sorting and trafficking is mutated. It has been shown in this mouse model that microglia contribute to the degeneration of Purkinje cells by engulfing and destroying their dendrites, in a process called disease-associated microglia, where unknown signals from degenerating neurons promote a transition in the microglia from a homeostatic state to a more proliferative and phagocytic state (74). The same study also reported that microglia accumulated phagosomes and autofluorescent material that coincided with the degeneration of dendrites and Purkinje cells. In a healthy brain, microglial cells are crucial factors modulating neuronal and synaptic development, adult synaptic plasticity and regulation of neurogenesis (75), however, in pathological conditions, their activation leads to the production of inflammatory cytokines that might lead to triggering of neuroinflammatory responses resulting in aggravated cell death.

Similarly to microgliosis, increased abundance and activation of astrocytes are observed in the majority of neurological LSD. Considering important roles of astrocytes in regulation of synaptic strength and plasticity, astrocytosis could be an important contributing factor in the pathological CNS changes associated with these diseases. For instance, HS fragments enhance integrin-based focal adhesions formation and activation in normal mouse astrocytes or in human neuronal progenitors, resulting in cell polarization and migration defects (76) Moreover, in a mouse model of mucolipidosis IV (ML IV), increased GFAP immunoreactivity was observed at 2 and 3 months and coincided with early behavioural deficits. With disease progression GFAP reactivity continued to increase until 7 months when it could be responsible for alterations in synaptic plasticity in the absence of neuronal loss (69). In the neuron-specific GCase knockout mouse model of Gaucher disease (*Gba*$^{flox/flox(Nestin\text{-}Cre)}$),

astrogliosis was observed at P10 in layer V of cerebral cortex, lateral globus pallidus and thalamic nuclei preceding the neuronal loss occurring at P14 (77). Co-culturing wild-type primary mouse neurons with astrocytes and glia from a mouse model of CLN1 (*Ppt1*$^{-/-}$), resulted in abnormal Ca^{2+}signaling, decreased neurite outgrowth and impaired neuronal survival (78). However, culturing mutant neurons with healthy glia reversed the phenotype (79). In a knock-in mouse model of CLN3 (*Cln3Deltaex7/8*), astrocytosis was more pronounced in the neocortex and thalamus than in other brain regions(80), while CLN6 mouse and ovine models revealed progressive astrocytosis in several thalamic nuclei, somatosensory cortex, visual cortex and caudate putamen (81, 82). Thus, it emerges, that at least in NCL, astrocytosis is a major pathological hallmark that precedes neurodegeneration.

In neurons affected by a LSD, the storage bodies are primarily confined to the perikarya, which might impair the transport of lysosomes, preventing them from merging with the early endosomes in the axon terminal (83). The storage may also disrupt normal retrograde transport of vesicles carrying the synaptic proteins along the axon (83). Furthermore, since lysosomes are the terminal compartments shared by the major autophagic and endocytic pathways of degradation (84), defective lysosomal homeostasis in LSD causes severe impairment of autophagy. Such instances have been reported in a variety of LSD including NCL, multiple sulfatase deficiency, MPS IIIA, MPS IIIC and NPC1 (63, 85-89) leading to cell death (85), especially for neurons. Neuronal loss can be observed at different timepoints during the progression of the disease. In *Npc1*$^{-/-}$ mice, for instance, neuronal degeneration is widely distributed in the brain and can be observed as early as at 3 weeks in the lateral geniculate nuclei (LGNd) and ventral posterior medial (VPM) thalamic nuclei (71), and by 10 weeks of age, most Purkinje cells disappear (72). In contrast, in MPS IIIC mouse model, NeuN-positive neurons in the somatosensory cortex are significantly reduced only at the age of 10 months (63).

Importantly, in multiple mouse models, signs of cognitive decline and behavioral abnormalities appear before the time when massive neuronal death emerges. For instance, MPS I mice at 8 months show severely affected motor function and cognitive decline but no signs of neuronal death, suggesting that the manifestations are caused mainly by a neuronal dysfunction (90). In the MPS IIIC mouse, behavior abnormalities such as hyperactivity appear around 6 to 8 months of age and learning impairment at the age of 10 months, when neuronal loss is significant (63). It is, thus, possible that at the initial stages of the disease, the neurological symptoms and behavioral deficits can be at least in part attributed to defects in synaptic transmission.

Indeed, one of such defects, synaptic pathology is a common feature for several animal models of LSD including feline models of G_{M1} gangliosidosis (91, 92), mouse model of NPC1 disease (71), the Twitcher mouse (the natural mouse model of Krabbe disease) (93) and others. The described defects include scarcity of synaptic vesicles (SV) in the axonal terminal leading to functional impairments in synaptic activity, impairment of the exocytosis (94) and endocytosis (93) of synaptic vesicles, loss of SNARE proteins, alterations in synaptic structures, dystrophic axons and reduction or mislocalization of proteins involved in pre- and postsynaptic processes (68, 88, 95, 96).

B. Synaptic transmission and its defects in neurological LSD

7. Synapses

Synapse refers to the communications between two nerve cells occurring in two main forms: electrical or chemical. In electrical synapses, pre and postsynaptic cells are connected by gap-junctions and because of that, the nerve impulse is transmitted in a very rapid manner. Most of the synapses, however, use chemical transmitters to communicate signals. At chemical

synapses, there is no structural continuity between pre- and postsynaptic neurons and the communicating cells are separated by so-called synaptic cleft. Chemical synaptic transmission depends on the release of neurotransmitters that are packed in the synaptic vesicles at the synaptic terminal and then released upon an action potential and influx of Ca^{2+} through voltage-gated Ca^{2+} channels that induces fusion of synaptic vesicles with plasma membrane in the active zone (AZ) of the synaptic terminal. Once released, neurotransmitters bind to their respective receptors on the postsynaptic neuron provoking opening or closing of ion channels, changing the membrane conductance and potential of the postsynaptic cell. (97) While excitatory (asymmetric) synapses are found mainly on dendrites and synaptic spines, inhibitory (symmetric) synapses concentrate on the cell soma and axonal initial segment (98).

a) Synaptic vesicles

Synaptic vesicles (SV) store neurotransmitters such as acetylcholine, glutamate, glycine and γ-aminobutyric acid (GABA) that are released at the synaptic terminal upon an action potential that causes the influx of Ca^{2+} and their exocytosis into the synaptic cleft (2). SV are transported in the neurons via microtubules(99) and move either anterograde (from the soma to the periphery) by the motor protein kinesin (100), or retrograde (from the periphery to the soma) by dynein (101).

At the nerve terminal, SV are found in three distinct pools (Fig. 7): the reserve pool, the recycling pool and the readily releasable pool (RRP). The reserve pool contains approximately 80-90% of the SV at the presynaptic terminal released only upon intense stimulation, that is thought not to happen at physiological levels. The vesicles of the recycling pool (approximately 5-20% of all) are released upon moderate stimulation, whereas in the RRP SV are docked on

the presynaptic plasma membrane in the AZ and are immediately available upon neuronal stimulation (102).

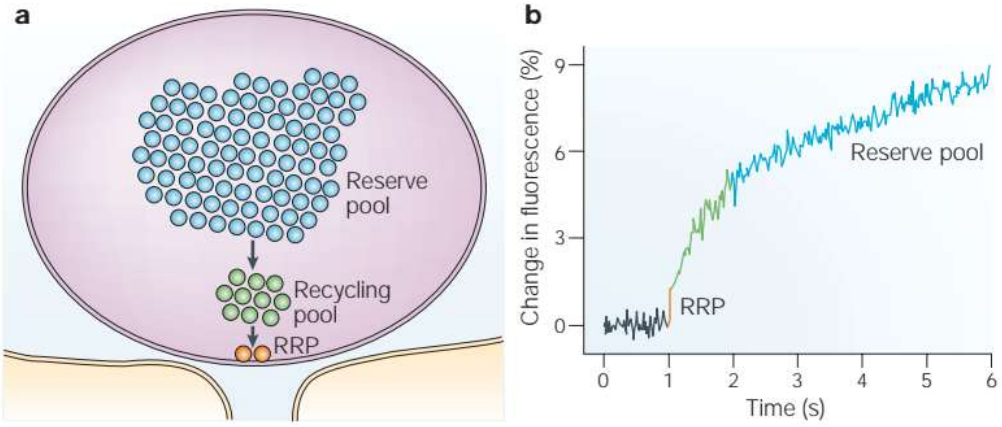

Figure 7: Three pools of synaptic vesicles.

(A) The diagram shows the 3 pools of SV, the reserve pool, the recycling pool and the RRP. (B) Three kinetic components of release on goldfish bipolar cells that were depolarized showing the pattern of exocytosis of SV from each pool. Reproduced with permission from Rizzoli and Betz, 2005 (Copyright© from Springer Nature).

SV are coated by synapsin-1 and synapsin-2 proteins that perform a regulatory function in SV maintaining them fusion-competent. In the absence of synapsins, SV are unstable and become partially degraded (103). Docking and fusion of SV with the presynaptic plasma membrane are mediated by SNARE proteins, v-SNAREs are found in the vesicle membrane, while t-SNAREs are found in the targeting membrane. They interact with each other to form a trans-SNARE-complex that brings the membranes together. In neurons, synaptobrevin (v-SNARE), syntaxin and SNAP25 (both t-SNAREs) (2, 104) are involved in docking and fusion of synaptic vesicles with the membrane of synaptic cleft, resulting in a release of neurotransmitters (2).

In order to allow rapid replacement of the synaptic vesicles upon the transmission of the nerve impulse, they need to be recycled in an efficient manner. Two tracks for the recycling of SV have been described, a slow track, in which the vesicles fuse completely with the presynaptic plasma membrane which is followed by clathrin-mediated endocytosis of the vesicle components and a fast track in which the vesicles do not fuse completely, but only a transient opening and closing of a fusion pore occurs (kiss-and- run). (104, 105)

b) Synaptic (dendritic) spines

Synaptic or dendritic spines were first observed in 1888 by the Spanish neuroscientist and pathologist Santiago Ramón y Cajal in pyramidal neurons (106). They are small protrusions on the plasma membrane of the dendritic branches that are responsible for receiving around 95% of all the excitatory inputs in pyramidal neurons (107-109). Typical spines have a small head (~1 μm in diameter, < 1fL volume) and are separated from the dendrite by a thin neck (< 0.2 μm in diameter) (108, 110) however different shapes of spines have been described and they can be classified morphologically as filopodia (thin and no head), stubby (lacking a neck), thin (thin with an apparent head) or mushroom (big head with big neck)(98, 111, 112) (Fig. 8).

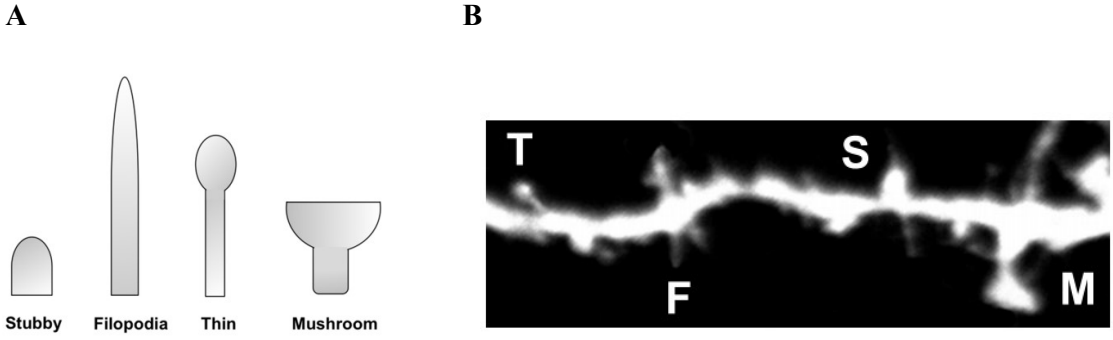

Figure 8: Morphology of synaptic spines.

(A) Schematic representation of spine morphologies. (B) Representative image of Dil-labelled spines. T: Thin; F: Filopodia, S: Stubby and M: Mushroom. Reproduced from Cheng *et al.* (2014) Fluorescent labeling of dendritic spines in cell cultures with the carbocyanine dye "DiI" (112);

Dendritic spines are important for synaptic plasticity and are believed to be the preferential site for the induction of long-term potentiation (113, 114). The lysosomes play an important role in the process of synaptogenesis, potentiation and pruning of the spines. Backpropagating action potentials provoke Ca^{2+} release from lysosomes to dendrites and trigger the fusion of the lysosome with the plasma membrane, resulting in the release of Cathepsin B. Metalloproteinase 9 (MMP-9), an enzyme involved in ECM remodeling, is increased by the action of Cathepsin B. Inhibiting either lysosomal Ca^{2+} signaling or Cathepsin B release prevents dendritic spine growth (115) while blocking Ca^{2+}-dependent fusion of lysosomes to the plasma membrane leads to an overall decrease in spine number and increase of their length resulting in filopodia-like spines (116).

c) Postsynaptic density

The postsynaptic density (PSD) is the most prominent excitatory postsynaptic component that lies at the distal tip of the spine head (117). It is identified as an electron-dense structure extending ~35–50 nm into the cytoplasm beneath the plasma membrane at asymmetric synapses (118, 119) (Fig. 9). The surface area of the PSD correlates with spine head volume and the total number of presynaptic vesicles (98) and the number of vesicles docked at the AZ (120-122).

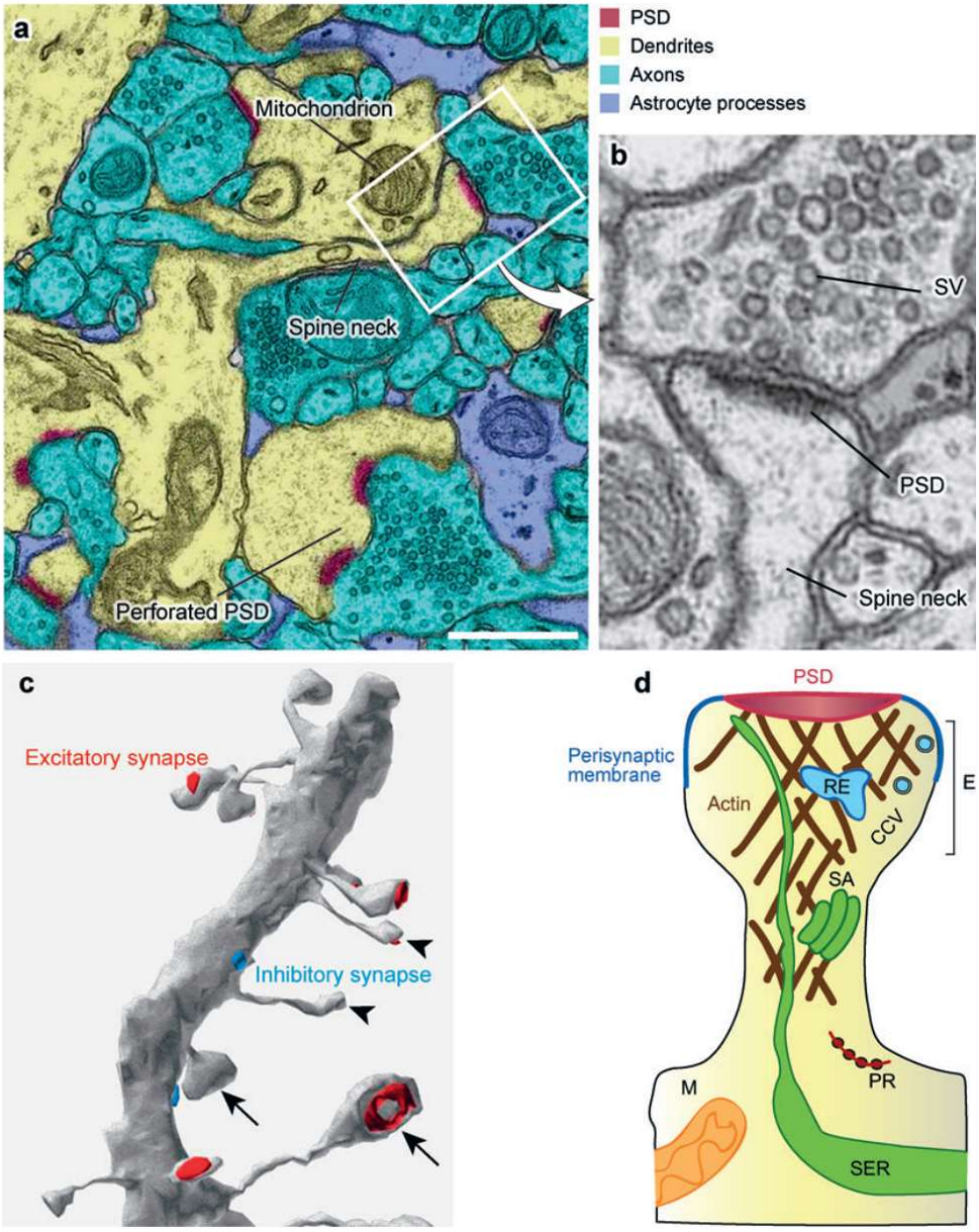

Figure 9: Microanatomy of the excitatory synapse and dendritic spine.

(A) Electron microscopy (EM) section from the CA1 region of the hippocampus colored for the following structures: PSD, dendrites, axons and astrocyte processes. The scale bas is 1µm. (B) EM morphology of an excitatory synapse. (C) Three-dimensional EM reconstruction of a segment of a dendrite from the CA1 region of the hippocampus. Red indicates excitatory synapses and blue indicates inhibitory synapses. Arrowheads in indicate thin spines while

arrows indicate mushroom spines. (D) Schematic diagram of mature mushroom-shaped spine. EZ, endocytic zone; CCV, clathrin-coated vesicles; RE, recycling endosomes; SER, smooth endoplasmic reticulum; PR, polyribosomes; M, mitochondria, SA, spine apparatus. Reproduced with permission from Sheng and Hoogenraad, 2007 (117), copyright© Annual Reviews. Inc.

The PSD may contain over 400 proteins the most abundant being those involved in actin-cytoskeletal structures, kinase signaling and GTPase signaling (123). The major PSD proteins are calcium calmodulin-dependent kinase II (CaMKIIα and CaMKIIβ), the scaffolding protein PSD-95 (124-126) and SynGAP (a Ras GTPase-activating protein [GAP] that binds to PSD-95). Other important PSD proteins are GKAP/SAPAP family (SAPAP1; SAPAP2; SAPAP3; SAPAP4), Shank/ProSAP family (Shank1; Shank2; Shank3), Septin-7, IRSp53, Homer family (Homer1; Homer2; Homer3), AMPA receptor subunits (GluR1; GluR2; GluR3), NMDA receptor subunits (NR1; NR2A; NR2B), β-Catenin, N-Cadherin, metabotropic receptor subunits (mGluR1; mGluR5), AKAP79/150 and PKCγ (127). The major families of PSD proteins are shown in Fig. 10.

The structure and composition of PSD change during maturation of synapses and expression of some PSD proteins including PSD-95, CaMKIIα and AMPA receptor subunits is increased during development (128, 129). Importantly alterations in the PSD components can lead to neurological and psychiatric diseases (127).

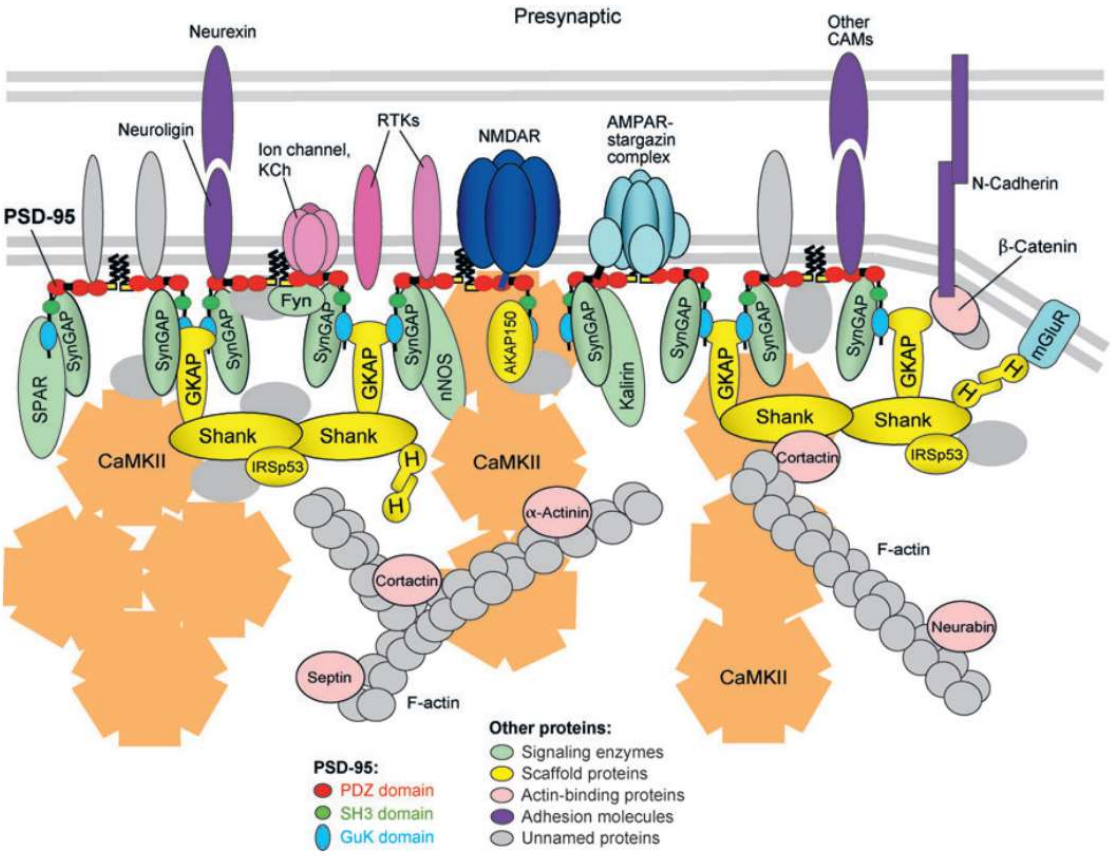

Figure 10: Organization and interaction of PSD proteins.

AKAP150, A-kinase anchoring protein 150 kDa; CAM, cell adhesion molecule; Fyn, a Src family tyrosine kinase; GKAP, guanylate kinase-associated protein; H, Homer; IRSp53, insulin receptor substrate 53 kDa; KCh, K^+ channel; mGluR, metabotropic glutamate receptor; nNOS, neuronal nitric oxide synthase; RTK, receptor tyrosine kinases (e.g., ErbB4, TrkB); SPAR, spine-associated RapGAP. Reproduced with permission from Sheng and Hoogenraad, 2007 (117), copyright© Annual Reviews. Inc.

8. Functional defects of neurons and synaptic dysfunction in LSD (20).

Impairment of endo- and exocytosis. Several studies have reported that endocytosis and exocytosis processes at the synaptic terminals are severely compromised by lysosomal storage.

In the Twitcher mouse, neurons from the dorsal root ganglia, present 2.5-fold decreased density of Ras-related protein Rab5-positive early endosomes. Besides, the percentage of Rab5+ vesicles containing the tyrosine kinase receptor A (TrkA) was decreased 1.4-fold (93). Trk signaling is activated when a neurotrophin binds to the Trk receptor. The receptor further recruits the machinery responsible for its endocytosis and gets internalized in a lipid raft-dependent manner forming a signaling endosome that traffics retrogradely to the cell body (130, 131). Retrograde transport of synaptophysin-positive vesicles was also decreased 1.5-fold, confirming that the early steps of endocytosis and retrograde transport of endocytic and synaptic vesicles are defective in the Twitcher neurons (93).

In hippocampal neuronal cultures of NPC1 mice labelled with the fluorescent dye FM4-64, the evoked vesicle exocytosis was impaired, with reduction in the fluorescence induced by potassium ion (61.9±03% in *Npc1*$^{-/-}$ mice; 71.6±2.7% in WT). Components of the readily released pool (RRP) of synaptic vesicles were reduced at both excitatory and inhibitory *Npc1*$^{-/-}$ synapses (94). The authors further tested synaptic vesicle turnover in *Npc1*$^{-/-}$ and WT neurons by delivering a set of 20 Hz stimuli followed by a test stimulus of 100 mV, 2 ms after various intervals, to allow for vesicle retrieval. In glutamatergic (excitatory) synapses, no difference between WT and NPC1 neurons was found, but the GABAergic (γ-aminobutyric acid, inhibitory) synapses in NPC1 cells exhibited impaired ability to retrieve synaptic vesicles after depletion (94). In hippocampal neuronal cultures from MPS IIIA mice, fluorescent FM1-43 labelling experiments revealed that the dye uptake was reduced in the synaptic boutons of MPS IIIA neurons as compared to the WT, and that the exocytosis rate was significantly attenuated in MPS IIIA presynaptic terminals (88).

Together, these data provide strong evidence that impairment of endo- and exocytosis is a common trend shared among the LSD. It is known that lysosomal storage can affect vesicle trafficking and merging (such as merging of primary autophagosomes and lysosomes) by

altering membrane lipid composition as well as interfering with the function of SNARE proteins (132-134). It is thus plausible that similar mechanisms can also cause a compromised endo- and exocytosis of synaptic vesicles. Nonetheless, further experimentation is needed to establish a direct causality.

Axonopathy. Dystrophic axons and demyelination have been reported in different neurological LSD. For instance, in a feline model of G_{M1} gangliosidosis, animals at the advanced stage of disease (7 to 9 months of age), exhibit slight distention of perikarya in the ventrolateral thalamocortical relay neurons as well as enlargements near the axon hillock area. The pyramidal neurons from the precruciate cortex present scarcity of excitatory response that can be interpreted as a manifestation of abnormal integration of somatodendritic inputs when analyzed *in vivo* within intracellular recordings of postsynaptic potentials evoked by ventrolateral thalamic stimulation (91). Another study of this model reported accumulation of complex lipids in membranous cytoplasmic bodies, causing the swelling of the cortical (precruciate) nonpyramidal neurons which however had no impact on intracellular recordings or evoked excitatory and inhibitory postsynaptic potentials by stimulating the medullary pyramidal tract or cerebral peduncle and the ventrolateral thalamic nucleus. (92). Axonal swelling was also observed in cultured hippocampal neurons from MPS IIIA mice at day *in vitro* 20-21 (88).

In NPC1 mice, large aggregates of presynaptic proteins, synaptophysin, synaptobrevin, VAMP2 and SNAP25, were observed in the subcortical grey and white matter (presumably in axonal enlargements) suggesting that a fraction of these proteins failed to reach the nerve terminals. Instead they accumulate within axonal spheroids in the white matter, providing evidence that axonal transport is disturbed in the *Npc1*$^{-/-}$ mice (71). Signs of defective retrograde axonal transport including unstable microtubules, and reduced dynein levels were also detected in the dorsal root ganglia of the Twitcher mice (93). Granular axonal spheroids

and dystrophic axons have been described also in other LSD such as mannosidosis, G_{M1} and G_{M2} gangliosidosis, prosaposin deficiency, and NPC1 (71, 92, 135-137). In NPC1 mice brain sections, axonal spheroids were immunoreactive for GAD65/67 (a marker of GABAergic neurons) and synaptophysin in the VPM/VPL (ventral posterior nucleus/ventral posterior lateral) of the thalamic nuclei (71).

Demyelination of axons occurs in several neurological LSD, including Krabbe disease, metachromatic leukodystrophy (MLD) and ML IV (69, 93, 138). In the Twitcher mouse, axonal demyelination in peripheral nerves is observed between postnatal day (P)15 to P30 (93, 139, 140). In three autopsy cases of human MLD patients, demyelination manifested as a continuous diminution of myelin density starting in late prelesional regions and following into early gliotic scar areas (138), whereas in ML IV (*Mcoln1*$^{-/-}$ mice), a thinning of axonal myelin sheaths coincided with malformation of the corpus callosum (69).

Thus, axonopathy appears to be a common trend among neurological LSD, especially sphingolipidoses. It is not known how the accumulation of specific substrates is linked to this phenomenon or whether other LSD also share the same characteristics.

Changes in synaptic proteins. Multiple studies reported changes in the levels and/or distribution of synaptic proteins associated with lysosomal storage (Table 3). Majority of this research has been conducted using animal, primarily, mouse models, but recent advances in availability and improvements in quality of induced pluripotent stem cells (iPSC)-derived neuronal cultures made them a valuable alternative to investigate changes specific to human neurons.

Several studies reported alterations in the levels and localization pattern of presynaptic vesicle membrane proteins with VAMP2 (vesicle-associated membrane protein 2) and synaptophysin, being among the most frequently studied. In the mouse models of MPS I, IIIA

and IIIB , VAMP2 punctate staining was reduced and more diffused in the neurons of primary motor, somatosensory and parietal areas of the cerebral cortex as compared to their WT counterparts, while no difference was observed for synaptophysin (68). The authors interpreted this as an indication for a possible rearrangement of presynaptic components without a loss in the overall number of synapses (68). In contrast, in NPC1 mice, both VAMP2 and synaptophysin presented aggregated pattern and overall reduction in the ventral medial posterior nucleus of the thalamus and the ventral posterior lateral nucleus (71). Another study in MPS IIIA mice, showed reduced levels of VAMP2 as well as of another presynaptic SNARE protein, SNAP25 (88). They also demonstrated reduced levels of synaptic vesicles in the synaptic terminals accompanied by the presence of abnormal vacuoles and/or enlarged mitochondria (88). Interestingly, the SNAP25 and VAMP2 mRNA levels were unchanged, suggesting that the decrease in both proteins in MPS IIIA neurons was rather caused by their increased degradation than impaired gene expression (88). The authors hypothesized that increased degradation/reduced stability of SNAP25 and VAMP2 in MPS IIIA neurons was caused by a loss of α-synuclein and CSPα (cysteine string protein α), two abundant presynaptic proteins that act as chaperones and assist SNARE complex formation at synaptic terminals (141-144). Interestingly, in a mouse model of the Finnish variant of CLN5 *(vLINCL(Fin)* early localized glial response at 4 months was followed by reduced expression of SNAP25 and synaptophysin in thalamic nuclei such as VPM/lPL and LGNd. At the same time, VAMP was found to be increased at 12 months. The authors propose a new sequence of events in the time course of neuronal loss, commencing in the cortex at 4 months, followed by subsequent neuronal loss in the thalamocortical system emerging at 12 months, which is opposite to what is observed in other animal models of NCL and propose synaptic pathology as the causality (145). In another comparative study in early infantile NCL mouse model (*Ppt1*$^{-/-}$) and a late onset CLN6$^{-/-}$ mouse model, neuronal loss was observed in the thalamus early symptomatic

stages followed by neuronal loss in cortical areas. Both mouse models displayed a concomitant reduction in the expression of synaptobrevin, synaptophysin and SNAP25 with voltage-dependent anion channel I (VDAC1) and pituitary tumor transforming gene 1 (Pttg1) being the two most downregulated proteins. The authors propose VDAC and Pttg1 to be potential *in vivo* biomarkers for synaptic vulnerability in NCL(146). On the other hand, a study by Hurtado *et al.* (2017), reported significantly reduced levels of synaptophysin in the thalamic nuclei in *Cln3*$^{-/-}$ mouse, while no reduction was observed in the cortical regions (147).

Reduced levels of synaptophysin were also reported in the mouse model of MPS IIIB (148), in human iPSC-derived neurons from MPS VII patients (149) and in the occipital and parietal lobes of sheep with NCL (CLN6) (150). Two different mechanisms have been proposed to explain this reduction. Vitry *et al*. (2009) have shown that in the rostral cortex of MPS IIIB mice, synaptophysin was decreased as early as at 10 days after birth, preceding the onset of clinical symptoms (148), which prompted them to propose that at the cellular level the disease starts long before the appearance of the clinical symptoms. They suggested that in the neurons HS oligosaccharides activate the degradation of synaptophysin by the proteasome which leads to its reduction (148). In contrast, Bayo-Puxan *et al*. (2018) explained lower synaptophysin levels in MPS VII cultured neurons by the reduced gene expression (149). In *Npc1*$^{-/-}$ mice, aggregations of synaptophysin were present in regions of the brain with reactive gliosis, including the striatum, substantia nigra, white matter tracts and the thalamus (71). The authors did not detect, however, a difference in the overall levels of protein expression, suggesting a redistribution rather than up- or down-regulation of these presynaptic markers (71). In the CLN5 sheep model, neurodegeneration and synaptic loss was more promiscuous in the motor cortex than in the cerebellum. In synaptosomes isolated from the motor cortex but not from cerebellum, several synaptic proteins including α-synuclein, CSP-α, α-neurofascin and rho-associated coiled-coil containing protein kinase 2 (ROCK 2) were decreased while

calretinin and ubiquitin protein ligase E3 component n-recognin 4 (UBR-4) increased suggesting the correlation of synaptic pathology with neuronal loss (151).

Homer-1, a protein enriched in the postsynaptic density of excitatory synapses was also significantly reduced in the MPS I, IIIA and IIIB mouse brains, suggesting that signaling at the postsynaptic density may also be altered (68) Conversely, another study by Dwyer *et al*. (2017) showed that MPS IIIA mice presented enhanced puncta for postsynaptic density 95 (PSD-95) in the somatosensory cortex at P21. Increased PSD-95 was also confirmed by western blot of whole tissue homogenates and synaptosomes (95). Furthermore, accumulation of heparan sulfate was found to increase the levels of AMPA (α-amino-3-hydroxy-5-methylisoxazole-4-propionic acid) receptor GluA2 on the cell surface, providing a possibility for arising of synaptic neurotransmission defects.

Proteomic analysis of the hippocampus of MPS I mice have revealed reduced levels of many synaptic proteins including syntaxin-1A, amphiphysin, complexin-1, synaptophysin, MAP1A and MAP1B (90). Syntaxin-1A is a part of the SNARE complex; amphiphysin and complexin-1 participate in the exocytosis of synaptic vesicles; synaptophysin is abundant in the synaptic vesicle membrane and is essential for their efficient endocytosis (152), MAP1A and MAP1B are microtubule-associated proteins involved in the filamentous cross-bridging between microtubules (153).

With an exception of Dwyer *et al*. (2017) who reported data showing increase of postsynaptic proteins PSD-95 and GluA2 in the neurons of MPS IIIA mice (95) and Baldo *et al.* (2015) who showed increased levels of PSD-95 in the hippocampus of MPS I mice (90), the majority of studies agree on a decrease in the levels of pre- and postsynaptic proteins potentially leading to synaptic function impairments in neurological forms of LSD. Further

studies are however necessary, to both expand the number of disorders and models analyzed and to clarify the mechanism underlying these changes.

Table 3: Synaptic proteins altered in neurological LSD (20).

LSD	Protein	Function	Change	Sample/Region	Reference
MPS I	Syntaxin-1A	SNARE complex	Reduction	Hippocampus	Baldo *et al.* (2015) (90)
	Amphiphysin	Exocytosis of synaptic vesicles	Reduction	Hippocampus	
	Complexin-1	Exocytosis of synaptic vesicles	Reduction	Hippocampus	
	Synaptophysin	Synaptic vesicle membrane protein involved in endocytosis	Reduction	Hippocampus	
	MAP1A	Microtubule cross-linking protein	Reduction	Hippocampus	
	MAP1B	Microtubule cross-linking protein	Reduction	Hippocampus	
	PSD-95	Postsynaptic density protein	Increased	Hippocampus	
	VAMP2	Vesicle-associated membrane protein 2 in the synaptic vesicles	Reduction	Primary motor, somatosensory and parietal areas of cerebral cortex	Wilkinson *et al.* (2012) (68)
	Homer-1	Protein in the postsynaptic density of excitatory synapses	Reduction	Primary motor, somatosensory and parietal areas of cerebral cortex	Wilkinson *et al.* (2012) (68)
MPS IIIA	SNAP25	t-SNARE	Reduction	Synaptosomes	Sambri *et al.* (2017) (88)
	VAMP2	Vesicle-associated membrane protein 2 in the synaptic vesicles	Reduction	Primary motor, somatosensory and parietal areas of cerebral cortex; synaptosomes	Wilkinson *et al.* (2012) (68); Sambri *et al.* (2017) (88)
	Homer-1	Protein in the postsynaptic density of excitatory synapses	Reduction	Primary motor, somatosensory and parietal areas of cerebral cortex	Wilkinson *et al.* (2012) (68)
	PSD-95	Postsynaptic density protein	Increased	Cortical layers I, II/III and V	Dwyer *et al.* (2017) (95)
	α-Synuclein	Presynaptic chaperone	Decreased	Cultured neurons and brain homogenates	Sambri *et al.* (2017) (88)
	CSPα	Presynaptic chaperone	Decreased	Cultured neurons and brain homogenates	
MPS IIIB	Synaptophysin	Synaptic vesicle membrane protein involved in endocytosis	Reduction	Rostral cortex	Vitry *et al.* (2009) (148)
	VAMP2	Vesicle-associated membrane protein 2 in the synaptic vesicles	Reduction	Suprachiasmatic Nucleus; Primary motor, somatosensory and parietal areas of cerebral cortex	Canals *et al* (2010) (96); Wilkinson *et al.* (2012) (68)
	Homer-1	Protein in the postsynaptic density of excitatory synapses	Reduction	Primary motor, somatosensory and parietal areas of cerebral cortex	Wilkinson *et al.* (2012) (68)
MPS VII	Synaptophysin	Synaptic vesicle membrane protein involved in endocytosis	Reduction	iPSC-derived neurospheroids	Bayo-Puxan *et al.* (2018) (149)
	GAD67	Enzyme that catalyzes the production of GABA	Reduction	iPSC-derived neurospheroids	
Niemann-Pick Type C	Synaptophysin	Synaptic vesicle membrane protein involved in endocytosis	Aggregation	Striatum, substantia nigra, white matter tracts and thalamus	Pressey *et al.* (2012) (71)
	VAMP2	Vesicle-associated membrane protein 2 in the synaptic vesicles	Aggregation	Striatum, substantia nigra, white matter tracts and thalamus	
Krabbe	Dynein	Retrograde transport of synaptic vesicles	Reduction	Dorsal Root Ganglia Neurons	Teixeira *at al.* (2014) (93)
Gaucher	α-synuclein	regulation of synaptic vesicle trafficking and neurotransmitter release	Accumulation	Striatum	Ginns *et al.* (2013) (70)
CLN3	Synaptophysin	Synaptic vesicle membrane protein involved in endocytosis	Reduction	Thalamic nuclei	Hurtado *et al.,* (2017) (147)

CLN5	α-synuclein	regulation of synaptic vesicle trafficking and neurotransmitter release	Reduction	Synaptosomes	Amorim *et al.,* (2015)(151)
	CSP-α	Presynaptic chaperone	Reduction	Synaptosomes	
	α-neurofascin	Cell adhesion molecule	Reduction	Synaptosomes	
CLN6	Synaptophysin	Synaptic vesicle membrane protein involved in endocytosis	Reduction	Occipital and parietal lobes	Kanninen *et al.* (2013) (150)
	Syntaxin-6	Intracellular vesicle trafficking	Reduction	Occipital lobe	

Alterations in generation and recycling of synaptic vesicles. As described in the sections above, lysosomal storage influences the homeostasis of the protein machinery involved in the synaptic vesicle trafficking and recycling and affects vesicles in all three pools. For instance, impairment of the early steps of endocytosis and the retrograde transport of endocytic and synaptic vesicles were reported for the dorsal root ganglia neurons of a Twitcher mouse (93). The authors linked vesicle trafficking deficits with decreased levels of dynein and reduced microtubule stability. Reduction in the number of SV in both excitatory and inhibitory synapses was also described in NPC1 neurons, mostly affecting the RRP in cultured hippocampal neurons (94). The same study also reported evoked vesicle exocytosis suggestive of functional presynaptic defects (94). Interestingly, the degree of impairment of synaptic vesicle turnover was different in excitatory and inhibitory neurons. At glutamatergic synapses the synaptic vesicle turnover was either normal or impaired just for a short period of time (< 0.2 s), while at GABAergic synapses the consistent blockage of the turnover was observed (94). In a similar fashion, neurons from MPS IIIA mice presented reduced density of synaptic vesicles at the synaptic terminals associated with a severe functional impairment in the synaptic activity (88). Docked SV were reduced by 30% in cortical neuronal cultures from the CLN1 mice (154).

Based on these studies, it seems that there is a reduction in number of synaptic vesicles at the synaptic terminals of LSD neurons caused by impaired vesicle turnover and intracellular trafficking that lead to functional impairment in synaptic transmission.

Defects in synaptic spines. Dendritic spines are important for synaptic plasticity and are believed to be the preferential site for the induction of long-term potentiation (113, 114).

Therefore, alterations affecting their shape or number can directly reflect on the cognitive defects observed in LSD patients.

Since lysosomal homeostasis plays an important role in maintaining the synaptic spines, and considering that impaired synaptic activity is observed in animal models of neurological LSD, one can expect that studies involving these models or post-mortem human samples should include analysis of synaptic spines. However, only a few reports took this into consideration. In 1976, using Golgi staining of neurons from either biopsies or post-mortem brain samples from G_{M2} gangliosidosis patients, Purpura & Suzuki revealed that dendritic spines on pyramidal and non-pyramidal neurons were abundant and normal in overt appearance (155). However, a loss of spines was detected in samples of other patients with G_{M2} gangliosidosis and NCL (155). Loss of spines in NCL (PPT1 deficient mice) was also documented by Bible *et al.* (156). Using Golgi silver-impregnation of layer II/III pyramidal neurons in the primary somatosensory cortex of MPS IIIA mouse at P21 it was demonstrated that synaptic spine density was not affected, but there was an increase in the width of the spine heads (mushroom spines) (95).

Two studies in NPC1 neurons obtained controversial results: while Xu *et al.* (2010) reported no differences in spine density (94), Tiscione *et al.* (2019) observed that NPC1 deficiency results in a decrease in neuronal spine density (157). Thus, based on the published data, it appears that alterations of synaptic spines do not follow the same trend among all neurological LSD.

Changes in postsynaptic density. Alterations in the levels of PSD components are known to cause neurological and psychiatric disorders (127) and therefore might be common to LSD and related neurodegenerative diseases. The reduction in size of PSDs has been described in 3 mouse models of Gaucher disease (knock-in mice homozygous for human L444P and R463C

missense mutations, and a CBE-induced model) (70). Elongated PSD in asymmetric excitatory synapses were described in the mouse model of ML IV (69) while no changes in the postsynaptic components were observed in NPC1 (71, 94). In general, spines with larger heads also have bigger PSD, indicating stronger synapses and the promotion of long-term potentiation (127). On the other hand, immature spines (filopodia) with smaller, or even absent PSDs, are a sign of weak synapses and could account for cognitive deficits observed in many types of neurological LSD.

Functional synaptic defects. Alterations in synaptic neurotransmission in LSD have recently received more attention and have been proposed to play a major role in pathophysiology of these disorders. Most studies could detect the emergence of defects in synaptic neurotransmission before the commencement of neurodegeneration and neurobehavioral impairments. For example, in 21-day-old MPSIIIA mice, electrophysiological recordings of miniature excitatory postsynaptic currents (mEPSCs) from layer II-III of the somatosensory cortex revealed fewer larger events and a smaller average mEPSC amplitude. However, the mEPSC frequency remained unaltered in comparison with control animals consistent with similar numbers of dendritic spines (95). In the same animals, field hippocampal synaptic neurotransmission from CA1 cells remained unaltered in response to increasing stimulation of Schaffer collaterals (SC) (95).Interestingly, in the same model, field recordings in hippocampal slices from 6-month-old animals revealed reduced synaptic activity. A decrease in the fEPSP (field excitatory postsynaptic potential) slope with increasing stimulus intensity and presynaptic response amplitude was detected suggesting a presynaptic deficit, consistent with the reduction of synapse density and a number of synaptic vesicles per synapse at the presynaptic terminals as detected by electron microscopy (88). In cultured rat hippocampal neurons, lysosomal trafficking was found to be a crucial modulator of postsynaptic spine remodeling(158). Inhibition of lysosomal proteolysis by cysteine protease inhibitor leupeptin,

resulted in the reduction of mEPSC frequency but not of the amplitude. A concomitant reduction in the number of spines at excitatory synapses was also observed suggesting that local lysosome-dependent degradation of synaptic proteins is essential for synaptic activity-mediated remodeling of synaptic spines (158). Early synaptic impairments have been also reported in a mouse model of CLN1 (*Ppt1*$^{-/-}$), in which the developmental switch in NMDA receptors from GluN2B to GluN2A was found to be arrested (159). Furthermore, SAP-102 and PSD95 proteins interacting with GluN2B and GluN2A, respectively were significantly reduced at P33-P60 and alterations in the kinetics of the NMDA EPSCs indicated longer activation times of GluN2B receptor (159).

Mechanisms by which lysosomal storage affects basal synaptic transmission and synaptic plasticity are not completely understood, however a substantial body of research provides evidence that these changes lead to neurodegeneration and neurobehavioral symptoms in the affected patients and animal models. One example of such impact has been provided by a study involving a mouse model of NPC1 (160). NPC1 mice display steeper hippocampal fEPSP slope in response to amplified SC-CA1 stimulation intensities indicating increased basal synaptic neurotransmission. Additionally, paired pulse facilitation was found to be increased in NPC1 mice, also indicating the possibility of an increased presynaptic release. The authors concluded that an increase in basal synaptic transmission could lead to chronic neuronal excitotoxicity and frequent seizures in NPC1 patients (160). In the same animals, hippocampal long-term potentiation (LTP) has been significantly reduced, which could potentially explain the cognitive impairments observed in NPC1 mice (161) and patients (162). Overall, a decrease in LTP in combination with induced basal transmission, could lead to a distinct pattern of neurobehavioral symptoms in the NPC1 patients.

Both human NPC1 patients and mice show drastic degeneration of cerebellar Purkinje cells (163). Interestingly, Sun *et al.* (2011) reported that this coincides with an increase in

parallel fiber-Purkinje cell basal synaptic transmission and a concomitant reduction in long-term depression (LTD) leading to increased vulnerability of these particular cell types (164). The authors propose that these synaptic defects stem from the decrease in ATP/adenosine release and deactivation of A1 receptors (164). However, a study by Xu *et al*. (2010) reports that defects in synaptic vesicle turnover in NPC1 mice were more severe in inhibitory than in excitatory synapses. Similarly, a reduction in the amplitude of evoked inhibitory postsynaptic currents (IPSCs) with increasing stimulation indicated decreased synaptic depression at inhibitory synapses while no changes in synaptic depression were found at excitatory synapses (94). Another evidence for vulnerability of GABAergic synapses in LSD comes from a recent study in which cathepsin D (CTSD), an aspartate protease whose genetic deficiency is associated with a subtype of NCL10 was found to be differentially regulating synaptic vesicle recycling processes in GABAergic and glutamatergic synapses (165). Acute pharmacological inhibition of CTSD led to a decrease of the RRP size in GABAergic but not glutamatergic synapses causing the decrease in the amplitude of the IPSCs but not the EPSCs. The authors proposed that CTSD is therefore an important regulator of synaptic vesicle recycling, and that its deficiency blocks this process causing neuronal dysfunction and the epilepsy prone behavior in NCL10. In another juvenile mouse model of NCL ($Cln3^{\Delta ex1\text{-}6}$), the authors reported specific synaptic neurotransmission deficits in multiple brain areas correlating with anxiety and memory impairments (166). Whole cell patch clamp recordings from principal neurons (PNs) in the basolateral amygdala (BLA) displayed reduced frequency of mIPSCs and sIPSCs (spontaneous inhibitory post synaptic currents) as well as reduction of peak amplitude in evoked GABAergic IPSCs. These observations indicated a higher vulnerability of the inhibitory interneurons at least in the BLA that could in part account for the observed increased anxiety. The authors also reported reduction in the frequency and amplitude of mIPSCs and sIPSCs in the dentate gyrus neurons of the hippocampus suggesting compromised presynaptic

release. The authors propose that the two affected brain regions mediate different behavioural impairments with a common signature of a GABAergic deficit (166). At the network level, a significant decrease in sharp-wave ripples in the hippocampus (a characteristic oscillation often implicated in memory consolidation) over the course of the disease was found in a CLN3 mouse model (*Cln3*$^{-/-}$) suggesting that neuronal network defects in conjunction with synaptic deficits aggravate with age (167).

C. Lentiviral-mediated gene therapy of LSD

Several LSD are currently treated with enzyme replacement therapy (168-170), substrate reduction therapy (171), pharmacological chaperones (172) or hematopoietic progenitor stem cell (HPSC) transplantation (173). The challenge in treating neurological LSD however lies on unraveling efficient therapeutic approach to cross the blood-brain barrier. For MPS III, for instance, there is currently no available specific therapy. Patients with MPS I (Hurler) often receive hematopoietic stem cell (HSC) transplantation (HSCT), which results in drastic amelioration of the disease. Following the transplantation and the engraftment, monocytes derived from healthy donor HSC traffic from the blood into the brain where they differentiate into microglial cells and mediate a cross-correction in the CNS. However, in MPS IIIA (heparan sulfamidase deficiency) patients and in the MPS IIIA mouse model, HSCT is not able to correct the neurological events most likely because the levels of heparan sulfamidase produced by the donor microglia are not sufficient to correct all neurons (174).

Lentiviral vectors show high efficacy in transduction of both dividing and non-dividing cells and support sustained expression of transgenes by their integration into the host genome, and have low toxicity (175-177), which makes them attractive tools for genetic therapy of lysosomal diseases. The gene therapy mediated by lentiviral transduction of HSC followed

by transplantation has already been used in clinical trials for another neurological LSD, MLD (178). The authors have successfully transduced and transplanted $CD34^+$ cells with the LV encoding for arylsulfatase A (ARSA) in 3 pre-symptomatic children with MLD, which resulted in high-level engraftment of the transduced HSC, reconstitution of ARSA activity and delay of disease progression.

Sergijenko and colleagues (2013) (174) have tested whether this approach shows efficacy in the mouse model of MPS IIIA. They transduced autologous MPS IIIA HSC with a lentivirus (LV) expressing codon-optimized N-sulfoglucosamine sulfohydrolase (SGSH) under CD11b myeloid-specific promoter. These experiments demonstrated that transplantation of the transduced HSC in MPS IIIA mice resulted in normalization of mouse behaviour and significantly reduced brain HS storage, secondary GM2 storage, lysosomal compartment size and neuroinflammation. Similarly, in MPS IIIB, transplantation of mice with HSPC transduced with the LV encoding for human α-N-acetylglucosaminidase (NAGLU) enzyme led to behavioral correction, normalization of heparan sulfate and sulfation patterning, reduced inflammatory cytokine expression and decreased astrocytosis, microgliosis and lysosomal compartment size across the brain (179). Gleitz *et al*. (2018)(180), used the same approach for MPS II, where they used a LV encoding for human iduronate-2-sulfatase fused with the a tandem repeat of receptor-binding domain of human apolipoprotein E (ApoE) under the control of CD11b myeloid-specific promoter. They observed that the procedure not only corrected peripheral disease, but also mediated complete normalization of brain pathology and behavior. Thus lentiviral-mediated gene therapy showed efficacy in several neurological LSD, however, this therapeutic approach has never been tested for a disease caused by defects in transmembrane proteins uncapable to cross-correct other cells.

9. Rationale and objectives

Understanding the neuropathophysiology of MPS IIIC is crucial to determine biomarkers of disease progression in the CNS and to support development of novel therapeutic strategies. As it was previously reported by Martins *et al.* (2015), the mouse model of MPS IIIC (HGSNAT KO) presented reduced anxiety and hyperactivity at the age of 6 and 8 months in the open field test and learning impairment at the age of 10 months observed with the Morris water maze test (63). It was also reported that significant neuronal loss was observed only after 10 months in the somatosensory cortex, however at 4 months, MPS IIIC mice were already exhibiting signs of neuroinflammation, with increased GFAP-positive astrocytes and CD68-positive microglial cells. Based on these data, the first hypothesis is that prior to neuronal death, behavior abnormalities occurring in the MPS IIIC mice are associated with defects on neurotransmission.

The therapeutic approaches based on using the LV to overexpress the deficient enzyme in microglia cells have been proven to be an efficacious tool to treat neurological forms of several LSD. This should slow down the neuronal death and improve clinical phenotype. Since microglia are derived from HSPC, they are the only brain cells that can be readily targeted without performing difficult, expensive, and potentially dangerous stereotactic or intrathecal viral injections. Importantly, published data indicate that this procedure can almost completely replace resident brain microglia in LSD mouse models with gene-modified HSPC (178, 181-183). When whole body irradiation was used as a method of myeloablation, HSPC-derived cells constituted 15-20% of all microglia in the mouse model of MLD) (181). Moreover, these numbers were significantly increased by using chemotherapeutic drugs (primarily busulfan) as a myeloablative regimen. After bone marrow conditioning of MLD mice with busulfan (4 daily 25 mg/kg doses) up to 75% of the microglia and close to 100% of brain macrophages were derived from transplanted HPSC (182). Together, these results strongly suggest that it is

possible to achieve a concentration of bone marrow (BM)-derived transduced microglia in the brains of MPS IIIC mice sufficient for a therapeutic effect. The gene-modified HSPC transplant procedure itself is safe in humans and provides long-term correction(178). We believe that even though the enzyme overproduced by microglia would not be able to cross-correct the neurons the therapy still would ameliorate the diseases by removing the excess of accumulated HS in the brain, reducing neuronal death, correcting synaptic abnormalities and behavior. The second hypothesis is that after bone marrow transduction with lentivirus and posterior transplantation in myeloablated MPS IIIC mouse, microglia derived from macrophages would be able to cross the blood brain barrier. This procedure will populate the brain with microglia overexpressing HGSNAT, reverse storage of toxic HS species in microglia and reduce inflammation. To prove both hypotheses, two specific objectives were defined. The first objective (Chapter 3), is to study the synaptic transmission in MPS IIIC mice hippocampus and the second objective (Chapter 4) is to test the efficacy of a lentiviral-based gene therapy in MPS IIIC mice.

Chapter 2

MATERIAL AND METHODS

10. Animals

The mouse models of MPS IIIC (*Hgsnat*^{Geo}) and sialidosis (*Neu1*$^{-/-}$) in C57BL/6J genetic background have been previously described (63, 184, 185). Briefly, the *Hgsnat*^{Geo} mice were generated by disrupting the *Hgsnat* gene using gene trap technology. A cassette with a functional fusion between β-galactosidase-encoding gene and the *neo* gene from Tn5 was inserted in the intron 7 of *Hgsnat* gene with a *Btk* exon in the trap construct that contains termination codons in all reading frames to prevent *Hgsnat* transcription. The *Neu1*$^{-/-}$ mice were also generated by gene trap technology, where the *LacZ/BactPNeo* cassette was inserted in the intron 2 of *neu1* gene by microinjections in the C57BL/6J blastocysts. The Thy1-EGFP transgene mice expressing EGFP under the control of a modified regulatory region of the mouse Thy1.2 gene promoter (containing the sequences required for neuronal expression but lacking the sequences required for expression in non-neural cells) and B6.SJL-*Ptprc*^{a} *Pepc*^{b}/BoyJ (CD45.1) mice, a C57BL/6 congenic strain that is used widely in transplant studies because it carries the differential *Ptprc*^{a} pan leukocyte marker commonly known as CD45.1 or Ly5.1 were obtained from The Jackson Laboratory (JAX stock #007788 and #002014, respectively)(186). All mice were bred and maintained in compliance with the Canadian Council on Animal Care (CCAC) in the accredited animal facility of the CHU Sainte-Justine. Mice were housed in an enriched environment with continuous access to food and water, under constant and controlled temperature and humidity, on a 12 h light/dark cycle. All experiments performed on mice have been approved by the Animal Care and User Committee of the Ste-Justine Hospital Research Center.

11. Neuronal cultures and transduction

Primary hippocampal neuronal cultures were established from mouse brain tissues at embryonic day 16. The hippocampi were dissected, treated with 2.5% trypsin (Sigma-Aldrich, T4674) for 15 minutes at 37ºC, washed 3 times with Hank's Balanced Salt Solution (HBSS, Gibco, 14025-092) and mechanically dissociated using borosilicate pipets with opening sizes of 3, 2 and 1 mm. The cells were then counted with the viability dye trypan blue (Thermo Fisher Scientific, 15250061) in a hemocytometer and resuspended in Neurobasal media (Gibco, 21103-049) supplemented with B27, N2, penicillin and streptomycin. The hippocampal cells were plated at a density of 60,000 cells per well in a 12-well plate, on Poly-L-Lysine hydrobromide (Sigma Aldrich, P9155) coated coverslips. Cells were cultured for 21 days and 50% of media was changed on days 3, 10 and 17. Primary hippocampal neurons were transduced at day *in vitro* (DIV) 3 with lentivirus encoding for HGSNAT fused to GFP under a CMV promoter, for the rescue experiments, or with lentivirus encoding for Syn1 fused to GFP (GeneCopoeia, Inc., cat.# LPP-Z5062-Lv103-100), for live-cell imaging. Transduction was performed in the presence of 8 µg/ml of protamine sulfate for 15 h.

12. Human brains

Cerebral cortices were obtained from post-mortem autopsies of seven cases of clinically and pathologically confirmed patients with MPS (1 case of MPS I, 1 case of MPS II, 2 cases of MPS IIIA, 1 case of MPS IIIC and 2 cases of MPS IIID) as well as seven age-matched controls with no pathological changes in the central nervous system. Due to limited access to human samples, it was not possible at the time to request samples of the hippocampus. The samples were provided by the NeuroBioBank (NIH) (project 1071, MPS Synapse) and were preserved with formalin. Upon arrival to our laboratory, the samples were embedded in Tissue-Tek® O.C.T. compound and stored in -80ºC. Brains were cut in 40 µm sections and stored in

cryopreservation buffer (0.05 M sodium phosphate buffer pH 7.4, 15% sucrose, 40% ethylene glycol) at -20ºC until labelling with immunofluorescence.

13. Immunofluorescence

Cultured neurons at DIV 21 were fixed in 4% paraformaldehyde/4% sucrose solution in PBS, pH 7.4, washed 3x with PBS and stored at 4ºC for posterior analysis. Mouse brains were collected from animals perfused with PBS followed by perfusion with 4% PFA and left in 4% PFA overnight. Brains were placed in 30% sucrose for 48 h and then they were embedded in Tissue-Tek® O.C.T. Compound and stored in -80ºC. Brains were cut in 40 µm sections and stored in cryopreservation buffer (0.05 M sodium phosphate buffer pH 7.4, 15% sucrose, 40% ethylene glycol) at -20ºC until labelling The cultured neurons were permeabilized with 0.1% Triton X-100 and blocked with 5% goat serum in PBS for 1 h, and then incubated overnight at 4ºC with primary antibodies in 5% goat serum. Brains (mouse and human) were washed 3x with PBS, with 15 min between washes and then they were permeabilized and blocked with PBS containing 5% BSA in 1% Triton X-100 for 2 h. The hybridization with primary antibodies was performed overnight at 4ºC in PBS containing 1% BSA, and 0.1% Triton X-100. The following antibodies were used: rabbit anti-mouse synapsin 1 (1:200, Abcam, catalog ab64581), rabbit anti-mouse synaptophysin (1:300, Millipore Sigma, catalog SAB4502906), rat anti-mouse lysosomal-associated membrane protein 1 (LAMP1, 1:200, DSHB, catalog 1D4B-s), rabbit anti-mouse NeuN (1:250, Millipore Sigma, catalog MABN140), chicken anti-mouse microtubule-associated protein 2 (MAP2, 1:2000, Abcam, catalog ab5392) rabbit anti-mouse vesicular glutamate transporter 1 (vGLUT1, 1:1000 for cells, 1:200 for tissues, Abcam, catalog ab104898), mouse anti-mouse postsynaptic density protein 95 (PSD-95, 1:1000 for cells, 1:200 for tissues, Abcam, catalog ab99009), rabbit anti-mouse vesicular GABA transporter (vGAT, 1:1000, Synaptic Systems, catalog #131003), mouse anti-mouse Gephyrin

(1:1000, Synaptic Systems, catalog #147021), mouse anti-mouse neurofilament medium chain (1:200, DSHB, catalog 2H3-s). The cells and brains were washed 3x with PBS 1x and counterstained with Alexa Fluor 488-, Alexa Fluor 555- or Alexa Fluor 633-conjugated goat anti-rabbit, anti-mouse, anti-rat or anti-chicken IgG (1:1000 for cells, 1:400 for tissues, all from Thermo Fisher Scientific) for one hour for cells or two hours for tissues at room temperature and the nuclei were stained with Draq5 (1:1000, Thermo Fisher Scientific) for 40 min or DAPI within the mounting media.

To visualize the synaptic spines in cultured neurons, on DIV 21 the culture media was replaced by 2.5 μM 1,1'-Dioctadecyl-3,3,3',3'-Tetramethylindocarbocyanine Perchlorate (Dil, Thermo Fisher Scientific) dissolved in fresh media and the cells were incubated for 15 min at 37ºC, washed 3x with media preheated to 37ºC, and fixed with 1.5% paraformaldehyde in PBS for 15 min. The slides were mounted with Prolong Gold Antifade mounting reagent (Thermo Fisher Scientific) and analyzed using Leica DM 5500 Q upright confocal microscope (63x oil objective, N.A. 1.4, zoom 1.5). Images were processed and quantified using ImageJ 1.50i software (National Institutes of Health, Bethesda, MD, USA). Quantification was blinded and performed for at least 3 different experiments. Quantifications of synaptic spine density and puncta were performed in 20 μm of dendrite length, respectively, 30 μm away from the neuronal soma.

14. Transmission electron microscopy

At 3 and 6 months, 3 mice per genotype were anesthetized with sodium pentobarbital and transcardiacally perfused with PBS followed by 2.5% glutaraldehyde in 0.2 M phosphate buffer (pH 7.2). The brains were extracted and post fixed in the same fixative for 24 h at 4ºC. The hippocampi were dissected in blocks of 1 mm^3 and sections of 1 μm thickness were cut,

mounted on glass slides, stained with toluidine blue and examined on a Leica DMS light microscope to select the CA1 region of the hippocampus for the electron microcopy. For the neuronal cultures, cells at DIV 21 were washed with PBS and fixed overnight in 2.5% glutaraldehyde in 0.1 M sodium cacodylate buffer (pH 7.4, Electron Microscopy Sciences) at 4ºC. Both tissue and cultured cell samples were stained with 1% osmium tetroxide (Mecalab) and 1.5 % potassium ferrocyanide (Thermo Fisher Scientific) followed by dehydration in a graded series of ethanol (30%-90%) and embedded in Epon. The polymerized blocks were trimmed, and 100 nm ultrathin sections were cut with an Ultracut E ultramicrotome (Reichert Jung), mounted on 200-mesh copper grids (Electron Microscopy Sciences), stained with uranyl acetate (Electron Microscopy Sciences) and lead citrate (Thermo Fisher Scientific) and examined on a FEI Tecnai 12 transmission electron microscope (FEI Company) operating at an accelerating voltage of 120 kV equipped with an XR-80C AMT 8 megapixel CCD camera. For quantification, the micrographs were taken with 13,000 x and 49,000 x magnification.

15. Whole-cell patch clamp recordings in dissociated hippocampal neuronal cultures

Experiments were performed after DIV 22-25 on dissociated hippocampal neuronal culture. Cultures were maintained in a humidified atmosphere of 5% CO_2 and 95% O_2 at 37°C. Coverslips with cultured hippocampal neurons were placed in a recording chamber mounted on an inverted microscope (Nikon Eclipse Ti-S). Whole-cell recordings were obtained from neurons, selected by visual identification in phase contrast, using borosilicate pipettes (3–6 MΩ). The intracellular solution for recording miniature EPSCs (mEPSCs) and IPSCs (mIPSCs) contained (in mM) 132 $CsMeSO_3$, 8 CsCl, 0.6 EGTA, 10 diNa-phosphocreatine, 10 HEPES, 4 ATP-Mg^{2+}, 0.4 GTP-Na_3. It was filtered and adjusted to pH 7.25-7.30 with 275-280 mOsmol CsOH. mEPSCs and mIPSCs were recorded in the presence of tetrodotoxin (TTX; 1 µM; Abcam) in artificial cerebrospinal fluid (ACSF) containing (in mM) 132.3 NaCl, 3 KCl,

15 HEPES, 1.25 NaH_2PO_4, 2 $CaCl_2$, 2 $MgSO_4$, 10 D-Glucose. ACSF was adjusted to pH 7.37-7.41 with 295-305 mOsm NaOH and perfused at 1 ml/min. Recordings were obtained using a Multiclamp 700B amplifier and a 1440A Digidata acquisition board (Molecular Devices). Signals were low-pass-filtered at 2 kHz, digitized at 20 kHz and stored on a PC. Upon whole cell configuration, holding potential was initially maintained at -70 mV for mEPSCs and subsequently reduced to 0 mV for mIPSCs for 5 min recordings of each in the same cell. Signal quality was routinely monitored and recordings were only included if access resistance was less than 30 MΩ and varied for less than 25%. For analysis, mEPSCs and mIPSCs were Bessel filtered at 2.8 kHz using pClamp10 software (Molecular Devices). Miniature events were analyzed using MiniAnalysis (Synaptosoft). Unpaired-sample t-tests ($p<0.05$; two-sided) were used for statistical comparison of mEPSC and mIPSC frequencies, amplitudes, rise and decay times.

16. Isolation of synaptosomes

At 3 and 6 months of age, mice (3 per genotype) were anesthetized with sodium pentobarbital and sacrificed by cranial dislodgement. Brains were removed, weighted and placed in a cold Dounce tissue grinder with 2 mL of Syn-PER Synaptic Protein Extraction Reagent (Thermo Scientific) per 200 mg of brain tissue in the presence of protease and phosphatase inhibitor cocktails (cOMplete Tablets EDTA-free and PhosSTOP EASYpack tablets, Roche). The brains were homogenized on ice with 10 slow strokes, transferred to centrifuge tubes and centrifuged at 1,200 *g* for 10 min at 4°C. The supernatants were collected and centrifuged at 15,000 *g* for 20 min at 4°C. The supernatant, corresponding to the cytosolic fraction was collected and the pellet (synaptosomes) was resuspended with the Syn-PER reagent (500 µL per 200-400 mg of brain tissue). The concentration of proteins in the synaptosomes was measured using the Bio-Rad Bradford kit.

17. Liquid Chromatography / Mass Spectrometry

Each sample was diluted with 630 µL of 50 mM ammonium bicarbonate containing 5 mM TCEP [Tris(2-carboxyethyl) phosphine hydrochloride; Thermo Fisher Scientific], 20 mM 2-chloroactamide and vortexed for 1 h at 37°C. One µg of trypsin was added, and digestion was performed for 8 h at 37°C. Digestion was stopped with the addition of 6.3 µL of TFA. The extracted peptide samples were dried and solubilized in 5% ACN-0.2% formic acid (FA). The samples were loaded on a home-made C18 precolumn (0.3-mm inside diameter [i.d.] by 5 mm) connected directly to the switching valve. They were separated on a home-made reversed-phase column (150-µm i.d. by 150 mm) with a 56-min gradient from 10 to 30% ACN-0.2% FA and a 600-nL/min flow rate on a Ultimate 3000 nano-LC connected to an Q-Exactive Plus (Thermo Fisher Scientific, San Jose, CA). Each full MS spectrum acquired at a resolution of 70,000 was followed by 12 tandem-MS (MS-MS) spectra on the most abundant multiply charged precursor ions. Tandem-MS experiments were performed using collision-induced dissociation (HCD) at a collision energy of 27%. The data were processed using PEAKS 8.5 (Bioinformatics Solutions, Waterloo, ON) and a mouse database. Mass tolerances on precursor and fragment ions were 10 ppm and 0.01 Da, respectively. Variable selected posttranslational modifications were carbamidomethyl (C), oxidation (M), deamidation (NQ), and phosphorylation (STY). The data were visualized with Scaffold 4.8.7 (protein threshold, 99%, with at least 2 peptides identified and a false-discovery rate [FDR] of 1% for peptides).

18. Live-cell imaging

Primary hippocampal neurons were plated on poly-L-lysine coated 4-well chambered glass slides at a density of 6 x10^4 cells. Neurons were transduced with LV-Syn1-GFP at DIV 3 and were imaged at DIV 21 using an inverted spinning disk confocal microscope (Leica DMi8, 63x objective). During image recording the cells were maintained in a humidified atmosphere

of 5% CO_2 at 37°C. Digital images were acquired with an EM-CCD camera. Cells were recorded every 2 s for a total of 600 s for 5 z-stacks of 0.4 μm each. The videos were played with 10 frames per second, all stacks combined. Kymographs were generated by analyzing the traffic of synaptic vesicles using ImageJ 1.50i software (National Institutes of Health, Bethesda, MD, USA).

19. Western blots

Brain tissues (frontal part of a hemisphere, approximately 25% of the brain) were homogenized in RIPA buffer (50 mM Tris-HCl pH 7.4, 150 mM NaCl, 1% NP-40, 0.25% sodium deoxycholate, 0.1% SDS, 2 mM EDTA, 1 mM PMSF, Roche protease and phosphate inhibitor cocktails, 2.5 ml per 1 g of tissue). Neuronal cells grown in culture were scraped in the same buffer (0.1 ml per million cells). The homogenates were kept on ice for 30 min and centrifuged at 13,000 RPM at 4ºC for 25 minutes. The supernatant was collected and centrifuged again for 15 min. The resulting lysates were separated by SDS-PAGE on 8% gels. Western blot analyses were performed according to standard protocols using the following antibodies: synapsin 1 (rabbit, 1:2000, Abcam, catalog ab64581), PSD-95 (rabbit, 1:2000, Abcam, catalog ab18258), Munc18-1 (rabbit, 1:3000, Abcam, catalog ab3451), CaMKII (mouse, 1:2000, Abcam, catalog ab22609), clathrin heavy chain (rabbit, 1:12000, Abcam, catalog ab21679) and α-Tubulin (1:2000, mouse, DSHB, catalog 12G10). Equal protein loading was confirmed by Ponceau S staining and the bands were quantified using ImageJ software.

20. Production of the Lentivirus

Human *HGSNAT* codon-optimized cDNA Tordo (187) fused to a GFP (*HGSNAT-GFP*) was cloned into a pENTR1A vector (Invitrogen, 11813-011) and then transferred to a 3rd generation lentiviral vector plasmid (pLenti PGK Blast DEST (w524-1), Fig. 11), Addgene, Plasmid #19065, (188)), using Gateway™ technology according to manufacturer's instructions. The lentivirus was produced in HEK293T cells cultured in RPMI media (Gibco) to 70-90% confluency and co-transfected with REV 6 µg per plate, VSVG 7.8 µg per plate, pMDL (gag-pol), 15 µg per plate, and *Hgsnat*-GFP, 9 µg per plate plasmids. Polyethylenimine 40 µg/ml (PEI, Linear, MW 25000, Transfection Grade, Polysciences Inc.) was used as a transfection reagent and incubated overnight at 37ºC, 5% CO_2. On the following day, the medium was replaced by Dulbecco's Modified Eagle's Medium (DMEM, Gibco™) supplemented with 10% fetal bovine serum (FBS, Wisent Inc.) and 1% Penicillin-Streptomycin (Gibco™) and the cells cultured for 30 hours at 37ºC, 5% CO_2. Medium was collected, filtered using a 0.22 µm low protein binding filter and then centrifuged at 50,000 g for 2 h, at 10ºC with maximum acceleration and slow brake. The pellet with the virus was resuspended in 100 µl PBS, aliquoted and stored at -80ºC.

Figure 11: Map of lentiviral plasmid encoding for HGSNAT-GFP under a PGK promoter.

21. Intracranial injections of AAV

Production of AAV and intracranial injections were performed by Tordo *et al.* (2018) (187). The AAV-CAG coHGSNAT transgene plasmid contains a codon-optimized human *HGSNAT* cDNA that was placed into SbfI and SphI sites, replacing the GFP coding sequence in the pTRUF-11 plasmid (ATCC, MBA-331). MPS IIIC and WT female mice at 8 weeks were anesthetized and placed in a stereotactic frame. The stereotactic coordinates are the following: striatal, 2mm lateral and 3mm deep to bregma. 2.6 x 10^9 vg/hemisphere were delivered using a 26-gauge Hamilton syringe into each striatum at a rate of 0.5µl/min (3µl/hemisphere). Sham

treated mice received PBS (3µl/hemisphere). Mice were sacrificed and brains were collected and fixed 6 months post-treatment by Tordo *et al.* (2018) (187).

22. HGSNAT enzyme activity

Tissues and cell homogenates in ddH_2O were prepared by sonication (3x of 10 sec) and HGSNAT activity assayed using the fluorogenic substrate 4-methylumbelliferyl-β-D-glucosaminide in the presence of 5 mM acetyl-CoA in a McIlvain phosphate-citrate (0.2 M phosphate / 0.1 M citrate buffer) buffer, pH 5.5. The assay mix contained 5 µl homogenate, 5 µl of 3 mM substrate, 5 µl of 10 mM acetyl-CoA, 5 µl buffer and 5 µl of water. After incubation at 37^{o}C for 3 h the reaction was stopped with 975 µl 0.4 M glycine buffer, pH 10.4 and 5 µl of homogenates was added in each blank tube. 250 µl of each reaction tube was transferred to a black 96-well plate and the reaction was read in a fluorometer. Protein concentration was measured using a Pierce^{TM} BCA Protein Assay kit (Thermo Scientific) according to the manufacturer's instructions.

23. Flow cytometry

HEK293, HSPC-derived macrophages and HSPCs transduced with either LV-GFP and LV-HGSNAT GFP were collected in PBS+1% FBS and analysis was performed using BD FACSCanto II instrument. For the engraftment studies, blood from the mouse tail vein (50 µl-100 µl) was collected in EDTA-containing capillary and was stained for 15 minutes in the dark with APC labeled anti-mouse CD45.1 Antibody (Biolegend, 1:20) and PE labeled anti-mouse CD45.2 Antibody (Biolegend, 1:20). Erythrocytes were lysed with RBC lysis buffer (155 mM NH_4Cl, 12 mM $NaHCO_3$, 0.1 mM EDTA) for 5 minutes and white cells were collected by centrifugation for 5 min at 350 g and resuspended in PBS+1% FBS twice. Fluorescence

compensation was performed with Anti-Mouse Ig, κ/Negative Control (FBS) Compensation Particles Set (BD™ CompBeads) according to manufacturer's instructions.

24. Isolation of HSPC and preparation of bone marrow-derived macrophages (BMDM).

To isolate bone marrow cells, tibia, femur and iliac bones were dissected and washed 1x with 70% ethanol followed by 3 washes with PBS containing 1% penicillin and streptomycin. Under sterile conditions, bone marrow was extracted with ice-cold SCGM media and cells were dissociated with a glass pipette. Cells were passed through a 70 μm nylon mesh strainer and centrifuged at 1500 RPM for 10 min, 4°C. The pellet was resuspended in 10 ml red blood cells (RBC) lysis buffer (155 mM NH_4Cl, 12 mM $NaHCO_3$, 0.1 mM EDTA) for 30 sec and 20 ml of ice-cold SCGM media was added. Mouse BMDM were prepared by culturing bone marrow cells with the median conditioned by L929 cells that secret granulocyte-macrophage colony stimulating factor (GM-CSF) as described by Trouplin *et al*.(189).

To isolate HSPC, the bone marrow cells were harvested by centrifugation at 1500 RPM for 10 min at 4°C and resuspended in EasySep™ Buffer (Stem Cell Technologies). HSPC were isolated with the EasySep™ Mouse Hematopoietic Progenitor Cell Isolation Kit (Stem Cell Technologies) according to the manufacturer's instructions and maintained in culture in SCGM media supplemented with 10 ng/ml rmIL-6, 100 ng/ml rmFlt-3L, 100 ng/ml rmTPO and 100 ng/ml rmSCF at 37°C with 5% CO_2.

25. Mice HSPC transduction and transplantation

HSPC were isolated as described above from donor B6.SJL-*Ptprc*^{a} *Pepc*^{b}/BoyJ (CD45.1-positive) WT mice and transduced with two hits (on the day HSPCs isolation and

after 24 h) of the LV vector at 30 multiplicity of infection (MOI) each time, in the presence of 8 µg/µl of protamine sulfate. Twenty-four hours after, the cells (2 x 10^6 in total) were resuspended in PBS and injected in the tail vein of *Hgsnat*^{Geo} mice previously treated for 5 consecutive days by busulfan (IP, 25 mg/kg each day). Starting from the first day of busulfan treatment, the mice were kept in sterile conditions. They were fed irradiated food and treated with Baytril® (enrofloxacin, 50 mg/ml in drinking water) for 10 days.

26. Open field test

The open field test was performed by placing a mouse in the center of the arena (45 cm length x 45 cm width x 40 cm height, Open-Field Box Panlab, Harvard Apparatus, Perspex (Plexiglass)). Mouse behavior was video recorded for 20 minutes and analyzed using the software Smart 3.0. The mouse trajectory, the number of entries in the center, the total distance traveled, the global activity and the immobility duration (s) were analyzed. A 30-minute room adjustment period was implemented before the start of each test and the arena was cleaned with 70% ethanol in before placing a new animal.

27. Novel object recognition test

The novel object recognition test (Fig. 12) was conducted in three phases, each of 10 minutes: the habituation phase, the familiarization with two equal objects and the novel object test. In the habituation phase, on the first day of the experiment, each mouse was placed individually in the arena (a transparent Plexiglas box of 40 cm length x 50 cm width x 20 cm height) and then returned to its home cage. After 24 h, each mouse was placed again in the arena and familiarized with 2 identical objects positioned 9.5 cm away from the right and left walls. Each mouse was placed on the opposite side of the objects, facing the wall. One hour

later, one object was replaced by a new object and each mouse was placed again in the arena. The exploration performance was video recorded and analyzed manually by the experimenter. Exploration was counted when the head of the mouse was in a 3 cm radius from the object facing the object, when it was sniffing the object, or when it was touching the object with the snout. A 30-minute room adjustment period was implemented before the start of each test and the arena and the objects were cleaned with 70% ethanol in before placing a new animal to avoid olfactory cue bias. Discrimination index (DI) was calculated as the difference in the time spent exploring the novel and the old object divided by the total exploration time. A DI significantly higher than 0 was interpreted as a preference for the novel object.

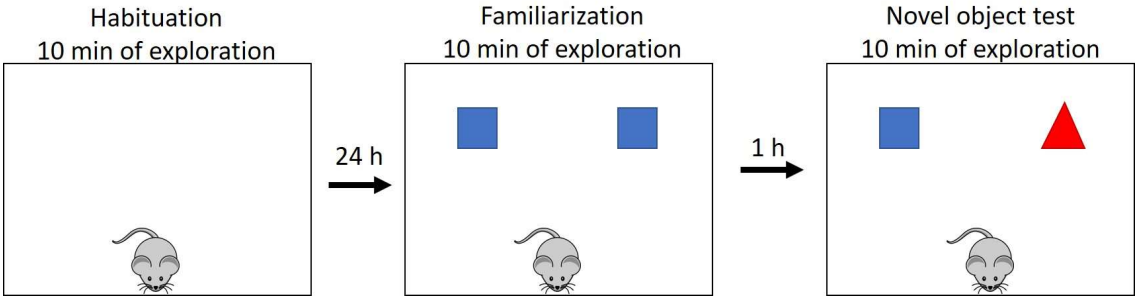

$$Discrimination\ index\ (DI) = \frac{(Time\ spent\ exploring\ novel\ object) - (Time\ spent\ exploring\ old\ object)}{Total\ exploration\ time}$$

Figure 12: Schematic of a novel object recognition test.

28. Statistics

All data in the figures represent the mean values ± SD or SEM from multiple experiments. Data were analyzed using the GraphPad Prism version 5.00 software (GraphPad Software, San Diego California USA). The numbers of experiments and replicates analyzed in each experiment are indicated in the figure legends. The statistical significance of differences between two conditions was calculated by Student's t test (two values) or ANOVA with level of significance of $p<0.05$. LC/MS data were analyzed using the Scaffold software v. 4.8.1.

Preface to Chapter 3

This chapter describes the first aim of this thesis, which is the analysis of synaptic transmission in neurons of MPS IIIC mice. Because progressive loss of spatial memory was previously identified as one of the major pathological clinical signs in MPS IIIC mouse model (190) we have chosen to study hippocampal pyramidal neurons, and explored both cultured primary neurons derived from dissociated E16 hippocampi and CA1 hippocampal neurons of MPS IIIC mice. This chapter generated the manuscript "Early defects in lysosomal storage disease disrupt excitatory synaptic transmission" that is currently in communication to be published. In this chapter, I report, for the first time, that MPS IIIC hippocampal neurons present alterations in synaptic spines, synaptic vesicles and synaptic proteins, and that the excitatory neurotransmission is mostly compromised.

Chapter 3

EARLY SYNAPTIC DEFECTS IN MUCOPOLYSACCHARIDOSIS TYPE IIIC DISRUPT THE EXCITATORY NEUROTRANSMISSION

29. Cultured primary hippocampal neurons from MPS IIIC mice present lysosomal storage phenotype

In order to study potential dysfunctions and pathological changes in MPS IIIC neurons we have established cultures of dissociated hippocampi from E16 mouse embryos cultured in neurobasal media for 21 DIV. Before assessing the synaptic characteristics of cultured primary MPS IIIC mouse neurons, we first gathered evidence of the lysosomal pathology by transmission electron microscopy (TEM). Analysis of primary cultures confirmed the presence of lysosomal storage vacuoles in the MPS IIIC neurons as well as in occasionally present microglia (about 1-2% of total cells) (Fig. 13A). Both types of cells contained electron-dense lamellar bodies compatible with secondary storage of gangliosides and misfolded proteins as well as electron-lucent vacuoles that can be attributed to the primary storage of HS (Fig. 13B).

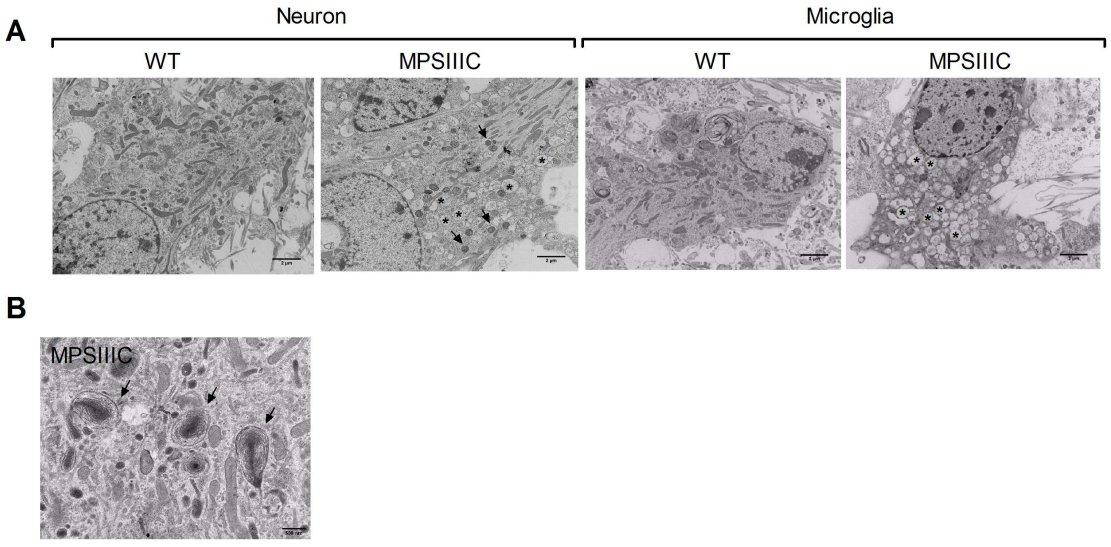

Figure 13: Lysosomal storage in MPS IIIC cultured hippocampal neurons.

(A, B) The dual pattern of storage is observed by electron microscopy in MPS IIIC neurons and microglia derived from the brains of MPS IIIC embryos. Electron-dense storage bodies (arrows) presumably contain lipids and misfolded proteins whereas electron-lucent organelles (*), glycans. Scale bar is 2 μm in (A) 500 nm in (B). Panels show representative images from 3 independent sets of experiments.

30. Hippocampal MPS IIIC neurons present immature and scarce synaptic spines *in vitro* and *in vivo*

To test if defects in synaptic neurotransmission in hippocampal neurons can be responsible for early-onset deficits in memory and learning reported in MPS IIIC mice (63), we first analyzed and quantified synaptic spines on the dendrites of hippocampal pyramidal neurons, which play an important role in learning and memory (191) . The density and morphology of spines on the dendrites of hippocampal cultured neurons were studied at DIV 21 by confocal microscopy after staining the cell membranes with the lipophilic fluorescent dye Dil. Although total spine density (number of spines per 20 μM of the dendrite) was similar for the WT and MPS IIIC neurons, the cells from MPS IIIC mice had ~2-fold higher density of immature filopodia spines and similarly decreased density of mature "mushroom" spines (Fig. 14A and B, left panels).

The synaptic spines were further studied *in vivo* on pyramidal neurons in the CA1 region of the hippocampus of MPS IIIC (*Hgsnat-Geo*) mice expressing the *Thy1-EGFP* transgene that expresses the enhanced green fluorescent protein (EGFP) under the control of a modified Thy1 promoter containing the sequences required for neuronal expression but lacking the sequences required for expression in non-neural cells. The resolution of confocal images did not allow us

to quantify different types of spines, however, we detected a reduction of total spine density. At P10, the mouse equivalent age to the human disease onset (3 to 5 years-old), the density of synaptic spines was reduced by ~22% (WT=12.2±3.9, MPS IIIC=9.5±2.9; Fig. 14A and B, right panels).

To assess whether reduced density of synaptic spines is a cellular pathology shared among different types of neurological lysosomal storage disorders, we quantified spines on pyramidal CA1 neurons in the mouse model of sialidosis. Sialidosis patients have mutations in the neuraminidase 1 (*Neu1*) gene, leading to lysosomal storage of sialylated glycoproteins (44, 192). Previously described *Neu1* KO mice (185) were crossed with the *Thy-1-EGFP* strain and GFP-positive pyramidal neurons from the CA1 region of the hippocampus were studied by confocal microscopy. Our data show that similarly to neurons of MPS IIIC mice neurons of 3 month-old sialidosis mice also present reduction of synaptic spine density (WT=20.7±4.4; *Neu1* KO=17.6±3.7; Fig. 14C), suggesting that this effect is not exclusively related to heparan sulfate storage.

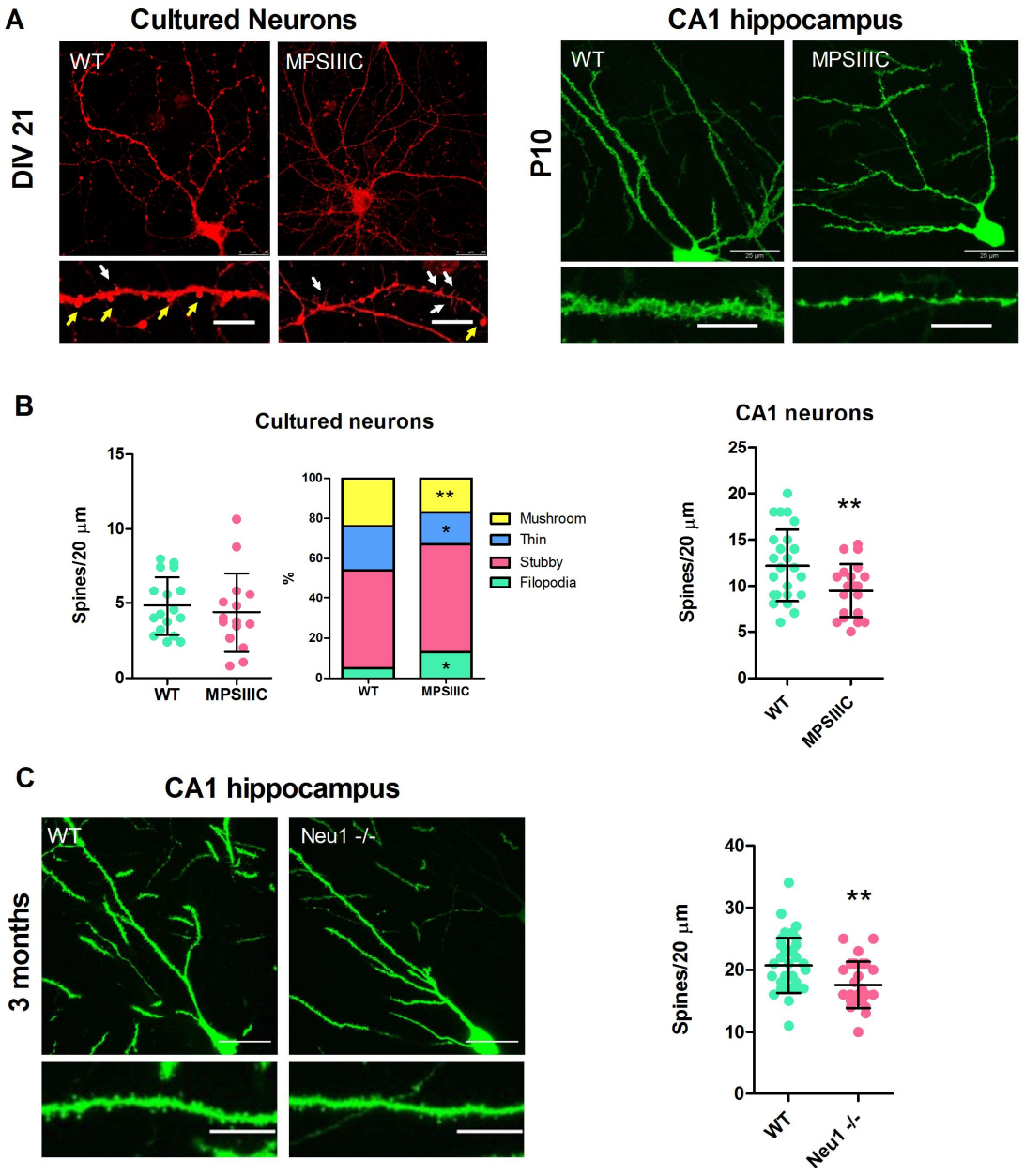

Figure 14: MPS IIIC hippocampal neurons present decreased density of mature synaptic spines *in vitro* and *in vivo*.

(A) Majority of dendritic spines in MPS IIIC cultured neurons are immature. Dissociated cultured hippocampal neurons from embryonic mice (E16) at DIV 21 were stained with the lipophilic dye DiI (left panel). In the inserts, mature (mushroom shape) spines are marked with

yellow arrows and immature spines (filopodia), with the white arrows. The right panel shows representative images of synaptic spines in pyramidal neurons expressing EGFP in the CA1 hippocampus region of mice at the age of P10. Dendrites in the WT neurons show uniform thickness whereas those in the MPS IIIC neurons present uneven thickness with thin areas alienating with the wider areas resembling spheroids or knots. (B) Graphs show dendritic spine densities (left), and distribution of different types of spines (middle) in hippocampal cultured neurons at DIV 21 and density of synaptic spines in the CA1 neurons (right). (C) Representative images and quantification of synaptic spines in pyramidal neurons from the CA1 region of the hippocampus of 3 month-old Neu1 KO (mouse model of sialidosis) and their respective WT littermates all expressing the Thy1-EGFP transgene. The analysis of spine subtypes and quantification of spine densities was performed in a blinded manner for 20 μm-long dendrite segments at 30 μm distance from the soma. Data on the graphs show mean values, and SD. P-value was calculated by t-test (*$p<0.05$ and ** $p<0.01$). Scale bar equals 25 μm for all panels and 10 μm for all inserts. At least 30 cells from 3 different mice for each age and genotype were analyzed.

31. Synaptic vesicles are reduced in the terminals of MPS IIIC hippocampal neurons

To test whether the levels of synaptic vesicles are changed in cultured MPS IIIC neurons we studied the cellular distribution and density of synapsin 1 (Syn1) by confocal immunofluorescent microscopy (Fig. 15A and B). Quantification of images demonstrated that in neurons from MPS IIIC mice at DIV 21, the density of Syn1-positive puncta specifically associated with the axonal marker, neurofilament medium chain (NF-M) was significantly reduced.

The density of synaptic vesicles at the synaptic terminals of hippocampal neurons in culture and in pyramidal neurons of the CA1 region of the hippocampus from 3 and 6 month-old mice was further analyzed by TEM. In cultured neurons the density of synaptic vesicles (total number of synaptic vesicles in the axonal terminal divided by the area of the terminal in μm^2) in the MPS IIIC neurons was decreased by 23% (WT=319.1±81.6, MPS IIIC=245.3±88.7) (Fig. 15C and D, upper panels). A similar phenotype was also observed *in vivo.* In 3 month-old MPS IIIC mice, the density of synaptic vesicles was decreased by 21.7% as compared with WT (WT=248.3±101.7, MPS IIIC=194.3±71.7). This reduction was even more prominent by the age of 6 months, when the difference between MPS IIIC and the WT reached 28.9% (WT=209.6±79, MPS IIIC=149.1±78) (Fig. 15C and D, middle and lower panels). Besides, around 10-20% of terminals in the MPS IIIC neurons *in vivo* and *in vitro* contained multivesicular vacuoles with double limiting membrane (Fig. 15C, arrowhead) resembling autophagosomes found in the neurons of patients with adult neurodegenerative disorders (reviewed in (193)). Overall, our TEM results directly confirm the reduction of synaptic vesicles *in vivo* and *in vitro* predicted from decrease of Syn1-positive puncta.

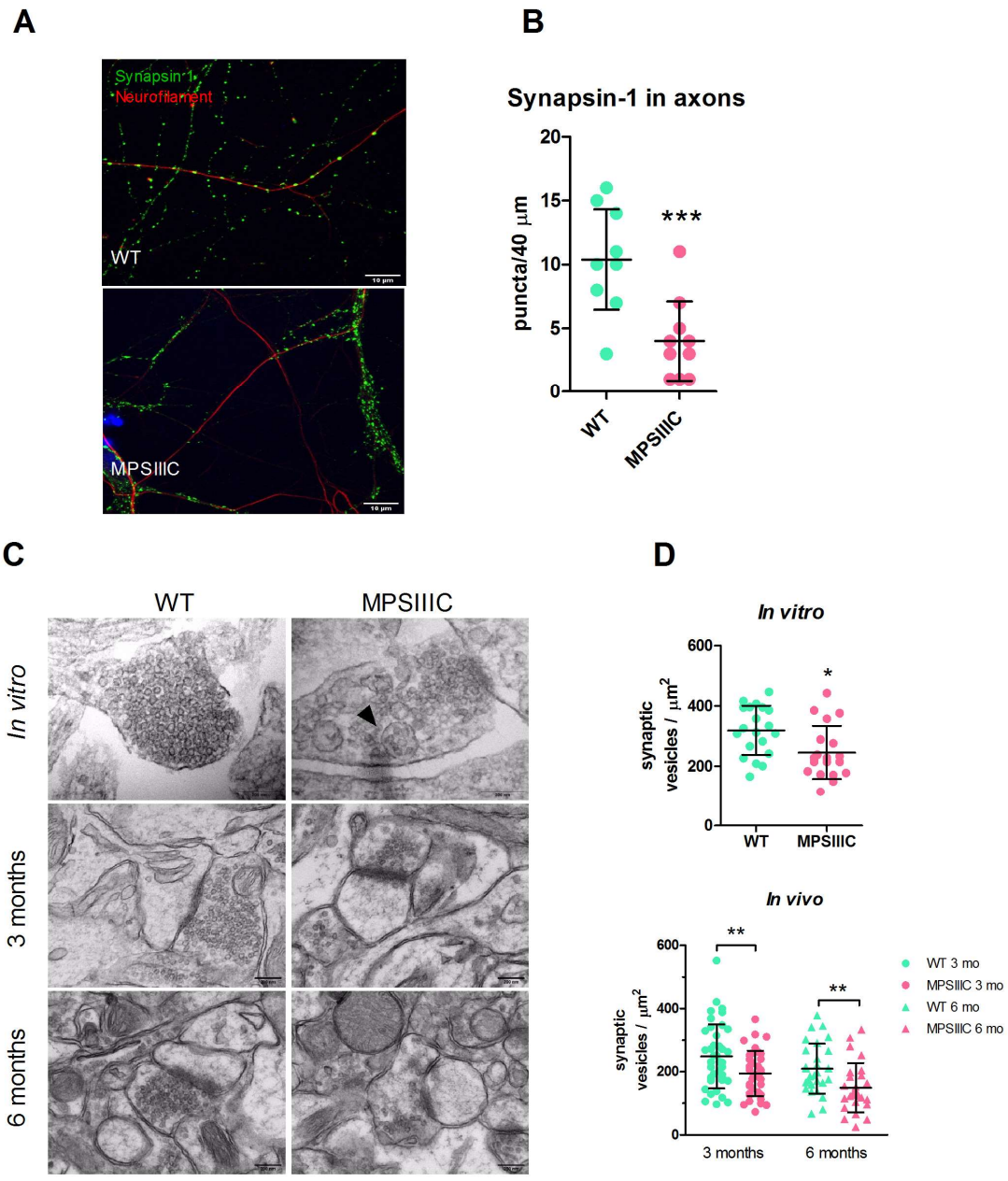

Figure 15: MPS IIIC hippocampal neurons present reduced densities of Syn1-positive puncta in the axons and scarcity of synaptic vesicles in the synaptic terminals.

(A) Representative images of cultured hippocampal neurons at DIV 21 from WT and MPS IIIC mice stained with antibodies against Syn1 and an axonal marker, neurofilament medium chain protein (NF-M). (B) When compared to the WT, MPS IIIC neurons have lower density of Syn1

puncta in the axons of the neurons. P-value was calculated by t-test (***p<0.001), data show mean values and SD of 3 independent experiments. Scale bar equals 10 μm. (C) Representative TEM images of synaptic terminals of cultured hippocampal neurons at DIV 21 and pyramidal neurons from the CA1 region of the hippocampus of 3 and 6 month-old mice. An autophagosome in the synaptic terminal is marked with an arrowhead. Scale bar equals 200 nm. (D) The density of synaptic vesicles is reduced in MPS IIIC neurons both in vitro and in vivo. At least 30 cells from 3 mice per each age and genotype were analyzed.

32. MPS IIIC neurons show alterations in excitatory synaptic marker

To test whether both excitatory and inhibitory synapses are affected in cultured hippocampal MPS IIIC neurons we studied by confocal immunofluorescent microscopy distribution and density of pre- and postsynaptic markers associated with either glutamate-mediated excitatory or GABA-mediated inhibitory neurotransmission. Puncta were quantified in 25 μm-long dendrite segments, 40 μm away from the soma. We counted separately isolated pre- and post-synaptic puncta and when they were in juxtaposition, indicating the presence of a functional synapse at the moment of fixation. The analysis of the excitatory markers, vGLUT1 (the presynaptic transporter of glutamate in the synaptic vesicles) and PSD-95 (postsynaptic density protein 95, a scaffold protein present in the areas of postsynaptic density that interacts with NMDA receptors (194)) demonstrated a significant difference between MPS IIIC and WT neurons (Fig. 16A-C). Quantification of puncta revealed decreased density of both vGlut1 (WT=10.63±4.74 and MPS IIIC=8.83±4.23 puncta/25μm) and PSD-95 (WT=2.52±1.38 and MPS IIIC=1.4±1.24 puncta/25μm) in MPS IIIC neurons and reduced number of PSD-95-positive puncta in juxtaposition with vGLUT1-positive puncta (WT=1.1±1 and MPS IIIC=0.6±0.6 puncta/25μm), meaning that fewer functional excitatory synapses were

occurring in these neurons (Fig. 16B). The reduction of PSD-95 in MPS IIIC cultured neurons was confirmed by Western blot (Fig. 16C). Conversely, both density and juxtaposition of puncta for the markers of the inhibitory synapse, vGAT (a transporter involved in the uptake of GABA into the synaptic vesicles) and Gephyrin (a protein that anchors GABA-A receptors) (Fig. 16D), were similar for MPS IIIC and the WT neurons (Fig. 16E).

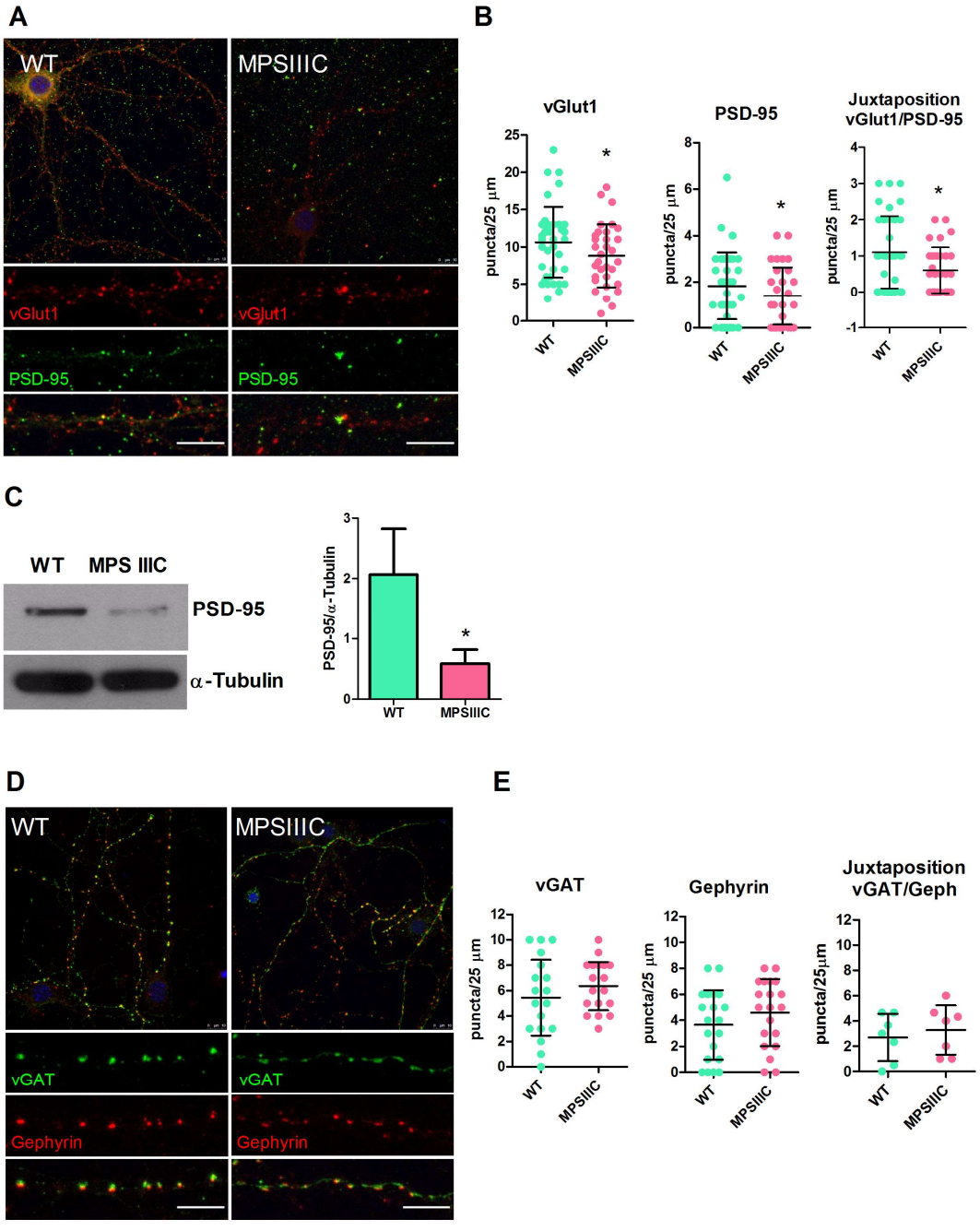

Figure 16: MPS IIIC hippocampal cultured neurons present alterations in protein markers of excitatory synapse.

(A) Representative images of hippocampal cultured neuron from at DIV 21 labeled with antibodies against markers of excitatory synapse, vGLUT1 and PSD-95 showing the characteristic punctate pattern. (B) Quantification of vGLUT1-positive puncta, PSD-95-positive puncta and their juxtaposition demonstrates significantly lower densities of PSD-95-positive puncta and PSD-95-positive puncta in juxtaposition with vGLUT1-positive puncta. (C) Western blot of protein extracts from cultured hippocampal neurons confirms the reduction of PSD-95 in MPS IIIC cells. (D) Representative images of hippocampal cultured neuron at DIV 21 labeled with antibodies against vGAT and Gephyrin. The insert shows the juxtaposition between the vGAT-positive and Gephyrin-positive puncta indicating functional synapses. (F) Quantification of vGAT-positive puncta, Gephyrin-positive puncta and their juxtaposition. The quantification of puncta was performed within 25 µm segments of dendrites at 30 µm distance from the soma in a blinded manner using cultures from 3 independent experiments with a total of 10 cells being analyzed for each experiment. P-value was calculated by t-test (*$p<0.05$). Scale bars equal 10 µm.

To test if PSD95-positive puncta and its juxtaposition with vGLUT1-positive puncta were also reduced *in vivo* we stained brain slices from 3 month and 6 month-old WT and MPS IIIC mice with antibodies against these proteins and analyzed at least three areas of 1252.57 μm^2 from the stratum radiatum layer of the CA1 area of the hippocampus by confocal microscopy (Fig. 17A). We found that density of PSD-95-positive puncta and PSD-95-positive puncta in juxtaposition with vGLUT1-positive puncta was significantly reduced in the brains of 6 month-old mice (Fig. 17B). vGlut1 puncta did not differ between WT and MPS IIIC (data

not shown). PSD-95 puncta were also reduced in density in human cortices from MPS patients (Fig.17F-G), confirming the results obtained in the mouse models.

The length and the area of postsynaptic densities (PSD) of asymmetric (excitatory) and symmetric (inhibitory) synapses of cultured hippocampal neurons and pyramidal neurons in the stratum radiatum of the CA1 region of hippocampus from 3 and 6-month-old mice were further studied by electron microscopy (Fig.17C). The length of excitatory PSD in MPS IIIC hippocampal neurons was generally smaller than that in the WT cells (Fig. 17D and E). In cultured neurons, the length of PSD for MPS IIIC mice was 37% smaller than for WT (WT=349.3±141.1 and MPS IIIC=220.3±48.6 nm). *In vivo*, excitatory PSD length was reduced by 12.5% (WT=339.3±91.5 and MPS IIIC=296.9±101.6) in 3 month-old mice, and by 14% in 6 month-old ones (WT=363.6±73.6 and MPS IIIC=312.2±85.8). The area of excitatory PSD was smaller in cultured neurons and *in vivo* at 6 months but not at 3 months (Fig. 17D and E). In cultured neurons, the area of PSDs in μm^2 of MPS IIIC was reduced by 42% as compared with WT cells (WT=0.013±0.009 and MPS IIIC=0.007±0.003). In 3 month-old mice, the area of excitatory PSD was similar between mouse strains (WT=0.013±0.005; MPS IIIC=0.013±0.006) but by the age of 6 months, it became 21% smaller in MPS IIIC mice (WT=0.018±0.006; MPS IIIC=0.014±0.004; $P<0.05$). We found that PSD length in symmetrical inhibitory synapses was similar between MPS IIIC and WT neurons *in vivo* and *in vitro* (Fig. 18), consistent with the results of immunolabeling for GABAergic markers (Fig. 16D and E),

Interestingly, TEM analysis also demonstrated that synapse localization in cultured MPS IIIC neurons was significantly altered as compared with the WT cells. While in the WT neurons the majority (~80%) of synapses were located on dendritic spines (axospinous synapses), MPS IIIC cells showed a shift towards axodendritic synapses (78% axodendritic;

22% axospinous, Fig. 17H and I). On the other hand, we did not detect any difference in synaptic localisation in vivo on dendrites of CA1 pyramidal cells between 6 month-old WT (54% spines; 46% dendrites) and MPS IIIC (53% spines; 47% dendrites) mice (Fig. 17I, right panel).

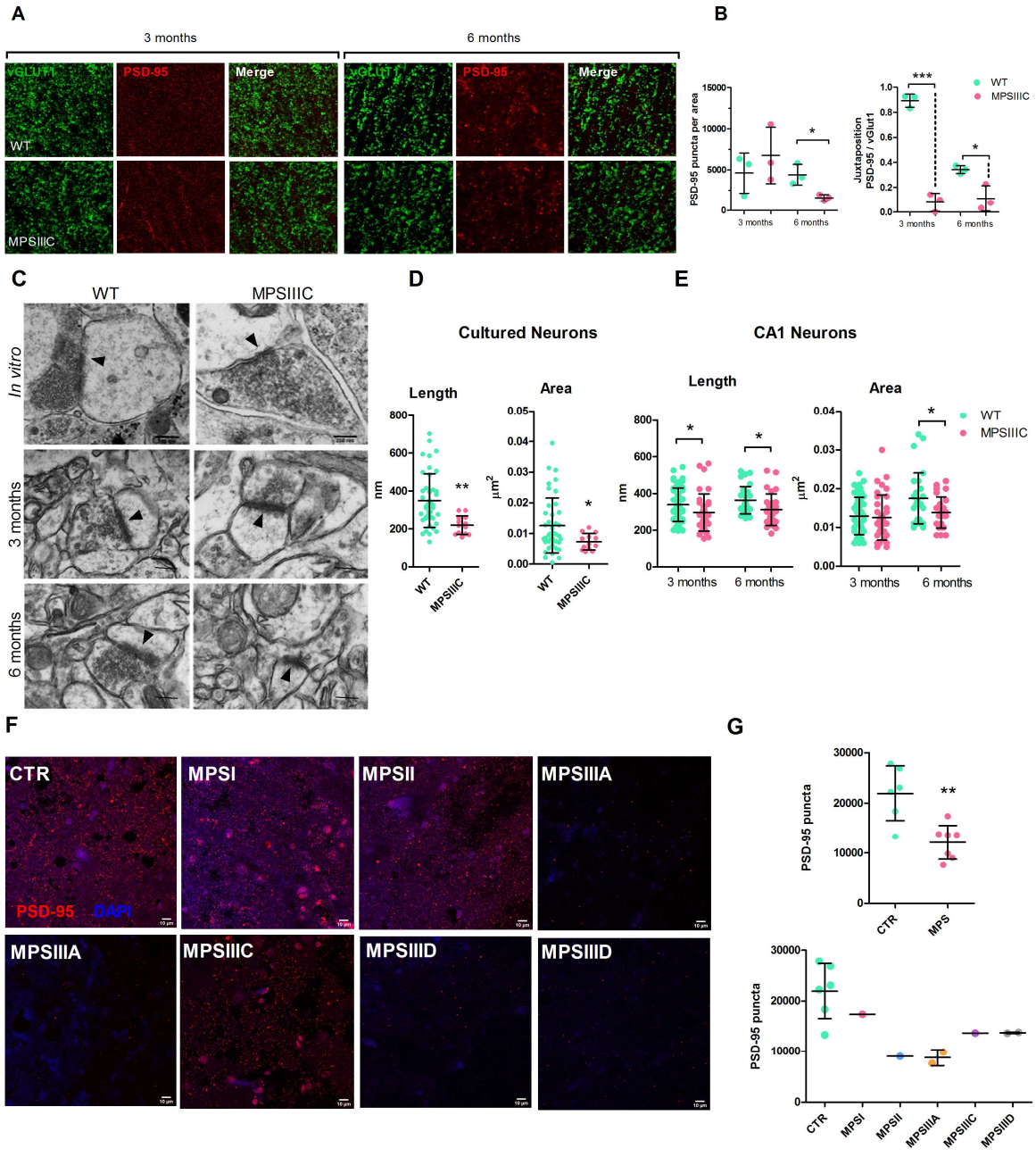

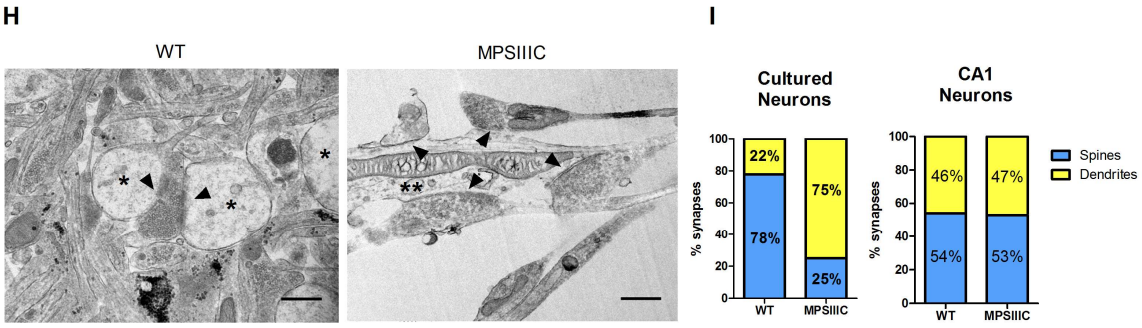

Figure 17: Reduction of postsynaptic densities in MPS IIIC mice and in human cortices of MPS patients.

(A) Representative confocal images of CA1 hippocampal regions of 3 and 6 month-old WT and MPS IIIC mice stained for the markers of excitatory synapse, PSD-95 and vGLUT1. (B) Density of PSD-95 and vGlut1-positive puncta and their colocalization (Pearson's correlation coefficient) were quantified using ImageJ software. The quantification of puncta was performed in a blinded manner using 3 mice per age per genotype. P-value was calculated by t-test (*$p<0.05$). Scale bar = 10 µm. (C) Representative TEM images of synapses in cultured hippocampal neurons at DIV 21 and in pyramidal neurons from the CA1 region of the hippocampus of 3 and 6 month-old mice. PSDs are marked with arrowheads. (D) Quantification of length (nm) and area (μm^2) of PSDs in hippocampal cultured neurons. (E) Quantification of length (nm) and area of PSDs (μm^2) in pyramidal neurons from the CA1 region of the hippocampus. Data show mean values and SD of 3 different sets of experiments with at least 10 images per experiment. Only asymmetric (excitatory) PSDs were considered for analysis. P-value was calculated by t-test (*$p<0.05$ and **$p<0.01$). Scale bar equals 250 nm. (F) Representative confocal images of human cortices from control and MPS patients stained with anti-PSD-95 (G) Density of PSD-95-positive puncta in human cortices. (H) Representative TEM images of synapses in WT and MPS IIIC cultured hippocampal neurons at DIV 21 showing alteration in the distribution of synapses. In MPS IIIC cultured neurons,

there is a shift from axospinous to an axodendritic pattern. Spine (*), synaptic cleft (arrowheads) and dendrite (**). Scale bar equals 500 nm. (I) Quantification of axospinous and axodendritic synaptic connections in cultured hippocampal neurons and in the pyramidal neurons in the CA1 region of the hippocampus of 6 month-old WT and MPS IIIC mice. Data show total values of 3 independent experiments with 3 mice per genotype.

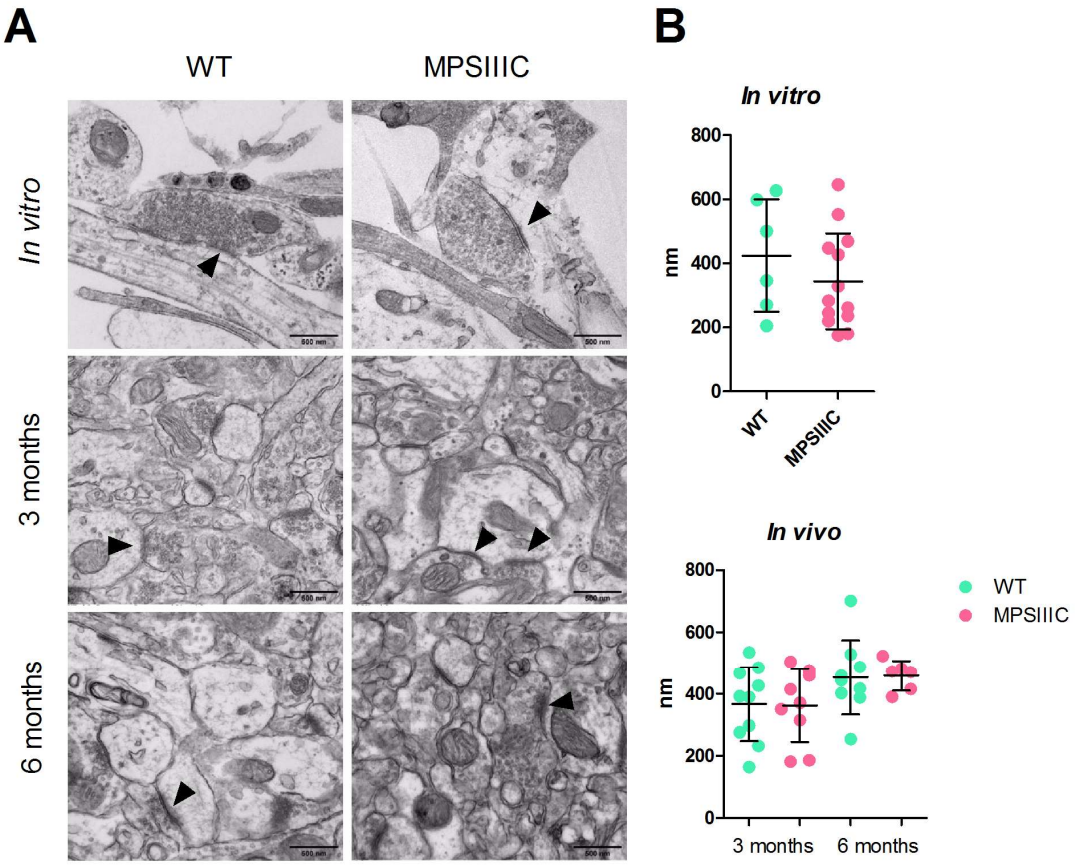

Figure 18: Lengths of PSD in symmetrical inhibitory synapses are similar between MPS IIIC and WT neurons *in vitro* and *in vivo.*

(A) Electron micrographs of inhibitory symmetric PSD (arrowheads) in cultured neurons and in the CA1 region of the hippocampus from 3 and 6 month-old mice. (B) Quantification of

length of PSD in vitro and in vivo. Graphs show mean and SD values from 3 independent sets of experiments. Panels show representative images from 3 independent sets of experiments.

33. MPS IIIC neurons show alterations in neurotransmission.

To test if alterations in the distribution of synaptic markers in MPS IIIC mice translate into changes in synaptic transmission we conducted electrophysiological recordings of miniature inhibitory (mIPSCs) and excitatory (mEPSCs) postsynaptic currents.

Miniature synaptic events were recorded in cultured hippocampal neurons from MPS IIIC and WT mice (DIV19-DIV21). We found that mEPSCs of cultured MPS IIIC neurons displayed a 3-fold increase in frequency (WT=1.3±1.1 Hz and MPS IIIC=4.1±3.7 Hz) and a significant increase in the amplitude (WT=13.8±6.2 pA and MPS IIIC=16.9±6.3 pA) (Fig. 19A). In contrast, the frequency and amplitude of the inhibitory events in cultured MPS IIIC hippocampal neurons were not significantly different from those in the WT cells (frequency, WT=1±1.6 Hz and MPS IIIC=1.6±1.8 Hz; amplitude, WT=12.2±4.2 pA and MPS IIIC=11.7±2.7 pA) (Fig. 19C).

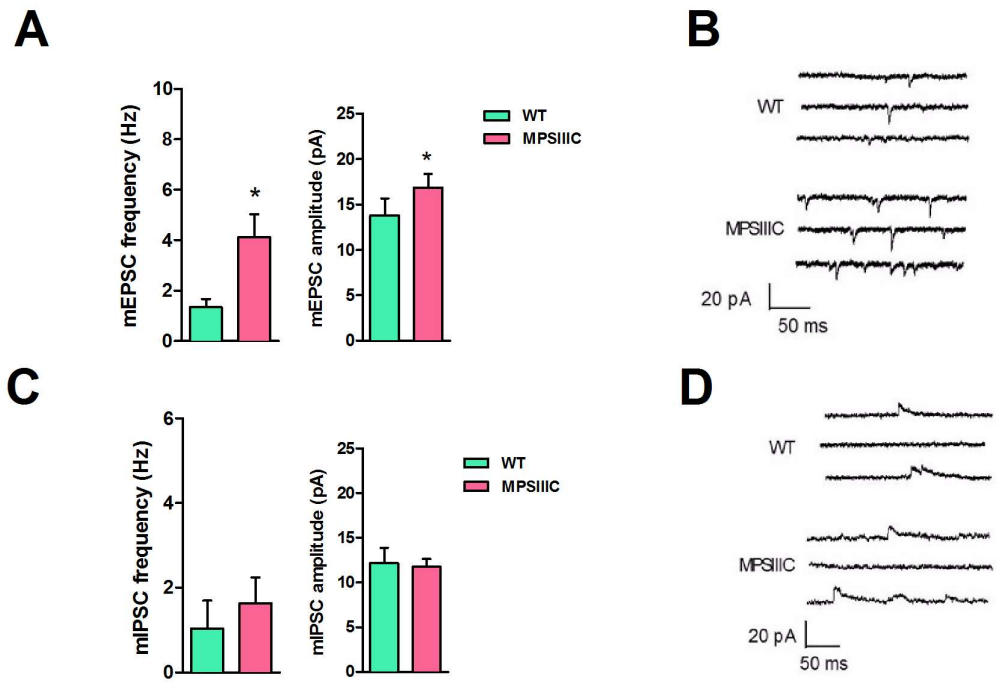

Figure 19: Miniature excitatory and inhibitory postsynaptic currents in MPS IIIC cultured neurons.

(A) Excitatory neurotransmission is enhanced in MPS IIIC cultured hippocampal neurons. Frequency (left) and amplitude (right) of the mEPSCs in WT and MPS IIIC cultured hippocampal neurons (n=11 cells from WT and 17 cells from MPS IIIC; t-test *$p < 0.05$) (B) Representative traces of the mEPSCs in WT and MPS IIIC cultured hippocampal neurons at DIV19-22. (C) Inhibitory neurotransmission mediated by GABA is not affected in MPS IIIC cultured hippocampal neurons. Frequency (left) and amplitude (right) of the mIPSCs in WT and MPS IIIC cultured hippocampal neurons (n=6 cells from WT and 9 cells from MPS IIIC; t-test: $p=0.53$ for frequency and $p=0.82$ for amplitude). (D) Representative traces of the mIPSCs in WT and MPS IIIC cultured hippocampal neurons at DIV19-22. For mE/IPSCs, the cells originated from at least 8 different neuronal cultures.

34. PSD-95 and Syn1 deficiency in MPS IIIC neurons can be rescued by correcting the primary genetic defect.

To establish causative relations between the deficits of protein markers of excitatory synapses and HGSNAT deficiency, we attempted to rescue this phenotype by correcting the genetic defect with a virus overexpressing the WT human enzyme. Human codon-optimized HGSNAT cDNA fused with that of GFP was cloned into a third-generation lentiviral vector (LV) under the control of a CMV promoter. The LV was tested in HEK 293 cells transduced with a multiplicity of infection (MOI) of 10. The transduced cells expressed HGSNAT-GFP fusion protein correctly targeted to the lysosomes and had 120-fold increased HGSNAT activity as compared with non-transduced cells (Fig. 20).

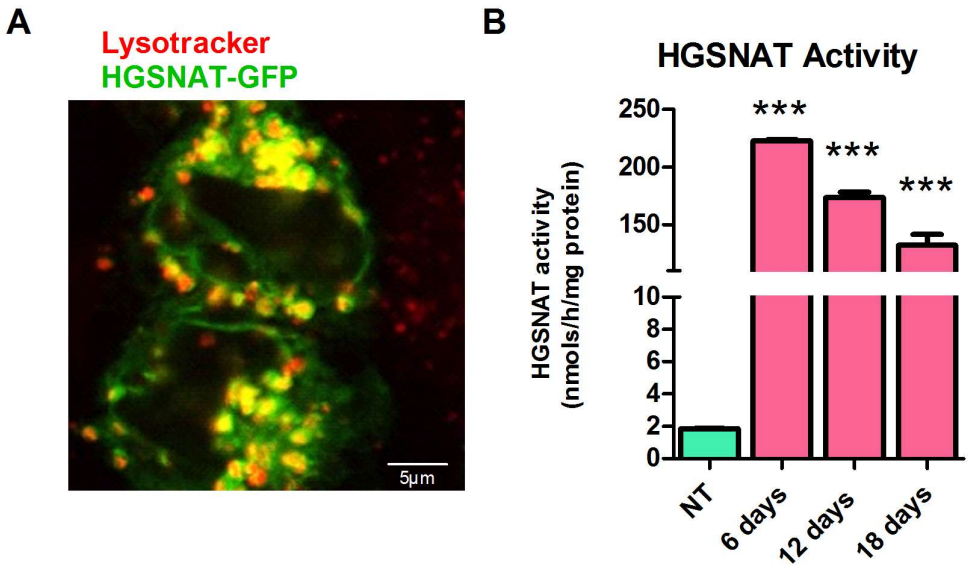

Figure 20: Transduction of HEK293 cells with LV-HGSNAT-GFP results in expression of enzymatically active and correctly targeted HGSNAT-GFP fusion protein.

(A) Fluorescent confocal images of HEK 293 cells transduced with LV-HGSNAT-GFP. Colocalization of GFP puncta and Lysotracker red staining demonstrates that HGSNAT-GFP fusion protein is correctly targeted to the lysosomes. (B) HGSNAT activity measured in homogenates of HEK293 cells transduced with LV-HGSNAT-GFP is >100-fold increased as compared with the cells transduced with LV-GFP.

We further transduced MPS IIIC primary hippocampal neurons at DIV 3 with either LV-GFP or LV-HGSNAT-GFP (Fig. 21A, C), kept them in culture until DIV 21, fixed and analyzed by confocal fluorescent microscopy to measure density of PSD-95 and Syn1. Our data show that density of PSD-95 puncta in MPS IIIC hippocampal neurons transduced with LV-HGSNAT-GFP was similar to WT neurons (Fig. 21B). We further stained the cells with anti-Syn1 antibodies and quantified the density of Syn1-positive puncta associated with NF-stained axons (Fig. 21C). The number of puncta calculated per 40 μm of the axon was significantly reduced in MPS IIIC neurons as compared with the WT cells and significantly increased in the MPS IIIC cells transduced with LV-HGSNAT-GFP as compared with the LV-GFP-transduced cells (Fig. 21D).

Previously, in collaboration with the University of Manchester, our laboratory demonstrated a rescue of the behavioral defects, primary and secondary lysosomal storage and neuroinflammation in MPS IIIC mice receiving intracranial injections of AVV vectors (AVV9 and AAV2 true type (TT)) encoding human untagged HGSNAT ((187). Since the females present hyperactivity and reduced anxiety 2 months earlier than males (63), only females were selected for this work. Eight week-old MPS IIIC and WT mice were injected into each striatum (2 mm lateral and 3 mm deep to bregma) with 2.6×10^9 vg/hemisphere. Control mice received sham injections of saline. After behavioral assessment at the age of 6 and 8 months, mice were sacrificed at 6 months post-treatment and their brains fixed with PFA and cryopreserved. Brain

slices of AVV9-HGSNAT treated and sham-treated MPS IIIC mice were stained with antibodies against PSD-95 and Syn1 and assessed the density of PSD-95-positive puncta in hippocampal CA1 area (Fig. 21E). We found that the treatment significantly increased the density of the puncta and the density of PSD-95-positive puncta in juxtaposition with Syn1-positive puncta (Fig. 21F). There was also a trend for the increase of Syn1-positive puncta density, but the results were not statistically significant perhaps due to high difference between the individual animals in the groups (data not shown). Thus, by restoring the primary defect of HGSNAT we could rescue PSD-95 defects both *in vivo* and *in vitro* and Syn1.

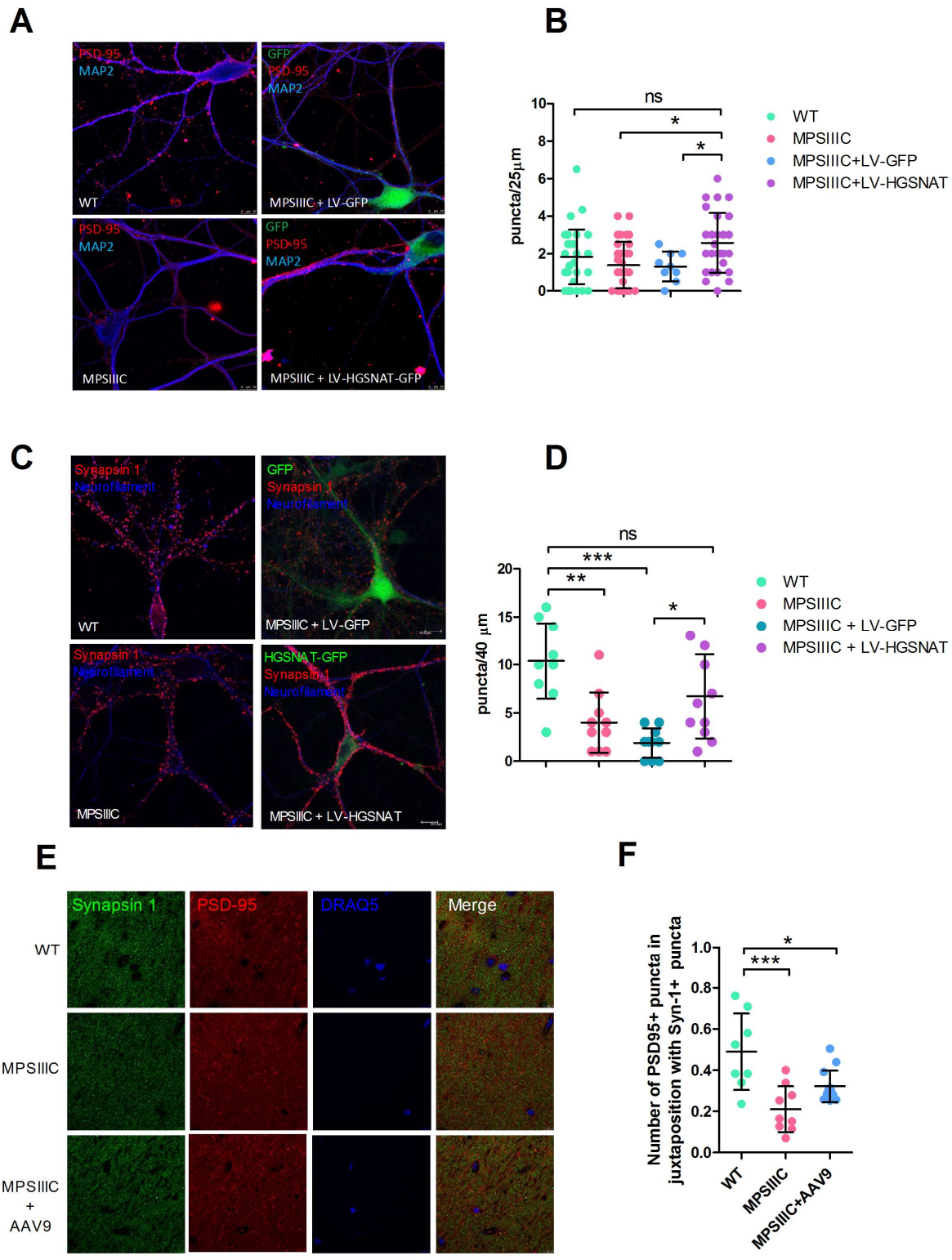

Figure 21: Deficits of PSD-95 and Syn1 in MPS IIIC neurons are rescued by transduction with viral vectors encoding for WT human HGSNAT.

(A) Representative images of cultured hippocampal WT, MPS IIIC neurons and MPS IIIC neurons transduced with either LV-GFP or LV-HGSNAT-GFP stained with anti-PSD-95 antibodies. (B) Quantification of PSD-95 puncta in WT, and MPS IIIC cells as well as in MPS IIIC cells treated with LV-GFP, and LV-HGSNAT-GFP. *p=0.03 and **p=0.002. (C) Representative images of cultured WT, and MPS IIIC neurons and MPS IIIC neurons transduced with either LV-GFP or LV-HGSNAT-GFP stained with anti-Syn1 antibodies. (D) Quantification of Syn1 puncta in the axons of cultured neurons. **p=0.0036 and ***p<0.0001 and 0.0008. (E) Thin sections of the CA1 region of the hippocampus from WT and MPS IIIC mice non-treated or treated with AAV9-HGSNAT stained with anti-Syn1 and anti-PSD-95 antibodies. (F) Quantification of Syn1-positive and PSD-95-positive puncta in juxtaposition (Pearson's correlation coefficient), *p=0.0114 and ***p<0.0001. Graphs show data from 3 different sets of experiments/mice with 10 images analyzed per experiment. P-value was calculated by one-way ANOVA (*p<0.05). Scale bar equals 5 μm in (A) and 10 μm in (C) and (E).

35. Proteomic analyses of synaptosomes reveal a dramatic decrease in synaptic, vesicle trafficking-associated and mitochondrial proteins in MPS IIIC mouse brains

To get insight into the molecular mechanisms underlying synaptic deficits in MPS IIIC neurons, we performed proteomic analyses of mouse brain synaptosomes (195). Synaptosomes were isolated from three MPS IIIC and three WT mice at 3 and 6 months of age, and their protein content analyzed by label-free quantitative proteomics using liquid chromatography tandem mass spectrometry (LC-MS/MS). LC-MS/MS analysis identified 1120 proteins in the synaptosomes from 3 month-old WT and 1248 proteins from MPS IIIC mice (FDR ≤ 1%). At 6 months, 809 proteins were identified in the WT and 1246 in the MPS IIIC animals (Fig. 22A).

A volcano plot distribution of synaptosome proteins from 3 month-old mice revealed that 133 proteins were reduced in abundance in MPS IIIC as compared to WT, whereas 395 proteins were reduced in MPS IIIC synaptosomes at 6 months (Fig. 22B, Appendices B and C). These proteins were then classified according to their biological function and linked to a particular metabolic or signaling pathway using automated GO (gene ontology terms) annotation (Fig. 22C and D) (196).

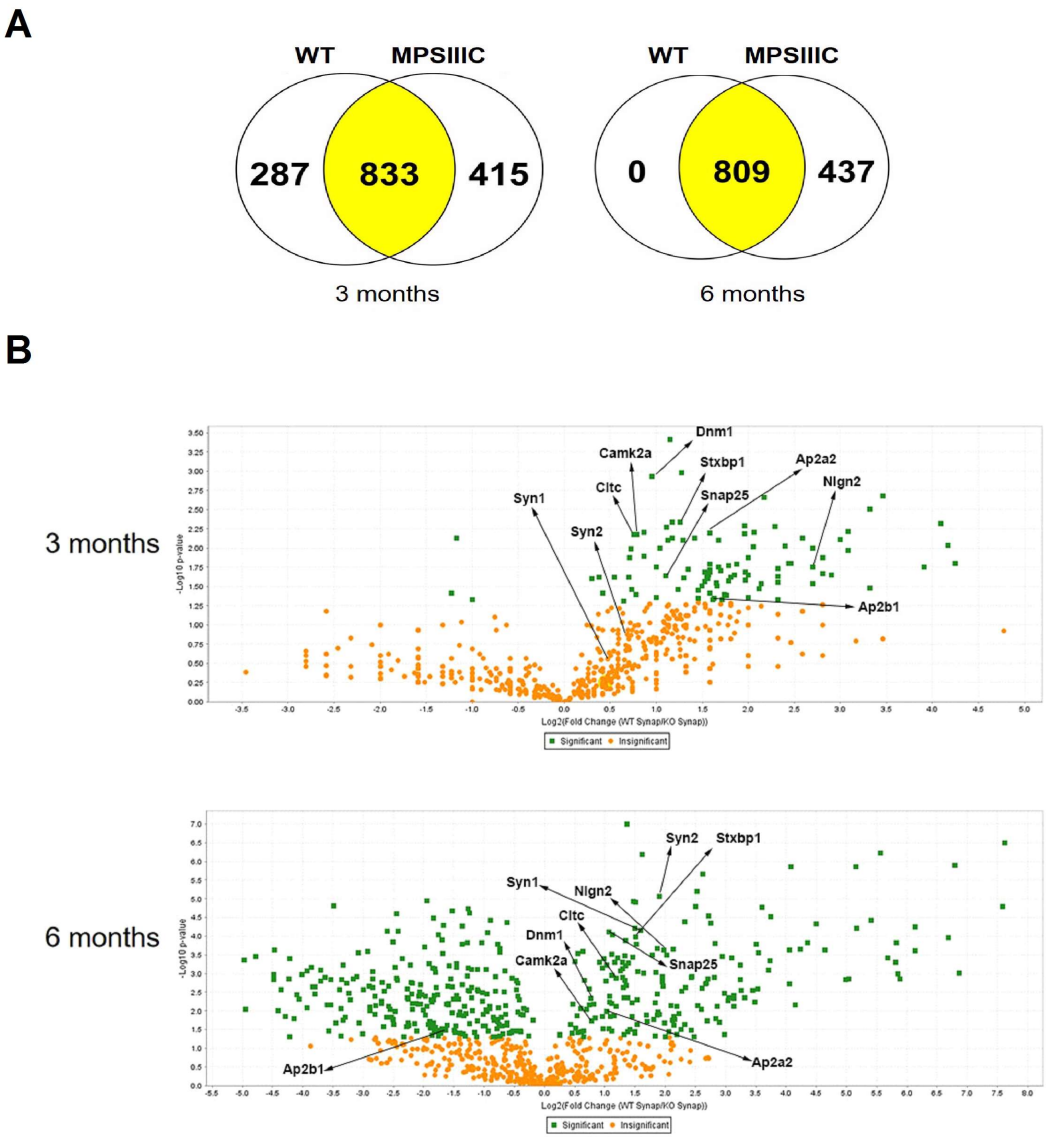

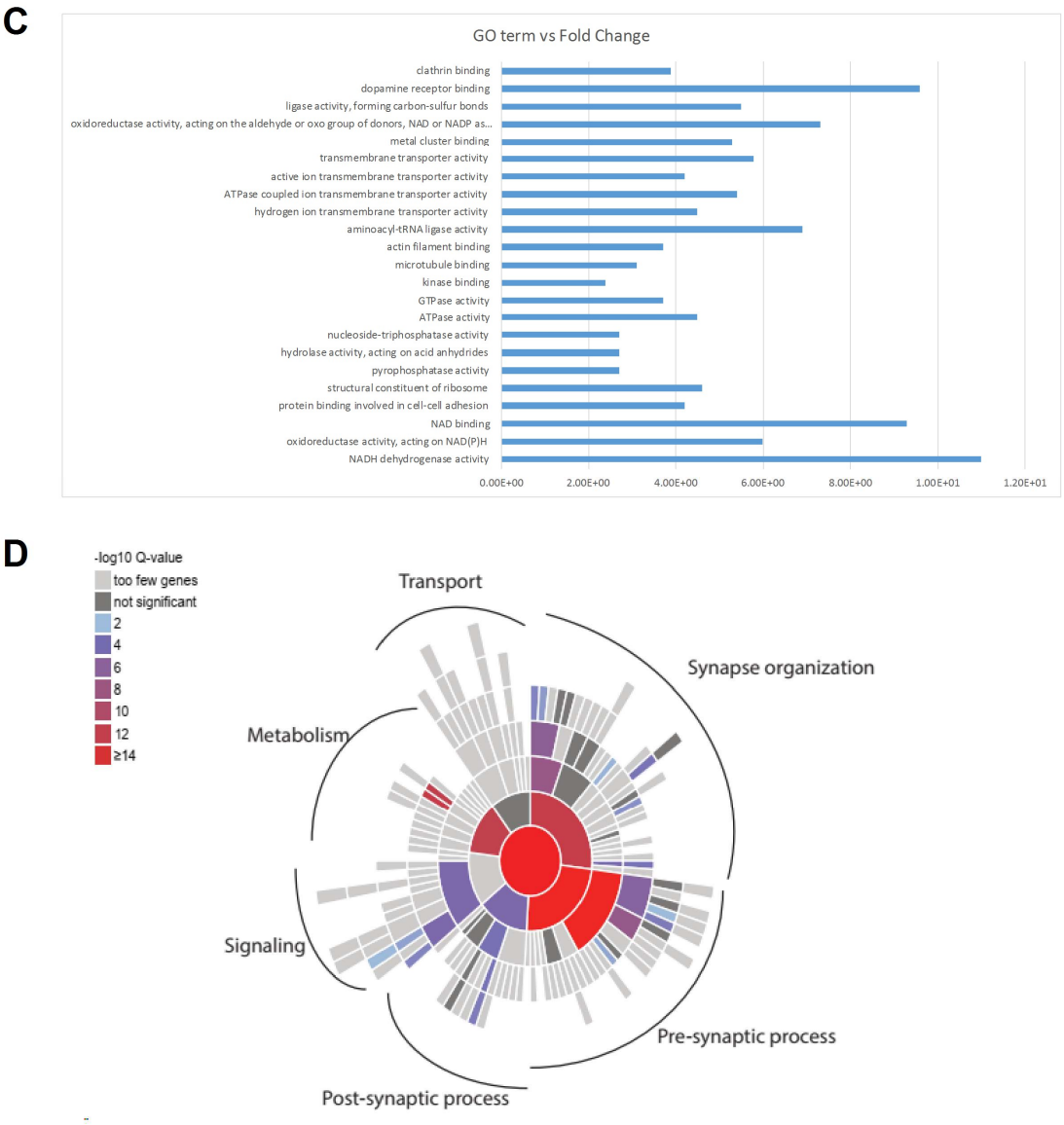

Figure 22: **Proteomics statistics.**

(A) Total number of proteins identified by LC/MS in synaptosomes extracted from the brains of WT and MPS IIIC mice at 3 and 6 months of age. (B) Volcano plots of the proteins identified in synaptosomes showing the proteins that are statistically different between WT and MPS IIIC. (C) Gene ontology terms (GO terms) versus fold-change of the proteins reduced in MPS IIIC synaptosomes. The data represent values where the Benjamini corrected p-value is below

the highest Benjamini corrected p-value for the GO terms. (D) q values per ontology term visualized for biological process enrichment.

The three protein groups that have shown major reduction in MPS IIIC synaptosomes both at 3 and 6 months were mitochondrial proteins (27.3% of all proteins) synaptic proteins (14%), and proteins involved in vesicle trafficking (5.5 %). In particular, synaptic proteins that were reduced in MPS IIIC mice at both ages (Fig. 23A) and/or showed further reduction with age included: syntaxin-binding protein 1 (Stxbp1/Munc18-1), responsible for docking and fusion of synaptic vesicles in the synaptic terminal; Syn1 and synapsin 2 (Syn2), that coat synaptic vesicles and function in the regulation of neurotransmitter release; calcium/calmodulin-dependent protein kinase II α (Camk2a), a member of the NMDAR signaling complex in excitatory synapses that functions in long-term potentiation and neurotransmitter release; and neuroligin-2 (Nlgn2), a transmembrane protein that acts on the recruitment and clustering of synaptic proteins. Specifically, Stxbp1 was reduced by 43.1% in MPS IIIC synaptosomes from 3 month-old mice (WT=36.3±3; MPS IIIC=20.7±5.1) and by 50% by the age of 6 months (WT=44.7±3.2; MPS IIIC=22.3±2). Syn1 was 29.8% lower at 3 months (WT=22.3±7.2; MPS IIIC=15.7±5.5) and reached 41.5% reduction at by the age of 6 months (WT=39.3±0.6; MPS IIIC=23±1.7). Syn2 was reduced 51.6% at the age of 6 months (WT=20.7±1.1; MPS IIIC=10±1). Camk2a was reduced by 22.4% at 3 months (WT=16.3±1.1, MPS IIIC=12.7±1.5). Nlgn2 was reduced by 83.3% at 3 months (WT=4±1; MPS IIIC=0.7±0.6). In general, deficiency of synaptic proteins detected by proteomics well correlated with the described above results of confocal immunofluorescent analysis (Syn1 and PSD-95). Significant reduction of Syn1, Stxbp1 and Camk2a in the brain (frontal part) homogenates from 6 month-old MPS IIIC mice has been also independently confirmed by Western blots (Fig. 23B).

The second group significantly changed in MPS IIIC neurons consisted of mitochondrial proteins and enzymes. Multiple proteins were reduced in MPS IIIC at the age of 3 months (Fig. 23C), with further drastic decrease by the age of 6 months when many of them were diminished to below the detection levels for LC-MS/MS technique. This confirmed progressive deficiency of mitochondrial function previously described for the neurons of MPS IIIC mice (63). The third major group of proteins deficient or reduced in the synaptosomes from MPS IIIC mouse brains contained those involved in vesicle trafficking and endocytosis (Fig. 23D). In particular, we observed major alterations in the levels of clathrin heavy chain 1 (Cltc/CHC) and dynamin-1 (Dnm1). Cltc was reduced by 31.7% at 3 months (WT=34.7±2; MPS IIIC=23.7±4.5) and by 43.9% by 6 months (WT=47±5.1; MPS IIIC=26.3±5) in the MPS IIIC synaptosomes. Its reduction in the MPS IIIC mouse brain homogenates has been also confirmed by Western blot (Fig. 23B). Dnm1 was reduced by 39% at 3 months (WT=26.3±2; MPS IIIC=16±0), but increased by 46.1% at the age of 6 months (WT=7±1; MPS IIIC=13±3.6). Subunits AP2a2 and AP2b1 of the adaptor protein complex 2 (AP-2) involved in recruiting clathrin for assembly of synaptic vesicles and selecting cargo for clathrin-mediated endocytosis (197) were also reduced in the MPS IIIC brain at the age of 3 months. The NSF attachment protein beta (Napb) was significantly reduced in MPS IIIC synaptosomes at the age of 6 months. Napb belongs to the group of SNAP proteins that play a role in SNARE complex dissociation and recycling (synaptic vesicle docking) and its deficiency has been associated with the emerging of seizures in patients (198) and in mouse models (199). Together, the deficiency of proteins involved in vesicle trafficking and endocytosis suggested that these processes could be affected in the MPS IIIC neurons.

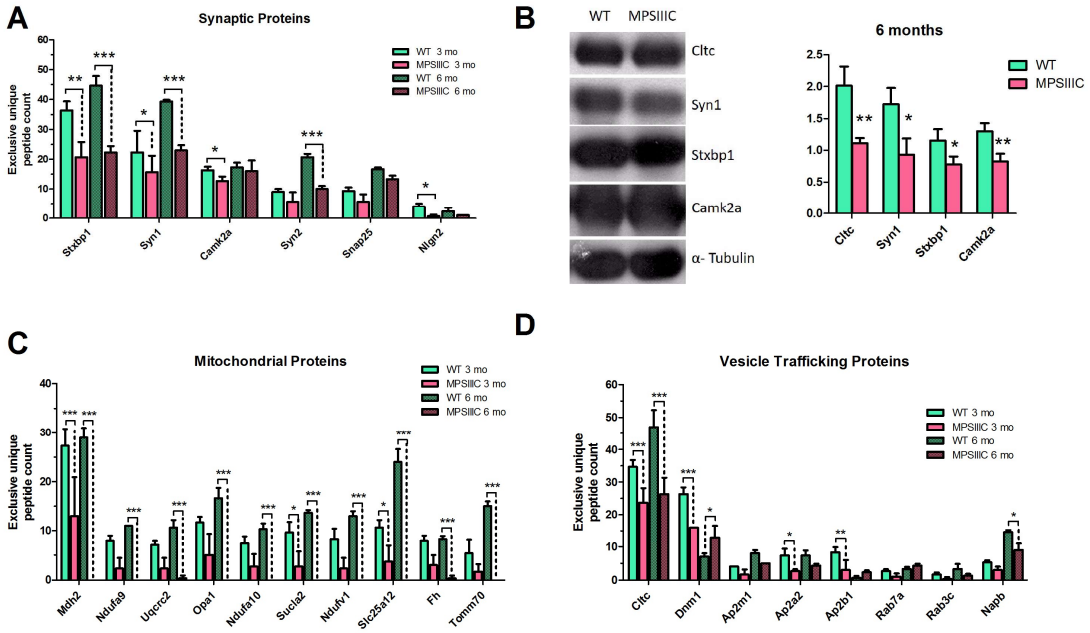

Figure 23: Semiquantitative LC-MS/MS analysis of proteins present in synaptosomes from brains of 3 and 6 month-old mice reveals deficiencies of synaptic, mitochondrial and trafficking vesicle-associated proteins in MPS IIIC mice.

(A) Exclusive unique peptide counts of synaptic proteins. (B) Western blots of total protein extracts from brains of 6 month-old mice and their respective quantifications confirming changes in protein abundance identified by proteomic analysis. (C) Exclusive unique peptide counts of mitochondrial proteins. (D) Exclusive unique peptide counts of proteins associated with intracellular vesicle trafficking and endocytosis. Data obtained from synaptosomes extracted from 3 different animals per genotype. P-value was calculated in the exclusive unique peptide count and area of LC peptides with 2-way ANOVA using Bonferroni as a post-test (*$p<0.05$, **$p<0.01$ and ***$p<0.001$).

36. MPS IIIC hippocampal neurons show partial impairment of synaptic vesicle trafficking and turnover

Besides reduced density of synaptic vesicles and smaller areas/lengths of PSD, TEM analysis identified defects of microtubules in the MPS IIIC cultured hippocampal neurons. The majority of microtubules were disorganized, sparse and non-parallel, with multiple storage bodies present between the microtubule filaments (Fig. 24A). This observation together with the reduction of proteins involved in vesicle targeting and turnover observed by proteomic analysis of synaptosomes suggested that the low density of synaptic vesicles at the axonal terminals could be caused by impaired vesicular trafficking of synaptic vesicle precursor organelles transported from the cell body. To test this hypothesis, we studied the axonal trafficking of synaptic vesicle precursors by live imaging in hippocampal neuronal cultures.

On DIV 3 cells were transduced with LV encoding for Syn1-GFP (GeneCopoeia^{TM}), and on DIV 21, 10-min videos were recorded using a spinning disk microscope to visualize trafficking of GFP-positive vesicles (Fig. 24B). In MPS IIIC neurons, the majority of Syn1-GFP-positive vesicles stayed stationary or wiggled back and forth instead of showing a constant motion in one direction (Fig. 24B). Conversely, in WT neurons, the moving vesicles were progressing in a stable direction (Fig. 24B), and their speed was faster as compared with that of vesicles in MPS IIIC cells (Fig. 24C). In addition, while majority of Syn1-GFP in WT neurons were associated with fine punctate distributed over the axons, in the MPS IIIC neurons they were localized in coarse intensely-stained spheroid granules (Fig. 24B). This type of staining was consistent with the hypothesis that Syn1-GFP is accumulated along the axon. These bodies however were negative for the lysosomal marker LAMP2, or autophagosomal marker LC3 suggesting that the inclusions containing Syn1-GFP were different from lysosomal storage bodies or autophagosomes (Fig. 24D).

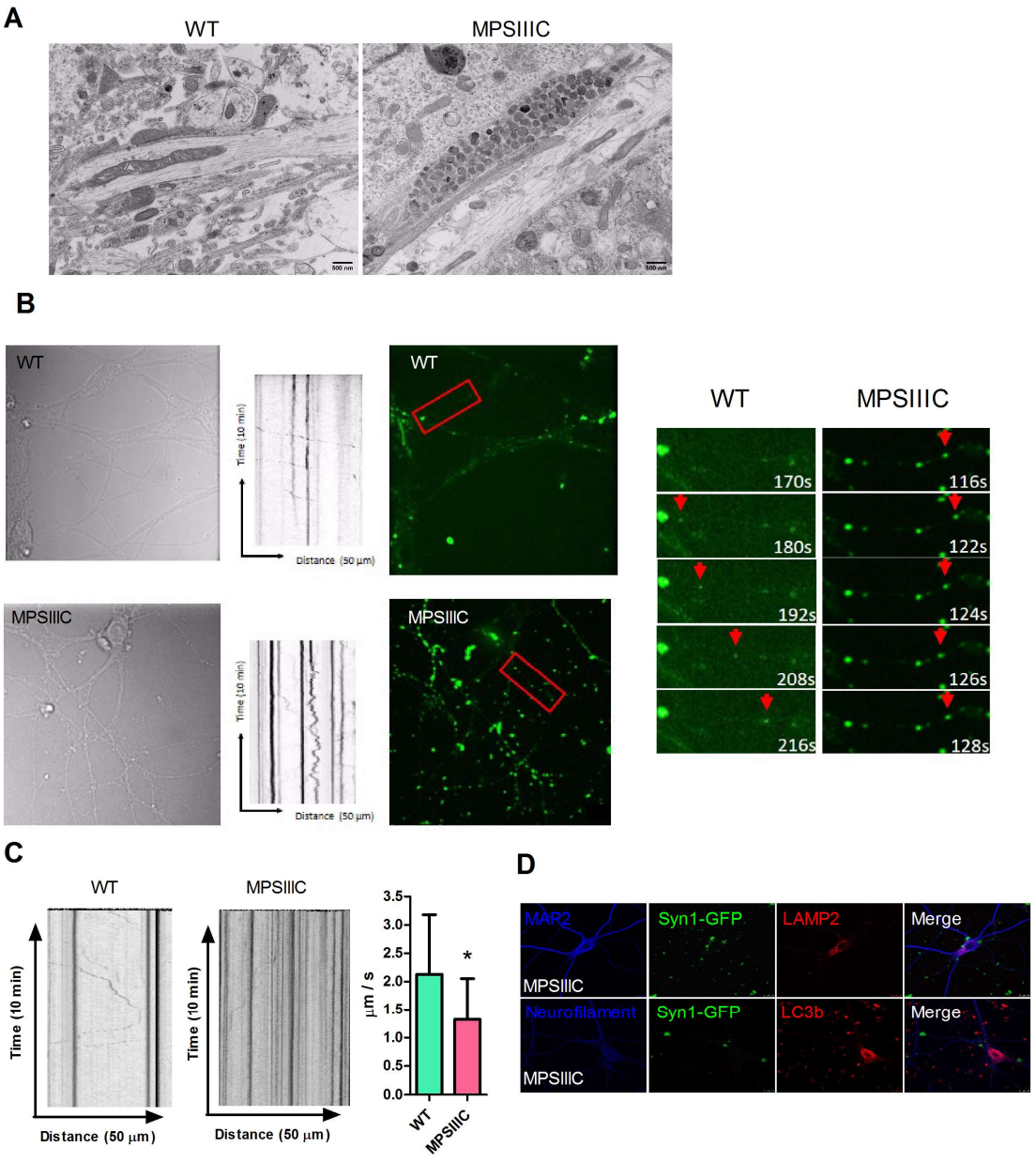

Figure 24: Vesicle transport defects in MPS IIIC neurons.

(A) Microtubule network in neurites of MPS IIIC cultured hippocampal neurons is disorganized, sparse and non-parallel, and multiple electron-lucent and electron-dense storage vacuoles are present between the microtubule filaments. Panels show representative images of at least 30 cells from 3 different experiments or 3 different animals per genotype. (B) Live imaging of Syn1-GFP positive vesicles in cultured hippocampal neurons. Brightfield images,

fluorescent images and kymographs of WT and MPS IIIC hippocampal neurons transduced with LV-Syn1-GFP. In MPS IIIC neurons, moving GFP-positive vesicles show a wiggling pattern, in contrast with the WT cells where the majority of moving vesicles travel in one direction. (C) Kymographs reveal that GFP-positive vesicles in the MPS IIIC neurons move at a slower speed than those in the WT cells. Videos were recorded for 10 min, with 1 recording every 2 s with a 63x objective. The bar graph shows the average speed on Syn1-positive vesicles and SD; P-value was calculated by t-test (*$p<0.05$ and **$p<0.01$). (D) The granules observed in the MPS IIIC neurons transduced with LV-Syn1-GFP do not co-localize with neither the lysosomal marker LAMP2, nor with autophagosomal marker LC3. For the quantification of vesicle velocity, 17 WT and 12 MPS IIIC cells originating from 3 different sets of experiments for each genotype were analyzed.

Preface to Chapter 4

In this chapter I describe the second aim of this thesis, in which I explored the applicability of LV-mediated gene HSPC therapy for treatment of MPS IIIC currently lacking a specific therapy. I developed a novel protocol for transduction of HSPC with LV encoding for human HGSNAT enzyme and transplanted in 4 MPS IIIC mice myeloablated with busulfan in a pilot study. The data generated in these experiments will serve to improve experimental approaches for future preclinical efficacy studies.

Chapter 4

LV MEDIATED GENE/HSPC THERAPY OF MPS IIIC

37. Development, production and testing of LV-HGSNAT-GFP vector expressing human HGSNAT enzyme under control of PGK promoter

To generate the lentiviral vector (LV) for gene/HSPC therapy of MPS IIIC the codon-optimized cDNA of human HGSNAT fused with that encoding for the GFP tag was cloned in a LV vector (pLenti PGK Blast DEST (w524-1) under a PGK promoter. The LV was further produced in HEK 293T cells co-transfected with REV 6 µg per plate, VSVG 7.8 µg per plate, pMDL (gag-pol), 15 µg per plate, and *Hgsnat*-GFP, 9 µg per plate. The vector was first tested in HEK 293 cells to investigate the potency of LV-PGK-HGSNAT-GFP in increasing the cellular levels of HGSNAT activity. At a MOI of 20, HEK 293 cells were transduced with either LV-GFP or LV-PGK-HGSNAT-GFP and kept in culture until DIV 13. By DIV 3, 56% of the cells transduced with LV-GFP were expressing GFP (Fig. 25A) while 17% of the cells transduced with LV-PGK-HGSNAT-GFP were expressing GFP (Fig. 25B). HGSNAT activity measured at DIV 06 and DIV 13 was increased 3.6-fold in cells transduced with LV-PGK-HGSNAT-GFP in comparison with cells transduced with LV-GFP (Non transduced: 1.57±0.63; LV-GFP:1.61±0.28; LV-PGK-HGSNAT-GFP: 5.88±0.15, Fig. 25C).

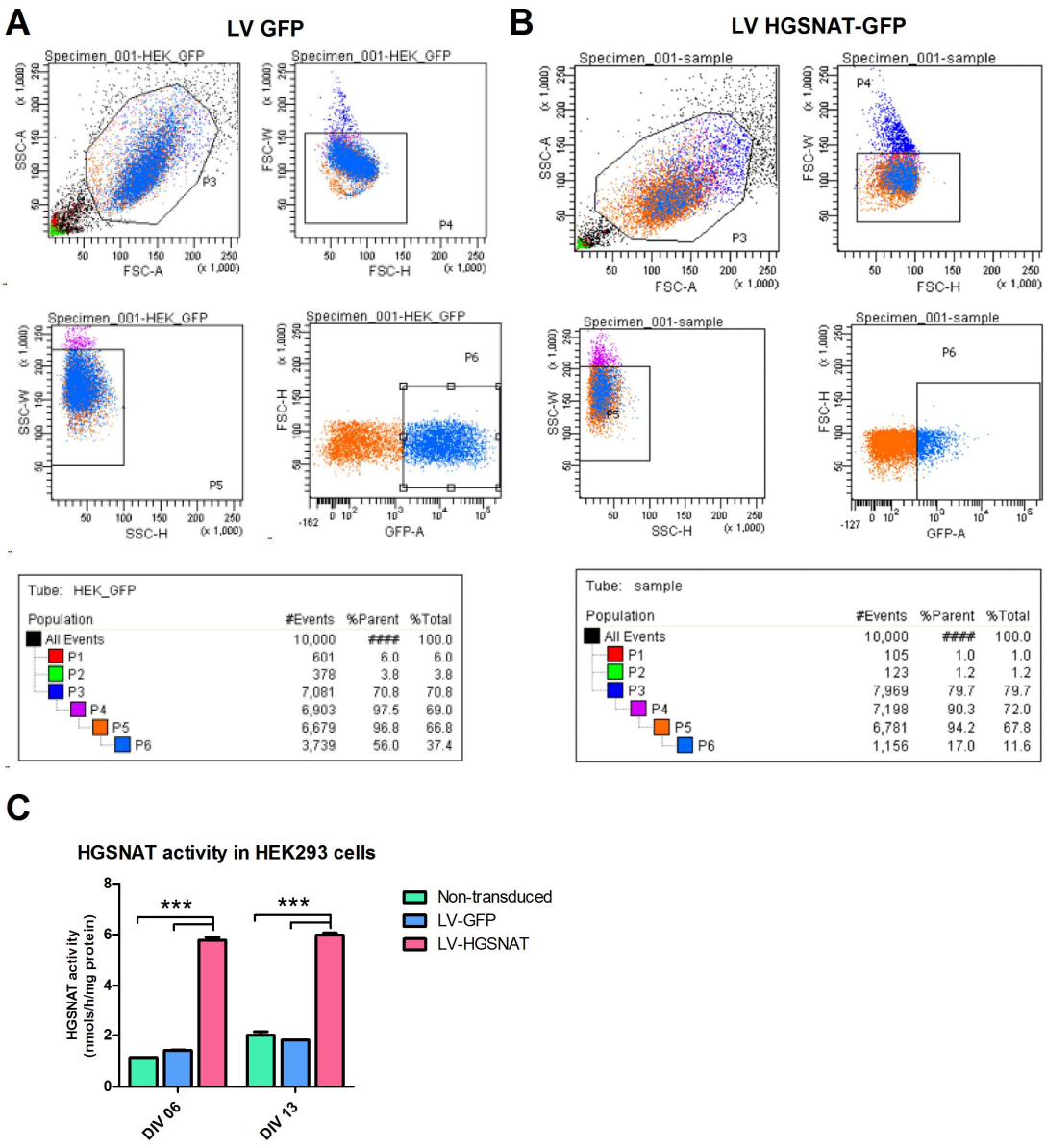

Figure 25: Transduction of HEK293 cells by LV-GFP and LV-HGSNAT-GFP lentiviral vectors.

(A) Flow cytometry panels of cells transduced with LV-GFP. (B) Flow cytometry panels of cells transduced with LV-HGSNAT-GFP. (C) HGSNAT specific activity in HEK 293 homogenates.

38. LV-HGSNAT-GFP shows low efficiency in transduction of HSPC-derived macrophages.

Our further goal was to test whether LV-HGSNAT-GFP vector is also capable to increase HGSNAT activity in mouse cultured HSPC-derived macrophages. We first tested whether HSPC isolated from mouse bone marrow by negative selection using the EasySep™ Mouse Hematopoietic Progenitor Cell Isolation kit are able to differentiate to macrophages. The total mouse bone marrow cells and purified HSPC cells were cultured in DMEM + 10% FBS + 2 mM glutamine + 1% penicillin/streptomycin for 7 days and treated with GM-CSF as previously described by Trouplin *et al.* (2013) (189). After one week in culture, all cells were morphologically similar to macrophages and expressing the macrophage markers CD11b and CD68 as detected by immunofluorescence and western blot (Fig. 26A and B). These data confirmed that HSPC isolated from total bone marrow can differentiate into macrophages upon stimulation with GM-CSF.

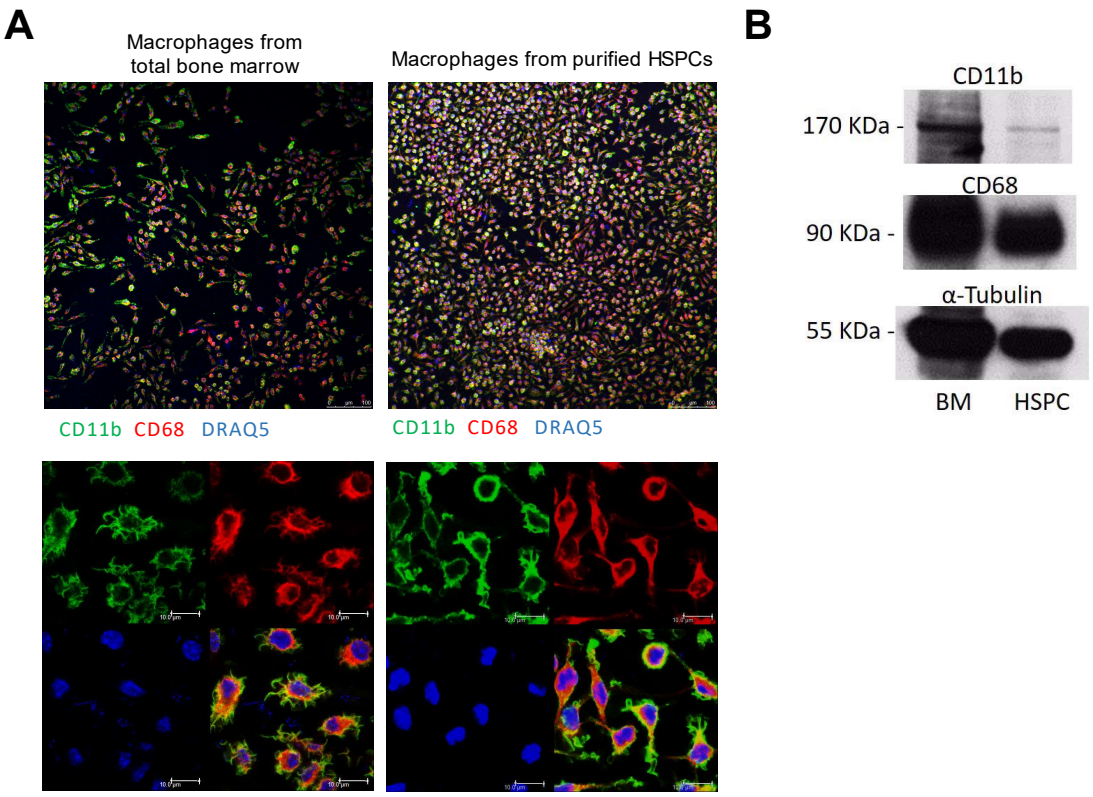

Figure 26: HSPC can be differentiated in macrophages after being negatively selected with EasySep™ kit.

(A) Bone marrow-derived macrophages and HSPC-derived macrophages both express macrophage markers CD11b and CD68. (B) Western blots from macrophage homogenates.

We further tested if we could efficiently transduce HSPC-derived macrophages with LV-GFP or LV-PGK-HGSNAT-GFP. For that, we transduced the cells with either LV, at a MOI of 20, on the first day in culture. After 7 days, fully differentiated macrophage cells were harvested and the percent of GFP-expressing cells measured by FACS. We found that only 1.6% of the cells transduced with LV-GFP and 0.5% of the cells transduced with LV-PGK-HGSNAT-GFP were expressing GFP (Fig. 27A, B). HGSNAT activity was further measured in cell homogenates and found to be similar between all the groups (Negative control: 18.3±0.57, LV-GFP: 13.7±0.7; LV-PGK-HGSNAT-GFP:17.75±0.5, Fig. 27C).

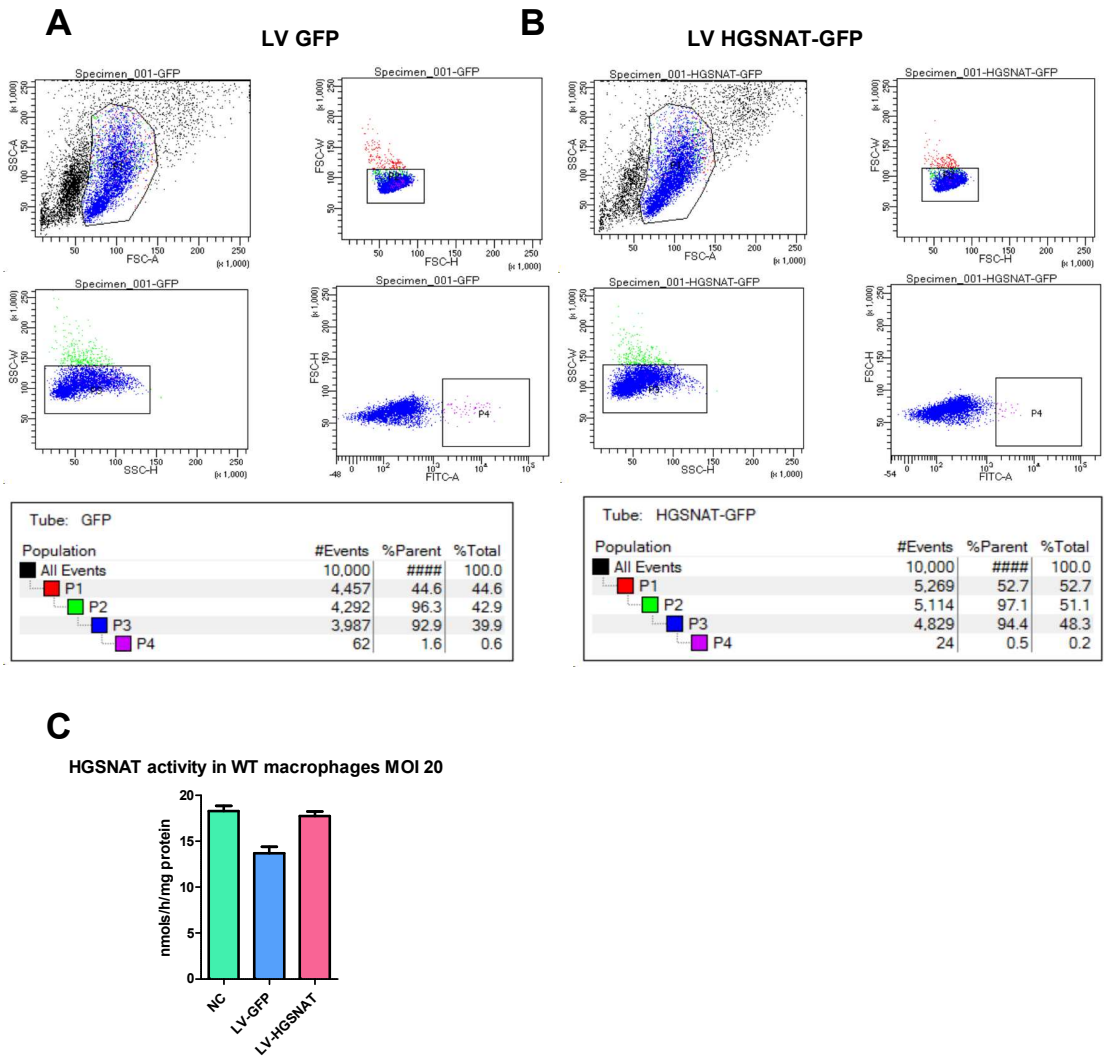

Figure 27: HSPC-derived macrophages show low transduction efficiency for LV.

Flow cytometry analysis of macrophages transduced with LV-GFP (A) and LV-HGSNAT-GFP (B). (C) HGSNAT activity in homogenates of HSPC-derived macrophages.

39. LV-PGK-HGSNAT-GFP significantly increases HGSNAT activity in HSPC

We further tested efficacy of the LV-PGK-HGSNAT-GFP vector for transfecting dividing non-differentiated HSPC. HSPC were kept in culture undifferentiated by addition of cytokine cocktail (10 ng/ml rmIL-6, 100 ng/ml rmFlt-3L, 100 ng/ml rmTPO and 100 ng/ml

rmSCF) in SCGM media and transduced with either LV-GFP or LV-PGK-HGSNAT-GFP at MOI of 30. After 3 days 13% of the HSPCs transduced with LV-GFP were expressing GFP (Fig. 28A) and 1.6% of the cells transduced with LV-PGK-HGSNAT-GFP were expressing GFP (Fig. 28B). HGSNAT activity was increased 2-fold (Fig. 28C) in the cells transduced with LV-PGK-HGSNAT-GFP in comparison with the those transduced with LV-GFP (Non transduced: 1.3±0.14, LV-GFP: 2.04±0.08; LV-PGK-HGSNAT-GFP: 4.07±0.17).

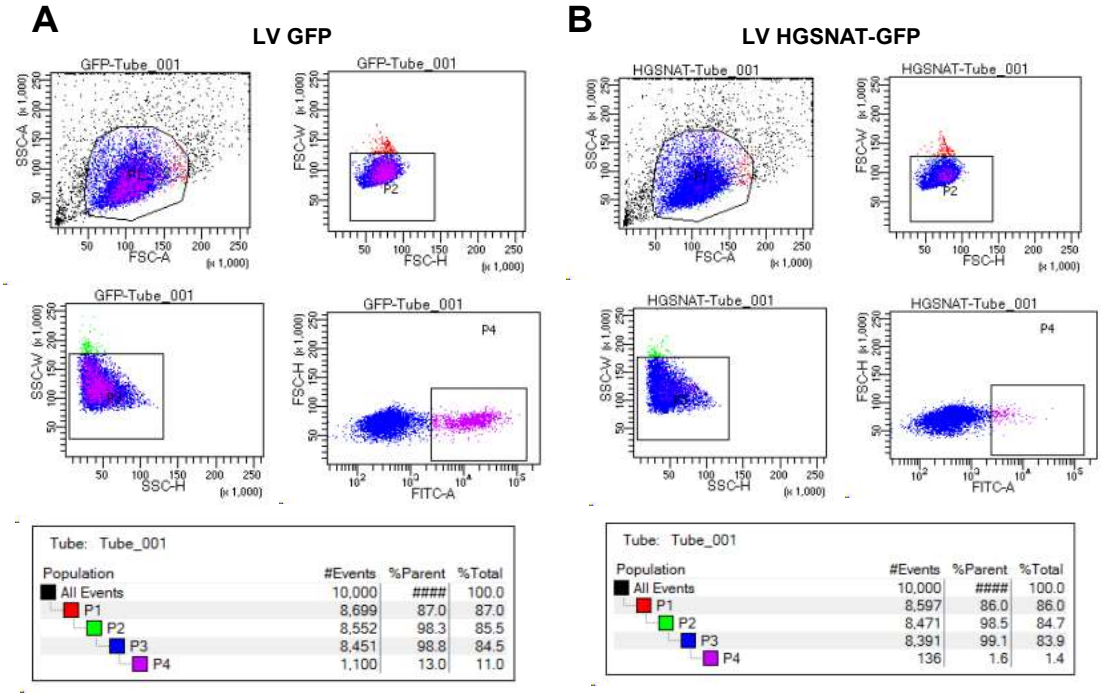

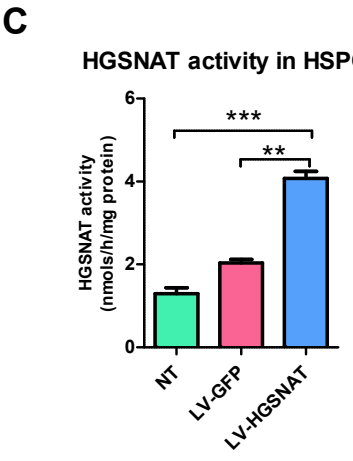

Figure 28: Transduction of HSPC with LV-HGSNAT-GFP at MOI 60 results in expression of HGSNAT-FGP in 1.6% of cells and 2-fold increased HGSNAT activity.

(A) Flow cytometry analysis of HSPC transduced with LV-GFP. (B) Flow cytometry analysis of HSPC transduced with LV-HGSNAT-GFP. (C) HGSNAT activity in HSPC homogenates.

40. Two hits of LV at MOI 30 are more efficient for transducing HSPC than one hit at MOI 60.

Finally, we have tested whether we can obtain the higher number of HGSNAT-expressing HSPC for transplantation by keeping cell in culture longer and transducing them twice within a 48-hour interval, each time at MOI 30. The amount of transduced cells was compared with that obtained when cells were transduced once at MOI 60 and kept in culture for 24 hours. This experiment was conducted only using LV-GFP which results in higher fluorescence intensity of transduced cells because the expressed GFP is located in the cytoplasm and not on the lysosomal membrane. With the one-hit strategy, we obtained a total of 505,375 cells, 62.2% of them expressing GFP (316,0000 transduced cells in total, (Fig. 29A), while with the two-hit strategy we obtained a total of 1,035,300 cells, 49.3% of them expressing GFP (510,000 transduced cells, Fig. 29B). Based on these results, we concluded that the two-hit strategy is more efficient, since the same amount of the virus is used but it generates more GFP-positive cells.

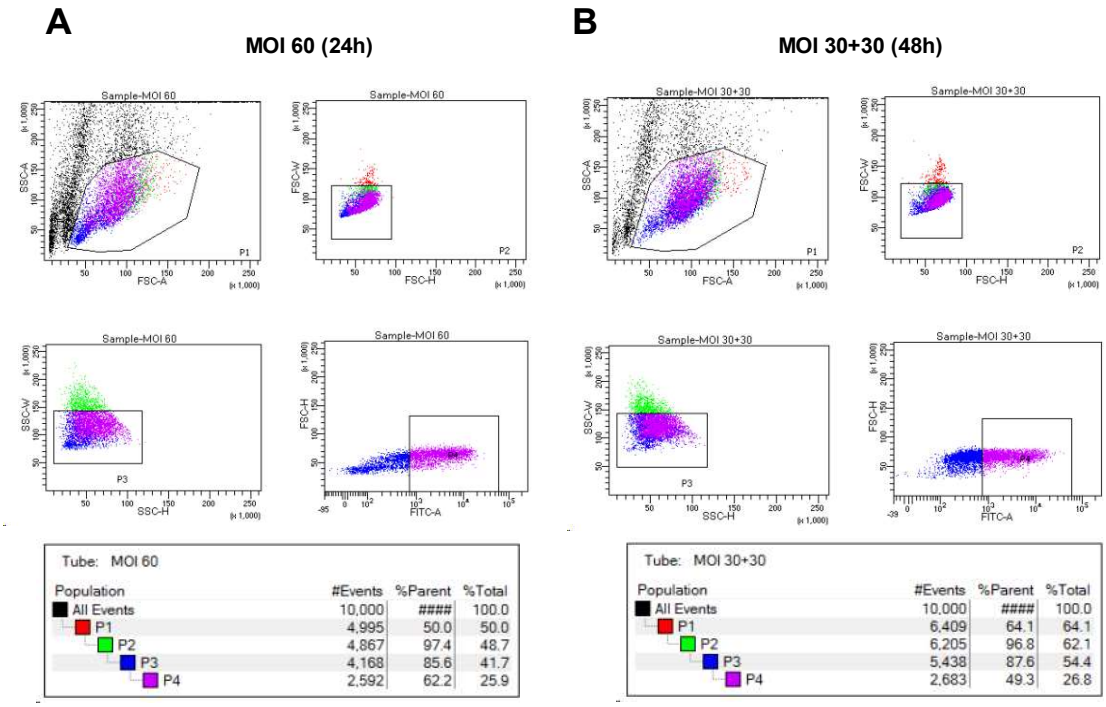

Figure 29: Two-hit transduction strategy allows to obtain more GFP-positive HSPC.

(A) Flow cytometry analysis of HSPC transduced with LV-GFP at 60 MOI within a period of 24 h in culture. (B) Flow cytometry analysis of HSPC transduced with two hits of LV-GFP at 30 MOI within a period of 48 h in culture.

41. MPS IIIC mice transplanted with HSPC transduced with LV-PGK-HGSNAT-GFP have variable engraftment rates

Our pilot transplantation study included four 2-months-old MPS IIIC mice (two males, two females) that were myeloablated with 5 consecutive intraperitoneal injections of busulfan at a dose of 25 mg/kg BW (total 125 mg/kg BW). HSPC were collected from five CD45.1+ C57BL/6 mice and transduced with two hits of 30 MOI of LV-PGF-HGSNAT-GFP. The cells were delivered to the MPS IIIC mice ($2x10^6$ cells per animal) by injection into the tail vein.

Using an epifluorescence microscope we confirmed that some of the HGSPC cells were expressing GFP, but the total amount of the cells left after transplantation was not sufficient to conduct their analysis by flow cytometry. Instead, the cells were used to measure HGSNAT activity which was found to be increased 11.4-fold in comparison with non-transduced HSPC of wild-type mice (Fig. 30).

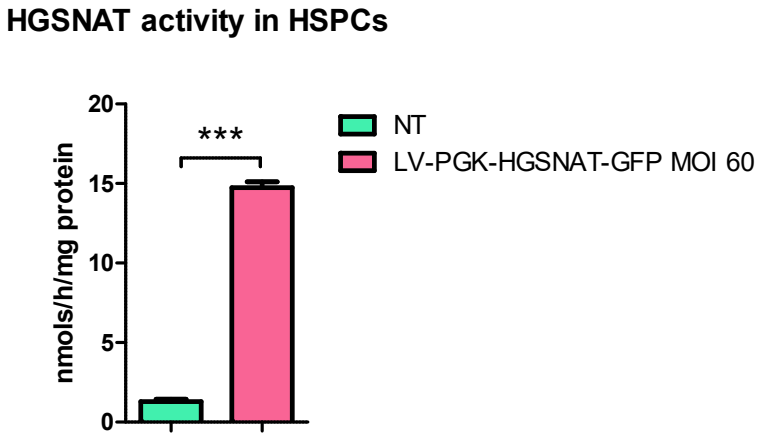

Figure 30: HGSNAT activity is significantly increased in HSPC transduced with LV-PGK-HGSNAT-GFP and used for transplantation.

Engraftment of transplanted HSPC was assessed by flow cytometry with anti-CD45.1 antibody at 6 and 13 weeks using the whole blood collected from the tail vein of mice. At 6 weeks, we obtained engraftment rates varying from 11.4% to 60.9% of donor cells. At 13 weeks, the engraftment rates ranged from 17% to 82.5%. The absolute values are presented in the Table 4 and flow cytometry data in appendices D and E. The mouse with the lowest levels of engraftment experienced health problems (lethargy, weakness, weight loss, trouble walking) and had to be euthanized, while other were kept until the age of 6 months.

Table 4: Engraftment of donor cells in transplanted MPS IIIC mice.

Mouse ID	Sex	6 weeks post-transplantation	13 weeks post-transplantation
6600*	Female	11.4%	NA
6601	Female	60.9%	82.5%
6598	Male	24.2%	17%
6599	Male	46%	50.%

(*) Sacrificed mouse. NA, not applicable.

42. MPS IIIC mice transplanted with LV-PGK-HGSNAT-GFP transduced HSPC show partial rescue of behavior abnormalities.

Four months after transplantation, mice (WT, non-transplanted MPS IIIC and MPS IIIC mice transplanted with LV-PGK-HGSNAT-GFP transduced HSPC) were studied by two different behavior tests, the open field test, that accesses their locomotion and levels of anxiety and the novel object recognition test, that accesses their memory and learning. Using the open field test, Martins *et al.* (63) have previously demonstrated that MPS IIIC mice are hyperactive and have reduced anxiety. Since our pilot study involved 3 mice we did not expect to observe statistical difference between the groups, however we recorded a trend for higher locomotion activity of MPS IIIC mice as compared with the WT counterparts, consistent with the previous report. MPS IIIC mice also crossed the center of the arena more frequently than the WT (Fig.31 A-E) which was suggesting their reduced anxiety and fear. In the MPS IIIC mice transplanted with LV-PGK-HGSNAT-GFP transduced HSPC we observed a trend for normalization of anxiety and hyperactivity (see Fig. 31A for representative traces of mice trajectory in the open field arena). Even though we did not observe any statistical differences between the three groups in the number of entries to the central areas (Fig. 31B) and the total distance traveled by mice (Fig. 31C) we did observe differences in the global activity (Fig. 31D) and the immobility duration (Fig. 31E), revealing that the behavior deficits of transplanted MPS IIIC

mice was partially rescued. In the novel object recognition test (the discrimination index is presented in Fig. 31F and the total exploration time of the old and the new object is presented in Fig. 31G), due to the limited number of mice tested, we were not able to find any differences between the three groups.

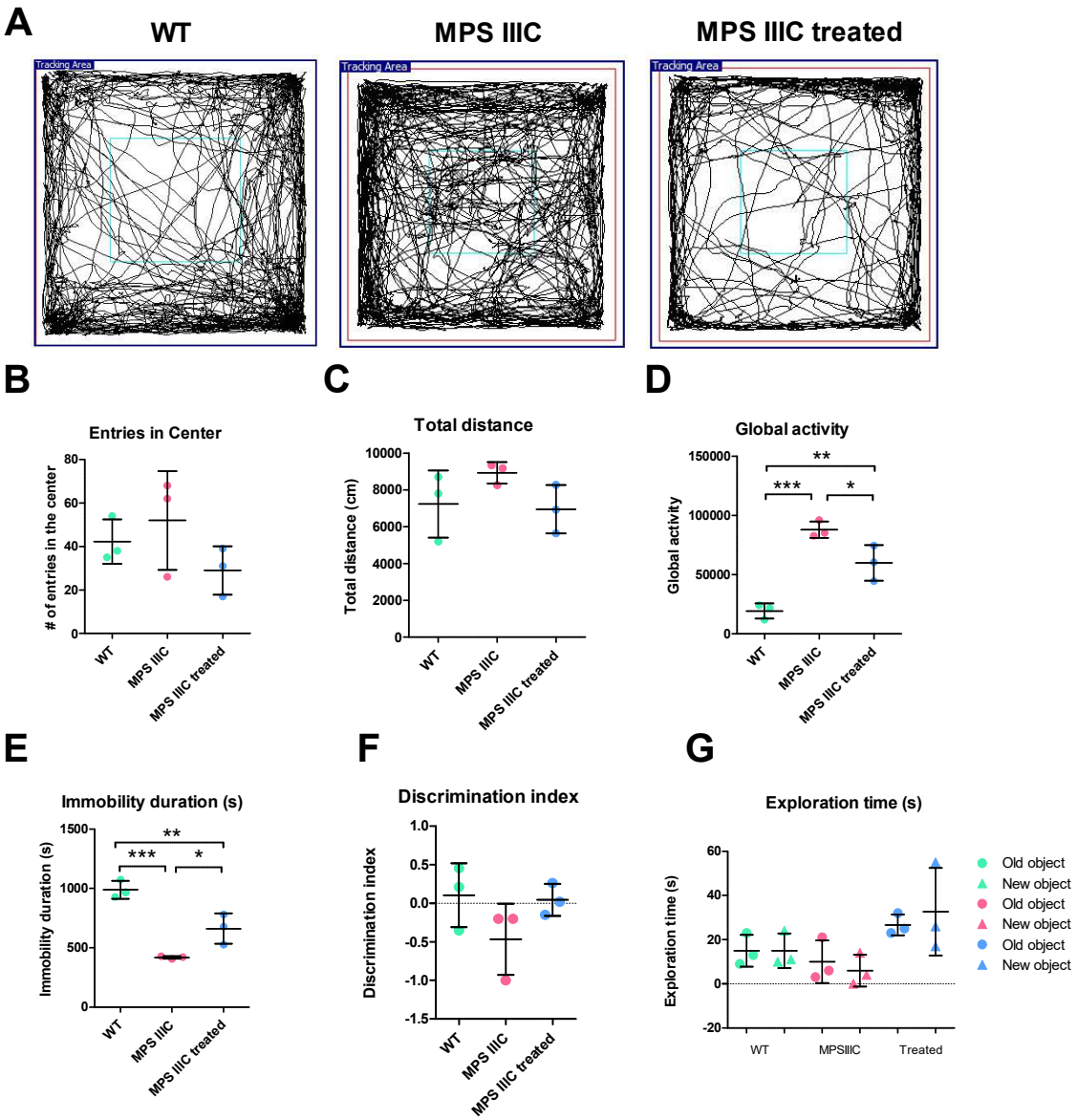

Figure 31: Reduction of hyperactivity in MPS IIIC mice transplanted with LV-PGK-HGSNAT-GFP transduced HSPC.

(A) Representative traces of the trajectory performed by WT, MPS IIIC and transplanted MPS IIIC mice in the open field arena. (B) Number of total entries in the center of the open field arena. (C) Total distance walked by each mouse (cm) in the open field arena. (D) Global activity of mice in the open field arena. (E) Immobility duration (s) of mice in the open field arena. (F) Discrimination index in novel object recognition test. (G) Exploration time (s) for old or new object in the novel object recognition test.

43. Mice transplanted with LV-PGK-HGSNAT-GFP-transduced HSPC have increased HGSNAT activity in the spleen and bone marrow.

In order to access whether transplantation resulted in correction of deficient levels of HGSNAT activity in the mouse tissues, we essayed the enzyme in bone marrow, spleen, brain, liver, kidney and lungs of transplanted and non-transplanted mice. We observed statistically significant increase of HGSNAT activity in the spleen (9.9-fold increase as compared with non-transplanted MPS IIIC mice)(Fig. 32). There was also a trend for increase HGSNAT activity in the bone marrow, but it was not statistically different due to the high variability among animals. Importantly, individual HGSNAT activity values in transplanted mice correlated with their engraftment rates (Fig. 33).

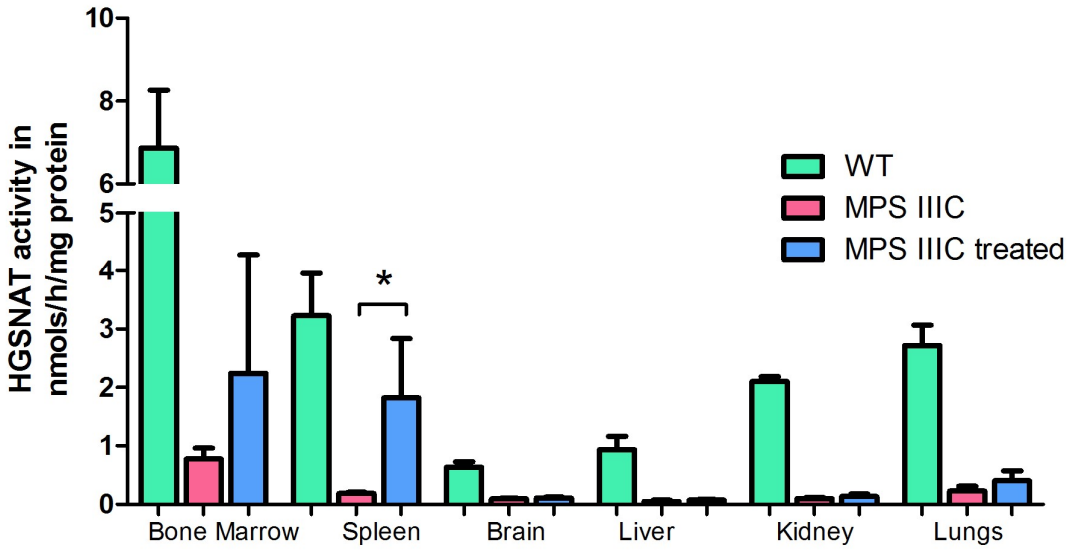

Figure 32: HGSNAT activity in different organs of WT, MPS IIIC and MPS IIIC transplanted with LV-PGK-HGSNAT-GFP transduced HSPC.

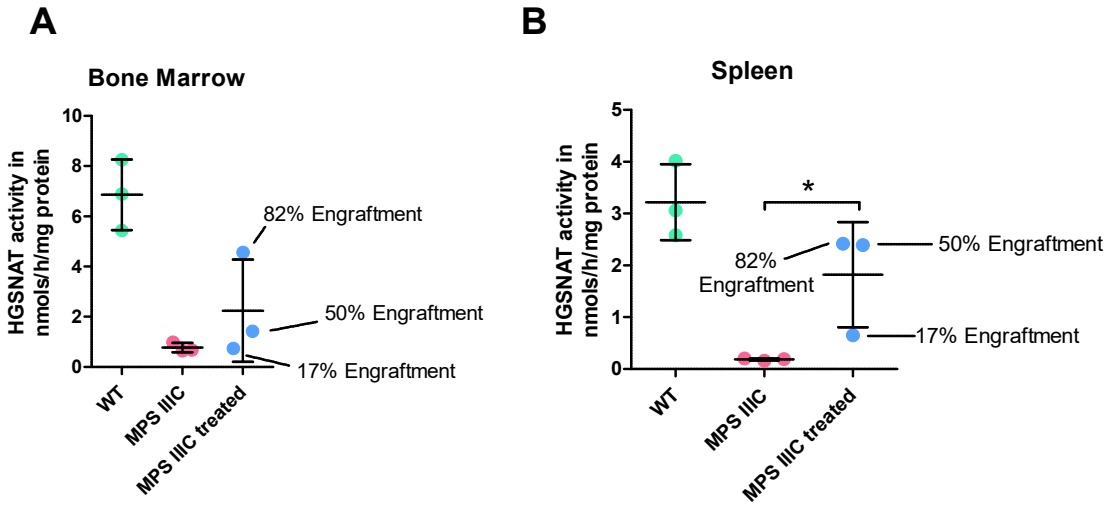

Figure 33: HGSNAT activity in bone marrow and spleen of individual transplanted mice.

HGSNAT activity values in the bone marrow (A) and the spleen (B) of transplanted mice correlate with their engraftment rates.

Chapter 5

DISCUSSION

Until now neurodegeneration and neuroinflammation caused by metabolite storage, defects in autophagy and microgliosis were recognized to be the major causes of behavioral alterations and developmental delay in patients with neurological LSD. However, effects of lysosomal storage in neurons on synaptic maintenance, plasticity and transmission remain largely unstudied although several reports provide evidence of pathological changes in these processes. For example, pluripotent stem cells-derived neurons generated from human MPS IIIC patients' fibroblasts presented firing episodes with reduced amplitudes while neuronal networks showed early defects in neuronal activity, network-wide degradation, and altered effective connectivity (96). Alteration of synaptic function has been also reported in several animal models of LSD. For instance, abnormal integration of excitatory and inhibitory postsynaptic potentials have been found in cortical neurons in feline models of GM1 gangliosidosis (91, 92). In the mouse model of Niemann-Pick C disease, abnormalities in several pre and postsynaptic markers were evident in both subcortical grey and white matter (71) while neurons presented enhanced glutamatergic neurotransmission in hippocampus leading to hyperexcitability (200). In the mouse model of MPS IIIA reduced excitatory synaptic strength was detected in the somatosensory cortex (95). Impairments of the early steps of endocytosis and transport of synaptic and endocytic vesicles have been also detected in the dorsal root ganglia neurons of the mouse model of Krabbe disease, together with decreased levels of dynein and unstable microtubules (93).

Our current data demonstrate that excitatory synaptic inputs to the pyramidal CA1 hippocampal neurons are drastically reduced in the mouse model of Sanfilippo C syndrome with reduction of synaptic spines at P10, at least 3 months before the development of other neuronal pathologies such as neuroinflammation, neuronal storage of gangliosides, misfolded

proteins and mitochondrial damage (63). Drastically reduced levels of synaptic vesicles in the terminals and smaller areas of post-synaptic densities were found both in pyramidal CA1 hippocampal neurons at 3 and 6 months of age and in cultured hippocampal neurons at DIV 21. These changes affect mainly excitatory circuits, and PSD-95 seems to be one the most severely reduced biomarkers. Importantly, the levels of this protein can be rescued *in vivo* and *in vitro* by correcting the primary genetic defect in neurons with the viral vectors expressing the WT human HGSNAT enzyme. This implicates the genetic defects in HGSNAT as a primary cause of synaptic deficits but also suggests that improvements in the behaviour of MPS IIIC mice treated by striatal administration of AAV-HGSNAT vectors (187) could be at least partially explained by the rescue of synaptic defects.

Major changes in the synaptic morphology and the levels and distribution of synaptic markers found in the hippocampus i.e. scarcity of synaptic vesicles in the excitatory terminals, reduced PSD length, reduced density of mature mushroom-shaped spines were mainly recapitulated in dissociated neuronal cultures. In contrast, miniature synaptic currents from hippocampal cultured neurons revealed no significant changes in amplitude or frequency of mIPSCs whereas an almost 3-fold increased frequency was detected in mEPSCs. We hypothesize that the increase in mEPSCs observed in cultured MPS IIIC neurons is linked to the major changes in the positioning of synapses on dendrites detected by both confocal and transmission electron microscopy. While the overwhelming majority of synapses in WT cultures were axospinous, in MPS IIIC neurons >75% of the synapses were axodendritic. Since MPS IIIC cultured neuron dendrites present mainly immature filopodia spines that lack the proper postsynaptic machinery for synaptic function (201), we speculate that they reallocate their excitatory synapses to the dendrites, altering their response to the presynaptic signaling which could potentially explain increased frequency and amplitude of mEPSC observed in neuronal cultures.

The disruption of the microtubule architecture in the axons of cultured MPS IIIC neurons (disorganized, sparse and non-parallel filaments) together with reduced levels of proteins involved in vesicle trafficking and endocytosis in the synaptosomes from MPS IIIC mouse brains allowed us to hypothesize that the scarcity of synaptic vesicles in the axonal terminals can be caused by partially impaired trafficking of synaptic vesicle precursors from the soma. Indeed, direct analysis of the axonal movement of Syn1-positive vesicles by live imaging microscopy demonstrated that in MPS IIIC neurons fewer vesicles were moving in a stable direction towards the terminal. Besides, vesicles that were moving in one direction had slower speed as compared to that of vesicles in WT neurons. In addition, the majority of newly synthesized Syn1-GFP in MPS IIIC neurons was localized in coarse spheroid granules distributed along the axon. Formation of focal granular enlargements within axons (axonal spheroids or "torpedoes"; neuroaxonal dystrophy) and dendrites is a phenomenon described in a variety of lysosomal storage diseases including mannosidosis, GM1and GM2-gangliosidosis, prosaposin deficiency, and Niemann-Pick type C (71, 92, 135-137, 202). In the axons, spheroids often contained electron-dense concentric lamellar bodies and neurofilaments (137).

The mechanism underlying formation of the axonal spheroids in LSD is not completely understood. They could form from merging of lysosomes in the proximal axon because accumulation of storage materials in lysosomes impairs their onward BORC-dependent axonal transport (203). Besides, the block in anterograde transport of lysosomes prevents their merging with early endosomes and autophagosomes in the axon terminal (204). As a result, the dynein-mediated retrograde transport of autophagosomes and their maturation to autolysosomes (205) is impaired causing their accumulation in distal axon and formation of axonal spheroids. Our data, however, show that the lysosomal storage bodies are primarily found in the soma, and axonal Syn1-positive spheroid granules are negative for the markers of endo-lysosomal pathway or for the autophagosomal marker LC3. We speculate, therefore, that

they appear in the process of accumulation of the synaptic vesicle precursors at the places in the axons where the transport was blocked due to the microtubule defects.

Together, our experiments demonstrate that lysosomal storage in MPS IIIC neurons results in appearance of early and drastic defects in the synapse of pyramidal CA1 neurons. Further studies are necessary to define the exact mechanism, however based on our current results we speculate that the defects are caused by the appearance of lysosomal storage bodies that disrupt microtubule structure and normal transport of vesicles carrying the synaptic proteins along the axon (83). This, in concert with impaired autophagy and endocytosis at the axonal terminals, could result in the deficit of synaptic vesicles affecting synaptic transmission and plasticity. The density of synaptic spines is also reduced in mouse model of sialidosis suggesting that similar pathogenic pathways can also exist in other lysosomal diseases. In the light of these findings it would be interesting to study if drugs known to affect synaptic transmission can improve synaptic function as well as behavioral and cognitive defects in MPS IIIC mice and in the animal models of other neurological LSD.

The effective treatment for MPS IIIC is yet to be discovered. Non-neurological forms of LSD are partially treatable by enzyme replacement therapy (ERT) but this approach is ineffective for the neurological forms due to the enzyme's inability to cross the blood-brain barrier (BBB). In MPS IIIC, and other diseases caused by defects in transmembrane proteins, an additional constraint is the absence of cross-correction between the cells. Delivering replacement enzyme intrathecally, thus bypassing the BBB (206) is difficult to implement clinically due to the invasive nature of the procedure. Furthermore, intrathecal delivery is not possible for membrane enzymes and proteins. HSPC transplant is the only effective approach currently used in clinics for a group of few neuropathic LSD where the missing enzyme is soluble and can be effectively secreted by donor cells (207). The treatment restores catabolism in HSPC which, in combination with cross-correction of other cell types, through secretion of

the enzyme, reduces storage in the tissues of peripheral organs. Importantly, after HSPC transplant the donor-derived monocytes also cross the BBB and differentiate into microglial cells, thus ameliorating the neuropathology via cross-correction of brain cells (181, 208). This approach is currently the treatment of choice worldwide for patients with a severe neuropathic form of MPS I. However, it did not show efficacy in other LSD (including MPS III) where the defective enzyme is secreted at a low level or is a membrane protein unable to diffuse between cells and be taken up by affected neurons. Finally, direct delivery of a gene therapy vector to the brain has shown good efficacy in mice and dogs (209, 210), but diffusion of the AAV vector commonly used in these protocols is limited to <0.5 cm^3 around the injection site (211) so multiple injection sites need to be used for the human brain. Besides, potential immunological problems and the long-term consequences of stereotaxic injection of AAV viruses are not well studied.

Several novel therapies are currently emerging including genome editing using CRISP-CAS or ZFN (zinc finger nucleases) technologies (Sangamo BioSciences) or ERT with BBB-penetrating enzymes (therapeutic enzyme linked with monoclonal antibody to insulin or transferrin receptor that professionally target their ligands to the brain parenchyma (Armagen). However, the results of clinical trial involving these therapies are either unknown or failed to produce treatment, like in the case of Sangamo trial where MPS II patients with iduronate-2-sulfatase gene inserted into the albumin locus in their liver tissues did not show reduction of circulating GAGs (https://www.bloomberg.com/news/articles/2019-02-07/sangamo-mediciine-benefits-remain-to-be-seen-in-early-stage-data). Thus, currently there is no effective treatment for MPS IIIC (or other neurological LSD) caused by defects in membrane proteins.

In this study we have attempted to test if MPS IIIC can be treated by lentiviral stem cell transplantation (LVST). Several studies in mouse models of neurological diseases including

those of rare genetic disorders and neurodegenerative diseases (179, 180, 212-217) have shown the therapeutic potential of LVST to treat the CNS. Moreover, this approach has even been used in clinical trials for humans patients with the peroxisomal disease X-linked adrenoleukodystrophy (218), the LSD MLD (178) and multiple sclerosis (219, 220).

Emerging data demonstrate that LV-mediated gene correction of HSPC followed by their transplantation provides an efficient method to treat neurological LSD by enzyme secreted from HSPC-derived brain microglia and macrophages (174, 178, 181-183, 221). In the healthy brain, microglia are derived from primitive myeloid progenitors that migrate into the CNS during development before the BBB is formed and are capable of self-renewal (reviewed in (222)). In addition, macrophages derived from bone marrow can pass through the BBB into the perivascular regions and ultimately take up residence in the parenchyma as resting ramified cells. In LSD, when the CNS damage occurs, cytokines and chemokines are generated from activated macrophages/microglia and astrocytes, which can stimulate the up-regulation of adhesion molecules on brain endothelial cells, resulting in enhanced trans-endothelial migration of monocytes from the blood into perivascular regions. These enzyme-deficient cells migrate into the parenchyma to sites of damage where they can secrete potentially cytotoxic pro-inflammatory cytokines, leading to further damage and cell death. However, if the hematopoietic precursors are gene-corrected, the macrophages and microglia gain the ability to transfer the missing lysosomal enzyme to the CNS and catabolize stored metabolites. This approach was shown to improve or completely treat the disease in several animal LSD models including the mouse model of MPS IIIA, deficient in the lysosomal enzyme heparan sulfate sulfaminidase (SGSH) (174). For MLD, caused by lysosomal arylsulfatase A (ARSA) deficiency, the first clinical trial showed promising results for 3 pediatric patients (178). A recent publication (221) describing the clinical outcome for 9 MLD children enrolled in 2010-2013 revealed exciting results. In brief, all patients showed stable, sustained engraftment of

gene-corrected HSPC, progressive reconstitution of ARSA activity in circulating haematopoietic cells and in the cerebrospinal fluid and reduction of the storage material in peripheral nerves. For seven patients, pre-symptomatic at the time of treatment, the disease onset was prevented. Furthermore, in one post-symptomatic patient the disease was ameliorated as compared with previously reported untreated MLD patients. Together, these data provide compelling evidence that LSD caused by deficiency of a soluble enzyme can be effectively treated using LV-HSPC gene therapy not only in mice but also in patients. In this work we attempted to transplant MPS IIIC mice with HSPC gene-modified to express the membrane enzyme HGSNAT. If we succeed in demonstrating pre-clinical efficacy, this will prove that beneficial effect in CNS can be achieved by targeting microglial cells only and provide a potential solution for therapeutic intervention for diseases caused by defects in membrane proteins (Niemann-Pick type C1, Cystinosis, Batten disease, Salla disease, methylmalonic acidemia with homocystinuria type cblF etc.).

Our *in vitro* studies revealed promising results for the LV-HGSNAT-GFP vector containing codon-optimized human *HGSNAT* cDNA which we have designed and produced. In HEK293 cells we obtained 17% efficacy of transduction and 3.6-fold increase of HGSNAT activity when we used MOI of 20. In mouse HSPC we achieved 2-fold increase of activity and 1.6% of transduction at MOI 30. We also demonstrated that bone marrow cells that undergo negative selection with the EasySep^{TM} kit can differentiate into CD11b and CD68-positive macrophages and that the transduction strategy with two hits of virus at 30 MOI each within 48 hours produces more gene-targeted cells while using the same amount of the viral vector as a single hit at MOI of 60.

In our pilot study, we used this strategy and generated HSPC with a 11.4-fold increase on HGSNAT activity over the normal endogenous level and transplanted these cells to MPS IIIIC mice previously conditioned with busulfan and obtained data that should help us to

optimize our strategy. First, we found that the engraftment rate highly varied between the animals (82.5%, 50% and 17%, 13 weeks after transplantation). Previously Gleitz *et al*. (2018) (180) used the same protocol for transplanting MPS II mice but achieved engraftment rates between 80% and 100%. In another study by Holley *et al*. (2018) (179) to treat MPS IIIB mice all animals with chimerism below 60% were excluded. Although the reasons for relatively low engraftment are not completely clear we propose that higher rates can be achieved by increasing the dose of busulfan.

Second, even in the mouse with the highest engraftment rate, we found a relatively modest of HGSNAT activity increase in the bone marrow (~4.6-fold) and spleen (~12-fold) while no activity increase was detected in the brain. Previously, Holley *et al*. (2018) observed clinical improvement in MPS IIIA and MPS IIIB mice when the enzyme activity in bone marrow was increased 50-fold over normal and in the brain to the 30% of normal. In the human clinical trial conducted by Biffi *et al.* (178), one month after transplant between 45 and 80% of the HSPC colonies from patients' bone marrow in the colony-forming cell (CFC) assay harbored the LV genome. They also showed about 5-fold increase of ARSA activity as compared with healthy donors in the most therapeutically relevant $CD15^+$ and $CD14^+$ myeloid populations which lasted until at least 20 months after treatment (when the last measurement has been done). We conclude, therefore, that besides achieving higher engraftment we also need to improve our gene-targeting strategy by either using higher MOI or re-designing the targeting vector to obtain supraphysiologic levels of HGSNAT activity in the myeloid cells.

The choice of the LV MOI used in transduction experiments depends on the strength of the gene promoter and on the tissues that treatment wishes to target. In the study involving the mouse model of Fabry disease, the LV was used at MOI 15, but still the transplantation of targeted HSPC restored α-Galactosidase A activity in plasma (~1.2-fold increased over healthy controls 6 weeks post-transplant) and in the bone marrow (~1.15-fold increase over healthy

controls). Importantly, the treatment also reduced Gb_3 substrate accumulation in spleen, lung, heart and kidney, the key target organs for the amelioration of Fabry disease in patients (217). However, since the key target organ for MPS IIIC patients is the brain, we believe that higher levels of activity in transplanted HSPC are necessary. In the case of MPS IIIB mice, Holley *et al.* (2018) used two hits with MOI of 60 and obtained 13% of the WT NAGLU enzyme level in the brain resulting in normalization of HS storage and behavior correction (179). We estimate, however, that even if we use the same MOI with our current LV we cannot achieve the necessary increase of the enzyme levels in the myeloid cells of transplanted mice. The cost of using even higher amounts of the virus would be prohibitive. We, therefore, need to improve the design of the vector by using stronger promoter and reducing the size of the plasmid. For example GFP protein can replaced by a smaller HA tag, that might improve the packaging of the LV during its production, increasing the titer of the virus. Besides, the PGK promoter can be replaced with stronger Ef1-α (elongation factor 1-α) promoter used by our collaborators in the Fabry study (217).

Interestingly, even despite high variation of engraftments and relatively modest increase of HGSNAT activity in bone marrow, we still observed partial improvement of behavior in transplanted mice, especially reduction of hyperactivity and improved anxiety detected by the open field test. The animal with the most improved behavior also had the highest engraftment of donor cells (82.5%), suggesting that this is not a random change or unspecific effect of myeloablation/transplantation procedure, although, increasing the number of treated mice would give more robust evidence. Because HGSNAT is a transmembrane enzyme we cannot expect to rely on cross-correction of brain cells, which might require higher levels of gene-corrected microglia cells in the brain to observe any beneficial effect in the treated MPS IIIC mice. Another approach that can be considered to achieve this is the direct intracerebroventricular administration of gene-corrected HSPC that according to Capotondo *et*

al (2017) (223) allows for a more rapid and robust engraftment of donor cells in the brain compared to intravenous administration. In their study they also used LV-transduced HSPC and conditioned the recipient mice with busulfan, so we can quickly adopt their protocol if necessary. In summary, our data reveal for the first time the effects of LV-corrected HSPC transplanted into MPS IIIC mice and shed light on the improvements that need to be implemented to increase our chances for success in alleviating the disease.

Chapter 6

REFERENCES

1. Xu H, Ren D. Lysosomal physiology. Annu Rev Physiol. 2015;77:57-80.
2. Alberts B. Molecular biology of the cell. [Hauptbd.]. [Hauptbd.]. New York, NY [u.a.]: Garland Science Taylor & Francis; 2008.
3. Mellman I, Fuchs R, Helenius A. Acidification of the endocytic and exocytic pathways. Annu Rev Biochem. 1986;55:663-700.
4. Luzio JP, Pryor PR, Bright NA. Lysosomes: fusion and function. Nat Rev Mol Cell Biol. 2007;8(8):622-32.
5. Staudt C, Puissant E, Boonen M. Subcellular Trafficking of Mammalian Lysosomal Proteins: An Extended View. Int J Mol Sci. 2016;18(1).
6. Bonifacino JS, Traub LM. Signals for sorting of transmembrane proteins to endosomes and lysosomes. Annu Rev Biochem. 2003;72:395-447.
7. Settembre C, Di Malta C, Polito VA, Garcia Arencibia M, Vetrini F, Erdin S, et al. TFEB links autophagy to lysosomal biogenesis. Science. 2011;332(6036):1429-33.
8. Martina JA, Chen Y, Gucek M, Puertollano R. MTORC1 functions as a transcriptional regulator of autophagy by preventing nuclear transport of TFEB. Autophagy. 2012;8(6):903-14.
9. Sardiello M, Palmieri M, di Ronza A, Medina DL, Valenza M, Gennarino VA, et al. A gene network regulating lysosomal biogenesis and function. Science. 2009;325(5939):473-7.
10. Napolitano G, Ballabio A. TFEB at a glance. J Cell Sci. 2016;129(13):2475-81.
11. Medina DL, Di Paola S, Peluso I, Armani A, De Stefani D, Venditti R, et al. Lysosomal calcium signalling regulates autophagy through calcineurin and TFEB. Nat Cell Biol. 2015;17(3):288-99.
12. Platt FM, Boland B, van der Spoel AC. The cell biology of disease: lysosomal storage disorders: the cellular impact of lysosomal dysfunction. J Cell Biol. 2012;199(5):723-34.
13. Zhao YG, Zhang H. Autophagosome maturation: An epic journey from the ER to lysosomes. J Cell Biol. 2019;218(3):757-70.
14. Saftig P, Klumperman J. Lysosome biogenesis and lysosomal membrane proteins: trafficking meets function. Nat Rev Mol Cell Biol. 2009;10(9):623-35.
15. Hers HG. alpha-Glucosidase deficiency in generalized glycogenstorage disease (Pompe's disease). Biochem J. 1963;86:11-6.
16. Filocamo M, Morrone A. Lysosomal storage disorders: molecular basis and laboratory testing. Hum Genomics. 2011;5(3):156-69.
17. di Ronza A, Bajaj L, Sharma J, Sanagasetti D, Lotfi P, Adamski CJ, et al. CLN8 is an endoplasmic reticulum cargo receptor that regulates lysosome biogenesis2018 Dec. 1370-7 p.
18. Moammar H, Cheriyan G, Mathew R, Al-Sannaa N. Incidence and patterns of inborn errors of metabolism in the Eastern Province of Saudi Arabia, 1983-2008. Ann Saudi Med. 2010;30(4):271-7.
19. Pastores GM, Maegawa GH. Clinical neurogenetics: neuropathic lysosomal storage disorders. Neurol Clin. 2013;31(4):1051-71.
20. Para C, Bose P, Pshezhetsky AV. Neuropathophysiology of Lysosomal Storage Diseases: Synaptic Dysfunction as a Starting Point for Disease Progression. J Clin Med. 2020;9(3).
21. Boustany RM. Lysosomal storage diseases--the horizon expands. Nat Rev Neurol. 2013;9(10):583-98.

22. Fraldi A, Klein AD, Medina DL, Settembre C. Brain Disorders Due to Lysosomal Dysfunction. Annu Rev Neurosci. 2016;39:277-95.
23. Jardim LB, Villanueva MM, de Souza CF, Netto CB. Clinical aspects of neuropathic lysosomal storage disorders. J Inherit Metab Dis. 2010;33(4):315-29.
24. Mink JW, Augustine EF, Adams HR, Marshall FJ, Kwon JM. Classification and natural history of the neuronal ceroid lipofuscinoses. J Child Neurol. 2013;28(9):1101-5.
25. Gan-Or Z, Liong C, Alcalay RN. GBA-Associated Parkinson's Disease and Other Synucleinopathies. Curr Neurol Neurosci Rep. 2018;18(8):44.
26. Barkhuizen M, Anderson DG, Grobler AF. Advances in GBA-associated Parkinson's disease--Pathology, presentation and therapies. Neurochem Int. 2016;93:6-25.
27. Sidransky E, Nalls MA, Aasly JO, Aharon-Peretz J, Annesi G, Barbosa ER, et al. Multicenter analysis of glucocerebrosidase mutations in Parkinson's disease. N Engl J Med. 2009;361(17):1651-61.
28. Robak LA, Jansen IE, van Rooij J, Uitterlinden AG, Kraaij R, Jankovic J, et al. Excessive burden of lysosomal storage disorder gene variants in Parkinson's disease. Brain. 2017;140(12):3191-203.
29. Mazzulli JR, Xu YH, Sun Y, Knight AL, McLean PJ, Caldwell GA, et al. Gaucher disease glucocerebrosidase and alpha-synuclein form a bidirectional pathogenic loop in synucleinopathies. Cell. 2011;146(1):37-52.
30. Li G, Cui S, Du J, Liu J, Zhang P, Fu Y, et al. Association of GALC, ZNF184, IL1R2 and ELOVL7 With Parkinson's Disease in Southern Chinese. Front Aging Neurosci. 2018;10:402.
31. Heon-Roberts R, Nguyen ALA, Pshezhetsky AV. Molecular Bases of Neurodegeneration and Cognitive Decline, the Major Burden of Sanfilippo Disease. J Clin Med. 2020;9(2).
32. Oberstadt M, Classen J, Arendt T, Holzer M. TDP-43 and Cytoskeletal Proteins in ALS. Mol Neurobiol. 2018;55(4):3143-51.
33. Dardis A, Zampieri S, Canterini S, Newell KL, Stuani C, Murrell JR, et al. Altered localization and functionality of TAR DNA Binding Protein 43 (TDP-43) in niemann- pick disease type C. Acta Neuropathol Commun. 2016;4(1):52.
34. Tropea TF, Mak J, Guo MH, Xie SX, Suh E, Rick J, et al. TMEM106B Effect on cognition in Parkinson disease and frontotemporal dementia. Ann Neurol. 2019;85(6):801-11.
35. Brady OA, Zheng Y, Murphy K, Huang M, Hu F. The frontotemporal lobar degeneration risk factor, TMEM106B, regulates lysosomal morphology and function. Hum Mol Genet. 2013;22(4):685-95.
36. Klein ZA, Takahashi H, Ma M, Stagi M, Zhou M, Lam TT, et al. Loss of TMEM106B Ameliorates Lysosomal and Frontotemporal Dementia-Related Phenotypes in Progranulin-Deficient Mice. Neuron. 2017;95(2):281-96 e6.
37. Schwenk BM, Lang CM, Hogl S, Tahirovic S, Orozco D, Rentzsch K, et al. The FTLD risk factor TMEM106B and MAP6 control dendritic trafficking of lysosomes. EMBO J. 2014;33(5):450-67.
38. Tetreault M, Gonzalez M, Dicaire MJ, Allard P, Gehring K, Leblanc D, et al. Adult-onset painful axonal polyneuropathy caused by a dominant NAGLU mutation. Brain. 2015;138(Pt 6):1477-83.
39. Rapin I, Goldfischer S, Katzman R, Engel J, Jr., O'Brien JS. The cherry-red spot--myoclonus syndrome. Ann Neurol. 1978;3(3):234-42.
40. Seyrantepe V, Poupetova H, Froissart R, Zabot MT, Maire I, Pshezhetsky AV. Molecular pathology of NEU1 gene in sialidosis. Hum Mutat. 2003;22(5):343-52.
41. Gowda VK, Srinivasan VM, Benakappa N, Benakappa A. Sialidosis Type 1 with a Novel Mutation in the Neuraminidase-1 (NEU1) Gene. Indian J Pediatr. 2017;84(5):403-4.

42. Pshezhetsky AV, Ashmarina M. Lysosomal multienzyme complex: biochemistry, genetics, and molecular pathophysiology. Prog Nucleic Acid Res Mol Biol. 2001;69:81-114.
43. Panayiotopoulos CP. The atlas of epilepsies. New York; London: Springer; 2010.
44. Lowden JA, O'Brien JS. Sialidosis: a review of human neuraminidase deficiency. Am J Hum Genet. 1979;31(1):1-18.
45. Khan SA, Peracha H, Ballhausen D, Wiesbauer A, Rohrbach M, Gautschi M, et al. Epidemiology of mucopolysaccharidoses. Mol Genet Metab. 2017;121(3):227-40.
46. Li JP, Kusche-Gullberg M. Heparan Sulfate: Biosynthesis, Structure, and Function. Int Rev Cell Mol Biol. 2016;325:215-73.
47. Kreuger J, Kjellen L. Heparan sulfate biosynthesis: regulation and variability. J Histochem Cytochem. 2012;60(12):898-907.
48. Kim BT, Kitagawa H, Tamura J, Saito T, Kusche-Gullberg M, Lindahl U, et al. Human tumor suppressor EXT gene family members EXTL1 and EXTL3 encode alpha 1,4- N-acetylglucosaminyltransferases that likely are involved in heparan sulfate/ heparin biosynthesis. Proc Natl Acad Sci U S A. 2001;98(13):7176-81.
49. Esko JD, Lindahl U. Molecular diversity of heparan sulfate. J Clin Invest. 2001;108(2):169-73.
50. Sarrazin S, Lamanna WC, Esko JD. Heparan sulfate proteoglycans. Cold Spring Harb Perspect Biol. 2011;3(7).
51. Ai X, Do AT, Kusche-Gullberg M, Lindahl U, Lu K, Emerson CP, Jr. Substrate specificity and domain functions of extracellular heparan sulfate 6-O-endosulfatases, QSulf1 and QSulf2. J Biol Chem. 2006;281(8):4969-76.
52. Gong F, Jemth P, Escobar Galvis ML, Vlodavsky I, Horner A, Lindahl U, et al. Processing of macromolecular heparin by heparanase. J Biol Chem. 2003;278(37):35152-8.
53. Freeman C, Hopwood J. Lysosomal degradation of heparin and heparan sulphate. Adv Exp Med Biol. 1992;313:121-34.
54. Meikle PJ, Hopwood JJ, Clague AE, Carey WF. Prevalence of lysosomal storage disorders. JAMA. 1999;281(3):249-54.
55. Poupetova H, Ledvinova J, Berna L, Dvorakova L, Kozich V, Elleder M. The birth prevalence of lysosomal storage disorders in the Czech Republic: comparison with data in different populations. J Inherit Metab Dis. 2010;33(4):387-96.
56. Valstar MJ, Ruijter GJ, van Diggelen OP, Poorthuis BJ, Wijburg FA. Sanfilippo syndrome: a mini-review. J Inherit Metab Dis. 2008;31(2):240-52.
57. Scriver CR, Beaudet AL, Sly WS, Valle D, Stanbury JB, Wyngaarden JB, et al. The metabolic and molecular bases of inherited disease. New York: McGraw-Hill, Health Professions Division; 2001.
58. Meikle PJ, Fuller M, Hopwood JJ. Lysosomal Degradation of Heparin and Heparan Sulfate-Chapter 10. 2005.
59. Wijburg FA, Wegrzyn G, Burton BK, Tylki-Szymanska A. Mucopolysaccharidosis type III (Sanfilippo syndrome) and misdiagnosis of idiopathic developmental delay, attention deficit/hyperactivity disorder or autism spectrum disorder. Acta Paediatr. 2013;102(5):462-70.
60. Martins C, de Medeiros PFV, Leistner-Segal S, Dridi L, Elcioglu N, Wood J, et al. Molecular characterization of a large group of Mucopolysaccharidosis type IIIC patients reveals the evolutionary history of the disease. Hum Mutat. 2019;40(8):1084-100.
61. Feldhammer M, Durand S, Mrazova L, Boucher RM, Laframboise R, Steinfeld R, et al. Sanfilippo syndrome type C: mutation spectrum in the heparan sulfate acetyl-CoA: alpha-glucosaminide N-acetyltransferase (HGSNAT) gene. Hum Mutat. 2009;30(6):918-25.
62. Bartsocas C, Grobe H, van de Kamp JJ, von Figura K, Kresse H, Klein U, et al. Sanfilippo type C disease: clinical findings in four patients with a new variant of mucopolysaccharidosis III. Eur J Pediatr. 1979;130(4):251-8.

63. Martins C, Hulkova H, Dridi L, Dormoy-Raclet V, Grigoryeva L, Choi Y, et al. Neuroinflammation, mitochondrial defects and neurodegeneration in mucopolysaccharidosis III type C mouse model. Brain. 2015;138(Pt 2):336-55.
64. Ohmi K, Greenberg DS, Rajavel KS, Ryazantsev S, Li HH, Neufeld EF. Activated microglia in cortex of mouse models of mucopolysaccharidoses I and IIIB. Proc Natl Acad Sci U S A. 2003;100(4):1902-7.
65. Villani GR, Gargiulo N, Faraonio R, Castaldo S, Gonzalez YRE, Di Natale P. Cytokines, neurotrophins, and oxidative stress in brain disease from mucopolysaccharidosis IIIB. J Neurosci Res. 2007;85(3):612-22.
66. Ausseil J, Desmaris N, Bigou S, Attali R, Corbineau S, Vitry S, et al. Early neurodegeneration progresses independently of microglial activation by heparan sulfate in the brain of mucopolysaccharidosis IIIB mice. PLoS One. 2008;3(5):e2296.
67. DiRosario J, Divers E, Wang C, Etter J, Charrier A, Jukkola P, et al. Innate and adaptive immune activation in the brain of MPS IIIB mouse model. J Neurosci Res. 2009;87(4):978-90.
68. Wilkinson FL, Holley RJ, Langford-Smith KJ, Badrinath S, Liao A, Langford-Smith A, et al. Neuropathology in mouse models of mucopolysaccharidosis type I, IIIA and IIIB. PLoS One. 2012;7(4):e35787.
69. Grishchuk Y, Sri S, Rudinskiy N, Ma W, Stember KG, Cottle MW, et al. Behavioral deficits, early gliosis, dysmyelination and synaptic dysfunction in a mouse model of mucolipidosis IV. Acta Neuropathol Commun. 2014;2:133.
70. Ginns EI, Mak SK, Ko N, Karlgren J, Akbarian S, Chou VP, et al. Neuroinflammation and alpha-synuclein accumulation in response to glucocerebrosidase deficiency are accompanied by synaptic dysfunction. Mol Genet Metab. 2014;111(2):152-62.
71. Pressey SN, Smith DA, Wong AM, Platt FM, Cooper JD. Early glial activation, synaptic changes and axonal pathology in the thalamocortical system of Niemann-Pick type C1 mice. Neurobiol Dis. 2012;45(3):1086-100.
72. Baudry M, Yao Y, Simmons D, Liu J, Bi X. Postnatal development of inflammation in a murine model of Niemann-Pick type C disease: immunohistochemical observations of microglia and astroglia. Exp Neurol. 2003;184(2):887-903.
73. Pshezhetsky AV. Crosstalk between 2 organelles: Lysosomal storage of heparan sulfate causes mitochondrial defects and neuronal death in mucopolysaccharidosis III type C. Rare Dis. 2015;3(1):e1049793.
74. Kavetsky L, Green KK, Boyle BR, Yousufzai FAK, Padron ZM, Melli SE, et al. Increased interactions and engulfment of dendrites by microglia precede Purkinje cell degeneration in a mouse model of Niemann Pick Type-C. Sci Rep. 2019;9(1):14722.
75. Kierdorf K, Prinz M. Microglia in steady state. J Clin Invest. 2017;127(9):3201-9.
76. Bruyere J, Roy E, Ausseil J, Lemonnier T, Teyre G, Bohl D, et al. Heparan sulfate saccharides modify focal adhesions: implication in mucopolysaccharidosis neuropathophysiology. J Mol Biol. 2015;427(4):775-91.
77. Vitner EB, Dekel H, Zigdon H, Shachar T, Farfel-Becker T, Eilam R, et al. Altered expression and distribution of cathepsins in neuronopathic forms of Gaucher disease and in other sphingolipidoses. Hum Mol Genet. 2010;19(18):3583-90.
78. Lange J, Haslett LJ, Lloyd-Evans E, Pocock JM, Sands MS, Williams BP, et al. Compromised astrocyte function and survival negatively impact neurons in infantile neuronal ceroid lipofuscinosis. Acta Neuropathol Commun. 2018;6(1):74.
79. Parviainen L, Dihanich S, Anderson GW, Wong AM, Brooks HR, Abeti R, et al. Glial cells are functionally impaired in juvenile neuronal ceroid lipofuscinosis and detrimental to neurons. Acta Neuropathol Commun. 2017;5(1):74.

80. Pontikis CC, Cotman SL, MacDonald ME, Cooper JD. Thalamocortical neuron loss and localized astrocytosis in the Cln3Deltaex7/8 knock-in mouse model of Batten disease. Neurobiol Dis. 2005;20(3):823-36.
81. Thelen M, Damme M, Schweizer M, Hagel C, Wong AM, Cooper JD, et al. Disruption of the autophagy-lysosome pathway is involved in neuropathology of the nclf mouse model of neuronal ceroid lipofuscinosis. PLoS One. 2012;7(4):e35493.
82. Oswald MJ, Palmer DN, Kay GW, Shemilt SJ, Rezaie P, Cooper JD. Glial activation spreads from specific cerebral foci and precedes neurodegeneration in presymptomatic ovine neuronal ceroid lipofuscinosis (CLN6). Neurobiol Dis. 2005;20(1):49-63.
83. Jeyakumar M, Dwek RA, Butters TD, Platt FM. Storage solutions: treating lysosomal disorders of the brain. Nat Rev Neurosci. 2005;6(9):713-25.
84. Nixon RA, Yang DS, Lee JH. Neurodegenerative lysosomal disorders: a continuum from development to late age. Autophagy. 2008;4(5):590-9.
85. Cao Y, Espinola JA, Fossale E, Massey AC, Cuervo AM, MacDonald ME, et al. Autophagy is disrupted in a knock-in mouse model of juvenile neuronal ceroid lipofuscinosis. J Biol Chem. 2006;281(29):20483-93.
86. Koike M, Shibata M, Waguri S, Yoshimura K, Tanida I, Kominami E, et al. Participation of autophagy in storage of lysosomes in neurons from mouse models of neuronal ceroid-lipofuscinoses (Batten disease). Am J Pathol. 2005;167(6):1713-28.
87. Settembre C, Fraldi A, Jahreiss L, Spampanato C, Venturi C, Medina D, et al. A block of autophagy in lysosomal storage disorders. Hum Mol Genet. 2008;17(1):119-29.
88. Sambri I, D'Alessio R, Ezhova Y, Giuliano T, Sorrentino NC, Cacace V, et al. Lysosomal dysfunction disrupts presynaptic maintenance and restoration of presynaptic function prevents neurodegeneration in lysosomal storage diseases. EMBO Mol Med. 2017;9(1):112-32.
89. Maetzel D, Sarkar S, Wang H, Abi-Mosleh L, Xu P, Cheng AW, et al. Genetic and chemical correction of cholesterol accumulation and impaired autophagy in hepatic and neural cells derived from Niemann-Pick Type C patient-specific iPS cells. Stem Cell Reports. 2014;2(6):866-80.
90. Baldo G, Lorenzini DM, Santos DS, Mayer FQ, Vitry S, Bigou S, et al. Shotgun proteomics reveals possible mechanisms for cognitive impairment in Mucopolysaccharidosis I mice. Mol Genet Metab. 2015;114(2):138-45.
91. Karabelas AB, Walkley SU. Altered patterns of evoked synaptic activity in cortical pyramidal neurons in feline ganglioside storage disease. Brain Res. 1985;339(2):329-36.
92. Purpura DP, Highstein SM, Karabelas AB, Walkley SU. Intracellular recording and HRP-staining of cortical neurons in feline ganglioside storage disease. Brain Res. 1980;181(2):446-9.
93. Teixeira CA, Miranda CO, Sousa VF, Santos TE, Malheiro AR, Solomon M, et al. Early axonal loss accompanied by impaired endocytosis, abnormal axonal transport, and decreased microtubule stability occur in the model of Krabbe's disease. Neurobiol Dis. 2014;66:92-103.
94. Xu S, Zhou S, Xia D, Xia J, Chen G, Duan S, et al. Defects of synaptic vesicle turnover at excitatory and inhibitory synapses in Niemann-Pick C1-deficient neurons. Neuroscience. 2010;167(3):608-20.
95. Dwyer CA, Scudder SL, Lin Y, Dozier LE, Phan D, Allen NJ, et al. Neurodevelopmental Changes in Excitatory Synaptic Structure and Function in the Cerebral Cortex of Sanfilippo Syndrome IIIA Mice. Sci Rep. 2017;7:46576.
96. Canals I, Soriano J, Orlandi JG, Torrent R, Richaud-Patin Y, Jimenez-Delgado S, et al. Activity and High-Order Effective Connectivity Alterations in Sanfilippo C Patient-Specific Neuronal Networks. Stem Cell Reports. 2015;5(4):546-57.
97. Principles of neural science. New York: McGraw-Hill; 2000.

98. Harris KM, Weinberg RJ. Ultrastructure of synapses in the mammalian brain. Cold Spring Harb Perspect Biol. 2012;4(5).
99. Kreutzberg GW. Neuronal dynamics and axonal flow. IV. Blockage of intra-axonal enzyme transport by colchicine. Proc Natl Acad Sci U S A. 1969;62(3):722-8.
100. Vale RD, Reese TS, Sheetz MP. Identification of a novel force-generating protein, kinesin, involved in microtubule-based motility. Cell. 1985;42(1):39-50.
101. Paschal BM, Shpetner HS, Vallee RB. MAP 1C is a microtubule-activated ATPase which translocates microtubules in vitro and has dynein-like properties. J Cell Biol. 1987;105(3):1273-82.
102. Rizzoli SO, Betz WJ. Synaptic vesicle pools. Nat Rev Neurosci. 2005;6(1):57-69.
103. Rosahl TW, Spillane D, Missler M, Herz J, Selig DK, Wolff JR, et al. Essential functions of synapsins I and II in synaptic vesicle regulation. Nature. 1995;375(6531):488-93.
104. Galli T, Haucke V. Cycling of synaptic vesicles: how far? How fast! Sci STKE. 2004;2004(264):re19.
105. Smith SM, Renden R, von Gersdorff H. Synaptic vesicle endocytosis: fast and slow modes of membrane retrieval. Trends Neurosci. 2008;31(11):559-68.
106. Yuste R. The discovery of dendritic spines by Cajal. Front Neuroanat. 2015;9:18.
107. Spacek J, Harris KM. Three-dimensional organization of cell adhesion junctions at synapses and dendritic spines in area CA1 of the rat hippocampus. J Comp Neurol. 1998;393(1):58-68.
108. Arellano JI, Espinosa A, Fairen A, Yuste R, DeFelipe J. Non-synaptic dendritic spines in neocortex. Neuroscience. 2007;145(2):464-9.
109. Chen JL, Villa KL, Cha JW, So PT, Kubota Y, Nedivi E. Clustered dynamics of inhibitory synapses and dendritic spines in the adult neocortex. Neuron. 2012;74(2):361-73.
110. Sorra KE, Harris KM. Overview on the structure, composition, function, development, and plasticity of hippocampal dendritic spines. Hippocampus. 2000;10(5):501-11.
111. Peters A, Kaiserman-Abramof IR. The small pyramidal neuron of the rat cerebral cortex. The perikaryon, dendrites and spines. Am J Anat. 1970;127(4):321-55.
112. Cheng C, Trzcinski O, Doering LC. Fluorescent labeling of dendritic spines in cell cultures with the carbocyanine dye "DiI". Front Neuroanat. 2014;8:30.
113. Lang C, Barco A, Zablow L, Kandel ER, Siegelbaum SA, Zakharenko SS. Transient expansion of synaptically connected dendritic spines upon induction of hippocampal long-term potentiation. Proc Natl Acad Sci U S A. 2004;101(47):16665-70.
114. Matsuzaki M, Honkura N, Ellis-Davies GC, Kasai H. Structural basis of long-term potentiation in single dendritic spines. Nature. 2004;429(6993):761-6.
115. Padamsey Z, McGuinness L, Bardo SJ, Reinhart M, Tong R, Hedegaard A, et al. Activity-Dependent Exocytosis of Lysosomes Regulates the Structural Plasticity of Dendritic Spines. Neuron. 2017;93(1):132-46.
116. Padamsey Z, McGuinness L, Emptage NJ. Inhibition of lysosomal Ca(2+) signalling disrupts dendritic spine structure and impairs wound healing in neurons. Commun Integr Biol. 2017;10(5-6):e1344802.
117. Sheng M, Hoogenraad CC. The postsynaptic architecture of excitatory synapses: a more quantitative view. Annu Rev Biochem. 2007;76:823-47.
118. Gulley RL, Reese TS. Cytoskeletal organization at the postsynaptic complex. J Cell Biol. 1981;91(1):298-302.
119. Landis DM, Reese TS. Cytoplasmic organization in cerebellar dendritic spines. J Cell Biol. 1983;97(4):1169-78.
120. Lisman JE, Harris KM. Quantal analysis and synaptic anatomy--integrating two views of hippocampal plasticity. Trends Neurosci. 1993;16(4):141-7.

121. Harris KM, Sultan P. Variation in the number, location and size of synaptic vesicles provides an anatomical basis for the nonuniform probability of release at hippocampal CA1 synapses. Neuropharmacology. 1995;34(11):1387-95.
122. Schikorski T, Stevens CF. Morphological correlates of functionally defined synaptic vesicle populations. Nat Neurosci. 2001;4(4):391-5.
123. Peng J, Kim MJ, Cheng D, Duong DM, Gygi SP, Sheng M. Semiquantitative proteomic analysis of rat forebrain postsynaptic density fractions by mass spectrometry. J Biol Chem. 2004;279(20):21003-11.
124. Cho KO, Hunt CA, Kennedy MB. The rat brain postsynaptic density fraction contains a homolog of the Drosophila discs-large tumor suppressor protein. Neuron. 1992;9(5):929-42.
125. Walsh MJ, Kuruc N. The postsynaptic density: constituent and associated proteins characterized by electrophoresis, immunoblotting, and peptide sequencing. J Neurochem. 1992;59(2):667-78.
126. Kennedy MB. Signal-processing machines at the postsynaptic density. Science. 2000;290(5492):750-4.
127. Sheng M, Kim E. The postsynaptic organization of synapses. Cold Spring Harb Perspect Biol. 2011;3(12).
128. Sans N, Petralia RS, Wang YX, Blahos J, 2nd, Hell JW, Wenthold RJ. A developmental change in NMDA receptor-associated proteins at hippocampal synapses. J Neurosci. 2000;20(3):1260-71.
129. Petralia RS, Sans N, Wang YX, Wenthold RJ. Ontogeny of postsynaptic density proteins at glutamatergic synapses. Mol Cell Neurosci. 2005;29(3):436-52.
130. Delcroix JD, Valletta JS, Wu C, Hunt SJ, Kowal AS, Mobley WC. NGF signaling in sensory neurons: evidence that early endosomes carry NGF retrograde signals. Neuron. 2003;39(1):69-84.
131. Zweifel LS, Kuruvilla R, Ginty DD. Functions and mechanisms of retrograde neurotrophin signalling. Nat Rev Neurosci. 2005;6(8):615-25.
132. Button RW, Roberts SL, Willis TL, Hanemann CO, Luo S. Accumulation of autophagosomes confers cytotoxicity. J Biol Chem. 2017;292(33):13599-614.
133. Sharma S, Lindau M. t-SNARE Transmembrane Domain Clustering Modulates Lipid Organization and Membrane Curvature. J Am Chem Soc. 2017;139(51):18440-3.
134. Button RW, Luo S. The formation of autophagosomes during lysosomal defect: A new source of cytotoxicity. Autophagy. 2017;13(10):1797-8.
135. March PA, Thrall MA, Brown DE, Mitchell TW, Lowenthal AC, Walkley SU. GABAergic neuroaxonal dystrophy and other cytopathological alterations in feline Niemann-Pick disease type C. Acta Neuropathol. 1997;94(2):164-72.
136. Walkley SU, Baker HJ, Rattazzi MC, Haskins ME, Wu JY. Neuroaxonal dystrophy in neuronal storage disorders: evidence for major GABAergic neuron involvement. J Neurol Sci. 1991;104(1):1-8.
137. Oya Y, Nakayasu H, Fujita N, Suzuki K, Suzuki K. Pathological study of mice with total deficiency of sphingolipid activator proteins (SAP knockout mice). Acta Neuropathol. 1998;96(1):29-40.
138. Bergner CG, van der Meer F, Winkler A, Wrzos C, Turkmen M, Valizada E, et al. Microglia damage precedes major myelin breakdown in X-linked adrenoleukodystrophy and metachromatic leukodystrophy. Glia. 2019;67(6):1196-209.
139. Tanaka K, Nagara H, Kobayashi T, Goto I. The twitcher mouse: accumulation of galactosylsphingosine and pathology of the sciatic nerve. Brain Res. 1988;454(1-2):340-6.
140. Smith B, Galbiati F, Castelvetri LC, Givogri MI, Lopez-Rosas A, Bongarzone ER. Peripheral neuropathy in the Twitcher mouse involves the activation of axonal caspase 3. ASN Neuro. 2011;3(4).

141. Chandra S, Gallardo G, Fernandez-Chacon R, Schluter OM, Sudhof TC. Alpha-synuclein cooperates with CSPalpha in preventing neurodegeneration. Cell. 2005;123(3):383-96.
142. Burre J, Sharma M, Tsetsenis T, Buchman V, Etherton MR, Sudhof TC. Alpha-synuclein promotes SNARE-complex assembly in vivo and in vitro. Science. 2010;329(5999):1663-7.
143. Burgoyne RD, Morgan A. Chaperoning the SNAREs: a role in preventing neurodegeneration? Nat Cell Biol. 2011;13(1):8-9.
144. Sharma M, Burre J, Sudhof TC. CSPalpha promotes SNARE-complex assembly by chaperoning SNAP-25 during synaptic activity. Nat Cell Biol. 2011;13(1):30-9.
145. von Schantz C, Kielar C, Hansen SN, Pontikis CC, Alexander NA, Kopra O, et al. Progressive thalamocortical neuron loss in Cln5 deficient mice: Distinct effects in Finnish variant late infantile NCL. Neurobiol Dis. 2009;34(2):308-19.
146. Kielar C, Wishart TM, Palmer A, Dihanich S, Wong AM, Macauley SL, et al. Molecular correlates of axonal and synaptic pathology in mouse models of Batten disease. Hum Mol Genet. 2009;18(21):4066-80.
147. Llavero Hurtado M, Fuller HR, Wong AMS, Eaton SL, Gillingwater TH, Pennetta G, et al. Proteomic mapping of differentially vulnerable pre-synaptic populations identifies regulators of neuronal stability in vivo. Sci Rep. 2017;7(1):12412.
148. Vitry S, Ausseil J, Hocquemiller M, Bigou S, Dos Santos Coura R, Heard JM. Enhanced degradation of synaptophysin by the proteasome in mucopolysaccharidosis type IIIB. Mol Cell Neurosci. 2009;41(1):8-18.
149. Bayo-Puxan N, Terrasso AP, Creyssels S, Simao D, Begon-Pescia C, Lavigne M, et al. Lysosomal and network alterations in human mucopolysaccharidosis type VII iPSC-derived neurons. Sci Rep. 2018;8(1):16644.
150. Kanninen KM, Grubman A, Meyerowitz J, Duncan C, Tan JL, Parker SJ, et al. Increased zinc and manganese in parallel with neurodegeneration, synaptic protein changes and activation of Akt/GSK3 signaling in ovine CLN6 neuronal ceroid lipofuscinosis. PLoS One. 2013;8(3):e58644.
151. Amorim IS, Mitchell NL, Palmer DN, Sawiak SJ, Mason R, Wishart TM, et al. Molecular neuropathology of the synapse in sheep with CLN5 Batten disease. Brain Behav. 2015;5(11):e00401.
152. Kwon SE, Chapman ER. Synaptophysin regulates the kinetics of synaptic vesicle endocytosis in central neurons. Neuron. 2011;70(5):847-54.
153. Conde C, Caceres A. Microtubule assembly, organization and dynamics in axons and dendrites. Nat Rev Neurosci. 2009;10(5):319-32.
154. Virmani T, Gupta P, Liu X, Kavalali ET, Hofmann SL. Progressively reduced synaptic vesicle pool size in cultured neurons derived from neuronal ceroid lipofuscinosis-1 knockout mice. Neurobiol Dis. 2005;20(2):314-23.
155. Purpura DP, Suzuki K. Distortion of neuronal geometry and formation of aberrant synapses in neuronal storage disease. Brain Res. 1976;116(1):1-21.
156. Bible E, Gupta P, Hofmann SL, Cooper JD. Regional and cellular neuropathology in the palmitoyl protein thioesterase-1 null mutant mouse model of infantile neuronal ceroid lipofuscinosis. Neurobiol Dis. 2004;16(2):346-59.
157. Tiscione SA, Vivas O, Ginsburg KS, Bers DM, Ory DS, Santana LF, et al. Disease-associated mutations in Niemann-Pick type C1 alter ER calcium signaling and neuronal plasticity. J Cell Biol. 2019;218(12):4141-56.
158. Goo MS, Sancho L, Slepak N, Boassa D, Deerinck TJ, Ellisman MH, et al. Activity-dependent trafficking of lysosomes in dendrites and dendritic spines. J Cell Biol. 2017;216(8):2499-513.

159. Koster KP, Francesconi W, Berton F, Alahmadi S, Srinivas R, Yoshii A. Developmental NMDA receptor dysregulation in the infantile neuronal ceroid lipofuscinosis mouse model. Elife. 2019;8.
160. Imrie J, Dasgupta S, Besley GT, Harris C, Heptinstall L, Knight S, et al. The natural history of Niemann-Pick disease type C in the UK. J Inherit Metab Dis. 2007;30(1):51-9.
161. Voikar V, Rauvala H, Ikonen E. Cognitive deficit and development of motor impairment in a mouse model of Niemann-Pick type C disease. Behav Brain Res. 2002;132(1):1-10.
162. Sevin M, Lesca G, Baumann N, Millat G, Lyon-Caen O, Vanier MT, et al. The adult form of Niemann-Pick disease type C. Brain. 2007;130(Pt 1):120-33.
163. Amritraj A, Peake K, Kodam A, Salio C, Merighi A, Vance JE, et al. Increased activity and altered subcellular distribution of lysosomal enzymes determine neuronal vulnerability in Niemann-Pick type C1-deficient mice. Am J Pathol. 2009;175(6):2540-56.
164. Sun CL, Su LD, Li Q, Wang XX, Shen Y. Cerebellar long-term depression is deficient in Niemann-Pick type C disease mice. Cerebellum. 2011;10(1):88-95.
165. Li X, Qin L, Li Y, Yu H, Zhang Z, Tao C, et al. Presynaptic Endosomal Cathepsin D Regulates the Biogenesis of GABAergic Synaptic Vesicles. Cell Rep. 2019;28(4):1015-28 e5.
166. Grunewald B, Lange MD, Werner C, O'Leary A, Weishaupt A, Popp S, et al. Defective synaptic transmission causes disease signs in a mouse model of juvenile neuronal ceroid lipofuscinosis. Elife. 2017;6.
167. Ahrens-Nicklas RC, Tecedor L, Hall AF, Lysenko E, Cohen AS, Davidson BL, et al. Neuronal network dysfunction precedes storage and neurodegeneration in a lysosomal storage disorder. JCI Insight. 2019;4(21).
168. Concolino D, Deodato F, Parini R. Enzyme replacement therapy: efficacy and limitations. Ital J Pediatr. 2018;44(Suppl 2):120.
169. Chen M, Zhang L, Quan S. Enzyme replacement therapy for infantile-onset Pompe disease. Cochrane Database Syst Rev. 2017;11:CD011539.
170. Li M. Enzyme Replacement Therapy: A Review and Its Role in Treating Lysosomal Storage Diseases. Pediatr Ann. 2018;47(5):e191-e7.
171. Coutinho MF, Santos JI, Alves S. Less Is More: Substrate Reduction Therapy for Lysosomal Storage Disorders. Int J Mol Sci. 2016;17(7).
172. Hughes DA, Nicholls K, Shankar SP, Sunder-Plassmann G, Koeller D, Nedd K, et al. Oral pharmacological chaperone migalastat compared with enzyme replacement therapy in Fabry disease: 18-month results from the randomised phase III ATTRACT study. J Med Genet. 2017;54(4):288-96.
173. Hoogerbrugge PM, Brouwer OF, Bordigoni P, Ringden O, Kapaun P, Ortega JJ, et al. Allogeneic bone marrow transplantation for lysosomal storage diseases. The European Group for Bone Marrow Transplantation. Lancet. 1995;345(8962):1398-402.
174. Sergijenko A, Langford-Smith A, Liao AY, Pickford CE, McDermott J, Nowinski G, et al. Myeloid/Microglial driven autologous hematopoietic stem cell gene therapy corrects a neuronopathic lysosomal disease. Mol Ther. 2013;21(10):1938-49.
175. Naldini L, Blomer U, Gallay P, Ory D, Mulligan R, Gage FH, et al. In vivo gene delivery and stable transduction of nondividing cells by a lentiviral vector. Science. 1996;272(5259):263-7.
176. Zufferey R, Dull T, Mandel RJ, Bukovsky A, Quiroz D, Naldini L, et al. Self-inactivating lentivirus vector for safe and efficient in vivo gene delivery. J Virol. 1998;72(12):9873-80.
177. Davidson BL, Breakefield XO. Viral vectors for gene delivery to the nervous system. Nat Rev Neurosci. 2003;4(5):353-64.

178. Biffi A, Montini E, Lorioli L, Cesani M, Fumagalli F, Plati T, et al. Lentiviral hematopoietic stem cell gene therapy benefits metachromatic leukodystrophy. Science. 2013;341(6148):1233158.
179. Holley RJ, Ellison SM, Fil D, O'Leary C, McDermott J, Senthivel N, et al. Macrophage enzyme and reduced inflammation drive brain correction of mucopolysaccharidosis IIIB by stem cell gene therapy. Brain. 2018;141(1):99-116.
180. Gleitz HF, Liao AY, Cook JR, Rowlston SF, Forte GM, D'Souza Z, et al. Brain-targeted stem cell gene therapy corrects mucopolysaccharidosis type II via multiple mechanisms. EMBO Mol Med. 2018;10(7).
181. Biffi A, De Palma M, Quattrini A, Del Carro U, Amadio S, Visigalli I, et al. Correction of metachromatic leukodystrophy in the mouse model by transplantation of genetically modified hematopoietic stem cells. J Clin Invest. 2004;113(8):1118-29.
182. Capotondo A, Milazzo R, Politi LS, Quattrini A, Palini A, Plati T, et al. Brain conditioning is instrumental for successful microglia reconstitution following hematopoietic stem cell transplantation. Proc Natl Acad Sci U S A. 2012;109(37):15018-23.
183. Wilkinson FL, Sergijenko A, Langford-Smith KJ, Malinowska M, Wynn RF, Bigger BW. Busulfan conditioning enhances engraftment of hematopoietic donor-derived cells in the brain compared with irradiation. Mol Ther. 2013;21(4):868-76.
184. Hansen GM, Markesich DC, Burnett MB, Zhu Q, Dionne KM, Richter LJ, et al. Large-scale gene trapping in C57BL/6N mouse embryonic stem cells. Genome Res. 2008;18(10):1670-9.
185. Pan X, De Aragao CBP, Velasco-Martin JP, Priestman DA, Wu HY, Takahashi K, et al. Neuraminidases 3 and 4 regulate neuronal function by catabolizing brain gangliosides. FASEB J. 2017;31(8):3467-83.
186. Feng G, Mellor RH, Bernstein M, Keller-Peck C, Nguyen QT, Wallace M, et al. Imaging neuronal subsets in transgenic mice expressing multiple spectral variants of GFP. Neuron. 2000;28(1):41-51.
187. Tordo J, O'Leary C, Antunes A, Palomar N, Aldrin-Kirk P, Basche M, et al. A novel adeno-associated virus capsid with enhanced neurotropism corrects a lysosomal transmembrane enzyme deficiency. Brain. 2018.
188. Campeau E, Ruhl VE, Rodier F, Smith CL, Rahmberg BL, Fuss JO, et al. A versatile viral system for expression and depletion of proteins in mammalian cells. PLoS One. 2009;4(8):e6529.
189. Trouplin V, Boucherit N, Gorvel L, Conti F, Mottola G, Ghigo E. Bone marrow-derived macrophage production. J Vis Exp. 2013(81):e50966.
190. He BJ, Nolte G, Nagata K, Takano D, Yamazaki T, Fujimaki Y, et al. Abstracts of Presentations at the International Conference on Basic and Clinical Multimodal Imaging (BaCI), a Joint Conference of the International Society for Neuroimaging in Psychiatry (ISNIP), the International Society for Functional Source Imaging (ISFSI), the International Society for Bioelectromagnetism (ISBEM), the International Society for Brain Electromagnetic Topography (ISBET), and the EEG and Clinical Neuroscience Society (ECNS), in Geneva, Switzerland, September 5-8, 2013. Clin EEG Neurosci. 2013.
191. Toni N, Buchs PA, Nikonenko I, Bron CR, Muller D. LTP promotes formation of multiple spine synapses between a single axon terminal and a dendrite. Nature. 1999;402(6760):421-5.
192. Pshezhetsky AV, Richard C, Michaud L, Igdoura S, Wang S, Elsliger MA, et al. Cloning, expression and chromosomal mapping of human lysosomal sialidase and characterization of mutations in sialidosis. Nat Genet. 1997;15(3):316-20.
193. Stavoe AKH, Holzbaur ELF. Axonal autophagy: Mini-review for autophagy in the CNS. Neurosci Lett. 2019;697:17-23.

194. Hunt CA, Schenker LJ, Kennedy MB. PSD-95 is associated with the postsynaptic density and not with the presynaptic membrane at forebrain synapses. J Neurosci. 1996;16(4):1380-8.
195. Whittaker VP, Michaelson IA, Kirkland RJ. The separation of synaptic vesicles from nerve-ending particles ('synaptosomes'). Biochem J. 1964;90(2):293-303.
196. Huang da W, Sherman BT, Lempicki RA. Bioinformatics enrichment tools: paths toward the comprehensive functional analysis of large gene lists. Nucleic Acids Res. 2009;37(1):1-13.
197. Robinson MS. Adaptable adaptors for coated vesicles. Trends Cell Biol. 2004;14(4):167-74.
198. Conroy J, Allen NM, Gorman KM, Shahwan A, Ennis S, Lynch SA, et al. NAPB - a novel SNARE-associated protein for early-onset epileptic encephalopathy. Clin Genet. 2016;89(2):E1-3.
199. Burgalossi A, Jung S, Meyer G, Jockusch WJ, Jahn O, Taschenberger H, et al. SNARE protein recycling by alphaSNAP and betaSNAP supports synaptic vesicle priming. Neuron. 2010;68(3):473-87.
200. D'Arcangelo G, Grossi D, De Chiara G, de Stefano MC, Cortese G, Citro G, et al. Glutamatergic neurotransmission in a mouse model of Niemann-Pick type C disease. Brain Res. 2011;1396:11-9.
201. Sekino Y, Kojima N, Shirao T. Role of actin cytoskeleton in dendritic spine morphogenesis. Neurochem Int. 2007;51(2-4):92-104.
202. Walkley SU, Blakemore WF, Purpura DP. Alterations in neuron morphology in feline mannosidosis. A Golgi study. Acta Neuropathol. 1981;53(1):75-9.
203. Farias GG, Guardia CM, De Pace R, Britt DJ, Bonifacino JS. BORC/kinesin-1 ensemble drives polarized transport of lysosomes into the axon. Proc Natl Acad Sci U S A. 2017;114(14):E2955-E64.
204. Maday S. Mechanisms of neuronal homeostasis: Autophagy in the axon. Brain Res. 2016;1649(Pt B):143-50.
205. Cheng XT, Zhou B, Lin MY, Cai Q, Sheng ZH. Axonal autophagosomes recruit dynein for retrograde transport through fusion with late endosomes. J Cell Biol. 2015;209(3):377-86.
206. Mader KM, Beard H, King BM, Hopwood JJ. Effect of high dose, repeated intra-cerebrospinal fluid injection of sulphamidase on neuropathology in mucopolysaccharidosis type IIIA mice. Genes, brain, and behavior. 2008;7(7):740-53.
207. Bonney DK, O'Meara A, Shabani A, Imrie J, Bigger BW, Jones S, et al. Successful allogeneic bone marrow transplant for Niemann-Pick disease type C2 is likely to be associated with a severe 'graft versus substrate' effect. J Inherit Metab Dis. 2010;33 Suppl 3:S171-3.
208. Krivit W, Sung JH, Shapiro EG, Lockman LA. Microglia: the effector cell for reconstitution of the central nervous system following bone marrow transplantation for lysosomal and peroxisomal storage diseases. Cell transplantation. 1995;4(4):385-92.
209. Cressant A, Desmaris N, Verot L, Brejot T, Froissart R, Vanier MT, et al. Improved behavior and neuropathology in the mouse model of Sanfilippo type IIIB disease after adeno-associated virus-mediated gene transfer in the striatum. J Neurosci. 2004;24(45):10229-39.
210. Ciron C, Desmaris N, Colle MA, Raoul S, Joussemet B, Verot L, et al. Gene therapy of the brain in the dog model of Hurler's syndrome. Ann Neurol. 2006;60(2):204-13.
211. Markakis EA, Vives KP, Bober J, Leichtle S, Leranth C, Beecham J, et al. Comparative transduction efficiency of AAV vector serotypes 1-6 in the substantia nigra and striatum of the primate brain. Molecular therapy : the journal of the American Society of Gene Therapy. 2010;18(3):588-93.

212. Wada R, Tifft CJ, Proia RL. Microglial activation precedes acute neurodegeneration in Sandhoff disease and is suppressed by bone marrow transplantation. Proc Natl Acad Sci U S A. 2000;97(20):10954-9.
213. Derecki NC, Cronk JC, Lu Z, Xu E, Abbott SB, Guyenet PG, et al. Wild-type microglia arrest pathology in a mouse model of Rett syndrome. Nature. 2012;484(7392):105-9.
214. Biffi A, Capotondo A, Fasano S, del Carro U, Marchesini S, Azuma H, et al. Gene therapy of metachromatic leukodystrophy reverses neurological damage and deficits in mice. J Clin Invest. 2006;116(11):3070-82.
215. Corti S, Locatelli F, Donadoni C, Guglieri M, Papadimitriou D, Strazzer S, et al. Wild-type bone marrow cells ameliorate the phenotype of SOD1-G93A ALS mice and contribute to CNS, heart and skeletal muscle tissues. Brain. 2004;127(Pt 11):2518-32.
216. Simard AR, Soulet D, Gowing G, Julien JP, Rivest S. Bone marrow-derived microglia play a critical role in restricting senile plaque formation in Alzheimer's disease. Neuron. 2006;49(4):489-502.
217. Pacienza N, Yoshimitsu M, Mizue N, Au BC, Wang JC, Fan X, et al. Lentivector transduction improves outcomes over transplantation of human HSCs alone in NOD/SCID/Fabry mice. Mol Ther. 2012;20(7):1454-61.
218. Cartier N, Hacein-Bey-Abina S, Bartholomae CC, Veres G, Schmidt M, Kutschera I, et al. Hematopoietic stem cell gene therapy with a lentiviral vector in X-linked adrenoleukodystrophy. Science. 2009;326(5954):818-23.
219. Gosselin D, Rivest S. Immune mechanisms underlying the beneficial effects of autologous hematopoietic stem cell transplantation in multiple sclerosis. Neurotherapeutics. 2011;8(4):643-9.
220. Atkins HL, Freedman MS. Hematopoietic stem cell therapy for multiple sclerosis: top 10 lessons learned. Neurotherapeutics. 2013;10(1):68-76.
221. Sessa M, Lorioli L, Fumagalli F, Acquati S, Redaelli D, Baldoli C, et al. Lentiviral haemopoietic stem-cell gene therapy in early-onset metachromatic leukodystrophy: an ad-hoc analysis of a non-randomised, open-label, phase 1/2 trial. Lancet. 2016;388(10043):476-87.
222. Larochelle A, Bellavance MA, Michaud JP, Rivest S. Bone marrow-derived macrophages and the CNS: An update on the use of experimental chimeric mouse models and bone marrow transplantation in neurological disorders. Biochim Biophys Acta. 2016;1862(3):310-22.
223. Capotondo A, Milazzo R, Garcia-Manteiga JM, Cavalca E, Montepeloso A, Garrison BS, et al. Intracerebroventricular delivery of hematopoietic progenitors results in rapid and robust engraftment of microglia-like cells. Sci Adv. 2017;3(12):e1701211.

Appendix A

List of HGSNAT mutations and their population distribution

Family	Patient	Variants		Origin	Population distribution
		Nucleotide change (cDNA)[a]	Effect on protein[b]		
1	Br1	c.[164T>A];[164T>A]	p.[(L55*)];[(L55*)]	Mogeiro, Paraiba, Brazil	Not yet reported
1	Br2	c.[164T>A];[164T>A]	p.[(L55*)];[(L55*)]	Mogeiro, Paraiba, Brazil	Not yet reported
2	Br3	c.[164T>A];[773A>T]	p.[(L55*)];[N258I]	Alagoa Nova, Paraiba, Brazil	Not yet reported/Not yet reported
3	Br4	c.[525dupT];[773A>T]	p.[(V176fs)];[N258I]	Taperoa, Paraiba, Brazil	Portugal/Not yet reported
4	Br5	c.[525dupT];[773A>T]	p.[(V176fs)];[N258I]	Cabaceiras, Paraiba, Brazil	Portugal/Not yet reported
5	Br6	c.[773A>T];[773A>T]	p.[N258I];[N258I]	Taperoa, Paraiba, Brazil	Not yet reported
6	Br7	c.[773A>T];[773A>T]	p.[N258I];[N258I]	Taperoa, Paraiba, Brazil	Not yet reported
7	Br8	c.[1348delG];[1348delG]	p.[D450fs];[D450fs]	Rio Janeiro, Rio Janeiro, Brazil	Not yet reported
8	Br9	c.[1348delG];[1348delG]	p.[D450fs];[D450fs]	S. Miguel de Campos, Alagoas, Brazil	Not yet reported
9	Br10	c.[1622C>T];[1622C>T]	p.[S541L];[S541L]	Sapiranga, Rio Grande Sul, Brazil	France, Ireland, Poland, Greece, Portugal
10	Br11	c.[1622C>T];[1622C>T]	p.[S541L];[S541L]	Sao Leopoldo, Rio Grande Sul, Brazil	France, Ireland, Poland, Greece, Portugal
11	Br12	c.[234+1G>A;710C>A];[234+1-G>A;710C>A][c]	p.[D40Valfs;P237Q];[D40-Valfs;P237Q]	Sao Paulo, Sao Paulo, Brazil	Spain, Portugal
12	Br13	c.[372−2A>G];[372−2A>G]	p.[R124fs,L125_R128del];[R124fs,-L125_R128del]	Rio Janeiro, Rio Janeiro, Brazil	Spain, Portugal
13	Br14	c.[372−2A>G];[372−2A>G]	p.[R124fs,L125_R128del];[R124fs,-L125_R128del]	Sao Paulo, Sao Paulo, Brazil	Morocco, Tunisia, Turkey, Korea, France, Italy, Spain, Portugal
14	Clb1	c.[372−2A>G];[372-2A>G]	p.[R124fs,L125_R128del];[R124fs,-L125_R128del]	Colombia	Morocco, Tunisia, Turkey, Korea, France, Italia, Spain, Portugal
15	Pt1	c.[234+1G>A;710-C>A][c];[372−2A>G]	p.[D40Valfs;P237Q];[R124fs,-L125_R128del]	Center/North or Center, Portugal	Morocco, Tunisia, Turkey, Korea, France, Italy, Spain, Portugal/Spain, Portugal
16	Alg1	c.[234+1G>A;710C>A];[234+1-G>A;710C>A][c]	p.[D40Valfs;P237Q];[D40-Valfs;P237Q]	Algeria	Spain, Portugal
17	USA1	c.[518G>A];[1267G>T]	p.[G173D];[G423W]	Massachusetts, New England, USA[d]	Turkey/Not yet reported
18	USA2	c.[1250+1G>A];[1466C>A]	p.[(G418*)];[A489E]	Minnesota, USA[e]/California, USA[f]	Poland, Turkey, UK/USA
19	Can1	c.[494−1G>A];[494−1G>A]	see[g]	Eastern Ontario, Canada	Not yet reported
20	Trk1	c.[852−1G>A];[852−1G>A]	p.[(W284*)];[(W284*)]	Turkey	Italy, Turkey
21	Trk2	c.[1030C>T];[1030C>T]	p.[R344C];[p.R344C]	Agri, Turkey	France, UK, Netherlands, Germany, Singapore

Family	Patient	Variants		Origin	Population distribution
		Nucleotide change (cDNA)[a]	Effect on protein[b]		
22	Trk3	c.[1271dupG];[1271dupG]	p.[(I425fs)];[(I425fs)]	Turkey	Greece
22	Trk4[h]	c.[1271dupG];[1271dupG]	p.[(I425fs)];[(I425fs)]	Turkey	Greece
23	Trk5	**c.[1479dupA];[1479dupA]**	**p.[(L494fs)];[(L494fs)]**	Turkey	**Not yet reported**
24	Azb1	c.[1345dupG];[c.1345dupG]	p.[(D449fs)];[(D449fs)]	Baku, Azerbaijan	Canada
25	Irn1	c.[848C>T];[848C>T]	p.[P283L];[P283L]	Isfahan, Iran	France, UK

Note: The novel *HGSNAT* variants detected in the patients are indicated in bold.

cDNA: complementary DNA.

[a]cDNA is numbered according to GenBank Reference sequence NM_152419.2.

[b]The ATG codon corresponds to the first amino acid in accordance with the GenBank protein reference sequence NP_689632.2.

[c]Besides the c.234+1G>A and c.710C>A variants the allele also presents in *cis* the intronic variant c.594-98T>C.

[d]The parent carrying c.518G>A allele has British and French Canadian ancestry and the parent carrying c.1267G>T, Bristish ancestry.

[e]The parent carrying c.1250+1G>A has British and German ancestry.

[f]The parent carrying the c.1466C>A allele has German, Swedish, Dutch, and British ancestry.

[g]p.[P165_L187delinsQSCYVTQAGVRWHHLGSLQALPPGFTPFSYLSLLSSWNC,P165fs].

[h]The patients Trk3 and Trk4 are siblings and have consanguineous parents. Molecular analysis was not performed for Trk4.

Appendix B

List of proteins reduced in the synaptosomes of 3 months old MPS IIIC mice detected by LC/MS

#	Identified Proteins	Alternate ID	T-Test (p-value): (p < 0.05)	Exclusive Unique Peptide Counts					
				KO S1	KO S2	KO S3	WT S1	WT S2	WT S3
1	Sodium/potassium-transporting ATPase subunit alpha OS=Mus musculus GN=Atp1a3 PE=1 SV=1	Atp1a3	0.013	27	30	37	46	50	50
2	Clathrin heavy chain 1 OS=Mus musculus GN=Cltc PE=1 SV=3	Cltc	0.0066	19	24	28	33	37	34
3	Excitatory amino acid transporter 2 OS=Mus musculus GN=Slc1a2 PE=1 SV=1	Slc1a2	0.024	9	9	13	13	13	14
4	Syntaxin-binding protein 1 OS=Mus musculus GN=Stxbp1 PE=1 SV=2	Stxbp1	0.0046	15	22	25	33	37	39
5	Sodium/potassium-transporting ATPase subunit alpha-2 OS=Mus musculus GN=Atp1a2 PE=1 SV=1	Atp1a2	0.049	12	15	18	23	27	22
6	Fructose-bisphosphate aldolase C OS=Mus musculus GN=Aldoc PE=1 SV=4	Aldoc	0.01	11	10	8	13	15	11
7	Fructose-bisphosphate aldolase A OS=Mus musculus GN=Aldoa PE=1 SV=2	Aldoa	0.035	16	9	16	18	24	18
8	Malate dehydrogenase, mitochondrial OS=Mus musculus GN=Mdh2 PE=1 SV=3	Mdh2	0.035	4	19	16	24	31	27
9	Dynamin-1 OS=Mus musculus GN=Dnm1 PE=1 SV=1	Dnm1	0.0012	16	16	16	28	24	27
10	Aconitate hydratase, mitochondrial OS=Mus musculus GN=Aco2 PE=1 SV=1	Aco2	0.023	0	17	17	24	28	27
11	Vesicle-fusing ATPase OS=Mus musculus GN=Nsf PE=1 SV=2	Nsf	0.04	12	12	13	16	22	17
12	Spectrin alpha chain, non-erythrocytic 1 OS=Mus musculus GN=Sptan1 PE=1 SV=1	Sptan1	0.047	1	10	17	17	31	27
13	Calcium/calmodulin-dependent protein kinase type II subunit alpha OS=Mus musculus GN=Camk2a PE=1 SV=2	Camk2a	0.0067	13	11	14	15	17	17
14	Neural cell adhesion molecule 1 OS=Mus musculus GN=Ncam1 PE=1 SV=3	Ncam1	0.0063	9	9	12	14	13	14

15	Spectrin beta chain, non-erythrocytic 1 OS=Mus musculus GN=Sptbn1 PE=1 SV=2	Sptbn1	0.0046	11	8	12	17	21	22
16	Hexokinase 1, isoform CRA_f OS=Mus musculus GN=Hk1 PE=1 SV=1	Hk1	0.024	2	11	12	14	15	18
17	60 kDa heat shock protein, mitochondrial OS=Mus musculus GN=Hspd1 PE=1 SV=1	Hspd1	0.0065	0	10	13	18	17	20
18	Serine/threonine-protein phosphatase 2A 65 kDa regulatory subunit A alpha isoform OS=Mus musculus GN=Ppp2r1a PE=1 SV=3	Ppp2r1a	0.008	8	3	8	9	9	9
19	Calcium-dependent secretion activator 1 OS=Mus musculus GN=Cadps PE=1 SV=3	Cadps	0.025	7	6	6	8	9	8
20	Stress-70 protein, mitochondrial OS=Mus musculus GN=Hspa9 PE=1 SV=3	Hspa9	0.021	0	7	7	13	16	17
21	Ankyrin-2 OS=Mus musculus GN=Ank2 PE=1 SV=2	Ank2	0.0054	7	8	9	14	20	16
22	Contactin-1 OS=Mus musculus GN=Cntn1 PE=1 SV=1	Cntn1	0.01	4	4	7	9	11	9
23	Synaptosomal-associated protein 25 OS=Mus musculus GN=Snap25 PE=1 SV=1	Snap25	0.023	3	6	8	8	10	10
24	Cytochrome c, somatic OS=Mus musculus GN=Cycs PE=1 SV=2	Cycs	0.0096	0	4	5	7	8	7
25	Calcium-binding mitochondrial carrier protein Aralar1 OS=Mus musculus GN=Slc25a12 PE=1 SV=1	Slc25a12	0.025	0	5	6	11	9	12
26	Cytochrome b-c1 complex subunit 1, mitochondrial OS=Mus musculus GN=Uqcrc1 PE=1 SV=2	Uqcrc1	0.02	0	5	7	8	7	8
27	Pyruvate dehydrogenase E1 component subunit beta, mitochondrial OS=Mus musculus GN=Pdhb PE=1 SV=1	Pdhb	0.045	0	6	9	9	10	7
28	AP-2 complex subunit alpha-2 OS=Mus musculus GN=Ap2a2 PE=1 SV=2	Ap2a2	0.0064	3	2	3	8	5	9
29	Beta-soluble NSF attachment protein OS=Mus musculus GN=Napb PE=1 SV=2	Napb	0.0011	2	3	4	5	6	5
30	Dynamin-like 120 kDa protein, mitochondrial OS=Mus musculus GN=Opa1 PE=1 SV=1	Opa1	0.02	0	7	8	11	13	11
31	2',3'-cyclic-nucleotide 3'-phosphodiesterase OS=Mus musculus GN=Cnp PE=1 SV=3	Cnp	0.017	1	3	4	6	7	10
32	Isocitrate dehydrogenase [NAD] subunit gamma 1, mitochondrial OS=Mus musculus GN=Idh3g PE=1 SV=1	Idh3g	0.026	0	2	1	5	6	6

33	Neurofilament 3, medium OS=Mus musculus GN=Nefm PE=1 SV=1	Nefm	0.027	4	1	4	4	8	8
34	ATP synthase subunit O, mitochondrial OS=Mus musculus GN=Atp5o PE=1 SV=1	Atp5o	0.031	0	6	5	8	8	9
35	ProSAAS OS=Mus musculus GN=Pcsk1n PE=1 SV=2	Pcsk1n	0.018	2	2	3	5	3	5
36	Dihydrolipoyllysine-residue acetyltransferase component of pyruvate dehydrogenase complex, mitochondrial OS=Mus musculus GN=Dlat PE=1 SV=2	Dlat	0.024	0	4	5	8	7	8
37	NADH dehydrogenase [ubiquinone] 1 alpha subcomplex subunit 9, mitochondrial OS=Mus musculus GN=Ndufa9 PE=1 SV=1	Ndufa9	0.0052	0	3	4	7	8	9
38	AP-2 complex subunit beta OS=Mus musculus GN=Ap2b1 PE=1 SV=1	Ap2b1	0.045	3	0	6	10	8	7
39	Fumarate hydratase, mitochondrial OS=Mus musculus GN=Fh PE=1 SV=3	Fh	0.027	1	3	5	7	8	9
40	Septin-7 OS=Mus musculus GN=Sept7 PE=1 SV=2	7-Sep	0.024	4	4	6	8	8	7
41	Cytochrome b-c1 complex subunit 2, mitochondrial OS=Mus musculus GN=Uqcrc2 PE=1 SV=1	Uqcrc2	0.0052	0	3	4	7	8	6
42	N(G),N(G)-dimethylarginine dimethylaminohydrolase 1 OS=Mus musculus GN=Ddah1 PE=1 SV=3	Ddah1	0.024	2	2	2	3	3	3
43	Peroxiredoxin-5, mitochondrial OS=Mus musculus GN=Prdx5 PE=1 SV=2	Prdx5	0.029	0	4	1	4	5	6
44	Succinate--CoA ligase [ADP-forming] subunit beta, mitochondrial OS=Mus musculus GN=Sucla2 PE=1 SV=2	Sucla2	0.021	0	2	6	8	9	12
45	Septin-11 OS=Mus musculus GN=Sept11 PE=1 SV=1	11-Sep	0.019	2	4	4	6	8	7
46	Reticulon-4 OS=Mus musculus GN=Rtn4 PE=1 SV=2	Rtn4	0.008	2	2	2	5	5	5
47	AP-2 complex subunit mu OS=Mus musculus GN=Ap2m1 PE=1 SV=1	Ap2m1	0.0062	3	0	2	4	4	4
48	Inositol 1,4,5-trisphosphate receptor type 1 OS=Mus musculus GN=Itpr1 PE=1 SV=2	Itpr1	0.019	2	3	4	7	11	10
49	Isocitrate dehydrogenase [NAD] subunit, mitochondrial OS=Mus musculus GN=Idh3b PE=1 SV=1	Idh3b	0.0094	0	4	3	9	8	11
50	Prohibitin OS=Mus musculus GN=Phb PE=1 SV=1	Phb	0.041	0	2	7	8	9	8
51	NADH dehydrogenase [ubiquinone] flavoprotein 1, mitochondrial OS=Mus musculus GN=Ndufv1 PE=1 SV=1	Ndufv1	0.024	0	3	4	6	10	9

52	Glutamate decarboxylase 2 OS=Mus musculus GN=Gad2 PE=1 SV=1	Gad2	0.00039	3	1	2	5	6	4
53	AP-2 complex subunit alpha-1 OS=Mus musculus GN=Ap2a1 PE=1 SV=1	Ap2a1	0.039	5	2	3	2	4	1
54	NADH dehydrogenase [ubiquinone] 1 alpha subcomplex subunit 10, mitochondrial OS=Mus musculus GN=Ndufa10 PE=1 SV=1	Ndufa10	0.02	0	3	5	6	7	9
55	Acyl-CoA-binding protein OS=Mus musculus GN=Dbi PE=1 SV=2	Dbi	0.011	0	0	2	2	2	2
56	V-type proton ATPase subunit E 1 OS=Mus musculus GN=Atp6v1e1 PE=1 SV=2	Atp6v1e1	0.041	3	0	2	2	4	5
57	Tropomyosin 1, alpha, isoform CRA_i OS=Mus musculus GN=Tpm1 PE=1 SV=1	Tpm1	0.039	0	1	1	4	3	5
58	Plasma membrane calcium-transporting ATPase 1 OS=Mus musculus GN=Atp2b1 PE=1 SV=1	Atp2b1	0.013	2	2	2	6	7	4
59	Alpha actinin 1a OS=Mus musculus GN=Actn1 PE=1 SV=1	Actn1	0.0079	2	1	2	4	5	5
60	Cytochrome c oxidase subunit 5A, mitochondrial OS=Mus musculus GN=Cox5a PE=1 SV=2	Cox5a	0.023	1	2	1	3	4	5
61	Mitochondrial import receptor subunit TOM70 OS=Mus musculus GN=Tomm70 PE=1 SV=2	Tomm70	0.028	0	2	3	7	7	2
62	Dihydrolipoyllysine-residue succinyltransferase component of 2-oxoglutarate dehydrogenase complex, mitochondrial OS=Mus musculus GN=Dlst PE=1 SV=1	Dlst	0.01	0	2	2	3	5	5
63	Calretinin OS=Mus musculus GN=Calb2 PE=1 SV=3	Calb2	0.019	0	0	0	3	3	2
64	Aldehyde dehydrogenase, mitochondrial OS=Mus musculus GN=Aldh2 PE=1 SV=1	Aldh2	0.028	0	3	4	7	7	6
65	Catenin alpha-2 OS=Mus musculus GN=Ctnna2 PE=1 SV=3	Ctnna2	0.047	0	3	4	6	9	4
66	Synaptophysin OS=Mus musculus GN=Syp PE=1 SV=2	Syp	0.022	0	1	1	2	3	3
67	LETM1 and EF-hand domain-containing protein 1, mitochondrial OS=Mus musculus GN=Letm1 PE=1 SV=1	Letm1	0.031	0	3	1	4	7	7
68	Anion exchange protein OS=Mus musculus GN=Slc4a4 PE=1 SV=1	Slc4a4	0.0065	0	0	0	4	6	3
69	Ras-related protein Rab-7a OS=Mus musculus GN=Rab7a PE=1 SV=2	Rab7a	0.018	0	2	1	2	3	3
70	Alpha-internexin OS=Mus musculus GN=Ina PE=1 SV=3	Ina	0.0092	0	0	1	4	6	6
71	Septin-5 OS=Mus musculus GN=Sept5 PE=1 SV=2	5-Sep	0.044	0	0	3	3	2	3

72	AP-1 complex subunit beta-1 OS=Mus musculus GN=Ap1b1 PE=1 SV=2	Ap1b1	0.044	2	2	2	2	3	2
73	Disks large homolog 4 OS=Mus musculus GN=Dlg4 PE=1 SV=1	Dlg4	0.021	0	1	2	4	5	7
74	Elongation factor 1-beta OS=Mus musculus GN=Eef1b PE=1 SV=5	Eef1b	0.016	1	0	1	1	1	1
75	NADH dehydrogenase [ubiquinone] iron-sulfur protein 7, mitochondrial OS=Mus musculus GN=Ndufs7 PE=1 SV=1	Ndufs7	0.024	0	2	1	3	2	3
76	Cytochrome b-c1 complex subunit 6, mitochondrial OS=Mus musculus GN=Uqcrh PE=1 SV=2	Uqcrh	0.018	0	1	1	2	2	2
77	Serine/threonine-protein phosphatase 2A catalytic subunit alpha isoform OS=Mus musculus GN=Ppp2ca PE=1 SV=1	Ppp2ca	0.016	1	0	1	2	2	2
78	NADH dehydrogenase [ubiquinone] 1 alpha subcomplex subunit 8 OS=Mus musculus GN=Ndufa8 PE=1 SV=3	Ndufa8	0.016	0	0	1	3	4	2
79	Protein disulfide-isomerase A6 OS=Mus musculus GN=Pdia6 PE=1 SV=1	Pdia6	0.0075	1	1	1	1	1	1
80	Actin-related protein 3 OS=Mus musculus GN=Actr3 PE=1 SV=3	Actr3	0.0021	0	1	0	4	3	2
81	Neuroligin-2 OS=Mus musculus GN=Nlgn2 PE=1 SV=2	Nlgn2	0.018	0	1	1	3	4	5
82	Dynamin-3 OS=Mus musculus GN=Dnm3 PE=1 SV=1	Dnm3	0.018	0	1	0	4	6	4
83	Rho-related GTP-binding protein RhoB OS=Mus musculus GN=Rhob PE=1 SV=1	Rhob	0.035	0	1	2	3	3	2
84	Importin subunit beta-1 OS=Mus musculus GN=Kpnb1 PE=1 SV=2	Kpnb1	0.00056	0	0	0	2	4	3
85	Methylmalonate-semialdehyde dehydrogenase [acylating], mitochondrial OS=Mus musculus GN=Aldh6a1 PE=1 SV=1	Aldh6a1	0.023	0	1	1	5	2	5
86	Voltage-dependent anion-selective channel protein 1 OS=Mus musculus GN=Vdac1 PE=1 SV=3	Vdac1	0.04	0	0	0	1	3	4
87	NADH dehydrogenase [ubiquinone] iron-sulfur protein 5 OS=Mus musculus GN=Ndufs5 PE=1 SV=3	Ndufs5	0.0048	0	0	1	2	3	3
88	Serine/threonine-protein phosphatase PP1-gamma catalytic subunit OS=Mus musculus GN=Ppp1cc PE=1 SV=1	Ppp1cc	0.047	1	1	0	2	3	4
89	Anion exchange protein OS=Mus musculus GN=Slc4a10 PE=1 SV=1	Slc4a10	0.018	0	1	0	6	3	4
90	Cytochrome b-c1 complex subunit 10 OS=Mus musculus GN=Uqcr11 PE=3 SV=1	Uqcr11	0.0061	0	2	0	2	2	2

91	Cytosolic non-specific dipeptidase OS=Mus musculus GN=Cndp2 PE=1 SV=1	Cndp2	0.013	1	1	0	1	2	3
92	V-type proton ATPase subunit G 2 OS=Mus musculus GN=Atp6v1g2 PE=1 SV=1	Atp6v1g2	0.013	0	1	1	2	1	2
93	F-actin-capping protein subunit alpha-2 OS=Mus musculus GN=Capza2 PE=1 SV=3	Capza2	0.0078	0	0	1	1	2	1
94	Superoxide dismutase [Mn], mitochondrial OS=Mus musculus GN=Sod2 PE=1 SV=3	Sod2	0.029	0	0	2	3	2	4
95	Electron transfer flavoprotein subunit beta OS=Mus musculus GN=Etfb PE=1 SV=3	Etfb	0.016	0	1	2	3	2	3
96	Casein kinase II subunit alpha OS=Mus musculus GN=Csnk2a1 PE=1 SV=2	Csnk2a1	0.016	0	0	0	2	3	1
97	MAGUK p55 subfamily member 2 OS=Mus musculus GN=Mpp2 PE=1 SV=1	Mpp2	0.016	0	0	2	3	2	3
98	Glycerol-3-phosphate dehydrogenase, mitochondrial OS=Mus musculus GN=Gpd2 PE=1 SV=2	Gpd2	0.033	0	0	1	3	4	2
99	Type I inositol 3,4-bisphosphate 4-phosphatase OS=Mus musculus GN=Inpp4a PE=1 SV=2	Inpp4a	0.0075	1	1	1	3	2	2
100	Glia maturation factor beta OS=Mus musculus GN=Gmfb PE=1 SV=3	Gmfb	0.025	0	0	0	2	1	2
101	Homer protein homolog 1 OS=Mus musculus GN=Homer1 PE=1 SV=1	Homer1	0.0065	0	0	0	1	2	2
102	NADH dehydrogenase [ubiquinone] 1 beta subcomplex subunit 10 (Fragment) OS=Mus musculus GN=Ndufb10 PE=1 SV=1	Ndufb10	0.0022	0	1	1	1	2	2
103	NADH dehydrogenase [ubiquinone] iron-sulfur protein 2, mitochondrial OS=Mus musculus GN=Ndufs2 PE=1 SV=1	Ndufs2	0.0078	0	0	1	2	2	2
104	Glutamate receptor 2 OS=Mus musculus GN=Gria2 PE=1 SV=1	Gria2	0.024	0	1	1	2	3	2
105	Metaxin-2 OS=Mus musculus GN=Mtx2 PE=1 SV=1	Mtx2	0.0031	0	1	0	3	3	3
106	Complement component 1 Q subcomponent-binding protein, mitochondrial OS=Mus musculus GN=C1qbp PE=1 SV=1	C1qbp	0.0065	0	0	0	2	2	2
107	Mitochondrial import receptor subunit TOM22 homolog OS=Mus musculus GN=Tomm22 PE=1 SV=3	Tomm22	0.0023	0	0	0	1	2	1
108	Basigin OS=Mus musculus GN=Bsg PE=1 SV=2	Bsg	0.0075	0	1	0	2	2	2

109	Arf-GAP with GTPase, ANK repeat and PH domain-containing protein 2 OS=Mus musculus GN=Agap2 PE=1 SV=1	Agap2	0.026	0	0	0	1	2	2
110	Dynamin-1 OS=Mus musculus GN=Dnm1 PE=1 SV=2	Dnm1	0.016	0	0	1	1	1	1
111	MCG10748, isoform CRA_b OS=Mus musculus GN=Rap1a PE=1 SV=1	Rap1a	0.024	0	1	1	2	3	2
112	Microtubule-associated protein RP/EB family member 3 OS=Mus musculus GN=Mapre3 PE=1 SV=1	Mapre3	0.0022	0	0	0	2	1	2
113	Serine/threonine-protein phosphatase 2A 56 kDa regulatory subunit epsilon isoform OS=Mus musculus GN=Ppp2r5e PE=1 SV=3	Ppp2r5e	0.0075	0	0	1	1	1	1
114	V-type proton ATPase subunit D OS=Mus musculus GN=Atp6v1d PE=1 SV=1	Atp6v1d	0.0022	0	0	0	2	1	1
115	Ras-related protein Rab-3C OS=Mus musculus GN=Rab3c PE=1 SV=1	Rab3c	0.034	0	1	0	1	2	2
116	Protein tweety homolog OS=Mus musculus GN=Ttyh1 PE=1 SV=1	Ttyh1	0.016	0	1	1	1	1	1
117	ADP-ribosylation factor-like protein 3 OS=Mus musculus GN=Arl3 PE=1 SV=1	Arl3	0.0075	0	0	0	1	1	1
118	Disks large homolog 2 OS=Mus musculus GN=Dlg2 PE=1 SV=2	Dlg2	0.0065	0	0	0	3	1	2
119	Voltage-dependent calcium channel subunit alpha-2/delta-1 OS=Mus musculus GN=Cacna2d1 PE=1 SV=1	Cacna2d1	0.013	0	0	1	2	3	2
120	Histone H1.0 OS=Mus musculus GN=H1f0 PE=2 SV=4	H1f0	0.0013	0	0	0	2	1	2
121	ERC protein 2 OS=Mus musculus GN=Erc2 PE=1 SV=2	Erc2	0.016	0	0	0	1	2	1
122	CB1 cannabinoid receptor-interacting protein 1 OS=Mus musculus GN=Cnrip1 PE=1 SV=1	Cnrip1	0.0022	0	0	0	1	2	2
123	Disks large-associated protein 2 OS=Mus musculus GN=Dlgap2 PE=1 SV=2	Dlgap2	0.016	0	0	0	1	2	1
124	Zinc transporter 9 OS=Mus musculus GN=Slc30a9 PE=1 SV=2	Slc30a9	0.016	0	0	0	1	2	1
125	Neuronal pentraxin-1 OS=Mus musculus GN=Nptx1 PE=1 SV=1	Nptx1	0.016	0	0	0	1	1	1
126	Syntaxin-binding protein 5 OS=Mus musculus GN=Stxbp5 PE=1 SV=1	Stxbp5	0.0075	0	0	0	1	2	2

127	3-ketoacyl-CoA thiolase, mitochondrial OS=Mus musculus GN=Acaa2 PE=1 SV=3	Acaa2	0.0075	0	0	0	2	2	1
128	Atlastin-2 OS=Mus musculus GN=Atl2 PE=1 SV=1	Atl2	0.0075	0	0	0	1	1	1
129	WD repeat-containing protein 7 OS=Mus musculus GN=Wdr7 PE=1 SV=3	Wdr7	0.016	0	0	0	1	2	1
130	Tetratricopeptide repeat protein 7B OS=Mus musculus GN=Ttc7b PE=1 SV=1	Ttc7b	0.016	0	0	0	2	1	1
131	Glutamate receptor 4 OS=Mus musculus GN=Gria4 PE=1 SV=1	Gria4	0.016	0	0	0	1	1	1
132	NADP-dependent malic enzyme, mitochondrial OS=Mus musculus GN=Me3 PE=1 SV=2	Me3	0.016	0	0	0	1	1	1
133	Microsomal glutathione S-transferase 3 OS=Mus musculus GN=Mgst3 PE=1 SV=1	Mgst3	0.016	0	0	0	1	1	1

Appendix C

List of proteins reduced in the synaptosomes of 6 months old MPS IIIC mice detected by LC/MS

#	Identified Proteins	Alternate ID	T-Test (p-value): (p < 0.05)	Exclusive Unique Peptide Counts					
				KO S4	KO S5	KO S6	WT S4	WT S5	WT S6
1	Sodium/potassium-transporting ATPase subunit alpha OS=Mus musculus GN=Atp1a3 PE=1 SV=1	Atp1a3	0.0015	46	52	57	54	59	62
2	Synapsin-1 OS=Mus musculus GN=Syn1 PE=1 SV=2	Syn1	< 0.00010	24	24	21	39	39	40
3	Aconitate hydratase, mitochondrial OS=Mus musculus GN=Aco2 PE=1 SV=1	Aco2	< 0.00010	13	9	13	64	59	61
4	Syntaxin-binding protein 1 OS=Mus musculus GN=Stxbp1 PE=1 SV=2	Stxbp1	0.0001	23	20	24	41	47	46
5	Dynamin-1 OS=Mus musculus GN=Dnm1 PE=1 SV=1	Dnm1	0.0046	43	41	33	53	53	54
6	Clathrin heavy chain 1 OS=Mus musculus GN=Cltc PE=1 SV=3	Cltc	0.0013	27	31	21	41	50	50
7	Fructose-bisphosphate aldolase A OS=Mus musculus GN=Aldoa PE=1 SV=2	Aldoa	0.00075	23	20	24	25	31	31
8	Brain acid soluble protein 1 OS=Mus musculus GN=Basp1 PE=1 SV=3	Basp1	< 0.00010	13	12	14	28	28	35
9	ATP synthase subunit beta, mitochondrial OS=Mus musculus GN=Atp5b PE=1 SV=2	Atp5b	< 0.00010	3	3	4	20	22	25
10	Microtubule-associated protein 6 OS=Mus musculus GN=Map6 PE=1 SV=2	Map6	0.00026	24	19	19	27	24	34
11	Vesicle-fusing ATPase OS=Mus musculus GN=Nsf PE=1 SV=2	Nsf	0.00048	28	26	27	29	30	31
12	Myelin basic protein (Fragment) OS=Mus musculus GN=Mbp PE=1 SV=1	Mbp	0.05	20	0	0	18	21	23
13	Glutamate dehydrogenase 1, mitochondrial OS=Mus musculus GN=Glud1 PE=1 SV=1	Glud1	< 0.00010	3	3	2	29	33	35
14	Excitatory amino acid transporter 2 OS=Mus musculus GN=Slc1a2 PE=1 SV=1	Slc1a2	0.0024	12	10	14	17	19	20

15	Hexokinase 1, isoform CRA_f OS=Mus musculus GN=Hk1 PE=1 SV=1	Hk1	< 0.00010	9	9	12	33	33	34
16	Spectrin alpha chain, non-erythrocytic 1 OS=Mus musculus GN=Sptan1 PE=1 SV=1	Sptan1	0.0059	1	28	24	45	42	47
17	Guanine nucleotide-binding protein G(o) subunit alpha OS=Mus musculus GN=Gnao1 PE=1 SV=3	Gnao1	0.0005	16	20	20	27	24	23
18	Sodium/potassium-transporting ATPase subunit alpha-2 OS=Mus musculus GN=Atp1a2 PE=1 SV=1	Atp1a2	0.00038	19	20	23	34	42	35
19	ATP synthase subunit alpha, mitochondrial OS=Mus musculus GN=Atp5a1 PE=1 SV=1	Atp5a1	< 0.00010	1	1	2	28	31	36
20	Synapsin-2 OS=Mus musculus GN=Syn2 PE=1 SV=2	Syn2	< 0.00010	11	10	9	20	20	22
21	Neuromodulin OS=Mus musculus GN=Gap43 PE=1 SV=1	Gap43	0.00071	17	12	14	21	17	20
22	Calcium/calmodulin-dependent protein kinase type II subunit alpha OS=Mus musculus GN=Camk2a PE=1 SV=2	Camk2a	0.018	20	15	13	19	16	17
23	14-3-3 protein zeta/delta OS=Mus musculus GN=Ywhaz PE=1 SV=1	Ywhaz	0.00029	14	14	13	16	15	16
24	Malate dehydrogenase, mitochondrial OS=Mus musculus GN=Mdh2 PE=1 SV=3	Mdh2	< 0.00010	0	0	0	27	29	31
25	60 kDa heat shock protein, mitochondrial OS=Mus musculus GN=Hspd1 PE=1 SV=1	Hspd1	< 0.00010	4	3	3	28	23	32
26	Citrate synthase, mitochondrial OS=Mus musculus GN=Cs PE=1 SV=1	Cs	< 0.00010	3	3	3	31	28	30
27	Ras-related protein Rab-3A OS=Mus musculus GN=Rab3a PE=1 SV=1	Rab3a	0.0087	14	16	17	15	14	15
28	Syntaxin-1B OS=Mus musculus GN=Stx1b PE=1 SV=1	Stx1b	< 0.00010	10	8	11	20	22	21
29	Microtubule-associated protein OS=Mus musculus GN=Mapt PE=1 SV=1	Mapt	0.034	20	20	15	19	17	20
30	Synaptosomal-associated protein 25 OS=Mus musculus GN=Snap25 PE=1 SV=1	Snap25	< 0.00010	14	14	12	17	17	16
31	Protein kinase C and casein kinase substrate in neurons protein 1 OS=Mus musculus GN=Pacsin1 PE=1 SV=1	Pacsin1	0.023	25	25	21	23	18	23
32	Cell cycle exit and neuronal differentiation protein 1 OS=Mus musculus GN=Cend1 PE=1 SV=1	Cend1	0.00022	10	8	7	19	20	21

33	V-type proton ATPase catalytic subunit A OS=Mus musculus GN=Atp6v1a PE=1 SV=2	Atp6v1a	0.039	13	14	13	15	14	18
34	Creatine kinase U-type, mitochondrial OS=Mus musculus GN=Ckmt1 PE=1 SV=1	Ckmt1	0.0014	3	3	3	27	19	23
35	NADH-ubiquinone oxidoreductase 75 kDa subunit, mitochondrial OS=Mus musculus GN=Ndufs1 PE=1 SV=2	Ndufs1	< 0.00010	0	0	1	28	28	31
36	Protein bassoon OS=Mus musculus GN=Bsn PE=1 SV=4	Bsn	< 0.00010	1	0	1	46	45	48
37	Pyruvate dehydrogenase E1 component subunit beta, mitochondrial OS=Mus musculus GN=Pdhb PE=1 SV=1	Pdhb	< 0.00010	1	0	0	17	18	17
38	Endophilin-A1 OS=Mus musculus GN=Sh3gl2 PE=1 SV=1	Sh3gl2	0.007	11	16	11	12	12	14
39	Acetyl-CoA acetyltransferase, mitochondrial OS=Mus musculus GN=Acat1 PE=1 SV=1	Acat1	< 0.00010	0	0	0	19	19	22
40	Vesicle-associated membrane protein 2 OS=Mus musculus GN=Vamp2 PE=1 SV=1	Vamp2	0.0026	11	9	11	10	11	11
41	Calcium-binding mitochondrial carrier protein Aralar1 OS=Mus musculus GN=Slc25a12 PE=1 SV=1	Slc25a12	0.00045	0	0	0	23	22	27
42	2-oxoglutarate dehydrogenase, mitochondrial OS=Mus musculus GN=Ogdh PE=1 SV=3	Ogdh	0.00015	1	1	1	23	26	30
43	Sodium/potassium-transporting ATPase subunit alpha-1 OS=Mus musculus GN=Atp1a1 PE=1 SV=1	Atp1a1	0.0005	12	12	12	14	18	16
44	MICOS complex subunit Mic60 OS=Mus musculus GN=Immt PE=1 SV=1	Immt	< 0.00010	0	0	0	28	31	34
45	Septin-7 OS=Mus musculus GN=Sept7 PE=1 SV=2	7-Sep	< 0.00010	9	8	7	20	23	18
46	Calcium/calmodulin-dependent protein kinase type II subunit beta OS=Mus musculus GN=Camk2b PE=1 SV=2	Camk2b	0.029	13	14	9	16	14	16
47	Stress-70 protein, mitochondrial OS=Mus musculus GN=Hspa9 PE=1 SV=3	Hspa9	< 0.00010	0	0	0	24	24	27
48	4-aminobutyrate aminotransferase, mitochondrial OS=Mus musculus GN=Abat PE=1 SV=1	Abat	< 0.00010	0	0	0	17	22	21
49	Pyruvate dehydrogenase E1 component subunit alpha, somatic form, mitochondrial OS=Mus musculus GN=Pdha1 PE=1 SV=1	Pdha1	< 0.00010	0	0	0	20	15	19

50	Neural cell adhesion molecule 1 OS=Mus musculus GN=Ncam1 PE=1 SV=3	Ncam1	< 0.00010	0	0	0	20	22	21
51	ADP/ATP translocase 1 OS=Mus musculus GN=Slc25a4 PE=1 SV=4	Slc25a4	< 0.00010	0	0	0	22	20	22
52	Peroxiredoxin-5, mitochondrial OS=Mus musculus GN=Prdx5 PE=1 SV=2	Prdx5	0.00032	8	5	5	12	13	15
53	Beta-soluble NSF attachment protein OS=Mus musculus GN=Napb PE=1 SV=2	Napb	0.00049	11	7	9	14	15	15
54	Ankyrin-2 OS=Mus musculus GN=Ank2 PE=1 SV=2	Ank2	0.00016	6	3	1	31	37	31
55	Isocitrate dehydrogenase [NAD] subunit gamma 1, mitochondrial OS=Mus musculus GN=Idh3g PE=1 SV=1	Idh3g	0.00097	0	0	0	10	14	13
56	Isocitrate dehydrogenase [NAD] subunit, mitochondrial OS=Mus musculus GN=Idh3b PE=1 SV=1	Idh3b	0.00012	0	0	0	13	17	22
57	Myc box-dependent-interacting protein 1 OS=Mus musculus GN=Bin1 PE=1 SV=1	Bin1	0.0013	9	8	5	12	13	15
58	ATP-dependent 6-phosphofructokinase, muscle type OS=Mus musculus GN=Pfkm PE=1 SV=3	Pfkm	0.014	9	5	9	15	14	21
59	Glutaminase kidney isoform, mitochondrial OS=Mus musculus GN=Gls PE=1 SV=1	Gls	< 0.00010	0	0	0	13	14	17
60	Isocitrate dehydrogenase [NAD] subunit alpha, mitochondrial OS=Mus musculus GN=Idh3a PE=1 SV=1	Idh3a	< 0.00010	0	0	0	17	15	20
61	Pyruvate carboxylase OS=Mus musculus GN=Pcx PE=1 SV=1	Pcx	< 0.00010	0	0	0	18	19	20
62	Excitatory amino acid transporter 1 OS=Mus musculus GN=Slc1a3 PE=1 SV=2	Slc1a3	0.0019	3	0	5	9	9	8
63	Elongation factor Tu, mitochondrial OS=Mus musculus GN=Tufm PE=1 SV=1	Tufm	< 0.00010	0	0	0	16	19	19
64	ATPase inhibitor, mitochondrial OS=Mus musculus GN=Atpif1 PE=1 SV=2	Atpif1	0.0019	2	2	0	8	10	10
65	Succinate--CoA ligase [ADP-forming] subunit beta, mitochondrial OS=Mus musculus GN=Sucla2 PE=1 SV=2	Sucla2	< 0.00010	0	0	0	14	13	14
66	Succinyl-CoA:3-ketoacid coenzyme A transferase 1, mitochondrial OS=Mus musculus GN=Oxct1 PE=1 SV=1	Oxct1	0.00099	1	0	0	17	18	18

67	V-type proton ATPase subunit H OS=Mus musculus GN=Atp6v1h PE=1 SV=1	Atp6v1h	0.042	10	9	9	9	8	9
68	Glutathione S-transferase Mu 1 OS=Mus musculus GN=Gstm1 PE=1 SV=2	Gstm1	0.03	6	5	9	11	8	11
69	Sarcoplasmic/endoplasmic reticulum calcium ATPase 2 OS=Mus musculus GN=Atp2a2 PE=1 SV=2	Atp2a2	0.0016	11	11	12	16	16	16
70	NADH dehydrogenase [ubiquinone] flavoprotein 1, mitochondrial OS=Mus musculus GN=Ndufv1 PE=1 SV=1	Ndufv1	< 0.00010	0	0	0	12	13	14
71	Alpha-synuclein OS=Mus musculus GN=Snca PE=1 SV=2	Snca	0.0064	4	6	9	7	6	5
72	Mitochondrial import receptor subunit TOM70 OS=Mus musculus GN=Tomm70 PE=1 SV=2	Tomm70	< 0.00010	0	0	0	15	14	16
73	Protein piccolo OS=Mus musculus GN=Pclo PE=1 SV=4	Pclo	0.0014	1	1	0	23	30	22
74	14-3-3 protein eta OS=Mus musculus GN=Ywhah PE=1 SV=2	Ywhah	0.0065	9	8	10	9	9	11
75	Rabphilin-3A OS=Mus musculus GN=Rph3a PE=1 SV=2	Rph3a	< 0.00010	6	6	6	14	10	12
76	Dynamin-like 120 kDa protein, mitochondrial OS=Mus musculus GN=Opa1 PE=1 SV=1	Opa1	0.00014	0	0	0	16	15	19
77	Cytochrome c oxidase subunit 5B, mitochondrial OS=Mus musculus GN=Cox5b PE=1 SV=1	Cox5b	0.00015	2	0	2	8	9	9
78	DmX-like protein 2 OS=Mus musculus GN=Dmxl2 PE=1 SV=3	Dmxl2	0.0015	8	8	7	15	18	16
79	AP-2 complex subunit mu OS=Mus musculus GN=Ap2m1 PE=1 SV=1	Ap2m1	0.0004	5	5	5	8	7	9
80	Amphiphysin OS=Mus musculus GN=Amph PE=1 SV=1	Amph	0.0051	7	8	3	12	11	13
81	Guanine nucleotide-binding protein G(I)/G(S)/G(T) subunit beta-1 OS=Mus musculus GN=Gnb1 PE=1 SV=3	Gnb1	< 0.00010	8	6	8	11	10	11
82	Succinate dehydrogenase [ubiquinone] flavoprotein subunit, mitochondrial OS=Mus musculus GN=Sdha PE=1 SV=1	Sdha	0.00011	0	0	1	17	16	17
83	ProSAAS OS=Mus musculus GN=Pcsk1n PE=1 SV=2	Pcsk1n	0.0057	5	5	5	8	6	10
84	Cathepsin D OS=Mus musculus GN=Ctsd PE=1 SV=1	Ctsd	0.0008	1	2	2	9	8	7
85	Plasma membrane calcium-transporting ATPase 1 OS=Mus musculus GN=Atp2b1 PE=1 SV=1	Atp2b1	0.00013	5	5	6	14	13	10

86	ATP synthase subunit O, mitochondrial OS=Mus musculus GN=Atp5o PE=1 SV=1	Atp5o	0.00013	0	0	0	10	11	12
87	Protein Ogdhl OS=Mus musculus GN=Ogdhl PE=1 SV=1	Ogdhl	0.00088	0	0	0	11	14	15
88	NADH dehydrogenase [ubiquinone] 1 alpha subcomplex subunit 10, mitochondrial OS=Mus musculus GN=Ndufa10 PE=1 SV=1	Ndufa10	0.00091	0	0	0	9	11	11
89	Aldehyde dehydrogenase, mitochondrial OS=Mus musculus GN=Aldh2 PE=1 SV=1	Aldh2	0.00064	0	0	0	16	15	12
90	Proline-rich transmembrane protein 2 OS=Mus musculus GN=Prrt2 PE=1 SV=1	Prrt2	0.016	2	5	6	7	7	9
91	Trifunctional enzyme subunit alpha, mitochondrial OS=Mus musculus GN=Hadha PE=1 SV=1	Hadha	< 0.00010	0	0	0	11	13	9
92	Sodium/potassium-transporting ATPase subunit beta-1 OS=Mus musculus GN=Atp1b1 PE=1 SV=1	Atp1b1	0.009	6	7	7	8	6	7
93	Immunoglobulin superfamily member 8 OS=Mus musculus GN=Igsf8 PE=1 SV=1	Igsf8	0.00061	5	6	7	9	8	10
94	Septin-11 OS=Mus musculus GN=Sept11 PE=1 SV=4	11-Sep	0.0024	4	3	4	11	12	7
95	Tubulin polymerization-promoting protein OS=Mus musculus GN=Tppp PE=1 SV=1	Tppp	0.003	5	6	1	12	9	9
96	Sodium- and chloride-dependent GABA transporter 3 OS=Mus musculus GN=Slc6a11 PE=1 SV=2	Slc6a11	0.004	5	4	5	8	7	6
97	Cytochrome b-c1 complex subunit 2, mitochondrial OS=Mus musculus GN=Uqcrc2 PE=1 SV=1	Uqcrc2	0.001	0	1	0	9	12	11
98	Neurofascin OS=Mus musculus GN=Nfasc PE=1 SV=1	Nfasc	< 0.00010	3	2	2	13	14	15
99	SRC kinase-signaling inhibitor 1 OS=Mus musculus GN=Srcin1 PE=1 SV=1	Srcin1	0.00024	1	2	0	19	15	18
100	Fumarate hydratase, mitochondrial OS=Mus musculus GN=Fh PE=1 SV=3	Fh	0.0005	0	0	1	8	9	8
101	Complexin-2 OS=Mus musculus GN=Cplx2 PE=1 SV=1	Cplx2	0.014	6	6	3	4	5	5
102	G protein-regulated inducer of neurite outgrowth 1 OS=Mus musculus GN=Gprin1 PE=1 SV=2	Gprin1	0.0011	7	7	10	12	14	14
103	Protein Rab1a OS=Mus musculus GN=Rab1a PE=1 SV=1	Rab1a	0.045	7	5	5	5	5	4

104	10 kDa heat shock protein, mitochondrial OS=Mus musculus GN=Hspe1 PE=1 SV=2	Hspe1	0.00024	1	0	0	8	7	9
105	NADH dehydrogenase [ubiquinone] 1 alpha subcomplex subunit 9, mitochondrial OS=Mus musculus GN=Ndufa9 PE=1 SV=1	Ndufa9	0.00012	0	0	0	11	11	11
106	Cytochrome c, somatic OS=Mus musculus GN=Cycs PE=1 SV=2	Cycs	< 0.00010	0	0	0	7	7	6
107	NADH dehydrogenase [ubiquinone] iron-sulfur protein 2, mitochondrial OS=Mus musculus GN=Ndufs2 PE=1 SV=1	Ndufs2	0.0051	0	0	0	4	6	9
108	Putative adenosylhomocysteinase 2 OS=Mus musculus GN=Ahcyl1 PE=1 SV=1	Ahcyl1	0.0061	8	2	8	9	11	10
109	Ras/Rap GTPase-activating protein SynGAP (Fragment) OS=Mus musculus GN=Syngap1 PE=1 SV=2	Syngap1	0.00035	3	4	0	9	12	10
110	Septin-5 OS=Mus musculus GN=Sept5 PE=1 SV=2	5-Sep	0.0022	2	1	2	8	7	7
111	Guanine nucleotide-binding protein G(I)/G(S)/G(T) subunit beta-2 OS=Mus musculus GN=Gnb2 PE=1 SV=1	Gnb2	0.00033	5	5	5	7	7	7
112	Cytochrome b-c1 complex subunit 1, mitochondrial OS=Mus musculus GN=Uqcrc1 PE=1 SV=2	Uqcrc1	0.00038	0	2	2	5	8	9
113	Septin-6 OS=Mus musculus GN=Sept6 PE=1 SV=4	6-Sep	0.00021	3	3	3	5	7	6
114	NADH dehydrogenase [ubiquinone] 1 alpha subcomplex subunit 12 OS=Mus musculus GN=Ndufa12 PE=1 SV=1	Ndufa12	< 0.00010	0	0	0	8	8	10
115	Actin-related protein 2 OS=Mus musculus GN=Actr2 PE=1 SV=1	Actr2	0.048	6	7	6	7	5	8
116	Clathrin coat assembly protein AP180 OS=Mus musculus GN=Snap91 PE=1 SV=1	Snap91	0.03	5	3	5	6	6	9
117	NADH dehydrogenase [ubiquinone] flavoprotein 2, mitochondrial OS=Mus musculus GN=Ndufv2 PE=1 SV=2	Ndufv2	< 0.00010	0	0	0	8	7	5
118	NADH dehydrogenase [ubiquinone] iron-sulfur protein 3, mitochondrial OS=Mus musculus GN=Ndufs3 PE=1 SV=2	Ndufs3	< 0.00010	0	0	0	9	11	11
119	Dihydrolipoyllysine-residue acetyltransferase component of pyruvate dehydrogenase complex, mitochondrial OS=Mus musculus GN=Dlat PE=1 SV=2	Dlat	0.00045	0	0	0	8	8	12

120	Dihydrolipoyl dehydrogenase, mitochondrial OS=Mus musculus GN=Dld PE=1 SV=2	Dld	< 0.00010	0	0	0	10	12	11
121	Cathepsin B OS=Mus musculus GN=Ctsb PE=1 SV=2	Ctsb	0.014	2	3	3	9	6	9
122	Succinate--CoA ligase [ADP/GDP-forming] subunit alpha, mitochondrial OS=Mus musculus GN=Suclg1 PE=1 SV=4	Suclg1	0.00028	2	2	0	6	5	6
123	Methylmalonate-semialdehyde dehydrogenase [acylating], mitochondrial OS=Mus musculus GN=Aldh6a1 PE=1 SV=1	Aldh6a1	< 0.00010	0	0	0	8	7	9
124	Calcium-transporting ATPase OS=Mus musculus GN=Atp2b3 PE=1 SV=1	Atp2b3	< 0.00010	3	5	6	12	12	14
125	Isocitrate dehydrogenase [NADP], mitochondrial OS=Mus musculus GN=Idh2 PE=1 SV=3	Idh2	< 0.00010	0	0	0	8	7	9
126	Capping protein (Actin filament) muscle Z-line, beta, isoform CRA_a OS=Mus musculus GN=Capzb PE=1 SV=1	Capzb	0.014	6	5	6	4	6	5
127	MICOS complex subunit Mic19 OS=Mus musculus GN=Chchd3 PE=1 SV=1	Chchd3	0.00085	0	0	0	13	10	12
128	Electron transfer flavoprotein subunit alpha, mitochondrial OS=Mus musculus GN=Etfa PE=1 SV=2	Etfa	0.00047	0	0	0	7	6	11
129	Transforming protein RhoA OS=Mus musculus GN=Rhoa PE=1 SV=1	Rhoa	0.00084	4	3	3	6	6	9
130	Solute carrier family 12 member 5 OS=Mus musculus GN=Slc12a5 PE=1 SV=2	Slc12a5	< 0.00010	2	3	3	7	9	9
131	Inositol 1,4,5-trisphosphate receptor type 1 OS=Mus musculus GN=Itpr1 PE=1 SV=2	Itpr1	0.00031	6	3	4	11	13	12
132	AP-2 complex subunit alpha-1 OS=Mus musculus GN=Ap2a1 PE=1 SV=1	Ap2a1	0.031	4	7	3	6	11	9
133	Synaptic vesicle glycoprotein 2A OS=Mus musculus GN=Sv2a PE=1 SV=1	Sv2a	0.0065	7	5	6	9	9	9
134	LETM1 and EF-hand domain-containing protein 1, mitochondrial OS=Mus musculus GN=Letm1 PE=1 SV=1	Letm1	0.0002	0	0	0	9	11	9
135	Sodium- and chloride-dependent GABA transporter 1 OS=Mus musculus GN=Slc6a1 PE=1 SV=2	Slc6a1	0.00017	3	2	1	3	3	3

136	Electron transfer flavoprotein subunit beta OS=Mus musculus GN=Etfb PE=1 SV=3	Etfb	0.00047	0	0	0	7	8	8
137	NADH dehydrogenase [ubiquinone] 1 alpha subcomplex subunit 8 OS=Mus musculus GN=Ndufa8 PE=1 SV=3	Ndufa8	0.00041	0	0	0	5	5	5
138	Phosphate carrier protein, mitochondrial OS=Mus musculus GN=Slc25a3 PE=1 SV=1	Slc25a3	< 0.00010	0	0	0	7	6	7
139	Limbic system-associated membrane protein OS=Mus musculus GN=Lsamp PE=1 SV=1	Lsamp	0.0006	0	2	2	5	5	8
140	ATP synthase subunit d, mitochondrial OS=Mus musculus GN=Atp5h PE=1 SV=3	Atp5h	0.002	0	0	0	6	10	10
141	Transgelin-3 OS=Mus musculus GN=Tagln3 PE=1 SV=1	Tagln3	0.0006	4	5	4	6	8	7
142	Cytochrome c oxidase subunit NDUFA4 OS=Mus musculus GN=Ndufa4 PE=1 SV=2	Ndufa4	0.0026	0	0	0	10	9	9
143	AP-2 complex subunit alpha-2 OS=Mus musculus GN=Ap2a2 PE=1 SV=2	Ap2a2	0.01	5	4	4	6	7	9
144	Complement component 1 Q subcomponent-binding protein, mitochondrial OS=Mus musculus GN=C1qbp PE=1 SV=1	C1qbp	0.0007	0	0	0	5	4	5
145	NADH dehydrogenase [ubiquinone] iron-sulfur protein 6, mitochondrial OS=Mus musculus GN=Ndufs6 PE=1 SV=2	Ndufs6	< 0.00010	0	0	0	8	8	9
146	RAS-related C3 botulinum substrate 1, isoform CRA_a OS=Mus musculus GN=Rac1 PE=1 SV=1	Rac1	< 0.00010	3	3	3	5	6	6
147	Cytochrome b-c1 complex subunit 6, mitochondrial OS=Mus musculus GN=Uqcrh PE=1 SV=2	Uqcrh	0.0001	0	0	0	4	3	3
148	Myelin proteolipid protein OS=Mus musculus GN=Plp1 PE=1 SV=2	Plp1	0.00052	2	3	2	2	3	3
149	Contactin-1 OS=Mus musculus GN=Cntn1 PE=1 SV=1	Cntn1	0.00016	2	1	1	7	8	11
150	Neuronal-specific septin-3 OS=Mus musculus GN=Sept3 PE=1 SV=2	3-Sep	0.00096	2	3	2	6	9	8
151	ATP synthase F(0) complex subunit B1, mitochondrial OS=Mus musculus GN=Atp5f1 PE=1 SV=1	Atp5f1	0.00022	0	1	1	7	7	6
152	Caskin-1 OS=Mus musculus GN=Caskin1 PE=1 SV=2	Caskin1	0.0025	2	3	2	12	11	10
153	3-hydroxyacyl-CoA dehydrogenase type-2 OS=Mus musculus GN=Hsd17b10 PE=1 SV=1	Hsd17b10	0.00025	0	0	0	5	7	6

154	Mitochondrial glutamate carrier 1 OS=Mus musculus GN=Slc25a22 PE=1 SV=1	Slc25a22	< 0.00010	0	0	0	7	7	6
155	Syntaxin-1A OS=Mus musculus GN=Stx1a PE=1 SV=1	Stx1a	< 0.00010	2	2	3	6	7	7
156	Septin-8 OS=Mus musculus GN=Sept8 PE=1 SV=1	8-Sep	0.0014	0	0	0	7	9	8
157	14-3-3 protein gamma OS=Mus musculus GN=Ywhag PE=1 SV=2	Ywhag	0.037	3	3	4	4	7	6
158	NADH dehydrogenase [ubiquinone] 1 alpha subcomplex subunit 7 OS=Mus musculus GN=Ndufa7 PE=1 SV=3	Ndufa7	0.0043	0	0	0	9	9	10
159	ATP synthase subunit gamma OS=Mus musculus GN=Atp5c1 PE=1 SV=1	Atp5c1	0.0031	0	0	0	7	6	8
160	D-beta-hydroxybutyrate dehydrogenase, mitochondrial OS=Mus musculus GN=Bdh1 PE=1 SV=2	Bdh1	0.00051	0	0	0	7	7	6
161	Plectin OS=Mus musculus GN=Plec PE=1 SV=3	Plec	0.012	6	1	1	12	9	10
162	Disks large homolog 4 OS=Mus musculus GN=Dlg4 PE=1 SV=1	Dlg4	< 0.00010	0	1	0	8	8	9
163	Sideroflexin-3 OS=Mus musculus GN=Sfxn3 PE=1 SV=1	Sfxn3	< 0.00010	0	1	0	5	7	5
164	NADH dehydrogenase [ubiquinone] 1 beta subcomplex subunit 4 OS=Mus musculus GN=Ndufb4 PE=1 SV=3	Ndufb4	0.00049	0	0	0	7	6	5
165	Protein NipSnap homolog 2 OS=Mus musculus GN=Gbas PE=1 SV=1	Gbas	< 0.00010	0	0	0	5	5	6
166	Succinate-semialdehyde dehydrogenase, mitochondrial OS=Mus musculus GN=Aldh5a1 PE=1 SV=1	Aldh5a1	< 0.00010	0	0	0	5	6	6
167	Nucleoside diphosphate kinase A OS=Mus musculus GN=Nme1 PE=1 SV=1	Nme1	0.011	0	2	3	3	5	3
168	NADH dehydrogenase [ubiquinone] 1 alpha subcomplex subunit 5 OS=Mus musculus GN=Ndufa5 PE=1 SV=3	Ndufa5	0.00046	0	0	0	4	4	6
169	Cytochrome b-c1 complex subunit Rieske, mitochondrial OS=Mus musculus GN=Uqcrfs1 PE=1 SV=1	Uqcrfs1	< 0.00010	0	0	0	4	4	4
170	NADH dehydrogenase [ubiquinone] iron-sulfur protein 8, mitochondrial OS=Mus musculus GN=Ndufs8 PE=1 SV=1	Ndufs8	0.0033	0	0	0	9	7	9
171	NADH dehydrogenase [ubiquinone] 1 alpha subcomplex subunit 13 OS=Mus musculus GN=Ndufa13 PE=1 SV=3	Ndufa13	0.0032	0	0	0	5	4	3
172	Thiosulfate sulfurtransferase OS=Mus musculus GN=Tst PE=1 SV=3	Tst	< 0.00010	0	0	0	7	5	7

173	Vesicle-associated membrane protein-associated protein A OS=Mus musculus GN=Vapa PE=1 SV=2	Vapa	0.00091	2	2	2	4	3	4
174	3-ketoacyl-CoA thiolase, mitochondrial OS=Mus musculus GN=Acaa2 PE=1 SV=3	Acaa2	< 0.00010	0	0	0	5	9	9
175	ADP/ATP translocase 2 OS=Mus musculus GN=Slc25a5 PE=1 SV=3	Slc25a5	< 0.00010	0	0	0	5	7	8
176	Neurofilament light polypeptide OS=Mus musculus GN=Nefl PE=1 SV=5	Nefl	0.046	1	2	1	6	3	4
177	NADH dehydrogenase [ubiquinone] 1 alpha subcomplex subunit 6 OS=Mus musculus GN=Ndufa6 PE=1 SV=1	Ndufa6	0.0014	1	0	0	3	3	4
178	Cytochrome c oxidase subunit 6B1 OS=Mus musculus GN=Cox6b1 PE=1 SV=2	Cox6b1	0.0018	0	0	0	3	5	5
179	NADH dehydrogenase [ubiquinone] iron-sulfur protein 7, mitochondrial OS=Mus musculus GN=Ndufs7 PE=1 SV=1	Ndufs7	< 0.00010	0	0	0	6	5	5
180	Trifunctional enzyme subunit beta, mitochondrial OS=Mus musculus GN=Hadhb PE=1 SV=1	Hadhb	< 0.00010	0	0	0	4	4	5
181	Serine/threonine-protein phosphatase OS=Mus musculus GN=Ppp3cb PE=1 SV=1	Ppp3cb	0.036	5	4	3	3	5	4
182	Thioredoxin-dependent peroxide reductase, mitochondrial OS=Mus musculus GN=Prdx3 PE=1 SV=1	Prdx3	< 0.00010	0	0	0	6	6	6
183	Ornithine aminotransferase, mitochondrial OS=Mus musculus GN=Oat PE=1 SV=1	Oat	0.0087	0	0	0	8	3	5
184	Lon protease homolog, mitochondrial OS=Mus musculus GN=Lonp1 PE=1 SV=2	Lonp1	0.0007	0	0	0	5	7	5
185	LanC-like protein 2 (Fragment) OS=Mus musculus GN=Lancl2 PE=1 SV=1	Lancl2	0.034	4	2	2	5	6	5
186	Alpha-internexin OS=Mus musculus GN=Ina PE=1 SV=3	Ina	0.0013	1	0	1	6	8	6
187	Guanine nucleotide-binding protein G(i) subunit alpha-2 OS=Mus musculus GN=Gnai2 PE=1 SV=5	Gnai2	0.0012	2	0	2	5	3	6
188	ATP synthase subunit e, mitochondrial OS=Mus musculus GN=Atp5i PE=1 SV=2	Atp5i	0.00047	0	0	0	4	3	3
189	GTPase HRas OS=Mus musculus GN=Hras PE=1 SV=2	Hras	0.0019	0	2	2	5	5	5
190	Neurotrimin OS=Mus musculus GN=Ntm PE=1 SV=1	Ntm	0.0076	3	2	1	7	4	3

191	Leucine-rich PPR motif-containing protein, mitochondrial OS=Mus musculus GN=Lrpprc PE=1 SV=2	Lrpprc	0.0017	0	0	0	8	6	11
192	Basigin (Fragment) OS=Mus musculus GN=Bsg PE=1 SV=1	Bsg	0.014	2	3	3	4	3	4
193	Cytoplasmic FMR1-interacting protein 2 OS=Mus musculus GN=Cyfip2 PE=1 SV=2	Cyfip2	0.0076	3	3	3	5	3	5
194	Brain-specific angiogenesis inhibitor 1-associated protein 2 OS=Mus musculus GN=Baiap2 PE=1 SV=1	Baiap2	< 0.00010	1	0	1	8	8	7
195	Propionyl-CoA carboxylase beta chain, mitochondrial OS=Mus musculus GN=Pccb PE=1 SV=2	Pccb	0.002	0	0	0	6	6	5
196	Oligodendrocyte myelin glycoprotein OS=Mus musculus GN=Omg PE=1 SV=1	Omg	0.0044	2	2	1	3	4	3
197	Long chain acyl-CoA synthetase 6 isoform 3 OS=Mus musculus GN=Acsl6 PE=1 SV=1	Acsl6	0.0017	2	1	2	5	4	6
198	Visinin-like protein 1 OS=Mus musculus GN=Vsnl1 PE=1 SV=2	Vsnl1	0.0015	0	1	0	4	6	5
199	AFG3-like protein 2 OS=Mus musculus GN=Afg3l2 PE=1 SV=1	Afg3l2	0.00019	0	0	0	6	7	5
200	Neuronal membrane glycoprotein M6-a OS=Mus musculus GN=Gpm6a PE=1 SV=1	Gpm6a	0.0021	2	2	2	4	5	3
201	Actin-related protein 2/3 complex subunit 2 OS=Mus musculus GN=Arpc2 PE=1 SV=3	Arpc2	0.039	2	0	3	2	3	3
202	ATP synthase-coupling factor 6, mitochondrial OS=Mus musculus GN=Atp5j PE=1 SV=1	Atp5j	0.0048	0	0	0	4	3	5
203	Enoyl-CoA hydratase, mitochondrial OS=Mus musculus GN=Echs1 PE=1 SV=1	Echs1	0.0027	0	0	0	4	5	7
204	Cytochrome c1, heme protein, mitochondrial OS=Mus musculus GN=Cyc1 PE=1 SV=1	Cyc1	0.016	0	0	0	2	4	3
205	Guanine nucleotide-binding protein G(I)/G(S)/G(O) subunit gamma-3 OS=Mus musculus GN=Gng3 PE=1 SV=1	Gng3	0.021	1	1	1	2	2	2
206	Pyruvate dehydrogenase protein X component, mitochondrial OS=Mus musculus GN=Pdhx PE=1 SV=1	Pdhx	< 0.00010	0	0	0	4	5	5
207	ES1 protein homolog, mitochondrial OS=Mus musculus GN=D10Jhu81e PE=1 SV=1	D10Jhu81e	0.0011	0	0	0	4	5	4

208	Sideroflexin-1 OS=Mus musculus GN=Sfxn1 PE=1 SV=3	Sfxn1	0.0016	0	0	0	5	6	6
209	Mitochondrial 2-oxoglutarate/malate carrier protein OS=Mus musculus GN=Slc25a11 PE=1 SV=3	Slc25a11	0.0044	0	0	0	4	5	4
210	Fumarylacetoacetate hydrolase domain-containing protein 2A OS=Mus musculus GN=Fahd2a PE=1 SV=1	Fahd2a	< 0.00010	0	0	0	3	5	2
211	Ganglioside-induced differentiation-associated protein 1-like 1 OS=Mus musculus GN=Gdap1l1 PE=1 SV=1	Gdap1l1	0.043	0	1	1	2	3	4
212	Methylglutaconyl-CoA hydratase, mitochondrial OS=Mus musculus GN=Auh PE=1 SV=1	Auh	< 0.00010	0	0	0	5	7	6
213	ATP synthase subunit delta, mitochondrial OS=Mus musculus GN=Atp5d PE=1 SV=1	Atp5d	0.0076	0	0	0	3	2	3
214	Secretogranin-2 OS=Mus musculus GN=Scg2 PE=1 SV=1	Scg2	0.0035	3	2	1	6	6	5
215	WD repeat-containing protein 7 OS=Mus musculus GN=Wdr7 PE=1 SV=3	Wdr7	0.00044	0	0	0	5	8	3
216	Very long-chain specific acyl-CoA dehydrogenase, mitochondrial OS=Mus musculus GN=Acadvl PE=1 SV=3	Acadvl	0.0013	0	0	0	6	6	8
217	Propionyl-CoA carboxylase alpha chain, mitochondrial OS=Mus musculus GN=Pcca PE=1 SV=2	Pcca	< 0.00010	0	0	0	4	4	4
218	Cytochrome c oxidase subunit 7A2, mitochondrial OS=Mus musculus GN=Cox7a2 PE=1 SV=2	Cox7a2	0.00046	0	0	0	3	3	3
219	NADH dehydrogenase [ubiquinone] 1 subunit C2 OS=Mus musculus GN=Ndufc2 PE=1 SV=1	Ndufc2	0.0044	0	0	0	4	4	2
220	Calcium-transporting ATPase OS=Mus musculus GN=Atp2b4 PE=1 SV=1	Atp2b4	0.00036	2	2	2	4	4	5
221	CDGSH iron-sulfur domain-containing protein 1 OS=Mus musculus GN=Cisd1 PE=1 SV=1	Cisd1	0.0028	0	1	1	3	3	3
222	Phospholipase D3 OS=Mus musculus GN=Pld3 PE=1 SV=1	Pld3	0.00014	0	0	0	3	2	3
223	Leucine-rich glioma-inactivated protein 1 OS=Mus musculus GN=Lgi1 PE=1 SV=1	Lgi1	0.0031	0	0	0	6	6	4
224	Paralemmin-1 OS=Mus musculus GN=Palm PE=1 SV=1	Palm	0.024	1	2	1	4	3	2
225	Catenin alpha-2 OS=Mus musculus GN=Ctnna2 PE=1 SV=3	Ctnna2	0.019	1	1	0	2	3	5

226	Glycerol-3-phosphate dehydrogenase, mitochondrial OS=Mus musculus GN=Gpd2 PE=1 SV=2	Gpd2	0.00049	0	0	0	4	4	3
227	Cysteine and glycine-rich protein 1 OS=Mus musculus GN=Csrp1 PE=1 SV=3	Csrp1	0.023	0	0	2	4	3	3
228	NADH dehydrogenase [ubiquinone] 1 alpha subcomplex subunit 2 OS=Mus musculus GN=Ndufa2 PE=1 SV=3	Ndufa2	0.0092	1	1	1	3	2	3
229	Disintegrin and metalloproteinase domain-containing protein 22 OS=Mus musculus GN=Adam22 PE=1 SV=2	Adam22	< 0.00010	0	0	0	5	6	4
230	Uncharacterized protein KIAA0513 OS=Mus musculus GN=Kiaa0513 PE=1 SV=1	Kiaa0513	0.0044	0	0	2	7	4	5
231	ATP synthase subunit g, mitochondrial OS=Mus musculus GN=Atp5l PE=1 SV=1	Atp5l	0.0027	0	0	0	2	2	2
232	Protein NipSnap homolog 1 OS=Mus musculus GN=Nipsnap1 PE=1 SV=1	Nipsnap1	0.0058	0	0	0	4	2	4
233	Catenin delta-2 OS=Mus musculus GN=Ctnnd2 PE=1 SV=1	Ctnnd2	0.0013	1	1	1	5	4	6
234	Hepatocyte cell adhesion molecule OS=Mus musculus GN=Hepacam PE=1 SV=2	Hepacam	0.043	2	0	2	2	2	2
235	Neural cell adhesion molecule L1 OS=Mus musculus GN=L1cam PE=1 SV=1	L1cam	0.0013	0	0	0	3	4	4
236	Mitochondrial import receptor subunit TOM22 homolog OS=Mus musculus GN=Tomm22 PE=1 SV=3	Tomm22	0.00044	0	0	0	3	3	4
237	Metaxin-2 OS=Mus musculus GN=Mtx2 PE=1 SV=1	Mtx2	0.0032	0	0	0	2	4	3
238	Ankyrin-2 (Fragment) OS=Mus musculus GN=Ank2 PE=1 SV=2	Ank2	0.0034	1	0	0	3	3	2
239	Homer protein homolog 1 OS=Mus musculus GN=Homer1 PE=1 SV=2	Homer1	0.007	1	0	0	3	6	3
240	Syntaxin-12 OS=Mus musculus GN=Stx12 PE=1 SV=1	Stx12	< 0.00010	0	0	0	3	4	4
241	Mitochondrial import inner membrane translocase subunit Tim9 OS=Mus musculus GN=Timm9 PE=1 SV=1	Timm9	0.0086	0	0	0	4	3	4
242	EH domain-containing protein 3 OS=Mus musculus GN=Ehd3 PE=1 SV=2	Ehd3	0.031	2	1	0	3	5	2
243	Rho-related GTP-binding protein RhoB OS=Mus musculus GN=Rhob PE=1 SV=1	Rhob	0.017	1	1	1	4	3	4

244	Alpha-actinin-1 OS=Mus musculus GN=Actn1 PE=1 SV=1	Actn1	0.013	1	1	0	3	3	3
245	Voltage-dependent anion-selective channel protein 1 OS=Mus musculus GN=Vdac1 PE=1 SV=3	Vdac1	0.0029	0	1	0	2	3	3
246	Succinate dehydrogenase [ubiquinone] iron-sulfur subunit, mitochondrial OS=Mus musculus GN=Sdhb PE=1 SV=1	Sdhb	0.0028	0	0	0	3	6	4
247	Talin-2 OS=Mus musculus GN=Tln2 PE=1 SV=1	Tln2	0.036	3	1	1	3	5	4
248	Breast carcinoma-amplified sequence 1 homolog OS=Mus musculus GN=Bcas1 PE=1 SV=3	Bcas1	0.0039	1	1	0	5	3	4
249	MICOS complex subunit Mic25 OS=Mus musculus GN=Chchd6 PE=1 SV=2	Chchd6	0.011	0	0	0	8	6	3
250	C2 domain-containing protein 2-like OS=Mus musculus GN=C2cd2l PE=1 SV=3	C2cd2l	0.0047	0	2	0	3	5	4
251	Mitochondrial amidoxime reducing component 2 OS=Mus musculus GN=Marc2 PE=1 SV=1	2-Mar	0.0024	0	0	0	4	5	4
252	NADH dehydrogenase [ubiquinone] flavoprotein 3, mitochondrial OS=Mus musculus GN=Ndufv3 PE=1 SV=1	Ndufv3	0.00028	0	0	0	1	1	1
253	Kinesin-like protein OS=Mus musculus GN=Kif2a PE=1 SV=1	Kif2a	0.0052	2	0	0	3	4	4
254	Acyl-CoA dehydrogenase family member 9, mitochondrial OS=Mus musculus GN=Acad9 PE=1 SV=2	Acad9	0.005	0	0	0	5	6	3
255	Synaptic vesicle glycoprotein 2B OS=Mus musculus GN=Sv2b PE=1 SV=1	Sv2b	0.031	0	0	0	2	3	7
256	Inorganic pyrophosphatase 2, mitochondrial OS=Mus musculus GN=Ppa2 PE=1 SV=1	Ppa2	0.0026	0	0	1	3	3	4
257	Prohibitin-2 OS=Mus musculus GN=Phb2 PE=1 SV=1	Phb2	0.0013	0	0	0	3	5	5
258	Protein Pcdh1 OS=Mus musculus GN=Pcdh1 PE=1 SV=1	Pcdh1	0.0059	0	0	0	5	4	3
259	Succinate--CoA ligase [GDP-forming] subunit beta, mitochondrial OS=Mus musculus GN=Suclg2 PE=1 SV=3	Suclg2	0.0059	0	0	0	5	3	3
260	Disintegrin and metalloproteinase domain-containing protein 23 OS=Mus musculus GN=Adam23 PE=1 SV=1	Adam23	0.00051	0	0	0	4	4	4

261	Vesicular inhibitory amino acid transporter OS=Mus musculus GN=Slc32a1 PE=1 SV=3	Slc32a1	0.015	0	0	0	3	2	2
262	Neurofilament heavy polypeptide OS=Mus musculus GN=Nefh PE=1 SV=3	Nefh	0.0059	1	0	0	4	3	2
263	Ganglioside-induced differentiation-associated protein 1 OS=Mus musculus GN=Gdap1 PE=1 SV=1	Gdap1	0.00044	0	0	0	4	6	6
264	Mitochondrial glutamate carrier 2 OS=Mus musculus GN=Slc25a18 PE=1 SV=4	Slc25a18	0.00085	0	0	0	3	3	4
265	Casein kinase II subunit alpha OS=Mus musculus GN=Csnk2a1 PE=1 SV=2	Csnk2a1	0.03	0	0	0	1	2	4
266	3-hydroxyisobutyryl-CoA hydrolase, mitochondrial OS=Mus musculus GN=Hibch PE=1 SV=1	Hibch	0.019	0	0	0	2	1	3
267	Acyl-coenzyme A thioesterase 13 OS=Mus musculus GN=Acot13 PE=1 SV=1	Acot13	0.0085	0	0	0	1	1	3
268	Homer protein homolog 3 OS=Mus musculus GN=Homer3 PE=1 SV=2	Homer3	0.0073	0	1	1	3	2	4
269	Phospholemman OS=Mus musculus GN=Fxyd1 PE=1 SV=1	Fxyd1	0.014	1	1	1	1	1	1
270	Adenylate kinase 4, mitochondrial OS=Mus musculus GN=Ak4 PE=1 SV=1	Ak4	0.0043	0	0	0	3	2	3
271	NADH dehydrogenase [ubiquinone] flavoprotein 3, mitochondrial OS=Mus musculus GN=Ndufv3 PE=1 SV=1	Ndufv3	< 0.00010	0	0	0	3	2	3
272	Alpha-soluble NSF attachment protein OS=Mus musculus GN=Napa PE=1 SV=1	Napa	0.023	2	0	1	2	3	4
273	Guanine nucleotide-binding protein G(i) subunit alpha-1 OS=Mus musculus GN=Gnai1 PE=1 SV=1	Gnai1	0.0012	1	1	1	1	2	2
274	Intercellular adhesion molecule 5 OS=Mus musculus GN=Icam5 PE=1 SV=2	Icam5	0.00024	1	0	0	4	4	4
275	Heat shock protein 75 kDa, mitochondrial OS=Mus musculus GN=Trap1 PE=1 SV=1	Trap1	< 0.00010	0	0	0	3	3	4
276	Delta-1-pyrroline-5-carboxylate dehydrogenase, mitochondrial OS=Mus musculus GN=Aldh4a1 PE=1 SV=3	Aldh4a1	0.012	0	0	0	4	2	2
277	Thioredoxin, mitochondrial (Fragment) OS=Mus musculus GN=Txn2 PE=1 SV=1	Txn2	0.006	0	0	0	2	2	2

278	Neurocalcin-delta OS=Mus musculus GN=Ncald PE=1 SV=4	Ncald	0.011	0	0	0	1	2	3
279	Synapsin-3 OS=Mus musculus GN=Syn3 PE=1 SV=2	Syn3	0.016	0	2	0	4	2	2
280	Peptidyl-prolyl cis-trans isomerase D OS=Mus musculus GN=Ppid PE=1 SV=3	Ppid	0.0015	0	0	1	1	1	2
281	Voltage-dependent calcium channel subunit alpha-2/delta-1 OS=Mus musculus GN=Cacna2d1 PE=1 SV=1	Cacna2d1	0.0043	0	0	0	3	6	5
282	Ankyrin repeat and sterile alpha motif domain-containing protein 1B OS=Mus musculus GN=Anks1b PE=1 SV=1	Anks1b	0.00068	0	0	0	3	2	3
283	Glutamate decarboxylase 2 OS=Mus musculus GN=Gad2 PE=1 SV=1	Gad2	0.0012	0	0	0	3	2	3
284	Neuroligin-2 OS=Mus musculus GN=Nlgn2 PE=1 SV=2	Nlgn2	0.00023	1	1	1	1	3	3
285	SH3 and multiple ankyrin repeat domains protein 1 OS=Mus musculus GN=Shank1 PE=1 SV=1	Shank1	0.016	1	1	0	1	2	1
286	Histidine triad nucleotide-binding protein 2, mitochondrial OS=Mus musculus GN=Hint2 PE=1 SV=1	Hint2	0.024	0	0	0	1	3	1
287	Ras-related protein Rab-35 OS=Mus musculus GN=Rab35 PE=1 SV=1	Rab35	0.036	0	1	0	3	3	3
288	Ras-related protein Ral-A OS=Mus musculus GN=Rala PE=1 SV=1	Rala	0.0076	0	1	0	3	2	3
289	Sodium channel protein OS=Mus musculus GN=Scn2a PE=1 SV=1	Scn2a	0.00046	1	0	0	3	3	3
290	Glutaredoxin-related protein 5, mitochondrial OS=Mus musculus GN=Glrx5 PE=1 SV=2	Glrx5	0.00044	0	0	0	2	3	3
291	OCIA domain-containing protein 1 (Fragment) OS=Mus musculus GN=Ociad1 PE=1 SV=1	Ociad1	0.03	0	0	0	3	1	2
292	Lymphocyte antigen 6H OS=Mus musculus GN=Ly6h PE=1 SV=2	Ly6h	< 0.00010	0	0	0	2	1	2
293	Contactin-associated protein-like 2 OS=Mus musculus GN=Cntnap2 PE=1 SV=2	Cntnap2	< 0.00010	0	0	0	2	3	3
294	Guanine nucleotide-binding protein G(z) subunit alpha OS=Mus musculus GN=Gnaz PE=1 SV=4	Gnaz	0.019	0	2	1	2	2	2
295	Trans-2-enoyl-CoA reductase, mitochondrial OS=Mus musculus GN=Mecr PE=1 SV=2	Mecr	0.00063	0	0	0	2	2	3
296	MCG9827 OS=Mus musculus GN=Opcml PE=1 SV=1	Opcml	0.022	0	0	0	2	2	2

297	Voltage-dependent anion-selective channel protein 2 (Fragment) OS=Mus musculus GN=Vdac2 PE=1 SV=1	Vdac2	0.0045	0	0	1	2	3	3
298	Neuroligin-3 OS=Mus musculus GN=Nlgn3 PE=1 SV=1	Nlgn3	0.0059	0	0	0	3	2	2
299	Anion exchange protein OS=Mus musculus GN=Slc4a10 PE=1 SV=1	Slc4a10	0.0024	0	0	0	2	3	2
300	ATP-dependent Clp protease proteolytic subunit, mitochondrial OS=Mus musculus GN=Clpp PE=1 SV=1	Clpp	0.0007	0	0	0	2	3	2
301	Probable G-protein coupled receptor 158 OS=Mus musculus GN=Gpr158 PE=1 SV=2	Gpr158	< 0.00010	0	0	0	3	4	3
302	Spectrin beta 1 OS=Mus musculus GN=Sptb PE=1 SV=1	Sptb	0.042	1	1	1	3	1	4
303	Synaptotagmin-1 OS=Mus musculus GN=Syt1 PE=1 SV=1	Syt1	0.0015	0	0	1	3	3	2
304	2,4-dienoyl-CoA reductase, mitochondrial OS=Mus musculus GN=Decr1 PE=1 SV=1	Decr1	< 0.00010	0	0	0	2	2	2
305	Neutral amino acid transporter A OS=Mus musculus GN=Slc1a4 PE=1 SV=1	Slc1a4	0.0003	0	0	0	1	1	1
306	Toll-interacting protein OS=Mus musculus GN=Tollip PE=1 SV=1	Tollip	0.036	1	1	1	2	2	2
307	Programmed cell death protein 5 OS=Mus musculus GN=Pdcd5 PE=1 SV=3	Pdcd5	0.013	1	0	1	2	2	2
308	Guanine nucleotide-binding protein G(s) subunit alpha isoforms XLas OS=Mus musculus GN=Gnas PE=1 SV=1	Gnas	0.0071	1	0	1	1	1	1
309	Contactin-2 OS=Mus musculus GN=Cntn2 PE=1 SV=2	Cntn2	0.017	0	1	1	2	2	2
310	Adenosylhomocysteinase OS=Mus musculus GN=Ahcyl2 PE=1 SV=1	Ahcyl2	0.0009	1	1	2	2	2	3
311	Gamma-aminobutyric acid type B receptor subunit 2 OS=Mus musculus GN=Gabbr2 PE=1 SV=2	Gabbr2	0.0085	0	0	0	2	2	4
312	OX-2 membrane glycoprotein OS=Mus musculus GN=Cd200 PE=1 SV=1	Cd200	0.00063	0	0	0	2	2	3
313	ATP synthase subunit f, mitochondrial OS=Mus musculus GN=Atp5j2 PE=1 SV=3	Atp5j2	0.019	0	0	0	1	2	2
314	Cytochrome c oxidase subunit 5A, mitochondrial OS=Mus musculus GN=Cox5a PE=1 SV=2	Cox5a	< 0.00010	0	0	0	1	1	1

315	Mitochondrial import inner membrane translocase subunit TIM50 OS=Mus musculus GN=Timm50 PE=1 SV=1	Timm50	0.00058	0	0	0	3	3	3
316	Microtubule-actin cross-linking factor 1 OS=Mus musculus GN=Macf1 PE=1 SV=1	Macf1	0.0043	1	1	1	2	2	3
317	Contactin-associated protein 1 OS=Mus musculus GN=Cntnap1 PE=1 SV=2	Cntnap1	0.0027	0	0	0	2	3	4
318	Mitochondrial fission 1 protein OS=Mus musculus GN=Fis1 PE=1 SV=1	Fis1	0.048	0	1	0	2	2	1
319	Electron transfer flavoprotein-ubiquinone oxidoreductase, mitochondrial OS=Mus musculus GN=Etfdh PE=1 SV=1	Etfdh	0.011	0	0	0	4	2	3
320	Regulating synaptic membrane exocytosis protein 1 OS=Mus musculus GN=Rims1 PE=1 SV=2	Rims1	0.027	0	0	0	3	2	1
321	Protein Tmed7 OS=Mus musculus GN=Tmed7 PE=1 SV=1	Tmed7	0.0044	0	0	0	2	3	3
322	ATPase family AAA domain-containing protein 3 OS=Mus musculus GN=Atad3 PE=1 SV=1	Atad3	0.027	0	0	0	2	1	1
323	Hydroxyacyl-coenzyme A dehydrogenase, mitochondrial OS=Mus musculus GN=Hadh PE=1 SV=2	Hadh	0.0024	0	0	0	1	2	1
324	Metabotropic glutamate receptor 3 OS=Mus musculus GN=Grm3 PE=1 SV=1	Grm3	0.0021	0	0	0	3	2	4
325	Palmitoyl-protein thioesterase 1 OS=Mus musculus GN=Ppt1 PE=1 SV=2	Ppt1	0.00044	0	0	0	2	3	3
326	Citrate lyase subunit beta-like protein, mitochondrial OS=Mus musculus GN=Clybl PE=1 SV=2	Clybl	0.00063	0	0	0	2	2	2
327	Ribosome-recycling factor, mitochondrial OS=Mus musculus GN=Mrrf PE=1 SV=1	Mrrf	0.00063	0	0	0	2	2	3
328	Cytochrome b-c1 complex subunit 9 OS=Mus musculus GN=Uqcr10 PE=1 SV=1	Uqcr10	0.024	0	0	0	1	1	1
329	Dolichyl-diphosphooligosaccharide--protein glycosyltransferase subunit 1 OS=Mus musculus GN=Rpn1 PE=1 SV=1	Rpn1	0.02	0	0	1	2	2	2
330	Glutamate receptor 3 OS=Mus musculus GN=Gria3 PE=1 SV=1	Gria3	0.0024	0	0	0	2	2	2

331	Mitochondrial import inner membrane translocase subunit Tim13 OS=Mus musculus GN=Timm13 PE=1 SV=1	Timm13	0.0044	0	0	0	1	1	2
332	L-2-hydroxyglutarate dehydrogenase, mitochondrial OS=Mus musculus GN=L2hgdh PE=1 SV=1	L2hgdh	0.0019	0	0	0	2	2	3
333	Prohibitin OS=Mus musculus GN=Phb PE=1 SV=1	Phb	< 0.00010	0	0	0	1	1	1
334	NADH dehydrogenase [ubiquinone] iron-sulfur protein 4, mitochondrial OS=Mus musculus GN=Ndufs4 PE=1 SV=1	Ndufs4	0.0085	0	0	0	2	1	2
335	Large neutral amino acids transporter small subunit 1 OS=Mus musculus GN=Slc7a5 PE=1 SV=2	Slc7a5	0.00063	0	0	0	1	1	1
336	Neuroligin 4-like OS=Mus musculus GN=Nlgn4l PE=1 SV=1	Nlgn4l	0.0003	1	1	1	1	1	1
337	Serine/threonine-protein kinase BRSK1 OS=Mus musculus GN=Brsk1 PE=1 SV=1	Brsk1	0.016	0	0	0	1	2	3
338	Actin-related protein 2/3 complex subunit 3 OS=Mus musculus GN=Arpc3 PE=1 SV=3	Arpc3	0.0085	0	0	0	1	1	2
339	Mitofusin-2 OS=Mus musculus GN=Mfn2 PE=1 SV=3	Mfn2	0.016	0	0	0	1	2	3
340	Cysteine desulfurase, mitochondrial OS=Mus musculus GN=Nfs1 PE=1 SV=3	Nfs1	0.049	0	0	0	1	1	2
341	ARF6 guanine nucleotide exchange factor IQArfGEF OS=Mus musculus GN=Iqsec2 PE=1 SV=1	Iqsec2	0.027	0	0	0	3	2	2
342	MICOS complex subunit MIC60 OS=Mus musculus GN=Immt PE=1 SV=1	Immt	0.00019	0	0	0	1	1	1
343	Glutamate receptor 2 OS=Mus musculus GN=Gria2 PE=1 SV=1	Gria2	0.0023	0	0	0	1	1	1
344	NADH dehydrogenase [ubiquinone] iron-sulfur protein 5 OS=Mus musculus GN=Ndufs5 PE=1 SV=3	Ndufs5	0.0027	0	0	0	2	3	3
345	Endophilin-A3 OS=Mus musculus GN=Sh3gl3 PE=1 SV=1	Sh3gl3	0.027	0	0	0	2	1	1
346	Potassium voltage-gated channel subfamily A member 1 OS=Mus musculus GN=Kcna1 PE=1 SV=1	Kcna1	0.012	1	0	1	1	2	2
347	Pyridoxal phosphate phosphatase OS=Mus musculus GN=Pdxp PE=1 SV=1	Pdxp	0.0044	0	0	0	1	2	2
348	Up-regulated during skeletal muscle growth protein 5 OS=Mus musculus GN=Usmg5 PE=1 SV=1	Usmg5	0.0024	0	0	0	2	2	2

349	Monoacylglycerol lipase ABHD12 OS=Mus musculus GN=Abhd12 PE=1 SV=2	Abhd12	0.0074	0	0	1	1	2	2
350	Catechol O-methyltransferase domain-containing protein 1 OS=Mus musculus GN=Comtd1 PE=1 SV=1	Comtd1	0.049	0	0	0	1	1	3
351	Arfaptin-2 OS=Mus musculus GN=Arfip2 PE=1 SV=2	Arfip2	0.032	0	1	0	1	2	1
352	Serine/threonine-protein kinase MARK2 (Fragment) OS=Mus musculus GN=Mark2 PE=1 SV=1	Mark2	0.019	0	0	0	2	1	3
353	MICOS complex subunit (Fragment) OS=Mus musculus GN=Chchd3 PE=1 SV=1	Chchd3	0.00038	0	1	0	1	1	1
354	Leucine-rich repeat-containing protein 7 OS=Mus musculus GN=Lrrc7 PE=1 SV=1	Lrrc7	0.0087	0	0	0	1	1	2
355	Long-chain-fatty-acid--CoA ligase 1 OS=Mus musculus GN=Acsl1 PE=1 SV=2	Acsl1	0.0085	0	0	0	1	1	2
356	GTPase NRas (Fragment) OS=Mus musculus GN=Nras PE=1 SV=1	Nras	0.00022	0	0	0	1	1	1
357	Thioredoxin-related transmembrane protein 2 OS=Mus musculus GN=Tmx2 PE=1 SV=1	Tmx2	0.024	0	0	0	1	2	2
358	ATPase family AAA domain-containing protein 1 OS=Mus musculus GN=Atad1 PE=1 SV=1	Atad1	0.027	0	0	0	2	1	1
359	Calcium-transporting ATPase OS=Mus musculus GN=Atp2b2 PE=1 SV=1	Atp2b2	< 0.00010	1	1	1	1	1	1
360	WD repeat-containing protein 37 OS=Mus musculus GN=Wdr37 PE=1 SV=1	Wdr37	0.016	0	0	0	1	1	1
361	Cytochrome b5 OS=Mus musculus GN=Cyb5a PE=1 SV=2	Cyb5a	0.0085	0	0	0	1	1	2
362	Regulating synaptic membrane exocytosis protein 1 (Fragment) OS=Mus musculus GN=Rims1 PE=1 SV=3	Rims1	0.0014	0	0	0	1	1	1
363	Peptidyl-prolyl cis-trans isomerase FKBP8 OS=Mus musculus GN=Fkbp8 PE=1 SV=2	Fkbp8	0.027	0	0	0	2	1	1
364	Radixin OS=Mus musculus GN=Rdx PE=1 SV=3	Rdx	0.0085	0	0	0	1	1	1
365	Leucine-rich repeat and immunoglobulin-like domain-containing nogo receptor-interacting protein 1 OS=Mus musculus GN=Lingo1 PE=1 SV=1	Lingo1	0.016	0	0	0	1	1	1
366	Metabotropic glutamate receptor 2 OS=Mus musculus GN=Grm2 PE=1 SV=2	Grm2	< 0.00010	0	0	0	2	2	2

367	Aspartyl/asparaginyl beta-hydroxylase OS=Mus musculus GN=Asph PE=1 SV=1	Asph	0.0085	0	0	0	1	1	2
368	Dehydrogenase/reductase SDR family member 1 OS=Mus musculus GN=Dhrs1 PE=1 SV=1	Dhrs1	0.028	0	0	0	2	3	1
369	Ras-related protein Rab-3B OS=Mus musculus GN=Rab3b PE=1 SV=1	Rab3b	0.0058	0	0	0	1	1	1
370	Phosphatidylinositol 4-kinase alpha OS=Mus musculus GN=Pi4ka PE=1 SV=2	Pi4ka	0.028	0	0	0	2	3	1
371	Apoptosis-inducing factor 1, mitochondrial OS=Mus musculus GN=Aifm1 PE=1 SV=1	Aifm1	< 0.00010	0	0	0	1	1	1
372	Synaptogyrin-1 OS=Mus musculus GN=Syngr1 PE=1 SV=2	Syngr1	< 0.00010	0	0	0	1	1	1
373	Bcl-2-like protein 13 OS=Mus musculus GN=Bcl2l13 PE=1 SV=2	Bcl2l13	< 0.00010	0	0	0	1	1	1
374	Versican core protein OS=Mus musculus GN=Vcan PE=1 SV=2	Vcan	0.027	0	0	0	2	1	1
375	Tricarboxylate transport protein, mitochondrial OS=Mus musculus GN=Slc25a1 PE=1 SV=1	Slc25a1	< 0.00010	0	0	0	2	2	2
376	28S ribosomal protein S28, mitochondrial OS=Mus musculus GN=Mrps28 PE=1 SV=1	Mrps28	0.037	0	0	0	2	2	1
377	Non-specific lipid-transfer protein OS=Mus musculus GN=Scp2 PE=1 SV=3	Scp2	< 0.00010	0	0	0	1	1	1
378	Ras-related protein Rab-33B OS=Mus musculus GN=Rab33b PE=1 SV=1	Rab33b	0.00081	0	0	0	1	1	1
379	Receptor-type tyrosine-protein phosphatase alpha OS=Mus musculus GN=Ptpra PE=1 SV=3	Ptpra	< 0.00010	0	0	0	1	1	1
380	Acyl-coenzyme A thioesterase THEM4 OS=Mus musculus GN=Them4 PE=1 SV=1	Them4	< 0.00010	0	0	0	1	1	1
381	Serine/threonine-protein phosphatase 2A catalytic subunit alpha isoform OS=Mus musculus GN=Ppp2ca PE=1 SV=1	Ppp2ca	0.0085	0	0	0	1	1	2
382	Voltage-dependent calcium channel subunit alpha-2/delta-2 OS=Mus musculus GN=Cacna2d2 PE=1 SV=2	Cacna2d2	0.027	0	0	0	2	1	1
383	UPF0598 protein C8orf82 homolog OS=Mus musculus PE=1 SV=1		< 0.00010	0	0	0	1	1	1

384	Tumor protein D52 (Fragment) OS=Mus musculus GN=Tpd52 PE=1 SV=1	Tpd52	< 0.00010	0	0	0	1	1	1
385	Neuronal proto-oncogene tyrosine-protein kinase Src OS=Mus musculus GN=Src PE=1 SV=1	Src	< 0.00010	0	0	0	1	1	1
386	Hydroxymethylglutaryl-CoA lyase, mitochondrial OS=Mus musculus GN=Hmgcl PE=1 SV=2	Hmgcl	< 0.00010	0	0	0	1	1	1
387	Vacuolar protein sorting-associated protein 51 homolog OS=Mus musculus GN=Vps51 PE=1 SV=2	Vps51	< 0.00010	0	0	0	1	1	1
388	Thioredoxin OS=Mus musculus GN=Txn PE=1 SV=3	Txn	0.0085	0	0	0	1	1	2
389	Cathepsin L1 OS=Mus musculus GN=Ctsl PE=1 SV=2	Ctsl	0.0087	0	0	0	1	1	1
390	Protein phosphatase 1 regulatory subunit 21 OS=Mus musculus GN=Ppp1r21 PE=1 SV=2	Ppp1r21	< 0.00010	0	0	0	1	1	1
391	CD166 antigen (Fragment) OS=Mus musculus GN=Alcam PE=1 SV=1	Alcam	< 0.00010	0	0	0	1	1	1
392	Actin-related protein 3B OS=Mus musculus GN=Actr3b PE=1 SV=1	Actr3b	0.024	0	0	0	1	1	1
393	Ras-related protein Rab-8A OS=Mus musculus GN=Rab8a PE=1 SV=2	Rab8a	0.00057	0	0	0	1	1	1
394	SH2 domain-containing adapter protein F (Fragment) OS=Mus musculus GN=Shf PE=1 SV=1	Shf	< 0.00010	0	0	0	1	1	1
395	Methionine--tRNA ligase, mitochondrial OS=Mus musculus GN=Mars2 PE=1 SV=2	Mars2	< 0.00010	0	0	0	1	1	1

Appendix D

Flow cytometry graphs from MPS IIIC mice whole blood 6 weeks after transplantation with LV-treated HSPC

MPS IIIC #6600 Female

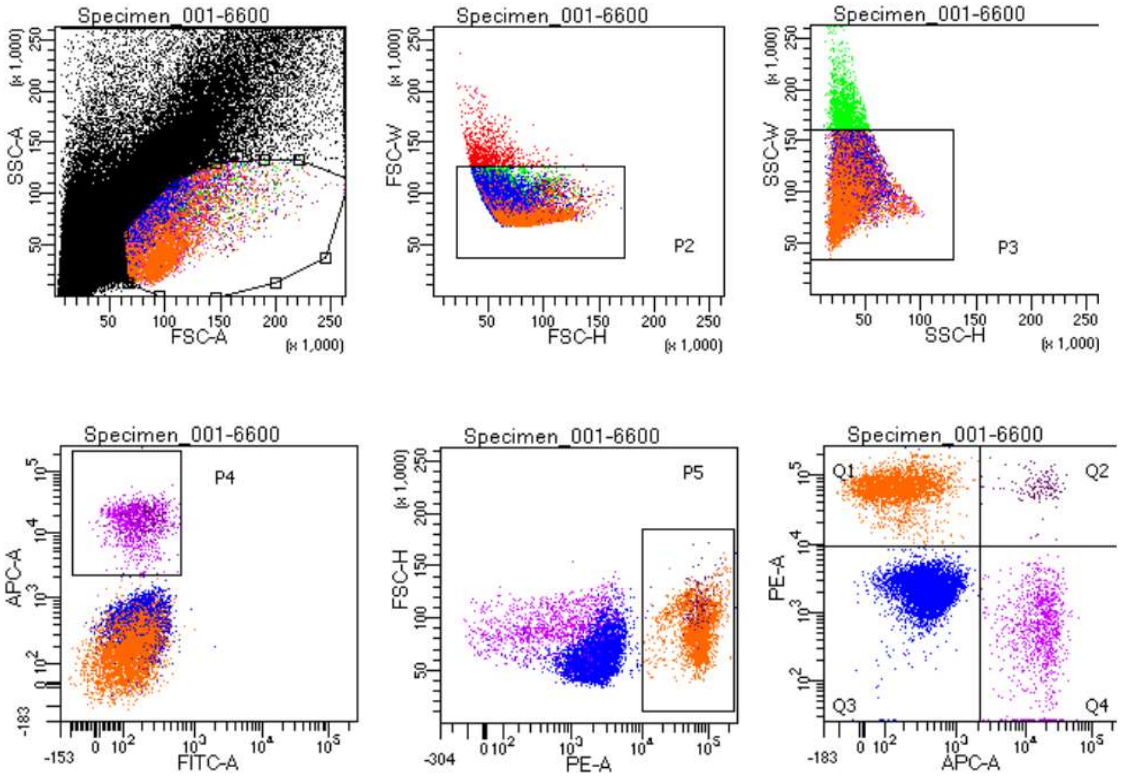

Tube: 6600

Population	#Events	%Parent	%Total
All Events	2,055,645	####	100.0
P1	11,874	0.6	0.6
P2	11,102	93.5	0.5
P3	9,839	88.6	0.5
P4	1,122	11.4	0.1
P5	3,305	33.6	0.2
Q1	3,171	32.2	0.2
Q2	138	1.4	0.0
Q3	5,542	56.3	0.3
Q4	988	10.0	0.0

MPS IIIC #6601 Female

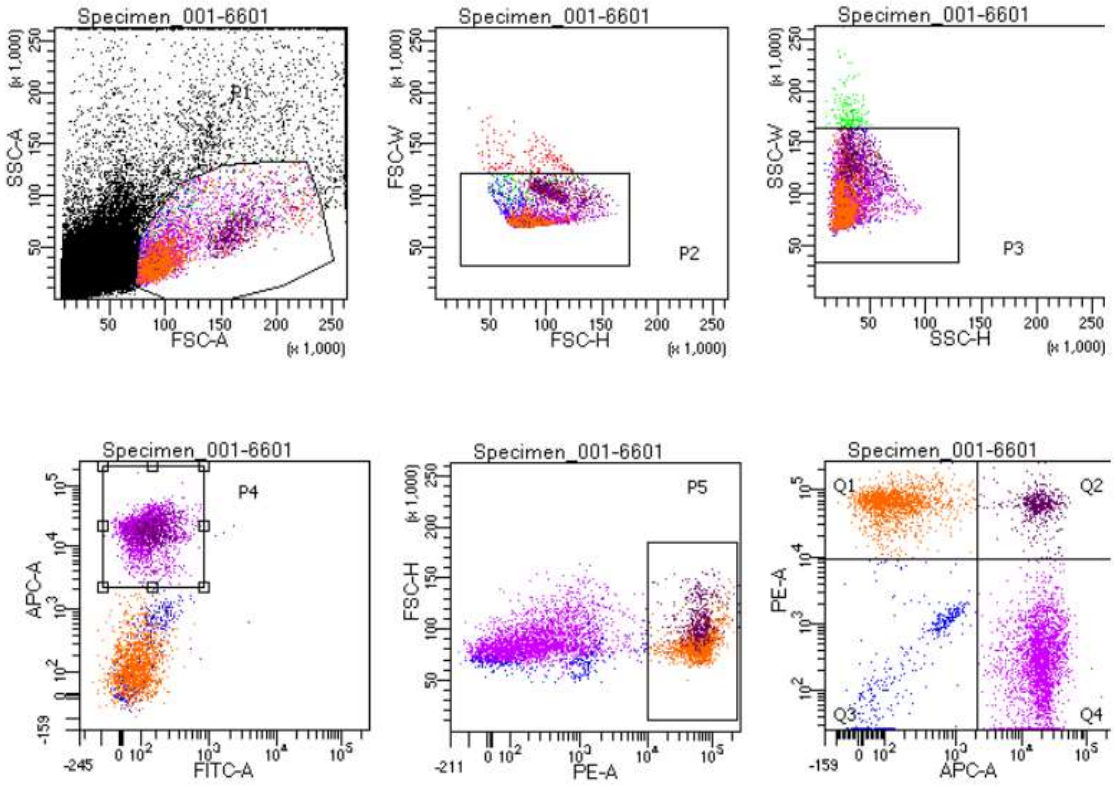

Tube: 6601

Population	#Events	%Parent	%Total
All Events	272,996	####	100.0
P1	5,223	1.9	1.9
P2	5,072	97.1	1.9
P3	4,908	96.8	1.8
P4	2,991	60.9	1.1
P5	1,970	40.1	0.7
Q1	1,515	30.9	0.6
Q2	465	9.5	0.2
Q3	397	8.1	0.1
Q4	2,531	51.6	0.9

MPS IIIC #6598 Male

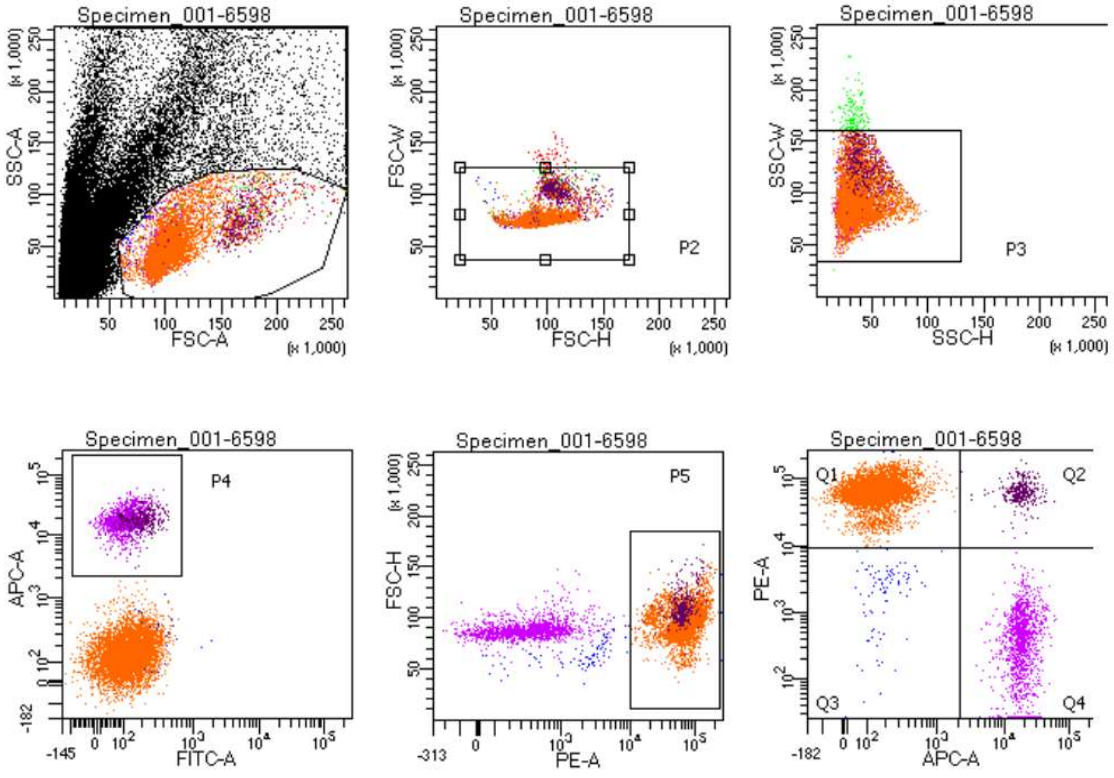

Tube: 6598

Population	#Events	%Parent	%Total
All Events	388,047	####	100.0
P1	7,588	2.0	2.0
P2	7,536	99.3	1.9
P3	7,398	98.2	1.9
P4	1,794	24.2	0.5
P5	5,872	79.4	1.5
Q1	5,515	74.5	1.4
Q2	361	4.9	0.1
Q3	89	1.2	0.0
Q4	1,433	19.4	0.4

MPS IIIC #6599 Male

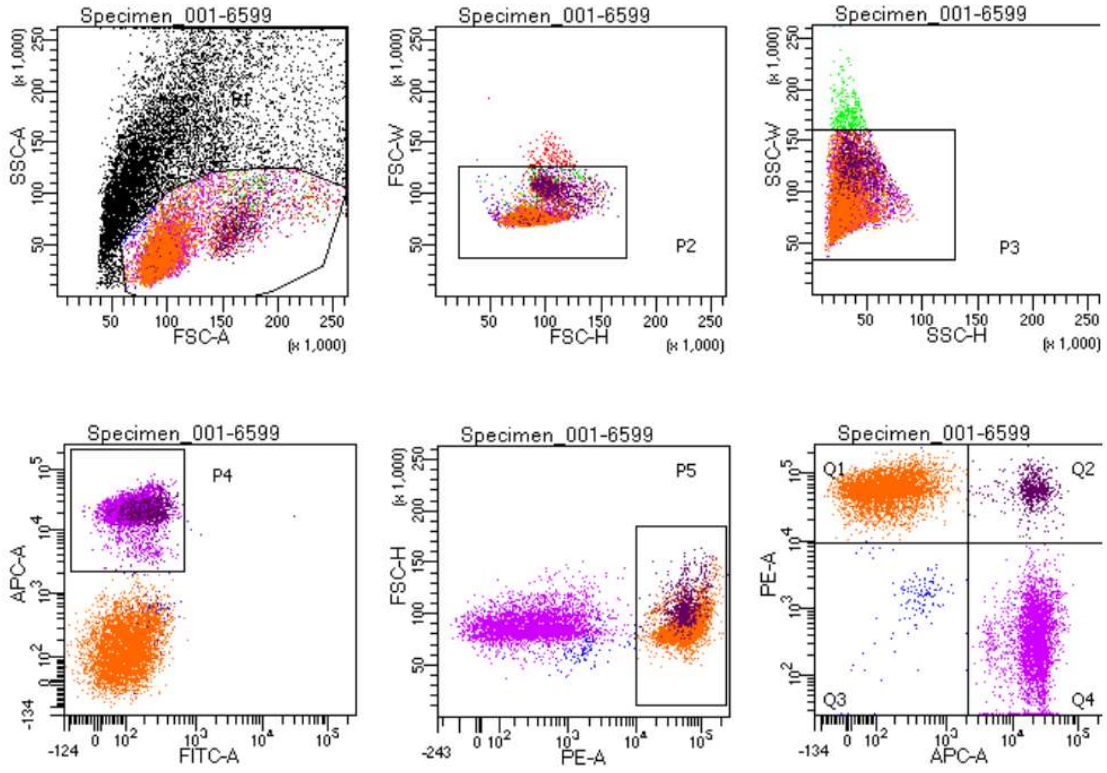

Tube: 6599

Population	#Events	%Parent	%Total
All Events	21,936	####	100.0
P1	9,451	43.1	43.1
P2	9,320	98.6	42.5
P3	9,019	96.8	41.1
P4	4,151	46.0	18.9
P5	5,451	60.4	24.8
Q1	4,726	52.4	21.5
Q2	730	8.1	3.3
Q3	136	1.5	0.6
Q4	3,427	38.0	15.6

Appendix E

Flow cytometry graphs from MPS IIIC mice whole blood 13 weeks after transplantation with LV-treated HSPC

MPS IIIC #6601 Female

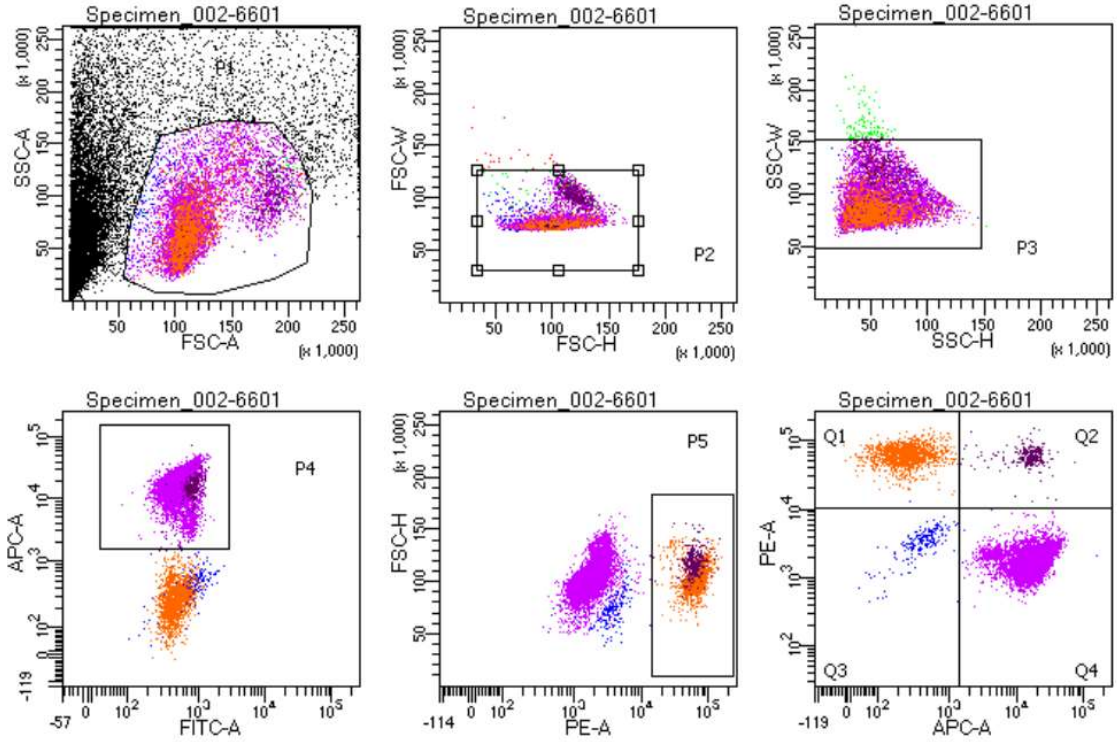

Tube: 6601

Population	#Events	%Parent	%Total
All Events	30,402	####	100.0
P1	9,892	32.5	32.5
P2	9,868	99.8	32.5
P3	9,751	98.8	32.1
P4	8,044	82.5	26.5
P5	1,794	18.4	5.9
Q1	1,503	15.4	4.9
Q2	294	3.0	1.0
Q3	199	2.0	0.7
Q4	7,755	79.5	25.5

MPS IIIC #6598 Male

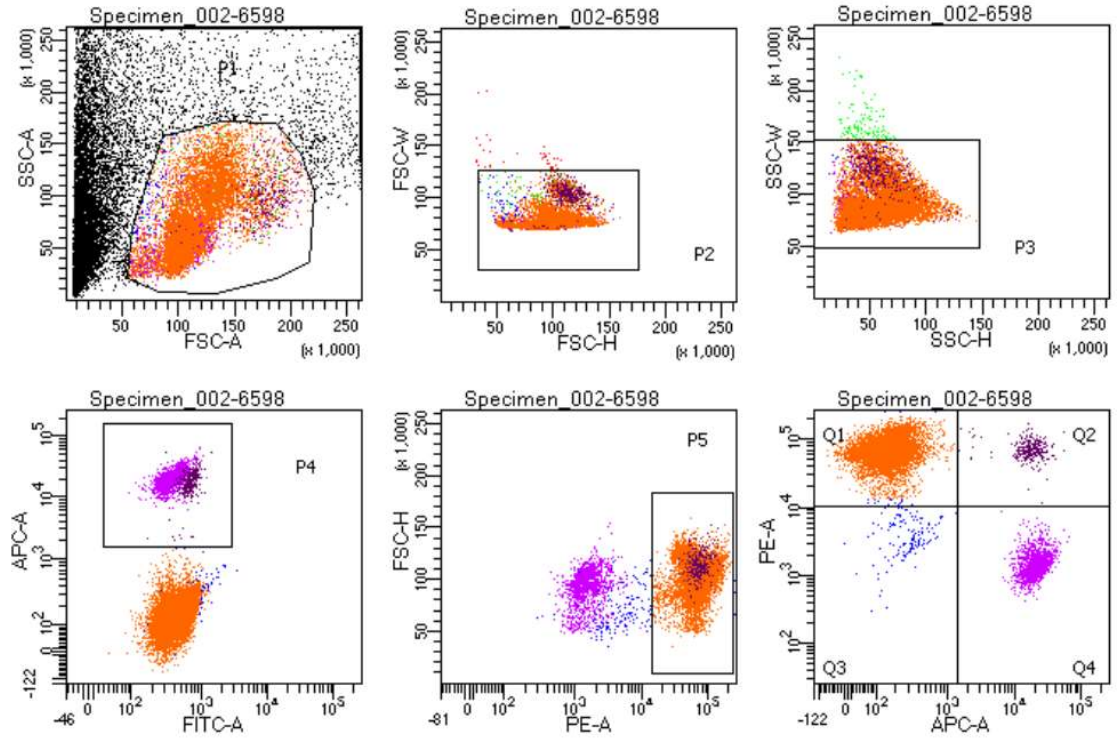

Tube: 6598

Population	#Events	%Parent	%Total
All Events	29,474	####	100.0
P1	9,893	33.6	33.6
P2	9,852	99.6	33.4
P3	9,738	98.8	33.0
P4	1,653	17.0	5.6
P5	8,209	84.3	27.9
Q1	7,947	81.6	27.0
Q2	284	2.9	1.0
Q3	136	1.4	0.5
Q4	1,371	14.1	4.7

MPS IIIC #6599 Male

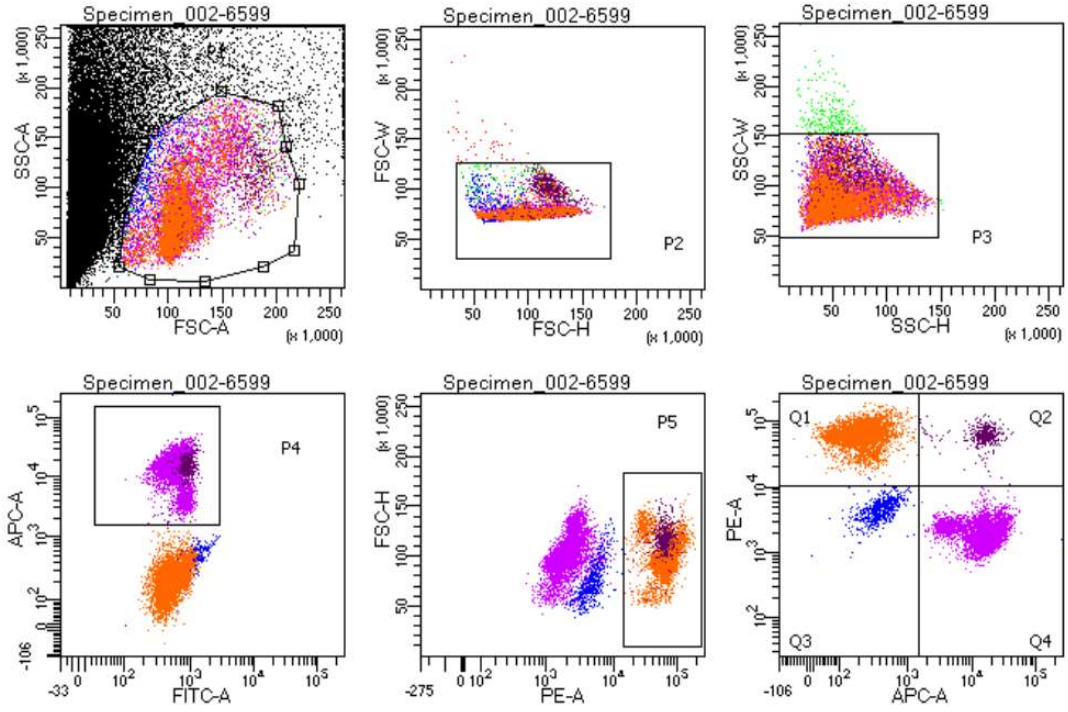

Tube: 6599

Population	#Events	%Parent	%Total
All Events	110,680	####	100.0
P1	10,309	9.3	9.3
P2	10,269	99.6	9.3
P3	10,036	97.7	9.1
P4	5,026	50.1	4.5
P5	4,811	47.9	4.3
Q1	4,410	43.9	4.0
Q2	407	4.1	0.4
Q3	595	5.9	0.5
Q4	4,624	46.1	4.2